

The effect of metallurgical structure on the chloride-induced corrosion of archaeological wrought iron

Eric A.S. Nordgren

Thesis submitted to Cardiff University in candidature for the
degree of PhD

June 2016

Summary

Archaeological wrought iron artefacts are subject to damaging corrosion while in the burial environment and when subjected to environmental changes after excavation. The role of water, oxygen, and chloride corrosion accelerators are central to iron corrosion processes. Intrinsic factors such as the amount and distribution of slag in wrought iron may also play a role in corrosion processes.

This study examined a range of factors that impact on understanding conservation desalination treatments to mitigate corrosion by removing chlorides. While examining the effect of slag on corrosion rate and chloride content formed the core of this project, cracking morphologies within corrosion product layers and their influence on corrosion rates measured by oxygen consumption produced outcomes of interest for designing the practicalities of treatment procedures.

The slag content of the wrought iron objects examined in this study did not correlate with either their corrosion rate or their chloride content. In line with other authors, clustering of chloride around slag inclusions was identified. This confirmed slag does act as a focus for developing corrosion centres, which will offer challenges for chloride removal and hence provide opportunity for post-treatment corrosion.

The alkaline sulphite washing applied to the iron nails produced results that aligned with those reported in other studies and confirmed its relative efficiency for removing chloride. Of major relevance to conservators designing alkaline washing techniques is assigning treatment time and specifying treatment environment. These decisions are aided by evidence provided in this study, which showed that immersing the chloride

containing corrosion product β -FeOOH in alkaline sulphite entirely transformed it to other iron oxides in only 30 days. During this process it will release its chloride, which will be available for diffusion into the wash solution making a more complete desalination process possible.

Acknowledgments

This research would not have been possible without the support of the people and institutions that made samples of archaeological wrought iron available for study: Dr. Peter Guest of Cardiff University and Emily Williams and Kelly Ladd-Kostro of the Colonial Williamsburg Foundation.

At Cardiff University, many thanks to Paul Nicholson for his excellent support as second supervisor, Yiota Manti, Jane Henderson, and Phil Parkes (with special mention for SEM assistance) in the Dept. of Archaeology and Conservation, Tim Young for discussion of Roman and early American metallurgy, Daniela Hofmann for help with German translation, and Yiannis Smyrnaiois for Greek translation and substantive discussions. Sue Virgo, Aled Cooke and Rob Thomas for keeping everything running, Helen Szewczyk for support in all things postgraduate administration, and Karen Heard and the staff of the UGC for providing an excellent writing space.

In the Cardiff Ferrous Metals Research Group, thanks to Nicola Emmerson for friendship, significant discussion and readings, Amber Lawson for many discussions and Melanie Rimmer for demonstrating research techniques and discussing her work. Thanks most of all to Prof. David Watkinson for excellent, unwavering supervision and advice throughout the course of this PhD.

Tom Cotterell and Amanda Valentine-Baars at the National Museum of Wales for their assistance with X-ray Diffraction, and Joseph Boesenberg at Brown University for EPMA analysis.

Thanks also to the many colleagues past and present who encouraged me to pursue my PhD research: G.H., Valentin Boissonnas, Eric Schindelholz, Anna Holloway, David Krop, Pedro Gonçalves, Will Hoffmann, Elsa Sangouard, Sarah Watkins-Kenney, Joseph Schwarzer, and many more.

Last but very much not least thanks to Marie Irshad for her constant support and encouragement.

Dedication

For my parents: Allan Curtis and Katia Nordgren

Table of Contents

1	Introduction	1
1.1	The Nature of Iron	1
1.2	Iron Smelting and Working.....	4
1.3	Wrought Iron	5
1.3.1	Methods of wrought iron production	7
1.4	Context of Nails Used in This Study.....	8
1.5	Nature of This Study	9
2	Corrosion of Iron	11
2.1	Corrosion of Metals.....	11
2.2	Iron Corrosion.....	16
2.2.1	In the atmosphere.....	16
2.2.2	Corrosion: wet and marine environments.....	19
2.2.3	Corrosion: soil	21
2.2.4	Iron corrosion products	22
2.2.5	Transformation of iron corrosion products	32
2.3	Corrosion of Archaeological Iron Artefacts	33
2.3.1	Description of corrosion product layers	33
2.3.2	Models of archaeological iron corrosion	36
2.3.3	Effect of iron alloy and production technique	38

2.3.4	Effect of inclusions	39
2.4	Post-Excavation Corrosion	41
2.4.1	Changes occurring after excavation.....	41
2.4.2	Long-term post excavation changes	43
3	Conservation of Archaeological Iron.....	45
3.1	Preventive Conservation	45
3.2	Interventive Treatment	46
3.2.1	Desalination techniques.....	47
3.3	Alkaline Sulphite Washing	57
3.3.1	Previous evaluation of alkaline sulphite washing.....	59
3.3.2	Further research on alkaline sulphite washing of archaeological iron	65
3.4	Akaganeite Transformation During Storage and Conservation	67
3.4.1	Akaganeite transformation in heritage iron: further questions	71
3.5	Investigating the Impact of Slag on the Corrosion of Archaeological Wrought Iron and its Response to Alkaline Sulphite Treatment	72
3.5.1	Aims and Objectives.....	72
4	Experimental Method	74
4.1	Research Method	74
4.2	Experimental Variables.....	74
4.3	Method of Corrosion Measurement	75
4.4	Experimental parameters: rationale	76

4.5	Akaganeite transformation	78
4.6	Sample material.....	79
4.6.1	Roman Caerleon.....	79
4.6.2	Colonial Williamsburg	80
4.7	Experimental Procedures	81
4.7.1	Sample selection, documentation, and preparation	82
4.7.2	Workflow.....	85
4.7.3	Measurement of oxygen consumption.....	87
4.7.4	Chloride measurement	88
4.7.5	Alkaline Sulphite washing treatment.....	89
4.7.6	Preparation of metallographic samples.....	90
4.7.7	Measurement of slag content.....	90
4.7.8	EPMA microanalysis	94
4.7.9	SEM imaging and microanalysis of treated samples	94
4.7.10	Digestion of samples to determine total remaining chloride.....	97
4.7.11	Akaganeite transformation	98
4.7.12	Data handling and statistical procedures	101
5	Results.....	102
5.1	Characterisation of Sample Material	102
5.1.1	Chloride content	112

5.1.2	Mass of samples	114
5.1.3	Slag content.....	116
5.2	Oxygen consumption rate	129
5.2.1	Untreated samples	129
5.2.2	Samples treated by alkaline sulphite washing at 60° C.....	135
5.2.3	Change in oxygen consumption rate	146
5.2.4	Chloride extraction treatment efficiency.....	151
5.2.5	Chloride content compared with oxygen consumption	158
5.2.6	Chloride compared with Percent Area Slag	160
5.2.7	Chloride in cross sections of treated objects.....	161
5.3	Akaganeite transformation	165
6	Discussion.....	171
6.1	Composition and Production Technique of Nails.....	171
6.1.1	Composition	171
6.1.2	Slag	172
6.2	Condition of Nails	176
6.3	Corrosion in Atmosphere	181
6.3.1	Oxygen consumption in relation to slag and mass	182
6.4	Alkaline Sulphite Treatment.....	184
6.4.1	Chloride Extraction treatment efficiency.....	184

6.4.2	Post Treatment atmospheric corrosion rate	186
6.4.3	Effect of chloride content	188
6.4.4	Effect of microcracks and post treatment rinsing	189
6.4.5	Effect of percent area slag	195
6.5	Microanalysis of treated samples	196
6.5.1	Location and concentration of chlorine in treated nails.....	196
6.6	Akaganeite Transformation.....	197
6.7	Discussion Summary.....	201
6.7.1	Oxygen consumption rate and chloride content of Caerleon nails	201
6.7.2	Oxygen consumption and chloride content of Colonial Williamsburg nails.	202
6.8	Conclusion	203
6.9	Further Work	205
7	References.....	207
8	Appendices.....	225
8.1	Appendix 1: Chloride Analysis	225
8.1.1	Specific Ion Meter Calibration Procedures	225
8.1.2	Specific Ion Meter Chloride Analysis Procedures	226
8.1.3	Preparation of chloride samples from alkaline sulphite wash solutions	226
8.1.4	Preparation of chloride samples from nitric acid digestion	227
8.2	Appendix 2: X-ray Diffraction	228

8.3	Appendix 3: FT-IR Spectroscopy	229
8.4	Appendix 4: Supplementary Analytical Data.....	230
8.4.1	SEM Images of Nails in Cross Section.....	230
8.4.2	Elemental Maps of Nails in Cross Section	240
8.4.3	SEM-EDS Elemental Analyses of Nails in Cross Section	260
8.4.4	X-ray Diffractograms of Synthetic Akaganeite Samples After Treatment (2-10)	280
8.5	Appendix 5: Archaeological Contexts of Sample Material.....	285
8.5.1	Roman Caerleon.....	285
8.5.2	Colonial Williamsburg	285
8.6	Appendix 6: Sample Photographs	287

List of Figures

Figure 1.1 Iron-carbon phase diagram.....	2
Figure 1.2 Detail of an iron-carbon phase diagram	3
Figure 1.3 SEM-BSE (backscattered electron image) at 20X magnification showing elongated silicate slag inclusions in a wrought iron nail	7
Figure 2.1 Schematic diagram of a metal corrosion cell.....	13
Figure 2.2 Simplified Potential/pH (Pourbaix) diagram for iron-water at 25°C.....	15
Figure 2.3 Eh/pH (Pourbaix) diagram for iron-water system showing ions and compounds and thermodynamically predicted regions of corrosion, passivation, and protection	16
Figure 2.4 Diagram of interactions occurring during the 3 phase wet-dry cycle of atmospheric corrosion.....	18
Figure 2.5 SEM-BSE image at 200X magnification of iron chloride corrosion products on a polished cross-section of an untreated wrought iron nail from Caerleon	24
Figure 2.6 Schematic diagram of iron corrosion product layers on an archaeological iron nail from Cabaret and Montbaron, France	26
Figure 2.7 Schematic diagram of iron corrosion product layers showing Cl ⁻ and O ₂ diffusion from outer layers down to the metal.....	26
Figure 2.8 SEM-BEI (backscattered electron image) of a corroded archaeological wrought iron object in cross-section.....	35
Figure 2.9 SEM-BEI image of a corroded wrought-iron nail from the site of Usk, Wales	35

Figure 3.1 Phase diagram (Pressure in bar as a function of Temperature in °C) for water showing physical conditions used in subcritical extraction of chloride from archaeological iron	54
Figure 4.1 Digital photograph at 1.5X (top) and SEM-BSE image at 20X (bottom) of nail sample CAER_01 from Caerleon.....	80
Figure 4.2 Digital photograph at 1.5X (top) and BSE-SEM image at 20X (bottom) of nail sample CW_09 from Colonial Williamsburg.....	81
Figure 4.3 Workflow for experimental procedures applied to wrought iron nail samples in the study	86
Figure 4.4 Flow chart of percent area slag measurement procedures.....	93
Figure 4.5 Comparison of SEM elemental mapping for chloride using EDS (left) and WDS (right) of a region of sample CAER_01.....	95
Figure 4.6 Flowchart of the procedures used for production of synthetic akaganeite (β -FeOOH) and the transformation experiment in alkaline sulphite solution (AS 60)	100
Figure 5.1 Digital photo at 1:1 scale (top) and SEM-BEI cross-sectional image (bottom) of CAER_10	102
Figure 5.2 Digital photo at 1:1 scale (top) and SEM-BEI cross-sectional image (bottom) of CW_19	103
Figure 5.3 SEM-BEI micrograph of sample CAER_08	104
Figure 5.4 Maximum thickness (in μm)of corrosion product layers (CPLs) on 10 wrought iron nails each from Caerleon and Colonial Williamsburg	106
Figure 5.5 Mean maximum corrosion product layer thickness (μm) of 10 nails each from the sites of Caerleon and Colonial Williamsburg.....	106

Figure 5.6 SEM-BSE image of Caerleon nail CAER_13 post alkaline sulphite treatment in polished cross-section	107
Figure 5.7 SEM-BSE image of nail CAER_13 post alkaline sulphite treatment at 25X showing metal core (M), wide radial cracking through TM and DPL corrosion layers and significant marbling	108
Figure 5.8 SEM-BSE image of nail CW_05 post alkaline sulphite treatment	108
Figure 5.9 SEM-BSE image of nail CW_05 post alkaline sulphite treatment	109
Figure 5.10 SEM-BSE image of slag inclusions in sample CW_16	109
Figure 5.11 Scatterplot showing ratio of wt % of P ₂ O ₅ .to wt % of MgO+Al ₂ O ₃ +K ₂ O/FeO as analysed by EPMA and SEM/WDS for samples from Caerleon and Colonial Williamsburg	112
Figure 5.12 Total chloride content of 10 wrought iron nails, 5 each from the sites of Roman Caerleon and Colonial Williamsburg	113
Figure 5.13 Histograms of the distribution of 30 samples of wrought iron nails by mass.	114
Figure 5.14 Boxplot of mass of sample nails (grams) by site of origin	115
Figure 5.15 Composite digital photomicrograph of sample CAER_01 in polished cross-section at 50X magnification.	118
Figure 5.16 Composite digital photomicrograph of sample CAER_07 in polished cross-section at 50X magnification.	118
Figure 5.17 Composite digital photomicrograph of sample CAER_08 in polished cross-section at 50X magnification.	119
Figure 5.18 Composite digital photomicrograph of sample CAER_10 in polished cross-section at 50X magnification.	119

Figure 5.19 Composite digital photomicrograph of sample CAER_13 in polished cross-section at 50X magnification	120
Figure 5.20 Composite digital photomicrograph of sample CAER_18 in polished cross-section at 50X magnification.	120
Figure 5.21 Composite digital photomicrograph of sample CAER_19 in polished cross-section at 50X magnification.	121
Figure 5.22 Composite digital photomicrograph of sample CAER_21 in polished cross-section at 50X magnification.	121
Figure 5.23 Composite digital photomicrograph of sample CAER_22 in polished cross-section at 50X magnification.	122
Figure 5.24 Composite digital photomicrograph of sample CAER_27 in polished cross-section at 50X magnification.	122
Figure 5.25 Composite digital photomicrograph of sample CW_05 in polished cross-section at 50X magnification.	123
Figure 5.26 Composite digital photomicrograph of sample CW_07 in polished cross-section at 50X magnification.	123
Figure 5.27 Composite digital photomicrograph of sample CW_08 in polished cross-section at 50X magnification.	124
Figure 5.28 Composite digital photomicrograph of sample CW_09 in polished cross-section at 50X magnification.	124
Figure 5.29 Composite digital photomicrograph of sample CW_14 in polished cross-section at 50X magnification.	125
Figure 5.30 Composite digital photomicrograph of sample CW_15 in polished cross-section at 50X magnification.	125

Figure 5.31 Composite digital photomicrograph of sample CW_16 in polished cross-section at 50X magnification.	126
Figure 5.32 Composite digital photomicrograph of sample CW_19 in polished cross-section at 50X magnification	126
Figure 5.33 Composite digital photomicrograph of sample CW_26 in polished cross-section at 50X magnification	127
Figure 5.34 Composite digital photomicrograph of sample CW_29 in polished cross-section at 50X magnification	127
Figure 5.35 Boxplot of percent area slag values for 10 wrought iron nails each from Caerleon and Colonial Williamsburg	128
Figure 5.36 Oxygen consumption in millibars (+/-2 mbar) of 30 untreated wrought iron nails within the first 18 days from the site of Roman Caerleon in conditions of 80% RH and 20°C.....	130
Figure 5.37 Oxygen consumption in millibars (+/-2 mbar) of 30 untreated wrought iron nails from the site of Colonial Williamsburg in conditions of 80% RH and 20°C	131
Figure 5.38 Comparison of oxygen consumption rate over 18 days in mbar/day/gram for untreated wrought iron nails from the sites of Caerleon and Colonial Williamsburg.....	132
Figure 5.39 Boxplot of oxygen consumption rate in mbar/day/gram for untreated wrought iron nails over 18 days for the sites of Roman Caerleon and Colonial Williamsburg.....	133
Figure 5.40 Oxygen consumption as a function of mass of sample over 18 days for 30 untreated samples from Caerleon.....	134

Figure 5.41 Oxygen consumption as a function of mass of sample over 18 days for 30 untreated samples from Colonial Williamsburg.....	134
Figure 5.42 Oxygen consumption in millibars (+/-2 mbar) of 15 wrought iron nails from the site of Roman Caerleon treated by alkaline sulphite washing at 60°C and rinsed in deionised water to pH 7	136
Figure 5.43 Oxygen consumption in millibars (+/-2 mbar) of 15 wrought iron nails from the site of Roman Caerleon treated by alkaline sulphite washing at 60°C and left unrinsed following treatment.....	137
Figure 5.44 Oxygen consumption in millibars (+/-2 mbar) of 15 wrought iron nails from the site of Colonial Williamsburg treated by alkaline sulphite washing at 60°C and rinsed in deionised water to pH 7	138
Figure 5.45 Oxygen consumption in millibars (+/-2 mbar) of 15 wrought iron nails from the site of Colonial Williamsburg treated by alkaline sulphite washing at 60°C and not rinsed following treatment	139
Figure 5.46 Oxygen consumption in millibars (+/-2 mbar) of 15 wrought iron nails from the site of Roman Caerleon treated by alkaline sulphite washing at 60°C and rinsed in deionised water to pH 7	140
Figure 5.47 Oxygen consumption in millibars (+/-2 mbar) of 15 wrought iron nails from the site of Roman Caerleon treated by alkaline sulphite washing at 60°C and left unrinsed after treatment.....	141
Figure 5.48 Oxygen consumption in millibars (+/-2 mbar) of 15 wrought iron nails from the site of Colonial Williamsburg treated by alkaline sulphite washing at 60°C and rinsed in deionised water to pH 7	142

Figure 5.49 Oxygen consumption in millibars (+/-2 mbar) of 15 wrought iron nails from the site of Colonial Williamsburg treated by alkaline sulphite washing at 60°C and left unrinsed after treatment	143
Figure 5.50 Boxplot of oxygen consumption rate over 18 days for wrought iron nails for the sites of Roman Caerleon and Colonial Williamsburg treated by alkaline sulphite washing at 60°C	144
Figure 5.51 Boxplot of oxygen consumption rate over 18 days for wrought iron nails for the sites of Roman Caerleon and Colonial Williamsburg treated by alkaline sulphite washing at 60°C	145
Figure 5.52 Oxygen consumption rate of 15 wrought iron nails from Caerleon in untreated, and treated rinsed state and conditions of 80% RH and 20°C.....	147
Figure 5.53 Oxygen consumption rate of 15 wrought iron nails from Caerleon in untreated, and Treated un rinsed state and conditions of 80% RH and 20°C	147
Figure 5.54 Oxygen consumption rate of 15 wrought iron nails from Colonial Williamsburg in untreated, and treated rinsed state and conditions of 80% RH and 20°C.....	148
Figure 5.55 Oxygen consumption rate of 15 wrought iron nails from Colonial Williamsburg in untreated, and treated not-rinsed state and conditions of 80% RH and 20°C	148
Figure 5.56 Comparison of oxygen consumption rate of wrought iron nails from Caerleon over 18 days in untreated and post AS60 conditions. Oxygen consumption rates are further compared between samples given rinsed and not rinsed post-treatment protocols.	149

Figure 5.57 Comparison of oxygen consumption rate of wrought iron nails from Colonial Williamsburg over 18 days in untreated and post AS60 conditions. Oxygen consumption rates are further compared between samples given rinsed and not rinsed post-treatment protocols.....	149
Figure 5.58 Remaining chloride in samples from Caerleon and Colonial Williamsburg after desalination with alkaline sulphite treatment at 60°C in ppm as measured by digestion in 5M nitric acid.	153
Figure 5.59 Comparison of total chloride and remaining chloride after alkaline sulphite treatment at 60°C for 30 wrought iron nails each from Caerleon and Colonial Williamsburg.....	154
Figure 5.60 Remaining chloride in 30 nails from Caerleon after alkaline sulphite treatment as a percentage of the total chloride measured in each sample.....	155
Figure 5.61 Remaining chloride in 30 nails from Colonial Williamsburg after alkaline sulphite treatment as a percentage of the total chloride measured in each sample.....	155
Figure 5.62 Total remaining chloride (ppm) in 30 samples from Caerleon after alkaline sulphite treatment: comparison of rinsed and not rinsed post-treatment protocols.....	156
Figure 5.63 Total remaining chloride (ppm) in 30 samples from Colonial Williamsburg after alkaline sulphite treatment: comparison of rinsed and not rinsed post-treatment protocols.	156
Figure 5.64 Comparison of total chloride and remaining chloride (ppm) measured for 30 nails from Caerleon with their assignment to rinsed or not rinsed protocols.	157

Figure 5.65 Comparison of total chloride and remaining chloride (ppm) measured for 30 nails from Colonial Williamsburg with their assignment to rinsed or not rinsed protocols.....	157
Figure 5.66 Oxygen consumption rate in mbar/day/gram over 18 days of 30 untreated samples each from Caerleon and Colonial Williamsburg (60 in total) as a function of total chloride in ppm measured by extraction and digestion.....	158
Figure 5.67 Oxygen consumption rate in mbar/day/gram over 18 days of 30 treated nails each from the sites of Caerleon and Colonial Williamsburg (60 in total) after alkaline sulphite treatment as a function of chloride remaining in ppm after treatment.....	159
Figure 6.1 Schematic representation of radial cracks present in corrosion product layers.....	180
Figure 6.2 Schematic representation of concentric cracks and partial radial cracks present in corrosion products layers.....	180
Figure 6.3 Post-treatment oxygen consumption rate as a function of presence or absence of radial cracks observed in cross-sections of 10 nails each for Caerleon and Colonial Williamsburg after alkaline sulphite treatment.	190
Figure 6.4 Remaining chloride after alkaline sulphite treatment as a function of presence or absence of radial cracks observed in cross-sections of 10 nails each for Caerleon and Colonial Williamsburg after alkaline sulphite treatment.	191
Figure 6.5 Post-treatment oxygen consumption of all samples as a function of rinsing protocol and presence or absence of radial cracks in the samples.	194
Figure 8.1 SEM-BSE image of Caerleon nail CAER_01 in polished cross-section at 13X magnification.	230

Figure 8.2 SEM-BSE image of Caerleon nail CAER_07 in polished cross-section at 13X magnification.	230
Figure 8.3 SEM-BSE image of Caerleon nail CAER_08 in polished cross-section at 20X magnification.	231
Figure 8.4 SEM-BSE image of Caerleon nail CAER_10 in polished cross-section at 15X magnification.	231
Figure 8.5 SEM-BSE image of Caerleon nail CAER_13 in polished cross-section at 13X magnification.	232
Figure 8.6 SEM-BSE image of Caerleon nail CAER_18 in polished cross-section at 15X magnification.	232
Figure 8.7 SEM-BSE image of Caerleon nail CAER_19 in polished cross-section at 20X magnification.	233
Figure 8.8 SEM-BSE image of Caerleon nail CAER_21 in polished cross-section at 13X magnification.	233
Figure 8.9 SEM-BSE image of Caerleon nail CAER_22 in polished cross-section at 20X magnification.	234
Figure 8.10 SEM-BSE image of Caerleon nail CAER_27 in polished cross-section at 25X magnification.	234
Figure 8.11 SEM-BSE image of Colonial Williamsburg nail CW_05 in polished cross-section at 24X magnification.	235
Figure 8.12 SEM-BSE image of Colonial Williamsburg nail CW_07 in polished cross-section at 20X magnification.	235
Figure 8.13 SEM-BSE image of Colonial Williamsburg nail CW_08 in polished cross-section at 25X magnification.	236

Figure 8.14 SEM-BSE image of Colonial Williamsburg nail CW_09 in polished cross-section at 20X magnification.	236
Figure 8.15 SEM-BSE image of Colonial Williamsburg nail CW_14 in polished cross-section at 20X magnification.	237
Figure 8.16 SEM-BSE image of Colonial Williamsburg nail CW_15 in polished cross-section at 15X magnification.	237
Figure 8.17 SEM-BSE image of Colonial Williamsburg nail CW_16 in polished cross-section at 20X magnification.	238
Figure 8.18 SEM-BSE image of Colonial Williamsburg nail CW_19 in polished cross-section at 20X magnification.	238
Figure 8.19 SEM-BSE image of Colonial Williamsburg nail CW_26 in polished cross-section at 20X magnification.	239
Figure 8.20 SEM-BSE image of Colonial Williamsburg nail CW_29 in polished cross-section at 20X magnification... ..	239
Figure 8.21 SEM-BSE image and corresponding EDS/WDS quantitative elemental maps for 5 elements detected in 2 sites of interest for sample CAER_01.....	240
Figure 8.22 SEM-BSE image and corresponding EDS/WDS quantitative elemental maps for 5 elements detected in 2 sites of interest for sample CAER_07.....	241
Figure 8.23 SEM-BSE image and corresponding EDS/WDS quantitative elemental maps for 5 elements detected in 2 sites of interest for sample CAER_08.....	242
Figure 8.24 SEM-BSE image and corresponding EDS/WDS quantitative elemental maps for 5 elements detected in 2 sites of interest for sample CAER_10.....	243
Figure 8.25 SEM-BSE image and corresponding EDS/WDS quantitative elemental maps for 5 elements detected in 2 sites of interest for sample CAER_13.....	244

Figure 8.26 SEM-BSE image and corresponding EDS/WDS quantitative elemental maps for 5 elements detected in 2 sites of interest for sample CAER_18.....	245
Figure 8.27 SEM-BSE image and corresponding EDS/WDS quantitative elemental maps for 5 elements detected in 2 sites of interest for sample CAER_19.....	246
Figure 8.28 SEM-BSE image and corresponding EDS/WDS quantitative elemental maps for 5 elements detected in 2 sites of interest for sample CAER_21.....	247
Figure 8.29 SEM-BSE image and corresponding EDS/WDS quantitative elemental maps for 5 elements detected in 2 sites of interest for sample CAER_22.....	248
Figure 8.30 SEM-BSE image and corresponding EDS/WDS quantitative elemental maps for 5 elements detected in 2 sites of interest for sample CAER_28.....	249
Figure 8.31 SEM-BSE image and corresponding EDS/WDS quantitative elemental maps for 5 elements detected in 2 sites of interest for sample CW_05.	250
Figure 8.32 SEM-BSE image and corresponding EDS/WDS quantitative elemental maps for 5 elements detected in 2 sites of interest for sample CW_07.	251
Figure 8.33 SEM-BSE image and corresponding EDS/WDS quantitative elemental maps for 5 elements detected in 2 sites of interest for sample CW_08.	252
Figure 8.34 SEM-BSE image and corresponding EDS/WDS quantitative elemental maps for 5 elements detected in 2 sites of interest for sample CW_09.	253
Figure 8.35 SEM-BSE image and corresponding EDS/WDS quantitative elemental maps for 5 elements detected in 2 sites of interest for sample CW_14.	254
Figure 8.36 SEM-BSE image and corresponding EDS/WDS quantitative elemental maps for 5 elements detected in 2 sites of interest for sample CW_15.	255
Figure 8.37 SEM-BSE image and corresponding EDS/WDS quantitative elemental maps for 5 elements detected in 2 sites of interest for sample CW_16.	256

Figure 8.38 SEM-BSE image and corresponding EDS/WDS quantitative elemental maps for 5 elements detected in 2 sites of interest for sample CW_19.	257
Figure 8.39 SEM-BSE image and corresponding EDS/WDS quantitative elemental maps for 5 elements detected in 2 sites of interest for sample CW_26.	258
Figure 8.40 SEM-BSE image and corresponding EDS/WDS quantitative elemental maps for 5 elements detected in 2 sites of interest for sample CW_29.	259
Figure 8.41 SEM (BEI) image of Caerleon sample CAER_01 with location of EDS line scan	260
Figure 8.42 SEM (BEI) image of Caerleon sample CAER_07 with location of EDS line scan.	261
Figure 8.43 SEM (BEI) image of Caerleon sample CAER_08 with location of EDS line scan	262
Figure 8.44 SEM (BEI) image of Caerleon sample CAER_10 with location of EDS line scan	263
Figure 8.45 SEM (BEI) image of Caerleon sample CAER_13 with location of EDS line scan	264
Figure 8.46 SEM (BEI) image of Caerleon sample CAER_18 with location of EDS line scan	265
Figure 8.47 SEM (BEI) image of Caerleon sample CAER_19 with location of EDS line scan	266
Figure 8.48 SEM (BEI) image of Caerleon sample CAER_21 with location of EDS line scan	267
Figure 8.49 SEM (BEI) image of Caerleon sample CAER_22 with location of EDS line scan	268

Figure 8.50 SEM (BEI) image of Caerleon sample CAER_27 with location of EDS line scan	269
Figure 8.51 SEM (BEI) image of Colonial Williamsburg sample CW_05 with location of EDS line scan	270
Figure 8.52 SEM (BEI) image of Colonial Williamsburg sample CW_07 with location of EDS line scan	271
Figure 8.53 SEM (BEI) image of Colonial Williamsburg sample CW_08 with location of EDS line scan	272
Figure 8.54 SEM (BEI) image of Colonial Williamsburg sample CW_09 with location of EDS line scan	273
Figure 8.55 SEM (BEI) image of Colonial Williamsburg sample CW_14 with location of EDS line scan	274
Figure 8.56 SEM (BEI) image of Colonial Williamsburg sample CW_15 with location of EDS line scan	275
Figure 8.57 SEM (BEI) image of Colonial Williamsburg sample CW_16 with location of EDS line scan	276
Figure 8.58 SEM (BEI) image of Colonial Williamsburg sample CW_19 with location of EDS line scan	277
Figure 8.59 SEM (BEI) image of Colonial Williamsburg sample CW_26 with location of EDS line scan	278
Figure 8.60 SEM (BEI) image of Colonial Williamsburg sample CW_29 with location of EDS line scan	279
Figure 8.61 XRD stick plot of sample β -FeOOH-AS60-2 after AS60 treatment.....	280
Figure 8.62 XRD stick plot of sample β -FeOOH-AS60-3 after AS60 treatment.....	280

Figure 8.63 XRD stick plot of sample β -FeOOH-AS60-4 after AS60 treatment.....	281
Figure 8.64 XRD stick plot of sample β -FeOOH-AS60-5 after AS60 treatment.....	281
Figure 8.65 XRD stick plot of sample β -FeOOH-AS60-6 after AS60 treatment.....	282
Figure 8.66 XRD stick plot of sample β -FeOOH-AS60-7 after AS60 treatment.....	282
Figure 8.67 XRD stick plot of sample β -FeOOH-AS60-8 after AS60 treatment.....	283
Figure 8.68 XRD stick plot of sample β -FeOOH-AS60-9 after AS60 treatment.....	283
Figure 8.69 XRD stick plot of sample β -FeOOH-AS60-10 after AS60 treatment.....	284

List of Tables

Table 2.1 Oxides commonly present as archaeological iron corrosion along with their transformation products	32
Table 3.1 Chloride removal methods for heritage iron objects.....	48
Table 4.1 Independent and dependent variables used in the study	74
Table 4.2 Source of archaeological wrought iron nail samples used in the study	79
Table 4.3 List of samples studied with analytical record.	84
Table 4.4 Sample nails analysed by EPMA.....	94
Table 4.5 Sample nails analysed for elemental composition by SEM-WDS.	97
Table 5.1 Maximum and minimum thickness of CPLs of 10 nails each from Caerleon and Colonial Williamsburg.....	105
Table 5.2 Mean values (in wt %) for elemental composition of iron metal (ferrite) phase of 12 wrought iron nail samples	111
Table 5.3 Mean values (in wt%) for elemental composition of silicate slag regions of 12 wrought iron nail samples	111
Table 5.4 Untreated wrought iron nails digested and analysed for total chloride.	113
Table 5.5 Shapiro-Wilk test of normality for mass of 60 wrought iron sample nails. ...	115

Table 5.6 Percent area of slag inclusions measured by computer image analysis of polished transverse sections of wrought iron nails from Roman Caerleon (CAER) and Colonial Williamsburg (CW).....	117
Table 5.7 Mean percent area slag as determined by computer image analysis of 10 sections of wrought iron nails each from Roman Caerleon and Colonial Williamsburg.....	128
Table 5.8 Non-parametric tests of correlation (Spearman rho) for mass of sample and oxygen consumption/day/gram of sample for 30 untreated nails each for Caerleon and Colonial Williamsburg	135
Table 5.9 Mean O ₂ consumption over 18 days of wrought iron nail samples from Caerleon and Colonial Williamsburg, untreated, and treated with alkaline sulphite washing at 60°C	150
Table 5.10 Chloride extracted during alkaline sulphite treatment of 60 wrought iron nails from Caerleon and Colonial Williamsburg	153
Table 5.11 Non-parametric (Spearman-rho) tests of correlation between oxygen consumption rates before and after alkaline sulphite treatment and total and remaining chloride.....	159
Table 5.12 Spearman correlation tests between remaining chloride in 30 sample nails treated by alkaline sulphite and percent area slag content.....	161
Table 5.13 SEM-EDS line scan results for Caerleon sample CAER_07	163
Table 5.14 Results of SEM microanalyses for chlorine	164
Table 5.15 Five XRD-RIR analyses of synthetic akaganeite before experimental alkaline sulphite treatment.....	165

Table 5.16 Percentage iron phases present after alkaline sulphite washing of 10 samples of synthetic β -FeOOH for 30 days	168
Table 6.1 Spearman tests of correlation between pre-treatment oxygen corrosion rate and percent area slag (as determined by OM and SEM-BEI imaging in 10 samples each from Caerleon and Colonial Williamsburg).....	183
Table 6.2 Post treatment rinsing protocol, presence or absence of radial cracks and post alkaline sulphite treatment oxygen consumption.....	193
Table 6.3 Tests of correlation for presence of radial cracking with post treatment rinsing protocol and post-treatment oxygen consumption with post treatment rinsing protocol.....	194
Table 6.4 Results of previous studies on the transformation of synthetic akaganeite in alkaline solutions.	199
Table 8.1 SEM-EDS line scan results for Caerleon sample CAER_01	260
Table 8.2 SEM-EDS line scan results for Caerleon sample CAER_07	261
Table 8.3 SEM-EDS line scan results for Caerleon sample CAER_08	262
Table 8.4 SEM-EDS line scan results for Caerleon sample CAER_10	263
Table 8.5 SEM-EDS line scan results for Caerleon sample CAER_13	264
Table 8.6 SEM-EDS line scan results for Caerleon sample CAER_18	265
Table 8.7 SEM-EDS line scan results for Caerleon sample CAER_19	266
Table 8.8 SEM-EDS line scan results for Caerleon sample CAER_21	267
Table 8.9 SEM-EDS line scan results for Caerleon sample CAER_22	268
Table 8.10 SEM-EDS line scan results for Caerleon sample CAER_27	269
Table 8.11 SEM-EDS line scan results for Colonial Williamsburg sample CW_05	270
Table 8.12 SEM-EDS line scan results for Colonial Williamsburg sample CW_07	271

Table 8.13 SEM-EDS line scan results for Colonial Williamsburg sample CW_08	272
Table 8.14 SEM-EDS line scan results for Colonial Williamsburg sample CW_09	273
Table 8.15 SEM-EDS line scan results for Colonial Williamsburg sample CW_14	274
Table 8.16 SEM-EDS line scan results for Colonial Williamsburg sample CW_15	275
Table 8.17 SEM-EDS line scan results for Colonial Williamsburg sample CW_16	276
Table 8.18 SEM-EDS line scan results for Colonial Williamsburg sample CW_19	277
Table 8.19 SEM-EDS line scan results for Colonial Williamsburg sample CW_26	278
Table 8.20 SEM-EDS line scan results for Colonial Williamsburg sample CW_29.	279

1 Introduction

Iron is the most common element on Earth by mass and, since the beginning of the Iron Age about 1200 BC, one of the most widely used by humans. The mechanical strength and workability of purified iron and its alloys make it ideal for the production of tools, weapons and objects with numerous industrial and domestic uses. The ubiquity of iron in history also means that, subject to favourable environmental conditions, a large quantity of it survives in the archaeological record.

1.1 The Nature of Iron

The element Iron is a silver-grey transition metal in Group VIII of the periodic table with an atomic number of 26 and atomic mass of 55.845g. It may have oxidation states of -2 to +6 allowing it to form a large number of compounds although +2 and +3 are most common and most important for the chemical reactions considered in this study (Graedel and Frankenthal 1990). At least four iron allotropes exist in different temperatures and conditions, of which three, α , γ and δ , exist at atmospheric pressure (Campbell 2008, 14) and are important in iron smelting and working. Iron forms alloys with other metals and elements, the most important of which is carbon, which lowers its melting point and increases its hardness. In the form of cast iron, it may contain up to 6.7 wt% of carbon though wrought irons and steels contain much less (0.008-2.1%) (Pollack 1998, 140) and carbon influences the phases present (Figure 1.1).

Iron containing only trace amounts of carbon (far left in Figure 1.1) melts at approximately 1550°C, but increasing amounts of carbon depress the melting point to as little as 1130°C when the carbon content is at 4%. Below the melting point at low

carbon contents, the BCC δ -phase is formed. The δ -phase transforms to first the FCC γ -phase (austenite) and then to BCC α -iron (ferrite) as it cools further. A small zone consisting exclusively of ferrite exists at the far left of Figure 1, which is shown in detail in Figure 1.2. Outside this zone of very low carbon content, a wide range of iron and iron carbide mixtures exist. Iron carbide may be in the form of cementite (Fe_3C) or pearlite, a laminar structure of alternating layers of ferrite and cementite.

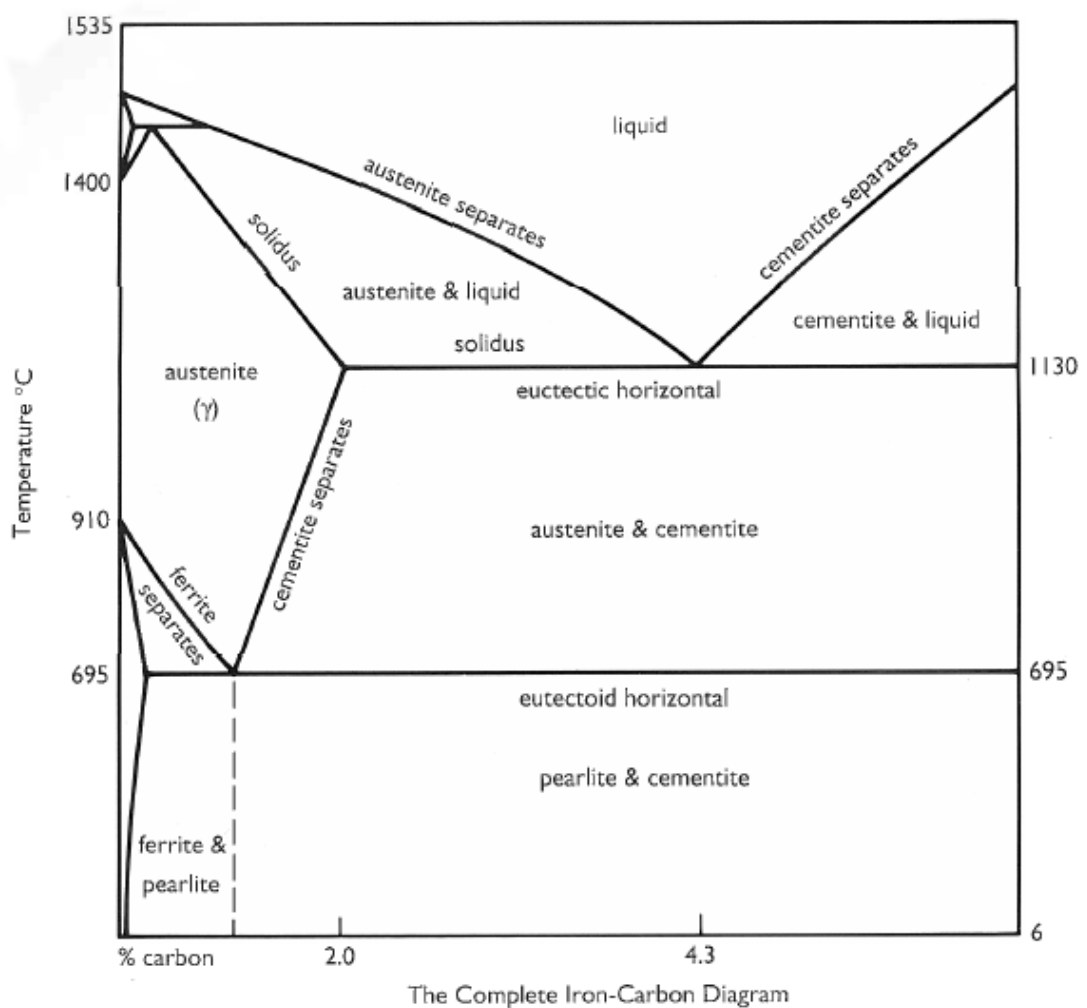


Figure 1.1 Iron-carbon phase diagram showing the occurrence of allotropic phases α (ferrite), γ (austenite) and iron carbide phases at different temperatures and carbon contents. The area at the top of the graph indicates molten, liquid iron above the melting point. The division between hypo and hyper-eutectoid steels is indicated by a dashed line at 0.8 % carbon. Alloys with > 2.0 % carbon are cast irons. The effect of carbon on the melting point of iron can also be seen. (Scott 1991, 132. Used with permission of the author and the Getty Conservation Institute.)

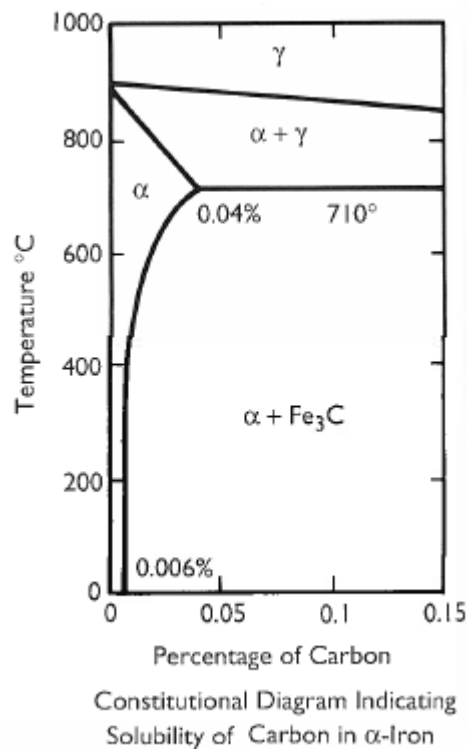


Figure 1.2 Detail of an iron-carbon phase diagram showing region of α -iron (ferrite) only at very low percentages of carbon, as well as α -iron+ Fe_3C (cementite) at slightly higher carbon contents. Above 700°C iron is in the form of α -iron + γ -iron (austenite) or as austenite alone. (Scott 1991, 132. Used with permission of the author and the Getty Conservation Institute.)

The amount of carbon and the structures it forms determine the properties of the iron alloy, particularly its hardness and mechanical strength. Iron alloys with carbon contents below 0.83% are known as hypo-eutectoid steels, whereas carbon levels between 0.93 and 2% are hyper-eutectoid steels. Alloys with between 2 and 6% carbon are termed cast irons. Greater amounts of carbon often, but not always, mean greater hardness or tensile strength, which depend significantly on the microstructure of the alloy. The hardest iron-carbon alloys have a needle-like microstructure of iron carbides called martensite formed by rapid cooling from the austenite phase (Scott 1991, 33).

Wrought iron has a relatively low carbon content of 0.02-0.03 wt% and does not contain hardened structures. Some wrought iron alloys may fall into the α -iron region

at the left of Figure 1.2 with all carbon in solid solution with the ferrite. Others may contain some cementite which typically precipitates along grain boundaries.

1.2 Iron Smelting and Working

Iron occurs naturally in the form of mineral ores in the Earth's crust. The majority of these are oxides such as hematite (Fe_2O_3) and magnetite (Fe_3O_4), oxyhydroxides (goethite, $\alpha\text{-FeOOH}$) or sulphides (pyrite, FeS_2) (Bowles et al. 2011). Pre Iron Age examples of objects made from worked native 'telluric' iron or achondritic iron-containing meteorites exist (Craddock 2010, 93), but the wider use of iron did not occur until the beginnings of iron smelting technology in the early 2nd millennium BC in the Indian subcontinent (Tripathi 2013) and approximately 1200 BC in Anatolia. The development of smelting furnaces allowed the reduction of iron minerals to useable iron alloys by heating in a reducing atmosphere of carbon monoxide (Craddock 2010, 199). Early iron smelting processes were limited by the temperatures that could be attained in simple furnaces, normally not more than 1200°C. Pure iron melts at 1550°C but its melting point is lowered considerably by carbon, phosphorus and other impurities. Iron may be worked in a semi-solid state at a temperature of 1100°C in the form of a 'bloom' that gives its name to the 'bloomery process' of iron smelting, the earliest method of iron ore refinement (Tylecote 1992, 48; Craddock 2010, 241). Later processes achieved temperatures high enough to melt iron and cast it into ingots or 'pigs' of high carbon cast iron. High temperature smelting works producing true molten iron were known as 'blast furnaces' and required a second stage process of fining or puddling to produce wrought iron or steel (Craddock 2010, 253).

Following smelting by bloomery or blast furnace and finery, iron was formed by blacksmiths into a useful shape by forging with hand or mechanical hammers. Alternatively, at later dates, molten pig iron was poured into a mold and cast into the desired shape. Evidence of the forging or casting technique used, as well as of the type of iron-carbon alloy (cast, wrought or steel) and method of smelting, can be seen in the microstructure of the metal as revealed by microscopy of cross sections (metallography) and microanalysis (Scott 1991, 12).

1.3 Wrought Iron

Wrought iron consists of polyhedral grains of relatively pure α -iron (ferrite) and 1-3% siliceous slag, normally present in the form of elongated 'stringers' oriented along the direction of forging (Craddock 2010; Aston and Story 1939). The carbon content of wrought iron is typically very low (between 0.02-0.03% by weight) compared to 0.05-2.1 wt% (steel), and 3-5 wt% (cast iron). Carbon is normally present in interstitial solid solution with the ferrite phase, although some examples may contain small amounts of precipitated carbon as cementite (Fe_3C) or pearlitic cementite/ferrite structures.

Wrought iron does not contain quenched or martensitic phases, with the result that it is typically in the hardness range of H_v 130-185 (Vickers Hardness), considerably softer than most steels (Scott 1991, 82).

The chemistry of wrought iron depends on a number of factors, including raw materials and smelting and smithing processes. As well as carbon, the ferritic phase may contain Si, S, Mn, Ni or Co in small amounts, and up to 0.5 wt% phosphorus in solid solution (Buchwald and Wivel 1998). Sulphur concentrations greater than 0.01 wt% may make wrought iron susceptible to tearing during hot working, known as 'hot

short', or 'red short' in blacksmith terminology (Cain 1924). Greater amounts of phosphorous limit the amount of carbon that can be dissolved, and also make the wrought iron harder, more brittle and susceptible to tears during cold-working, a condition termed 'cold shortness' by smiths. Significant carbon and phosphorus are not normally found together in wrought iron solid solution (Craddock 2010 238).

During smelting, a significant amount (up to 50%) of the iron may combine with the silica to form slag, with the result that most wrought iron slag contains significant amounts of iron in the form of wüstite (FeO). The microstructure of the slag itself is often multi-phasic in nature, with a wüstite phase surrounded by a silica glass phase commonly occurring. In addition to silica and iron, wrought iron slag may contain P, Ti, Al, Mn, Mg, Ca, Na, K, and S, most often incorporated into a non-crystalline glassy matrix, but also in some cases incorporating mineral inclusions of fixed composition such as phosphoran olivine (Boesenberg 2006).

Wrought iron can be clearly distinguished from other iron-carbon alloys metallographically by the presence of silicate slag inclusions in its structure, which do not appear in other types of iron (Figure 1.3). Slag inclusions may be of different size, morphology and distribution within the iron metal matrix which reflect the smelting and working process.

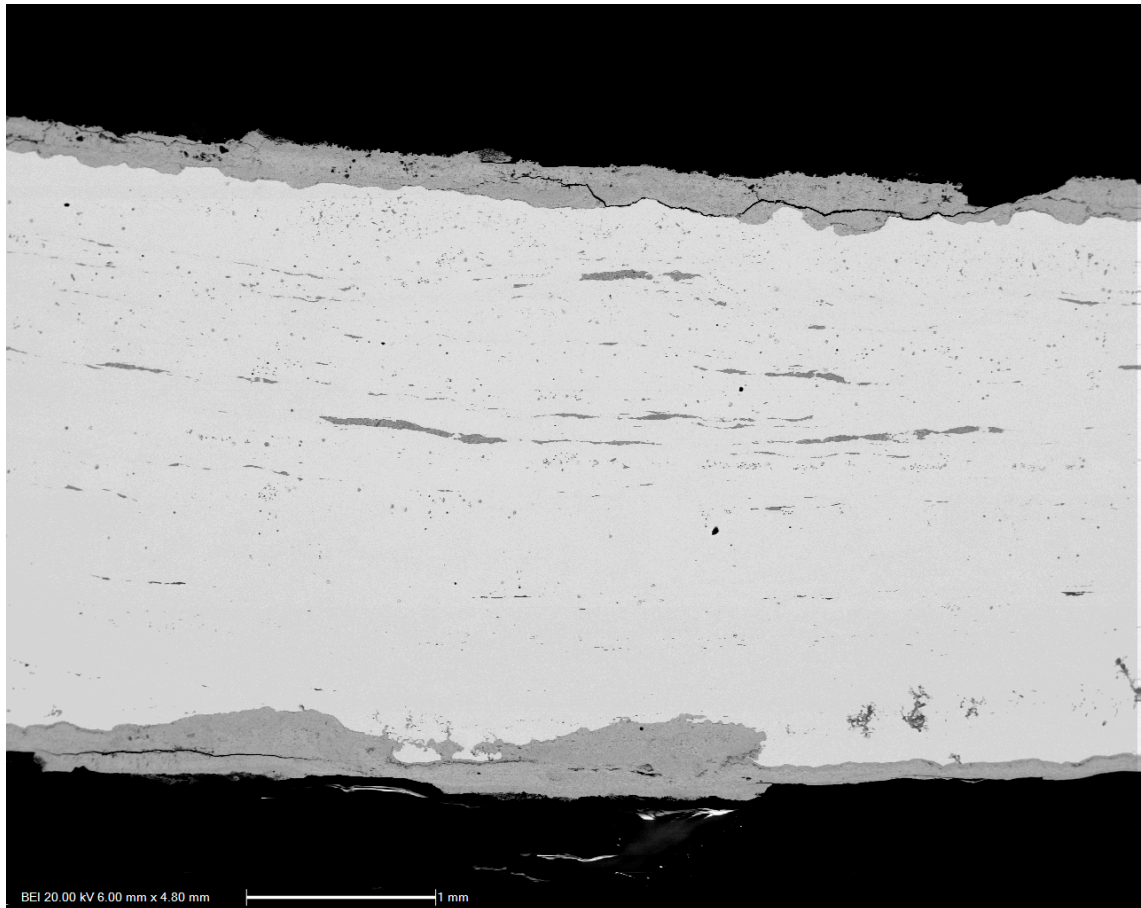


Figure 1.3 SEM-BSE (backscattered electron image) at 20X magnification showing elongated silicate slag inclusions in a wrought iron nail from Colonial Williamsburg, USA. (Sample: CW_31, sectioned longitudinally and polished).

1.3.1 Methods of wrought iron production

The bloomery process was the earliest form of iron smelting beginning with the Iron Age in the late 2nd millennium BC. Inclusions of glassy, silicate slag are an integral part of wrought iron produced by bloomery smelting, in which silicon-rich iron ores are heated to approximately 1100°C with charcoal and the iron remains in a spongy, semi-solid state with the molten slag acting as a natural flux (Craddock 2010, 241). The 'bloom' is smithed by hammering while hot to squeeze out excess slag and compact the iron to produce a more homogeneous product. Refinements to bloomeries by the

Roman period included slag tapping furnaces which drew off more of the slag during the smelt, resulting in a lower slag content wrought iron (Paynter 2007).

The blast furnace and finery, or 'indirect', methods of wrought iron production were utilised in Scandinavia from 13 C AD (Buchwald and Wivel 1998), in France as early as the late 14th C AD (L'Héritier et al. 2013) and developed in England from the 16th C onwards (Tylecote 1962, 300). Indirect processes were more efficient than bloomeries but involved more complex procedures and a greater variety of conditions and additives, leading to more varied microstructures and compositions within the slag and wrought iron as a whole. In blast furnace smelting, temperatures of 1300-1400°C are achieved producing truly molten iron (Craddock 2010 250) which is then cast into iron pigs containing silicate slag and a carbon content of 3-5 wt%. The cast iron is refined in a secondary heating process or finery that removes the carbon to the low levels typical of wrought iron (Tylecote 1962, 302-3). Fined iron was then smithed or milled hot to produce wrought iron bar or plate, with the iron being folded back on itself and hammered or rolled. Bars of wrought iron were also combined in a process called piling followed by forging or rolling to achieve a more uniform product. A more thorough smithing process resulted in a more homogeneous microstructure and distribution of slag inclusions in the wrought iron (Gordon 1988).

1.4 Context of Nails Used in This Study

The nails from Roman Caerleon were produced in the 2nd C AD in South Wales, where local iron production and smithing is attested at a number of sites (Young 2014).

Archaeological information on samples from Caerleon is given in Appendix 8.5.1. The

slag-tapping bloomery furnace was the method in use for Roman iron production at this time (Paynter 2007).

The nails from Williamsburg, Virginia examined in this study were produced between the 17-19th C AD and most likely by the blast furnace and finery method (Schwartz 2016). Archaeological information on nails from Colonial Williamsburg is given in Section 8.5.2. It is likely that sources of the raw material were bog ores from eastern Virginia in the U.S.A., neighbouring areas such as Maryland, or possibly imported from England due to lower cost than locally produced nails in the colonial economy (Schwartz 2016). The blast furnace and finery method may result in higher slag content than bloomery iron, as the slag which contains less iron is more viscous and difficult to smith out (Tylecote 1992). Additional slags may be formed by additives during the blast furnace process (Gordon 1996) and as their removal is more difficult the wrought iron produced will have a homogeneous structure only if thoroughly smithed or rolled. Less than thorough smithing results in uneven microstructure with the forging direction clearly visible in the slag distribution pattern, with slag inclusions concentrated in some regions and scarce in others. Even semi-automated processes of nail manufacturing in use at the end of 18th C America may result in variable microstructures (Ryzewski and Gordon 2008).

1.5 Nature of This Study

Understanding how people lived, the structure of their everyday life, and the technologies that supported them is embedded in both archaeological remains and the artefacts unearthed from them. Studying the microstructure of iron and the objects fashioned from it provides data that reveals manufacturing processes and

technological know-how that can be aligned with archaeological evidence to create a full picture of the technological landscape of ferrous metals. Their survival in museums is essential for this to occur and presents a challenge due to the inherent instability of wrought iron.

In this study of the conservation of wrought iron, characterisation of the sample nails focused on the microstructure, slag inclusions, corrosion product layers and elemental composition. This allowed the composition and morphology of the nails to be considered alongside data on corrosion rates, chloride content, and response to conservation treatment. This combined approach allowed relationships between the nature of wrought iron objects, corrosion, and conservation to be explored.

Wrought iron nails, widely used in the past and frequently found in archaeological contexts, were examined and their corrosion rate before and after treatment to remove chloride corrosion accelerators measured. Nails from two sites of differing age, Caerleon and Colonial Williamsburg, were chosen to compare results across archaeological contexts. The possible effects of slag inclusions and of naturally occurring corrosion product layers on corrosion rate and chloride removal were considered in terms of current models of archaeological iron corrosion and response of iron objects to desalination treatment.

2 Corrosion of Iron

2.1 Corrosion of Metals

Corrosion can be broadly defined as an interaction between a material and its environment that results in the deterioration of the material as well as alterations to the environment (Groysman 2010, 2). Discussion of corrosion will relate only to deterioration of wrought iron. Metal corrosion is a chemical or electrochemical process, although physical factors also play a role. Environmental conditions including temperature, pressure and the presence of water, oxygen, and other chemical species determine corrosion reactions, which are governed by thermodynamic and kinetic factors (Groysman 2010, 9). Since a significant amount of energy input in the form of heat is required to reduce metals from ores to a pure metallic state (Chapter 1), then corrosion is a natural process of recombination with other elements, releasing energy and returning metals to a more stable lower energy state (Jones 2014, 5).

Metal corrosion may occur in a number of forms. It may attack uniformly or cause pitting in localised areas (Alvarez and Galvele 2010, 773). It may form a protective oxide layer that will reduce the rate of further corrosion (Dillmann et al. 2004) or the products of corrosion reactions may be porous and non-protective (Graedel and Frankenthal 1990). The presence of different metals, alloys, or variations in composition and structure in electrical contact with each other may result in galvanic corrosion (Hack 2010, 829) and micro-variations in environment also promote corrosion (Neff et al. 2007, 42). A complete discussion of metal corrosion phenomena is beyond the scope of this study, but an overview of corrosion as it affects iron is presented below.

The simplest corrosion reactions involve the combination of a pure metal with oxygen, and nearly all metal surfaces are covered with at least a thin layer of oxide as its formation is thermodynamically favoured (Scully 1990, 4). Oxidation can occur without the need for an electrolyte as in the example (Groysman 2010, 10) of the corrosion of iron by oxygen to form magnetite:



This reaction can proceed at ambient temperatures, although significant iron corrosion resulting in growth of thicker oxide layers without an electrolyte mainly occurs at higher temperatures $> 500^\circ\text{C}$ (Hou 2010, 197). At lower temperatures of $\leq 100^\circ\text{C}$ in atmospheric, wet, or soil conditions, electrochemical corrosion requiring an aqueous solution predominates (Evans 1960).

Electrochemical corrosion requires both an anodic reaction in which metal ions and electrons are produced, and a cathodic reaction in which oxygen is reduced and electrons are consumed, that together form a corrosion cell (Leygraf and Graedel, 2000, 33). Examples of anodic [2.2] and cathodic [2.3] reactions for iron are:



An electrolyte (water containing dissolved conductive species) is required in which the resulting ions dissociate and may be transported between the sites of the anodic and cathodic reactions. Electrons must also be carried through a solid, electrically conductive phase such as metal or conductive metal oxide within the corrosion cell as shown in Figure 2.1.

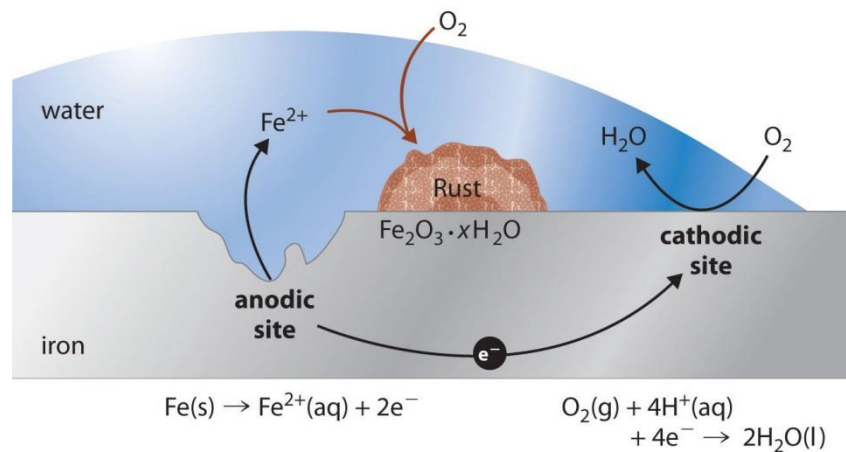


Figure 2.1 Schematic diagram of a metal corrosion cell showing flow of ions and electrons between the anode and cathode. Ions are transported through the electrolyte (water-based solution) and electrons through the conductive metal. (Principles of General Chemistry 2012 Licensed via CC).

Electrochemical reactions on metals that are fully immersed in aqueous solutions are not limited by availability of water whereas corrosion of partially hydrated metals is limited by requirements of electrochemical processes. The amount of water available in a given atmosphere is expressed by the term relative humidity (RH), defined as:

$$\text{RH} = p \text{ H}_2\text{O} / p^* \text{ H}_2\text{O}$$

where $p \text{ H}_2\text{O}$ is the vapour pressure of water and $p^* \text{ H}_2\text{O}$ is the equilibrium vapour pressure at a given temperature (Lide et al. 2005). Higher RH (expressed as a percentage) means that a greater amount of water is present in the air, with an RH value of 100% equalling the maximum amount of water that can be held in air at a given temperature.

The cathodic reaction in [2.3] involves oxygen, which is required for many corrosion processes, but other cathodic reactions, such as the reduction of water in [2.4] (Turgoose 1993), are possible.



Other chemical species, such as sulphides made available by sulphate reducing bacteria may also be reduced [2.5] (Allan Hamilton 2000, 5).



Cathodic reactions that do not require oxygen lead to the possibility of anaerobic corrosion but this only occurs to a significant degree in specific environments. Many further and more complex electrochemical corrosion reactions are possible, particularly when anions such as chloride are also present.

Ferrous ions initially produced by the anodic dissolution of iron oxidize to ferric (Fe^{3+}) ions when sufficient oxygen is present, leading to the formation of ferric compounds such as the ferric oxyhydroxide lepidocrocite ($\gamma\text{-FeOOH}$), a principal product of atmospheric iron corrosion (Leygraf and Graedel 2000, 282).

The types of corrosion thermodynamically likely to occur for a given metal in a given environment can be described by an Eh/pH or Pourbaix diagram, an example of which for iron metal in water is given in Figure 2.2. Specific iron oxides or hydroxides may form depending on the pH (x-axis) and redox potential (y-axis) which corresponds to the amount of oxygen present. Kinetic factors which determine the rate at which products of corrosion reactions form are not described by Pourbaix diagrams (Jones 2014, 75). In some cases, kinetics and energy required by chemical reactions mean that

thermodynamically predicted corrosion products will not occur naturally in practice (Pourbaix 1974).

Simplified Eh/pH diagrams (Figure 2.3) can also be used to indicate conditions under which a given metal may actively corrode, may be passivated (limiting corrosion), or protected from corrosion by specific environmental conditions, or by the application of corrosion control measures designed to prevent corrosion reactions from occurring. Figures 2.2 and 2.3 show that higher potentials corresponding to greater oxygen availability and lower pH result in corrosion, while low potentials cause cathodic protection. Higher pH values at mid-high potential result in anodic passivation.

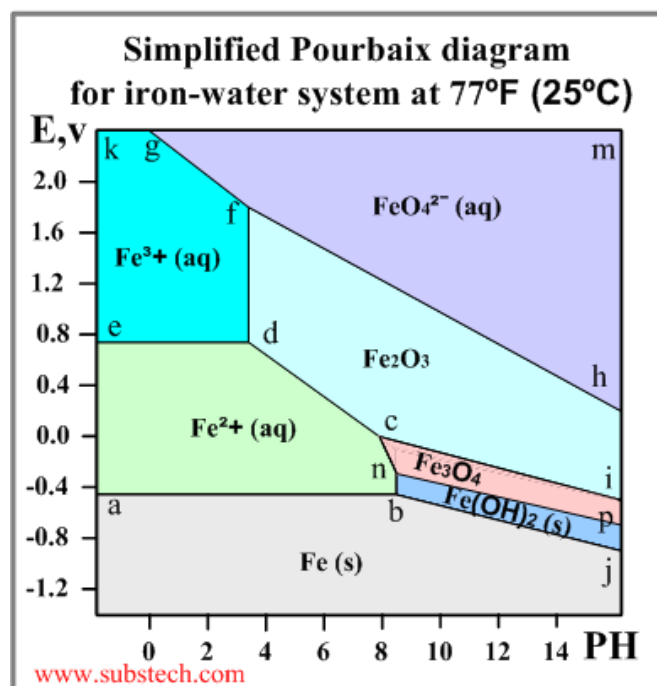


Figure 2.2 Simplified Potential/pH (Pourbaix) diagram for iron-water at 25°C showing thermodynamically stable phases. (www.substech.com 2016 Licensed under CC).

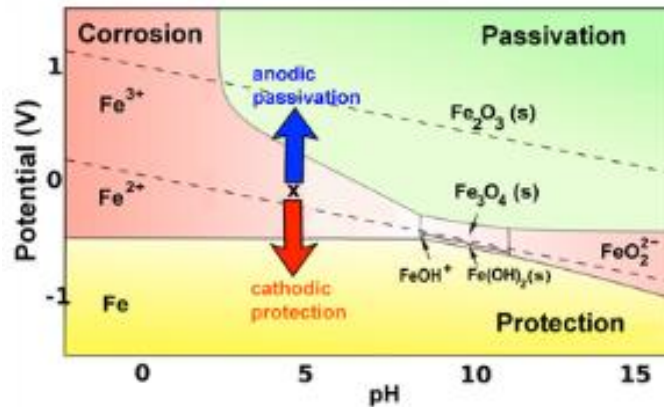


Figure 2.3 Eh/pH (Pourbaix) diagram for iron-water system showing ions and compounds and thermodynamically predicted regions of corrosion, passivation, and protection. (UC Davis 2012 Licensed under CC)

2.2 Iron Corrosion

Iron corrosion may take many forms depending on the alloy and environment involved. Discussion of corrosion here will be limited to iron-carbon alloys in conditions encountered during use, burial, and post-excavation storage of archaeological artefacts.

2.2.1 In the atmosphere

Corrosion of iron in atmospheric conditions is a complex phenomenon affected by atmospheric gases, thin layers of water on the metal surface, metal oxide layers, the metal itself and interactions between these regions (Leygraf and Graedel 2000, 9).

Basic factors contributing to atmospheric corrosion of iron will be briefly described.

All clean metals have a tendency to form surface oxides followed by a hydroxyl layer.

This will in turn have an overlying thin film of water adsorbed from atmospheric moisture (Schindelholz and Kelly 2012) in most conditions apart from arid regions or very dry indoor environments. Thickness of this water film will increase with relative humidity and the nature of the metal surface and may be 1 or more 'monolayers'

thick. A monolayer is equivalent to a thin film of water at least 1 molecule thick if spread evenly over a surface. Adsorbed water layers more than 3 monolayers thick act in a similar way to bulk water (Henderson 2002). Iron will adsorb multiple monolayers of water above 60% RH leading to corrosion (Graedel and Frankenthal 1990) and corrosion will increase substantially when RH reaches 80% (Maréchal et al. 2007). Hygroscopic materials such as dirt or salts on the surface of the iron can also attract thicker layers of water (Leygraf and Graedel 2000).

Water present on the iron surface allows electrochemical corrosion reactions to take place according to the anodic and cathodic half reactions [2.2] and [2.3]. The anodic and cathodic reaction may occur at different sites in atmospheric corrosion provided that ion and charge transfer are possible. Both half-reactions are required for corrosion to proceed, leading to the fact that if one is prevented, corrosion will stop, or if limited it will become the rate-limiting step of the corrosion mechanism.

Corrosivity of the iron-oxide-water layer system is affected by external factors from the atmosphere which enter the aqueous layer in the form of gases or particulates. Examples are O_2 , O_3 , CO_2 , NO_2 , SO_2 , HCl and H_2S as gases or $NaCl$ and Na_2SO_4 as aerosol particulates (Leygraf and Graedel 2000, 13). These species dissolve into this adsorbed water layer, dissociate and undergo aqueous reactions, among which is the production of acids such as HNO_3 , H_2SO_4 and HCl . Mobile Cl^- ions are also produced.

The amount of water on the surface determines its availability for electrochemical corrosion reactions, and solvation of ions such as metals, salts or pollutants present in the water layer (Leygraf and Graedel 2000, 13). This in turn has an acute effect on the corrosivity of the solution (Leygraf and Graedel 2000, 17). Water is needed for

corrosion but highly concentrated solutions produced by drying of surface water can cause severe attack, particularly in the form of pitting or crevice corrosion produced by ion or oxygen concentration gradients (Jones 2014, 200). The dynamic effects of exposure to solutions of higher or lower concentrations depend on time, and the concept of Time of Wetness (TOW) has been developed as a measure of the effects of wetting and drying cycles on atmospheric corrosion (Schindelholz and Kelly 2012). The cycle of wetting and drying (Figure 2.4) of corroding iron surfaces in the atmosphere has three stages; wetting, wet and drying (Stratmann 1990; Hoerlé et al. 2004; Maréchal et al. 2007). The initial wetting stage involves production of ferrous ions [2.2] and reduction of the previously formed ferric oxyhydroxide lepidocrocite as the cathodic reaction, consuming no new oxygen. The second, fully wet stage is characterised by corrosion reactions [2.2], [2.3] consuming oxygen from the atmosphere. The third stage involves drying of the electrolyte, oxidation of Fe^{2+} to Fe^{3+} ions and precipitation of ferric corrosion products. The third, drying stage is particularly important for growth of corrosion layers and can result in the regeneration of lepidocrocite, or formation of the more protective goethite (Maréchal et al. 2007, 138; Dillmann et al. 2004).

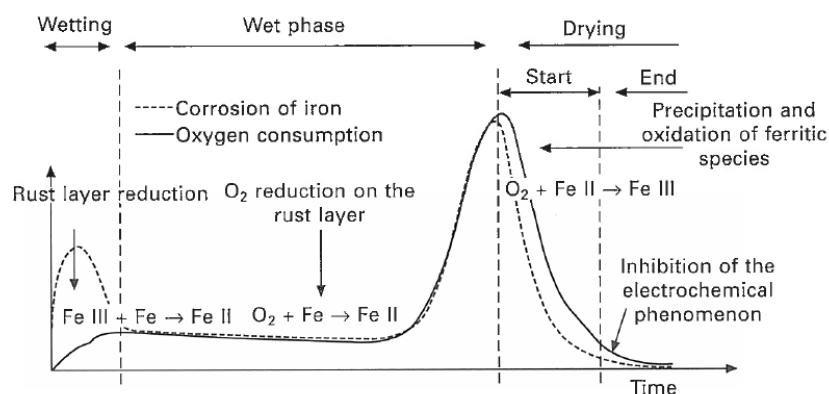


Figure 2.4 Diagram of interactions occurring during the 3 phase wet-dry cycle of atmospheric corrosion. (Maréchal et al. 2007 with data from Stratmann 1990) Reproduced with permission of Taylor and Francis Group LLC in the format Thesis/Dissertation via Copyright Clearance Center.

2.2.2 Corrosion: wet and marine environments

Iron corrosion in waterlogged environments involves similar reactions to electrochemical corrosion of iron in atmospheric conditions [2.1, 2.2, 2.3], but is not subject to the effects of wet-dry cycles that result in periodic high concentration of ions. Availability of oxygen may be less than for atmospheric corrosion but more constant and governed by O₂ solubility in water at the prevailing temperature of the iron object. Oxygen solubility at 1 atmosphere and 20°C is 8.4 mgL⁻¹ in pure water (Lyon 2010, 1097) and 7.5 mgL⁻¹ in seawater of 3.5% salinity (Phull 2010, 1110) and oxygen content of water at the surface will be close to these levels. Solubility of O₂ decreases with increasing temperature and salinity and its concentration is also dependent on depth and biological activity within both marine and freshwater contexts (North and MacLeod 1987, 74). Access of oxygen to cathode sites is a rate controlling factor in iron corrosion (Vega et al. 2007, 107) and reduced O₂ concentrations may limit corrosion in wet environments (Angelini et al. 2013, 239; Memet 2007, 155).

Marine corrosion of iron may initially be rapid and aggressive due to the presence of high mean concentrations of 19.85 g/kg of chloride ions in seawater (North and MacLeod 1987, 71). As with iron corrosion in other environments, actual concentration of chloride at the corroding metal surface may be even higher than in the surrounding environment due to concentration of Cl⁻ as a counter ion to the production of Fe²⁺ ions (Turgoose 1982b).

Characteristic of marine iron corrosion is the formation of a layer of hard calcareous concretion (North 1976). Concretion forms over actively corroding iron in a bio-chemical process and acts as a partial barrier to oxygen and ion exchange, normally

resulting in the reduction of corrosion rate. Ferrous ions migrate from the metal surface at least part way through the calcareous layer, forming ferric oxyhydroxides and iron carbonates (North 1982; North and MacLeod 1987, 77; Memet 2007, 158).

Microbially Influenced Corrosion (MIC) may occur in anaerobic conditions found in freshwater and marine environments as well as in anaerobic soils. Sulphate Reducing Bacteria (SRB) species such as *Desulfovibrio desulphuricans* are capable of reducing environmental sulphate to sulphide (Allan-Hamilton 2000, 4; Scott and Eggert 2009, 102) which is then reduced in a cathodic reaction, allowing corrosion to proceed anaerobically:



The reduced sulphur is then available to form iron sulphide corrosion products such as mackinawite (FeS):



SRB-enabled anaerobic corrosion is a significant factor in the corrosion of marine archaeological iron in the upper layers of the seabed where bacteria are found and sulphates are available for bacterial reduction. Such marine iron often has a layer of iron sulphide in the calcareous concretion layer (North and MacLeod 1987, 78). Several species of bacteria and archaea (single celled prokaryotic organisms) also have the ability to reduce Fe^{3+} ions (Allan-Hamilton 2000, 11), further modifying corrosion reactions.

2.2.3 Corrosion: soil

Most soils retain water producing damp and periodically waterlogged conditions. The result is an environment between atmospheric and wet conditions but with additional considerations. Concentration of environmental O₂, CO₂ and other gases present in soil depend on depth of burial and are significantly different than in the atmosphere (Knight 1990). Amount of O₂ is 17% as opposed to 20% in the atmosphere and CO₂ 3%. Provided enough O₂ is available, aerobic iron corrosion will proceed but as with corrosion in fresh or marine waters, its rate will be limited by access of oxygen to cathodic sites (Vega et al. 2007, 107). Chlorides in soil accelerate corrosion and are unlikely to be removed by solvation as they can be on rain-washed iron in atmospheric conditions or reduced to low-concentrations in fully-wet conditions. More extensive corrosion, thicker corrosion layers, and a higher Cl⁻ concentration at the surface of the metal often result from their role as a counter ion in charge balance within electrolytic corrosion.

Some soil conditions have very little oxygen whether due to depth, geology or depletion by biological activity. Anaerobic iron corrosion may occur in such soils, particularly in low pH and where sulphate reducing bacteria are active (Rémazeilles et al. 2010a and b). Burial conditions influence which compounds are thermodynamically stable and iron carbonates such as siderite (FeCO₃) may occur within corrosion in anaerobic conditions.

2.2.4 Iron corrosion products

Corrosion processes in the environments described result in production of a range of iron corrosion products, according to their thermodynamic stability within the prevailing environment. With greater availability of oxygen, Fe²⁺ may oxidize into Fe³⁺ to form the ferric oxyhydroxide polymorphs goethite (α-FeOOH), akaganeite (β-FeOOH) or lepidocrocite γ-FeOOH (Selwyn et al 1999; Neff et al. 2005). Ferrous and ferric ions also combine with anions such as chloride (Cl⁻) which facilitates many iron corrosion reactions. The most common iron corrosion products are described below together with their properties and formation pathways.

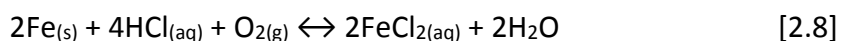
2.2.4.1 Iron Chlorides: FeCl₂, FeCl₃

Negatively charged chloride ions (Cl⁻) from the environment are drawn towards corroding iron surfaces where Fe²⁺ ions are produced (Figure 2.5), leading to the formation of a ferrous chloride (FeCl₂) solution near the metal/corrosion interface (Turgoose 1982a and b). This solution is acidic due to hydrolysis of Fe²⁺ ions (Turgoose 1993)



Hydrolysis of Fe²⁺ may lead to a series of further reactions including formation of Green Rust 1, ferrous hydroxychloride, and akaganeite. In the presence of sufficient oxygen, FeCl₂ oxidizes to ferric chloride (FeCl₃) (Selwyn et al. 1999). Both compounds are associated with 'weeping iron' (Figure 2.5) a condition in which a solution containing FeCl₂ and FeCl₃ is present as yellow, acidic droplets on the surface of corroding iron, which may further oxidize and dry to form hard shells of ferric oxyhydroxide (FeOOH) (Selwyn et al. 1999).

Chloride ions are important facilitators of iron corrosion since they balance charge as counter ions, function as electrolytes, attract water allowing electrochemical reactions to proceed and participate in metal dissolution via HCl acid regeneration cycles (Askey et al. 1993):



and



Where HCl is consumed in the production of FeCl₂ and then regenerated to continue the corrosion cycle.

The very high solubility of FeCl₂ and FeCl₃ means they only occur as solutions when water is present, only precipitating on drying out. As a solid they remain a reservoir for Cl⁻ release with increasing RH or water availability. Solid FeCl₂ is hygroscopic and found in hydration states of FeCl₂·2H₂O and FeCl₂·4H₂O (Turgoose 1982b; Selwyn et al. 1999). Conversion to the higher hydration state occurs above 19% RH and this change is a corrosion driver in chloride contaminated iron at RH over 20% (Turgoose 1985, 1993; Watkinson and Lewis 2005b).

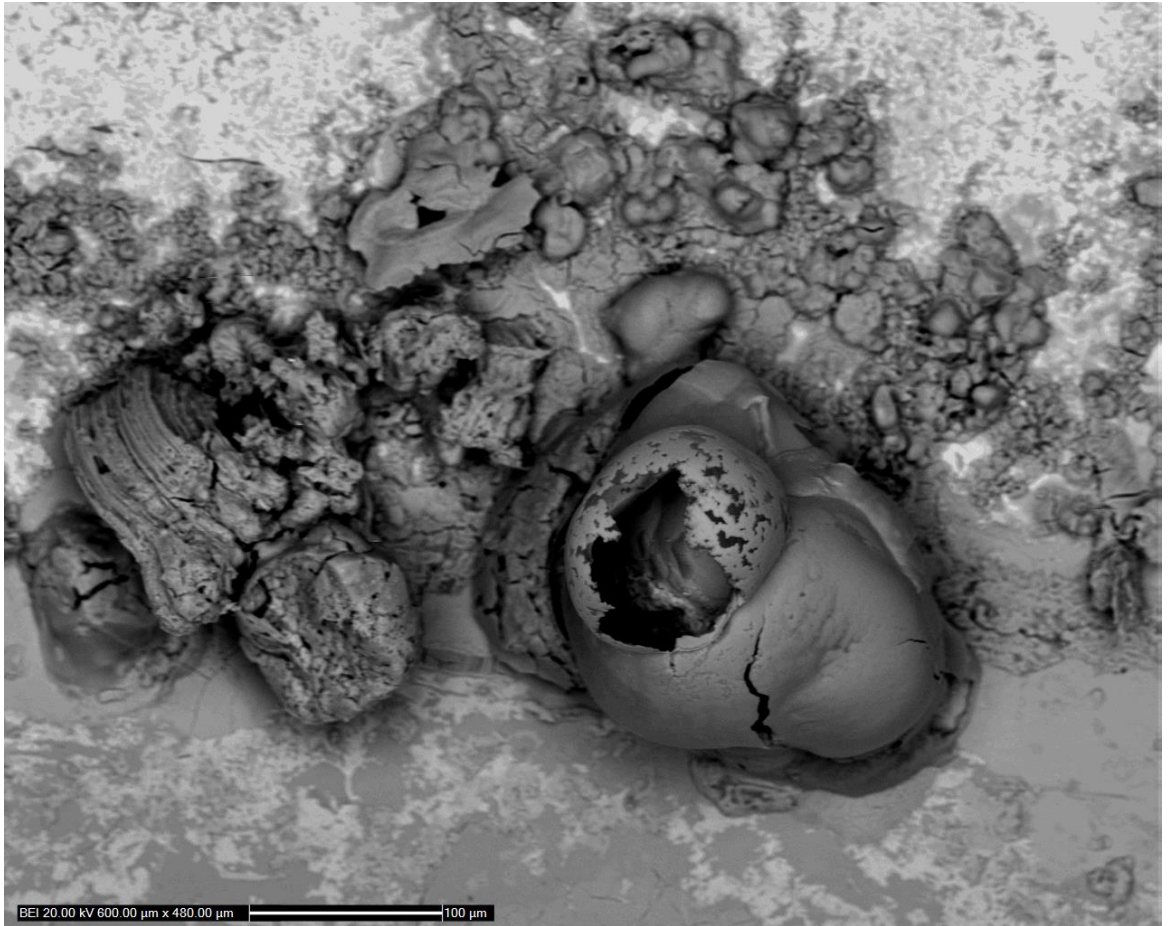


Figure 2.5 SEM-BSE image at 200X magnification of iron chloride corrosion products on a polished cross-section of an untreated wrought iron nail from Caerleon, left in ambient conditions of 20°C 45-55 % RH for 6 months. Fresh corrosion identified by SEM-EDS as containing chlorine has developed at the interface between metal and corrosion product layers. Broken shells consistent with weeping iron chloride corrosion can be seen on the right and tubular structures with the form of akaganeite (β -FeOOH) on the left.

2.2.4.2 Green Rusts

Green Rust 1 ($[\text{Fe}_2^3\text{Fe}^3(\text{OH})_8]^+[\text{Cl } n\text{H}_2\text{O}]^-$) and Green Rust 2 ($[\text{Fe}_2^2\text{Fe}^3(\text{OH})_5]^+[\text{SO}_4 \cdot n\text{H}_2\text{O}]^-$) are intermediate iron corrosion phases formed in the presence of chloride and sulphide ions respectively. They form in anoxic conditions in place of $\text{Fe}(\text{OH})_2$ when the pH is only slightly acidic or alkaline (Cornell and Schwertmann 2003, 357) and are an intermediate metastable phase in the formation of ferric oxyhydroxides such as akaganeite (Refait and Génin 1997).

2.2.4.3 Magnetite: Fe_3O_4

Magnetite (Fe_3O_4) is a black, electrically conductive iron oxide containing both Fe^{2+} and Fe^{3+} ions. It may form by oxidation of Fe^{2+} in solution through intermediate stages of green rust, $\text{Fe}(\text{OH})_2$ or precipitation of mixed $\text{Fe}^{2+}/\text{Fe}^{3+}$ solutions (Cornell and Schwertmann 2003, 346). Magnetite is normally formed in conditions of limited oxygen availability, such as water at temperatures $> 20^\circ\text{C}$ and $< 100^\circ\text{C}$ or within layers of corrosion products that do not contain enough O_2 to form ferric oxyhydroxides. A mechanism in which Fe^{2+} ions migrate outward from the metal into cracks within corrosion layers, then oxidize into Fe_3O_4 when more O_2 is available has been proposed (Neff et al. 2005) to explain the occurrence of strips or 'marblings' of Fe_3O_4 and maghemite ($\gamma\text{-Fe}_2\text{O}_3$) within a matrix of ferric oxyhydroxides occurring on archaeological iron (Figure 2.6).

Magnetite is important as a site for cathodic corrosion reactions involving O_2 reduction. Its electrical conductivity allows the flow of electrons from anodic reactions to cathodic sites, which may be physically separated from anodic regions (Réguer et al. 2007a) (Figure 2.7). Some models of corrosion in archaeological iron have sited

cathodic reactions primarily in magnetite layers located away from, but electrically connected to, anodic reactions at the metal surface which is consistent with observed pH variations (Turgoose 1985).

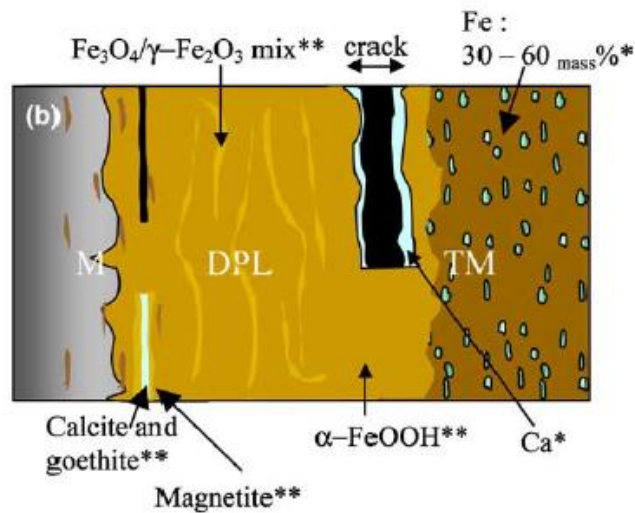


Figure 2.6 Schematic diagram of iron corrosion product layers on an archaeological iron nail from Cabaret and Montbaron, France showing a mix of Fe_3O_4 and $\gamma\text{-Fe}_2\text{O}_3$ present in 'marblings' surrounded by a Dense Product Layer (DPL) of goethite ($\alpha\text{-FeOOH}$) overlying the metal surface (M). Reprinted from *Corrosion Science* 47(2), Neff et al., Corrosion of iron archaeological artefacts in soil: characterisation of the corrosion system., Figure 8b p. 527, Copyright 2005, with permission of Elsevier.

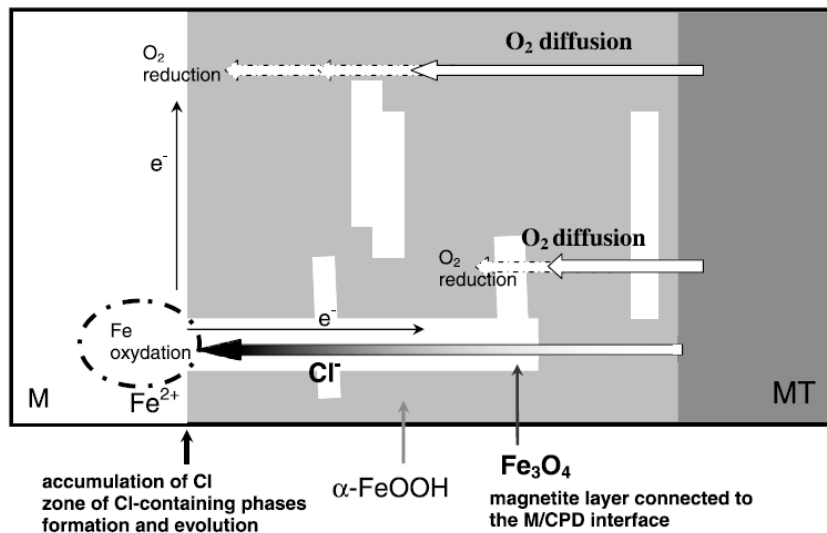


Figure 2.7 Schematic diagram of iron corrosion product layers showing Cl^- and O_2 diffusion from outer layers (MT, on right) down to the metal (M, left). The Cl^- is drawn in as a counter ion to Fe^{2+} produced by anodic reactions at the metal surface. Some of the O_2 is reduced in cathodic reactions in magnetite (Fe_3O_4) layers that are electrically connected but physically separated from the metal. Reprinted from *Corrosion Science* 49(6), Réguer et al., Buried iron archaeological artefacts: Corrosion mechanisms related to the presence of Cl^- containing species., Figure 11 p. 2741, Copyright 2007, with permission of Elsevier.

2.2.4.4 Maghemite: $\gamma\text{-Fe}_2\text{O}_3$

Maghemite ($\gamma\text{-Fe}_2\text{O}_3$) is produced by the transformation of magnetite at room temperature, and contains primarily Fe^{3+} ions (Cornell and Schwertmann 2003, 32). It is an alteration product of initial corrosion to magnetite and is seen in corrosion product layers, such as the veins of 'marbling' in archaeological iron objects (Neff et al. 2005) (Figure 2.6). Maghemite maintains a similar structure and surface area to the magnetite that preceded it (Cornell and Schwertmann 2003, 109) and so does not disrupt the physical structure of corrosion layers upon its formation.

2.2.4.5 Ferrihydrite: $\text{Fe}_5\text{OH}_8\cdot 9\text{H}_2\text{O}$

Ferrihydrite ($\text{Fe}_5\text{OH}_8\cdot 9\text{H}_2\text{O}$) is a hydrated, poorly crystalline iron oxide. It is less stable than goethite or hematite and may transform into them (Cudennec and Lecerf 2006; Bayle et al. 2016). Ferrihydrite may form veins of 'marbling' in iron corrosion product layers and may provide a conductive pathway for electrons in atmospheric corrosion (Monnier et al. 2011) after being reduced to magnetite during wetting of corrosion product layers (CPLs) (Stratmann and Hoffmann 1989).

2.2.4.6 Lepidocrocite: $\gamma\text{-FeOOH}$

Lepidocrocite ($\gamma\text{-FeOOH}$) is a semi-conductive ferric oxyhydroxide that forms in neutral pH solutions and is a principal early product of atmospheric iron corrosion that is reduced and re-oxidized during wet-dry cycles (Hœrlé et al. 2004). Lepidocrocite is less stable and less protective than other iron oxyhydroxides and may transform into goethite over time (Dillmann et al. 2004). In archaeological iron objects, lepidocrocite may form part of thicker iron corrosion layers in the form of bands of 'marbling'

running through a goethite matrix which may also play a role as oxygen reduction sites in atmospheric corrosion (Monnier et al. 2011).

2.2.4.7 Goethite: α -FeOOH

Goethite (α -FeOOH) is the most geologically stable iron oxyhydroxide (Bowles et al. 2011). It may be formed in corrosion processes by direct oxidation of Fe^{2+} ions and it forms the greater proportion of corrosion product layers in many instances. Goethite formation is favoured by the presence of Fe^{2+} ions where chloride concentrations are low or non-existent and there is abundance of oxygen (Cornell and Schwertmann 2003). It occurs in the voluminous middle layers of corrosion products, rather than at the metal/corrosion interface (Neff et al. 2005) (Figures 2.5, 2.6). Once formed, goethite is protective, stable and non-reactive and ratios of the amount of goethite and magnetite to lepidocrocite and akaganeite present in iron corrosion layers have been proposed as a measure of stability of iron objects (Dillmann et al. 2004).

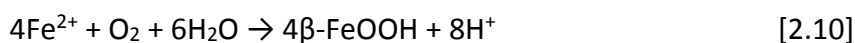
2.2.4.8 Ferrous Hydroxychloride: β -Fe₂(OH)₃Cl

Ferrous hydroxychloride β -Fe₂(OH)₃Cl (Réguer et al. 2015) exists in low oxygen conditions close the surface of corroded iron such as archaeological iron ingots recovered from a marine context (Kergourlay et al. 2011). β -Fe₂(OH)₃Cl contains high levels of chloride (up to 18 wt%). It is a precursor to the formation of β -FeOOH (Refait and Génin 1997) and may exist at the metal/corrosion interface of archaeological iron objects *in situ* without causing damage. Exposure to greater levels of O₂ after excavation causes oxidation to more destructive β -FeOOH (Réguer et al. 2007a). It has been shown that β -Fe₂(OH)₃Cl may be reduced to Fe(OH)₂ in archaeological iron objects by alkaline washing treatments (Kergourlay et al. 2011).

2.2.4.9 Akaganeite: β -FeOOH

Akaganeite (β -FeOOH) is a ferric oxyhydroxide with a tunnel structure similar to hollandite (BaMnO_{16}). It appears as a reddish brown solid with a tubular structure, similar to that seen on the left in Figure 2.5. Akaganeite incorporates chloride ions in two forms; adsorbed on the outside of the structure and occluded inside tunnels (Stahl et al. 2003). Varying amounts of chloride adsorbed on the surface of β -FeOOH are likely responsible in large part for differences in reported chloride content of akaganeite, which has ranged from 4-17 wt% in synthetic samples (Watkinson and Lewis 2005b). Réguer et al. (2007b) found that precipitated synthetic akaganeite contained 12 wt% chloride which could be reduced to 4.5% by washing to remove adsorbed chloride.

Akaganeite forms naturally from FeCl_2 in the presence of oxygen at $\text{RH} \geq 20\%$ as:



with chloride becoming incorporated into the β -FeOOH structure (Turgoose 1982b, 1993). More recently it has been shown (Rémazeilles and Refait 2007) to require significant quantities of Fe^{2+} and Cl^- ions (at least 3.2 and 1.6 mol l^{-1}) as well as oxygen to form, with higher O_2 levels increasing the reaction rate. In the presence of oxygen, ferrous hydroxychloride ($\beta\text{-Fe}_2(\text{OH})_3\text{Cl}$) present in FeCl_2 solutions converts to chloride containing Green Rust 1 ($[\text{Fe}^2_3\text{Fe}^3(\text{OH})_8]^+[\text{Cl nH}_2\text{O}]^-$) which further oxidizes to γ -FeOOH, α -FeOOH, or if there is sufficient chloride, β -FeOOH (Refait and Génin 1997). The role of $\beta\text{-Fe}_2(\text{OH})_3\text{Cl}$ as a precursor to β -FeOOH in the corrosion of archaeological iron has only recently been understood (Kergourlay et al. 2007; Réguer et al. 2015).

Akaganeite can be physically damaging to iron due to its rapid growth and large volume compared with other corrosion products such as ferrous chloride or magnetite. It is associated with cracking or spalling-off of protective corrosion product layers, exposing the corroding metal surface to more oxygen and further corrosion cycles.

The presence of chloride in β -FeOOH promotes corrosion of metallic iron at > 12% RH (Watkinson and Lewis 2005a, b). This occurs due to mobile hygroscopic surface adsorbed Cl^- rather than that occluded in tunnels. Surface adsorbed chloride forms an electrolyte promoting corrosion above 35% RH. Chloride adsorbed on β -FeOOH can be removed by aqueous washing, removing its hygroscopic and corrosive properties (Watkinson and Lewis 2005a; Réguer et al. 2009; Watkinson and Emmerson 2016).

While akaganeite has been reported to be metastable in room temperature conditions (Gilberg and Seely 1981) changing into magnetite or goethite, some long-term studies have not identified this (Watkinson and Lewis 2005b).

2.2.4.10 Hematite: Fe_2O_3

Hematite (Fe_2O_3) is a stable semi-conductive iron oxide (Cornell and Schwertmann 2003). Hematite is not normally found in iron corrosion layers but can be formed as a result of exposure of iron to elevated temperatures (Scott and Eggert 2009, 40). It may be formed by the transformation of akaganeite in aqueous solutions \geq pH 11 and elevated temperatures (Cornell and Giovanoli 1990).

2.2.4.11 Carbonates and Sulphides

Iron carbonates such as siderite (FeCO_3) or chukanovite $\text{Fe}_2(\text{OH})_2\text{CO}_3$ are formed in anaerobic soils, as in the case of iron nails from the site of Glinet, France (Neff et al. 2005). Siderite is especially common in neutral pH waterlogged sites (Matthiesen et al. 2003).

Iron sulphides such as mackinawite (FeS) may result from reaction of Fe^{2+} with HS^- [2.6] or reaction of goethite or magnetite with H_2S (Walker 2001). Their formation also requires anaerobic conditions and the presence of sulphate reducing bacteria, and iron sulphide and carbonate compounds may be found in the same conditions (Rémazeilles et al. 2010a and b).

2.2.5 Transformation of iron corrosion products

Iron oxides and oxyhydroxides can transform from one form to another under certain physico-chemical conditions (Cornell and Schwertmann 2003). Such changes may involve precipitation and dissolution, solid state topotactic transformations, or oxidation-reduction reactions. Iron oxide transformations relevant to corrosion and conservation of archaeological iron are given in Table 2.1.

Iron Oxide	Transformation Products	Conditions Required
Akaganeite (β -FeOOH)	Goethite, Hematite (Fe_2O_3)	pH 11-15 and $\geq 60^\circ\text{C}$ in aqueous solution, $\geq 200^\circ\text{C}$ in air (rapid), 20°C (slow).
Goethite (α -FeOOH)	Hematite	260 - 320°C
Magnetite (Fe_3O_4)	Maghemite, Hematite	20°C (Maghemite), $\geq 300^\circ\text{C}$ (Hematite)
Lepidocrocite (γ -FeOOH)	Goethite, hematite	Alkaline solution (Goethite), $>80^\circ\text{C}$ (Goethite+Hematite)
Akaganeite, Lepidocrocite, Goethite	Magnetite	High concentration of Fe^{2+} , anoxic and or external polarization current
Ferrihydrite	Magnetite, $\text{Fe}(\text{OH})_2$ Goethite, Hematite	Reduction during wetting of corrosion products

Table 2.1 Oxides commonly present as archaeological iron corrosion along with their transformation products and physico-chemical conditions required. (Data from Cornell and Schwertmann 2003).

In the absence of extreme temperatures, most transformations occur in aqueous solutions apart from slow transformation of magnetite to maghemite at 20°C (Cornell and Schwertmann 2003). The transformation of akaganeite, lepidocrocite, and goethite in alkaline solutions is of interest to archaeological conservators as they may potentially occur in alkaline washing treatments designed to remove chloride (desalination) and reduce post-excavation corrosion of iron artefacts.

2.3 Corrosion of Archaeological Iron Artefacts

Archaeological iron artefacts are subject to corrosion phenomena outlined above, but have specific considerations due to age, burial environment, and original composition. Excavated iron commonly exhibits complex corrosion product layers from tens of micrometres to several millimetres thick produced during *in situ* corrosion and which affect post-excavation corrosion. While corrosion layers may be protective and limit further corrosion, they may also harbour high concentrations of chemical species such as chlorides or sulphides that facilitate corrosion reactions. Terminology for description of corrosion layers will be reviewed together with models of determining factors in archaeological iron corrosion before and after excavation.

2.3.1 Description of corrosion product layers

Corrosion product layers (CPLs) on archaeological iron vary in composition, thickness, density and morphology, reflecting complex corrosion processes occurring naturally over a long period of time (Watkinson et al. 2013, 408). Until more recent studies, archaeological iron corrosion was mainly described as voluminous and obscuring of shape and surface details. Recent work by Bertholon (2000, 2007) and analytical studies by (Neff et al. 2004) have helped to refine descriptive terminology and understanding of CPLs to better reflect their complexity.

The concept of markers for the description of corrosion layers on archaeological metals were pioneered by Bertholon (2000). In this terminology, the original surface of an object is considered to be the surface of the object at the time it went out of use and entered its archaeological context. Markers such as sand grains from the burial

environment or slag inclusions in the metal core are indicative that a layer is above, below, or at the original surface.

The extended terminology of Neff et al. (2004, 2005) is illustrated by examples of archaeological wrought iron nails in cross section (Figures 2.8 and 2.9). The metal core labelled 'M' contains internal markers such as slag inclusions (SI), while the dense product layer (DPL) consists of less oxidized iron oxides, oxyhydroxides and/or carbonates covering the metal and above this the transformed medium (TM) comprises a mix of corrosion products and burial environment material such as sand grains and more oxidized corrosion products. The boundary between the DPL and the TM is the original surface (OS) that may have moved since the object entered its context. The thickness and morphology of these layers may vary greatly with factors such as soil chemistry, hydrology, oxygen availability and microbial activity. Maintaining the integrity of the information-containing original surface is important archaeologically and aesthetically.

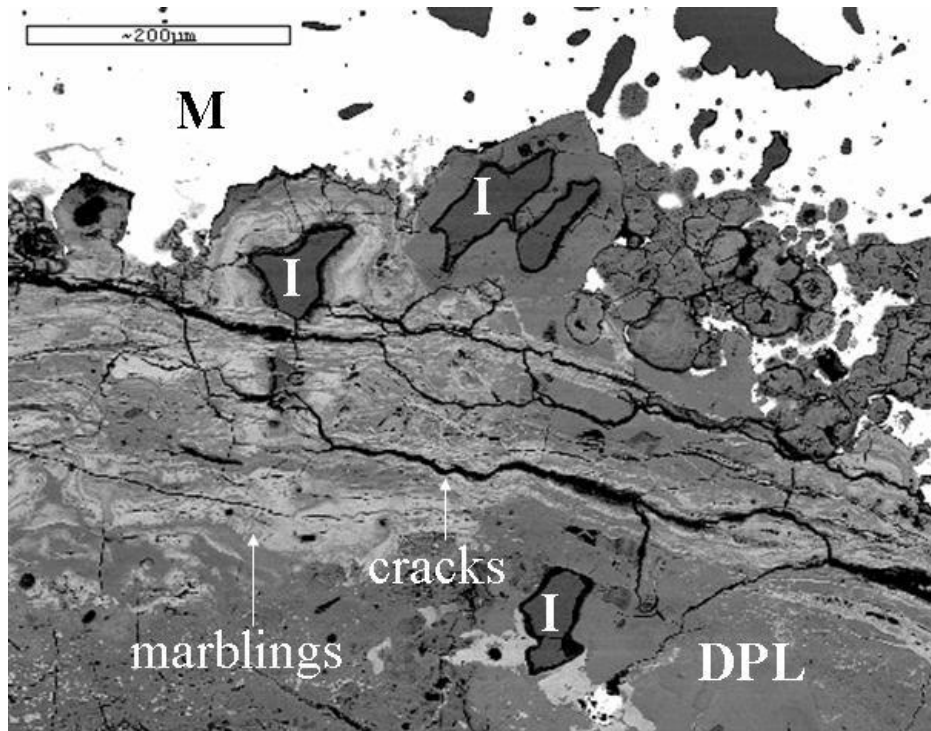


Figure 2.8 SEM-BEI (backscattered electron image) of a corroded archaeological wrought iron object in cross-section, showing the preserved metal (M), dense product layer (DPL), marblings, cracks, and slag inclusions (I). Reprinted from *Corrosion Science* 47(6), Chitty et al., Long-term corrosion resistance of metallic reinforcements in concrete-a study of corrosion mechanisms based on archaeological artefacts., Figure 7, p. 1566, Copyright 2005 with permission from Elsevier.

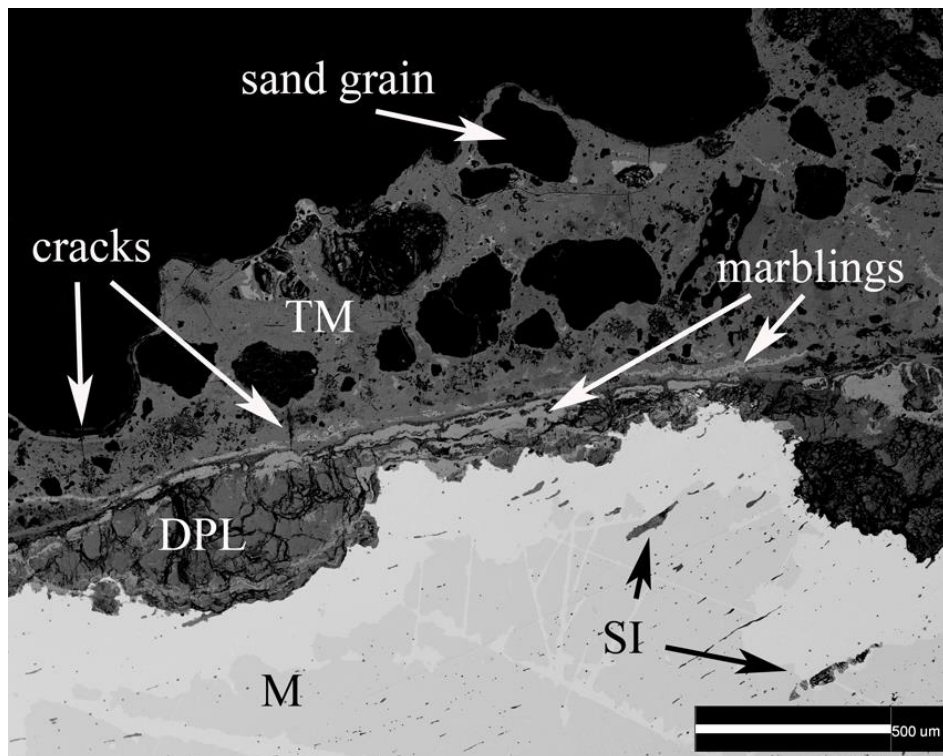


Figure 2.9 SEM-BEI image of a corroded wrought-iron nail from the site of Usk, Wales in cross section at 50X magnification. The metal core (M), slag inclusions (I), dense product layer (DPL), marblings, cracks, transformed medium (TM) and sand grains (S) can be seen. (Image: Nordgren-Labeling system adapted from Chitty et al. 2007).

2.3.2 Models of archaeological iron corrosion

Archaeological iron corrosion during burial has been identified as a system (Turgoose 1982b, 1985, 1993; Selwyn 2004a, 105) in which a remaining metal core is overlaid by CPLs primarily of Fe_3O_4 and ferric oxyhydroxides such as $\alpha\text{-FeOOH}$, $\gamma\text{-FeOOH}$, and $\beta\text{-FeOOH}$. When there is sufficient moisture present, cracks and pores in the CPLs contain an acidic solution of ferrous chloride formed by anodic dissolution of iron metal to Fe^{2+} ions, which partially hydrolyse [2.7] reducing pH at the metal/CPL interface. The cathodic reaction is normally the reduction of oxygen [2.3]. Provided there is solid phase conductivity of electrons to cathode sites these need not be located next to the anode reaction. Location of both anodic and cathodic reactions at the corroding metal surface seems unlikely as together the H^+ and OH^- reaction products would produce a neutral pH at the metal/CPL interface, rather than the acidic values observed inside marine wrought iron objects (MacLeod 1981) or the low-pH $\text{FeCl}_2/\text{FeCl}_3$ weeping solutions in terrestrial iron objects (Turgoose 1982b). The cathodic reaction was therefore thought to occur mainly at magnetite corrosion further out in the CPL matrix where there is greater access to oxygen (Turgoose 1993). This model requires a pathway of conductive corrosion products to facilitate electron transfer, as well as an aqueous solution to allow ion transfer. If sufficient oxygen is present, Fe^{2+} ions may also oxidize to form the ferric oxyhydroxides goethite and lepidocrocite. Akaganeite is formed as a post-excavation corrosion product when Cl^- is concentrated upon drying (Section 2.4) whereas during burial Cl^- exists in solution next to anode sites on the metal surface.

Recent work (Neff et al. 2004, 2005, 2007) has characterised corroded archaeological iron artefacts and refined understanding of their corrosion mechanisms. Samples of

ancient wrought iron (Chitty et al. 2007) (Figure 2.8) have been found to consist of a preserved metal core (M) covered by a dense product layer (DPL) consisting mainly of goethite with magnetite or maghemite marblings, seen in Figure 2.8 as lighter areas in a darker matrix of goethite. In some cases, the DPL contained lepidocrocite, akaganeite, or siderite. The DPL contained numerous cracks, mainly parallel to the M/DPL interface but some perpendicular to it.

The location of the cathodic reaction [2.3] in buried archaeological iron has been re-examined in recent studies (Chitty et al. 2007; Réguer et al. 2007a) which reveal that conductive CPLs such as Fe_3O_4 may not always be in contact with the metal to allow electron transfer and that the site of the cathodic reduction of oxygen is instead at the metal/CPL interface. Location of the cathodic reduction of oxygen at the metal surface has been confirmed by ^{18}O radio-oxygen tracer studies of archaeological iron in aqueous solution (Vega et al. 2005, 2007) suggesting diffusion of dissolved oxygen into the CPL structure controls corrosion kinetics, lending importance to the thickness of corrosion layers.

Location of both anodic and cathodic reactions at the metal/CPL interface is inconsistent with observed concentrations of chloride as a counter ion at this location as the positive charge that attracts it would be cancelled out by the negative charge of the cathodic sites (Rimmer 2010). It has been suggested (Réguer et al. 2007a) that partial contact between metal and conductive corrosion phases such as magnetite in marblings may allow separation of the anodic and cathodic reactions in localised areas (Figure 2.8). Oxygen could therefore be reduced after diffusing part way into the DPL. This would result in local increases in chloride concentration at the metal/CPL interface

where conductive phases make contact, fitting the observed location of chloride at the metal/CPL interface, but not distributed homogeneously around the metal core (Réguer et al. 2007a). This mechanism likely exists alongside cathodic reactions at the metal.

2.3.3 Effect of iron alloy and production technique

Ore composition, smelting and working techniques have significant effects on the chemical and physical profile of the resulting iron. Bloomery smelted iron has a different chemical makeup than that produced in a blast furnace (L'Héritier et al. 2013). Physical working techniques such as forging leave stresses and physical irregularities such as crystal dislocations that form natural sites of attack for corrosion processes (Procter 2010). Stress corrosion cracking may also result from precipitation of elements such as C, P, and N along grain boundaries (Jones 2014). This creates energy differences in the alloy matrix, which facilitate electrolytic corrosion.

2.3.4 Effect of inclusions

Inclusions in iron such as precipitated carbon phases, silicate slag or impurities modify the mechanical and chemical properties of the metal. Inclusions may have a beneficial effect on mechanical properties (Aston and Story 1939, 47; Schmidt and Lucas 2009) but may also enhance corrosion. The presence of inclusions may affect corrosion of iron in three ways which are often interconnected: acting as a physical locus of corrosion processes; providing a site of physical breakdown; or having a chemical effect on the tendency of iron to corrode.

Modern ferrous metals are produced according to stringent protocols and subject to quality controls designed to detect unwanted inclusions which are viewed as contaminants. Possible corrosion effects of such inclusions have been studied in modern ferrous metals. The presence of iron oxide and sulphide inclusions were found to correlate with weaker protective oxide films in low carbon steels (Shibaeva et al. 2014) and distribution and morphology of carbon phases was shown to affect the electrochemical corrosion of steel in NaCl electrolytes (Haisch et al. 2002).

Archaeological iron objects were not produced with such strict controls and their corrosion may be influenced by much more extensive naturally occurring inclusions.

Carbon phases such as graphite flakes present in quantities of 3-5 wt% as a continuous network in grey cast iron can drive corrosion as they are electrically conductive, cathodic to the metal and act as corrosion sites (Jones 2014, 324). In contrast, carbon present in wrought iron is at very low levels (< 1 %) and not present as a network and is therefore much less significant for corrosion.

Slag inclusions in uncorroded wrought iron add to its mechanical strength (Schmidt and Lucas 2009) but can also act as fault lines leading to mechanical breakup of the metal through delamination when corrosion has proceeded around them (Krejslova et al. 2013, 322). Slag inclusions are particularly likely to collect chloride when a developing corrosion pit comes in contact with them. This is at least in part because they act as cathodes promoting anodic dissolution of surrounding metal which in turn attracts chloride as a counter ion. Migration of ions may be facilitated by defects at slag metal interfaces (Neff et al. 2005). The extent to which these effects occur in a given archaeological iron artefact depends on accessibility of slag to corrosion, and are promoted by localised slag close to the original surface rather than homogenous distribution throughout the metal.

2.4 Post-Excavation Corrosion

2.4.1 Changes occurring after excavation

Excavating archaeological iron artefacts changes their environmental conditions, disturbing equilibria with the prevailing physicochemical conditions within soil or marine contexts that have developed over time. Reduction in carbon dioxide levels, changes in relative humidity and temperature and greater availability of oxygen are only some of the factors (Knight 1990). For wet or marine sites, damage often occurs from rapid drying and physical and chemical changes also result from drying iron objects excavated from damp soil. Post-excavation drying is similar to the third drying phase within an atmospheric corrosion wet-dry cycle (Section 2.2.1) producing increased concentration of chemical species and better access of oxygen to corrosion layers.

Corrosion product layers surrounding archaeological iron have pores and cracks containing ferrous chlorides and hydroxychlorides (Turgoose 1982b; Réguer et al. 2007a). Oxygen will oxidise ferrous chloride through intermediate stages to form β -FeOOH at the metal/CPL interface. The increased molar volume of β -FeOOH (three times that of iron metal) exerts physical pressure on overlying corrosion layers causing cracking, spalling and breakup of iron objects (Selwyn 2004b; Jegdić et al. 2011). This allows more oxygen to access the metal/CPL interface where it feeds cathode reactions and replenishes O₂ in the adsorbed water film. The hygroscopicity of ferrous chloride and akaganeite (Sections 2.2.4.1, 2.2.4.9) attracts atmospheric water to support corrosion reactions.

Consideration of how atmospheric corrosion models fit archaeological iron offers understanding of post-excavation behaviour of iron artefacts in storage and display. The main difference between atmospheric corrosion of archaeological iron and modern ferrous metal surfaces is the thicker and more complex iron oxide corrosion layers (CPLs) of the former. Dissolved oxygen transport through cracks and pores to cathode reactions at the metal/CPL interface was found to be the rate-limiting step in aqueous archaeological iron corrosion (Vega et al. 2005, 2007, 107). Oxygen transport through pores to cathode sites is crucial in the wet and drying phases of atmospheric corrosion models (Hoerlé et al. 2004). In thicker corrosion layers, such as in 15th C AD atmospherically corroded iron, oxygen reduction may take place in ferrihydrite or lepidocrocite marblings reduced during the wetting phase (Monnier et al. 2011). In the absence of chloride, these atmospheric corrosion mechanisms will produce ferric oxyhydroxides including goethite during the drying phase, growing protective, stable CPLs (Dillmann et al. 2004).

Oxygen must be reduced in post-excavation atmospheric corrosion of excavated archaeological iron, consequently its diffusion to cathode sites at the metal surface is governed by porosity and cracking of CPLs. Large cracks present in CPLs will become a path of least resistance for oxygen transport and soluble chloride at the metal/CPL interface will facilitate rapid oxidation to akaganeite.

2.4.2 Long-term post excavation changes

Corrosion processes and corrosion product transformations occurring in archaeological iron artefacts during the months or years of post-excavation storage have important implications for their long-term preservation and availability for study and display.

Corrosion will continue provided metallic iron, oxygen, and water are present, often aided by chloride. Even relatively slow reactions can eventually result in damage or, in some cases, total disintegration of iron objects. Rates of corrosion and the role of chloride as corrosion promoter are also affected by changes in environmental conditions over time. Transformation of corrosion products such as from akaganeite to goethite or hematite may also occur (Thickett and Odlyha 2014). Such transformations reflect corrosion products moving towards a more stable state, but may also result in slow release of chloride stimulating fresh corrosion.

The prospect of applying effective conservation measures to archaeological iron may also be affected by post-excavation corrosion and chemical changes. Iron which is completely mineralised is normally stable and does not need further conservation (Watkinson 1983). Most iron retaining a metal core will require preventive conservation often linked to interventive measures to limit further deterioration and loss of information.

Post excavation, the form of iron corrosion and of chloride-containing compounds change over time. Akaganeite forms from ferrous chloride causing physical damage and making chloride more difficult to remove (Kergourlay et al. 2010). These changes need to be considered if removal of chloride ions rather than control of the storage environment is to be adopted as a long-term preservation strategy.

Loeper-Attia (2007, 192) has suggested 'Reactivated Corrosion' as a term to describe corrosion evidenced by weeping, macro-cracks, flaking and spalling occurring on archaeological objects post-excavation as opposed to pre-excavation. This assumes objects are either stable (no reactivated corrosion) or unstable (subject to reactivated corrosion). These definitions are useful for visual surveys based on macro-indications of corrosion-related change, but do not offer quantitative measurement of corrosion rates. Few iron objects are likely to be completely 'stable' after excavation. Even if they lack chloride they will corrode at a slow rate unless kept in desiccated or oxygen free environments (Turgoose 1982b). An important question is: "At what rate do macroscopic and microscopic changes occur which result in reduction or destruction of the information potential and heritage value of the object" (Watkinson and Rimmer 2013).

3 Conservation of Archaeological Iron

Conservation treatments for archaeological iron may be divided into preventive and interventive strategies. The former seek to prevent corrosion through control of their storage or display environment, primarily by reducing the availability of oxygen or water for corrosion reactions. The latter normally seek to remove chemical species such as chlorides which accelerate corrosion reactions or apply corrosion inhibitors or protective coating systems to disrupt corrosion mechanisms. While protective coatings can be highly effective (Emmerson 2015), they are not part of this study.

3.1 Preventive Conservation

Preventive conservation methods aim to protect heritage materials from deterioration by controlling their environment. They normally limit or prevent activation of corrosion mechanisms requiring water and oxygen. This requires no direct physical intervention to the objects, whereas interventive conservation treatments such as desalination using chemical washing techniques do. Preserving objects in their original state is an important ethical goal of conservation practice (Muñoz-Viñas 2009) but is often difficult to achieve in practice. It may be more productive to consider conservation measures in terms of mitigating loss of information (Muñoz-Viñas *op. cit.*) and intervention measures appropriate to the desired outcome (Cronyn 1990; Caple 2000).

Desiccated storage of archaeological iron with moisture absorbing material such as silica gel or by mechanical de-humidification has been practiced extensively for over 50 years (Robinson 1998; Knight 1997; Watkinson and Neal 1998; Thompson 2003, Rimmer et al. 2013a). Recent studies (Watkinson and Lewis 2004, 2005a, 2005b, 2008; Thickett 2012; Thickett et al 2011; Thickett and Odlyha 2010, 2014) have refined

understanding of the interaction of iron, chlorides, and iron corrosion products with changes in relative humidity. Iron will corrode at any RH above 15% in the presence of akaganeite and corrosion is rapid above 60% as monolayers of water form (Leygraf and Graedel 2000, 293). Experiments with synthetic akaganeite powder mixed with iron did not result in corrosion below 12% RH (Watkinson and Lewis 2005a).

Removal of oxygen can be employed to prevent iron corrosion during storage (Turgoose 1982b; Knight 1990). Its use and effectiveness are based on increased availability of oxygen scavenging materials such as Mitsubishi Gas Chemical Corporation RP-System and effective gas-tight barrier films such as Escal (MacPhail et al. 2003; Laboratory of the Oriental Institute of The University of Chicago 2014; Paterakis and Hickey-Friedman 2011; Paterakis and Mariano 2013). Disadvantages include the need to refresh the scavenger and gas barrier film periodically and inaccessibility of objects.

Storage of archaeological iron in deep freeze conditions $\leq -20^{\circ}\text{C}$ has been investigated (Kuhn and Eggert 2010) and found to have some success in temporarily slowing down the formation of akaganeite, but akaganeite formation was confirmed in samples stored frozen for more than 750 days making it unsuitable for long-term storage.

3.2 Interventive Treatment

Most interventive conservation techniques seek to remove corrosion-promoting anions such as chlorides from heritage iron in order to reduce corrosion rates and are termed desalination. Such treatments utilise either washing techniques or high temperature volatilization methods (Section 3.2.1). While minimum intervention with object composition, appearance and the evidence it contains is the goal for treatment

of archaeological iron, it must be a flexible ethic balanced against predicted success in reducing corrosion rate.

Treatment time, cost, and the expertise required for interventive conservation coupled with concerns about the act of intervention and the effectiveness of treatments means a preventive approach based on environmental control prevails. Balanced against this is the expense of long-term preventive conservation measures which are not insignificant (MacLeod 2015).

Efficient application of interventive treatments such as desalination of iron may be employed synergistically with preventive conservation measures. Recent studies recognise that quantifying the effectiveness of desalination treatments underpins such approaches and aids predictive management.

3.2.1 Desalination techniques

Desalination has utilised many techniques (Table 3.1). These normally employ additional pre or post-treatment procedures, such as concretion removal before treatment or post-treatment steps such as post-treatment rinsing and the application of protective coatings.

Chloride Removal Methods for Archaeological Iron			
Washing Methods			
	Reference	Advantages	Disadvantages
Hotwashing/Soxhlet/ Boiling	Scott and Seely 1986, Watkinson 1996.	Low-cost, no chemicals required	Limited effectiveness compared with alkaline washing
Simple Washing (NaOH)	North 1987, Schmutzler 2012	Low-cost, fewer chemicals, less equipment	Limited evidence of effectiveness, slower than other methods
Ethylenediamine	Argo 1982, Argyropoulos and Selwyn 2005	May increase effectiveness of NaOH washing	Not effective alone, may complex iron
Electrolytic Reduction	North 1987, Hamilton 1976 Barker 2003 Lacoudre 1992 Kergourlay 2010	Faster/more effective than simple washing alone in some cases	Equipment required, damaging if improperly applied
Alkaline Sulphite	North and Pearson 1975, Gilberg and Seely 1982, Watkinson and Al-Zaharani 2008, Schmitt-Ott and Oswald 2006, Rimmer 2010, Rimmer et al. 2012, Schmutzler 2012	Effective for chloride extraction extensively tested	Sealed container required difficult to apply to large objects.
De-oxygenated Alkaline Washing by Inert gas	Al-Zahrani 1999, Rimmer 2010, Schmutzler 2012	Effective, fewer chemicals required than alkaline sulphite	Requires inert gas supply
Subcritical Water Extraction	Drews et al. 2004, de Viviés et al. 2007, González-Pereyra et al. 2010, 2014	Highly effective, fast, does not require deconcretion of marine objects	Specialised equipment and training, cost, limited object size
High Temperature Methods			
Hydrogen Reduction	Barkman 1977 O'Shea et al. 1982, North 1987, Barker 2003	Effective chloride removal, relatively short treatment time	Equipment, cost, risk of explosion, metallurgical alteration
Plasma Reduction	Daniels 1979, Veprek and Patscheider 1986, Schmidt Ott and Boissonnas 2002	Can improve results of washing treatments	Specialised equipment, cost, plasma alone found ineffective for removing Cl ⁻

Table 3.1 Chloride removal methods for heritage iron objects, divided into aqueous washing and high temperature methods.

3.2.1.1 Hotwashing, Soxhlet, and Boiling

Boiling or hot washing of archaeological iron offered a low cost solution for chloride removal, and reached its zenith in Soxhlet washing (Scott and Seeley 1987). Watkinson (1996) obtained chloride mean extraction efficiencies of 64% using Soxhlet washing, while Scott and Seeley (1987) utilised nitrogen gas to deoxygenate the treatment water to prevent corrosion and improve washing efficiency by releasing Cl^- from its role as a counter ion. This increased efficiency as Watkinson and Al-Zahrani (2008) obtained 67-93 % desalination efficiency (a mean of 80.9 % for 10 samples) using nitrogen gas de-oxygenated Soxhlet washing but found the results unpredictable. These methods are no longer widely used. Risk of damage to iron artefacts, their metallurgical structure (Ehrenreich and Strahan 1987) or their corrosion layers from high temperatures, heating/cooling cycles and dynamic flow of washing cycles may be one reason and specialised apparatus which limits the size of object treated may be another (Scott and Eggert 2009, 139). The long term corrosion rate of Soxhlet-washed archaeological iron has not been assessed, making it difficult to evaluate the effectiveness of this method.

3.2.1.2 Sodium Hydroxide

Soaking in solutions of sodium hydroxide, sodium carbonate or sesquicarbonate has been recommended for objects too fragile to undergo other treatments and is a cheap treatment option (North 1987, 221-2; Schmutzler 2012). In theory, the elevated pH limits corrosion of iron during treatment, causes micro-porosity of the corrosion products and extracts chloride more efficiently than neutral pH solutions due to the presence of OH^- ions that can displace chloride (North 1987, 214), lower surface

tension, and cause softening and cracking of iron corrosion layers which increases their porosity (Selwyn and Argyropoulos 2005).

Washing in NaOH relies on diffusion of chloride from the metal surface, whereas electrolytic reduction draws out chloride and maintains a concentration gradient in solution (Kergourlay et al. 2010). It is less effective than alkaline sulphite (NaOH/Na₂SO₃) at preventing corrosion during treatment which will limit Cl⁻ extraction (Turgoose 1985, 1993; Watkinson 1996). Schmutzler (2012) contends that low concentration sodium hydroxide solutions may be nearly as effective in extracting chloride as alkaline sulphite or gas-de-oxygenated washing treatments in terms of amount of chloride removed, although they require longer durations. This differs from earlier research (Watkinson 1996; Watkinson and Al-Zahrani 2008) showing chloride extraction in NaOH solutions without de-oxygenation to be erratic and less efficient than de-oxygenated NaOH. The archaeological iron samples tested by Schmutzler were very low in chloride content before treatment, which may account for the apparent comparable performance of simple washing with other methods.

3.2.1.3 Ethylenediamine

Argo (1982) developed the use of ethylenediamine solutions for washing chloride contaminated iron and this method has undergone further research (Selwyn, Argyropoulos and Logan 1997; Selwyn and Argyropoulos. 2005). It was seen as a synergetic treatment involving ethylenediamine and NaOH but ethylenediamine did not improve chloride extraction either in combination with NaOH or alone. Further, it caused dissolution of metal from objects during treatment due to complexing of iron by ethylenediamine (Selwyn and Argyropoulos 2005).

3.2.1.4 Electrolytic Reduction

Electrolytic reduction, also known as electrochemical polarization, has been applied to the conservation of metals for over 100 years (Rathgen 1905; Plenderleith and Werner 1971; Wihl 1975; Hamilton 1976; North 1987, 223; LaCoudre et al. 1991; Guilminot et al. 2007; Argyropoulos et al. 2015). A low voltage DC electric current supplied by a battery or power supply makes the metal object a cathode within a circuit created in an electrolyte employing passive anodes. Electrochemical reduction of corrosion products results, increasing porosity and allowing diffusion of chloride ions away from the object (Kergourlay et al. 2010). The applied current prevents corrosion, freeing up chloride from its counter ion role to facilitate its release (Turgoose 1993). This formerly popular treatment is now used less frequently due to concerns about damage or loss of information through loss of corrosion product layers. Additionally, if the applied potentials exceed the hydrogen evolution potential, vigorous evolution of hydrogen gas occurs producing loss of corrosion products, physical damage or breakup of objects (North 1987, 225; Scott and Eggert 2009, 156).

It is claimed to deliver faster and more effective desalination than other iron washing treatments, particularly for large objects and marine archaeological objects such as cannons. Gil et al. (2003) reported transformation of akaganeite into goethite and magnetite in a marine cast iron cannonball. It was recorded to be the most efficient chloride extractor for samples from a single marine cast iron cannon ball compared with galvanic reduction, alkaline sulphite washing and immersion in KOH (Oliveira and Fonseca 2014). Beaudoin et al. (1997) reported increased rates of chloride release when electrochemical polarisation was compared to alkaline sulphite solutions in the retreatment of terrestrial wrought iron objects.

Electrolytic reduction continues to be used extensively for treatment of shipwreck material from sites such as the *Queen Anne's Revenge* and the *USS Monitor*.

Refinement of the method includes (Scott and Eggert 2009, 155) carefully controlled current densities and measurement of applied potentials with reference electrodes (LaCoudre et al 1991), and automatic potentiostatic control of treatments by remote control (Guilminot et al. 2007).

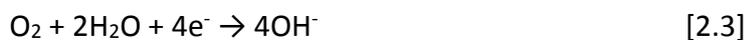
The relative effectiveness of electrolytic reduction when compared with washing techniques without polarization or other iron conservation approaches has been questioned. Drews et al. (2004) have found electrolytic reduction to be no faster or more effective at extracting chloride from wrought iron than alkaline sulphite or sodium hydroxide washing, using a small number of samples. The claimed relative effectiveness of electrolytic reduction is anecdotal, with few large scale surveys of treatment outcomes (Selwyn and Logan 1993) and no quantitative statistical measures of its effectiveness for removing chloride or reducing corrosion rate in controlled tests.

3.2.1.5 Alkaline Washing De-oxygenated by Inert Gas

Washing of iron in sodium hydroxide solutions de-oxygenated by a flow of inert gas was pioneered by Al-Zahrani (Al-Zahrani 1999; Watkinson and Al-Zahrani 2008). It is similar in principle to alkaline sulphite washing but achieves low oxygen conditions in solution by bubbling a stream of inert gas such as nitrogen or argon through the solution rather than by reaction with sodium sulphite.

De-oxygenation of the alkaline wash solution is carried out to prevent ongoing iron corrosion processes that would otherwise occur during treatment, hindering chloride release by continuing to hold it as a counter ion (Turgoose 1982b). Removal of oxygen

prevents the cathodic half of the iron corrosion reaction in which oxygen is reduced from occurring:



This in turn disrupts the charge balancing anodic reaction of the oxidation of iron to positively charged ferrous ions at the metal surface:



Without the continued production of positively charged ferrous ions at the metal surface, negatively charged chloride ions are no longer held as counter ions and are free to be released into the desalination solution. De-oxygenation and prevention of iron corrosion therefore allows chloride extraction to be more efficient than in oxygenated solutions where it continues to be held as a counter ion (Turgoose 1985 1993; Watkinson and Al-Zahrani 2008).

Inert gas washing has the advantage of exposing the object to fewer chemicals during treatment and leaving fewer residues behind than alkaline sulphite washing. It produces less chemical waste, but requires a constant low pressure flow of inert gas. Initial promising results (Al-Zahrani 1999; Watkinson and Al-Zahrani 2008) were replicated by Rimmer (2010) and Schmutzler (2012) and the method was found to be as effective as alkaline sulphite washing in removing chloride. It has not found widespread use in conservation practice presumably because of the requirement for a compressed gas supply, pressure regulator and appropriate health and safety measures.

3.2.1.6 Subcritical Water Extraction

The use of subcritical fluids was pioneered by Drews, González, Mardikian, de Viviés and others at Clemson University during research into the most effective conservation methods for treating marine archaeological iron from the American Civil War submarine *H.L. Hunley* (Drews et al. 2004; de Viviés et al. 2007; González-Pereyra et al. 2010; González et al. 2013; Drews et al. 2014; González-Pereyra et al. 2014). The principle is based on the unusual properties of fluids at temperatures and pressures slightly below (subcritical) the 'critical point' on a Pressure/Temperature fluid phase diagram for water. Subcritical water can exhibit properties of both a liquid and a gas, and act as a low viscosity super solvent, penetrating the structure of corrosion products more easily than normal water and solvating chloride ions at many times the efficiency. A phase diagram showing subcritical water treatment parameters is given in Figure 3.1.

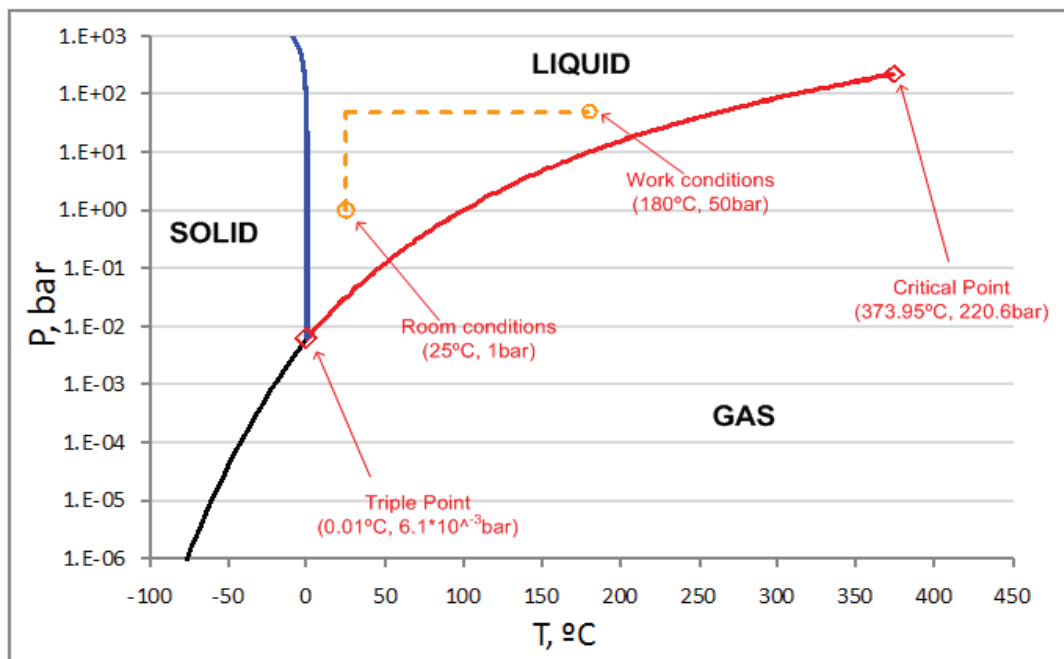


Figure 3.1 Phase diagram (Pressure in bar as a function of Temperature in °C) for water showing physical conditions used in subcritical extraction of chloride from archaeological iron. Source: González-Pereyra et al. 2010 Figure 1b p. 23. Used with permission of the Warren Lasch Conservation Center, Clemson University.

Treating iron objects in a subcritical reaction vessel in a low concentration of NaOH at a pressure of 50 bar and temperature of 180°C removed virtually all traces of chloride in a matter of days, resulting in a highly stable object (González et al. 2013, 460).

Further research involved examining treatment parameters and their effects on cast and wrought iron artefacts from marine and terrestrial archaeological contexts.

Temperature, rather than pressure, was found to be the important factor for chloride extraction (Bayle et al. 2016; González et al. 2013, 441). It is also clear that some transformation of corrosion products occurs, including breakdown of akaganeite, notably to hematite (de Viviés et al. 2007; Drews et al. 2014; Bayle et al. 2016).

Experiments with marine and terrestrial iron objects have found that unlike many desalination treatments, subcritical extraction does not require the removal of marine concretions, insoluble salt accretions, or thick layers of corrosion products before desalination, as the fluid is capable of penetrating through to the object below (González-Pereyra et al. 2010).

Operating temperatures for subcritical extraction are considerably less than for hydrogen reduction but could still result in alteration of some metallurgical structures, particularly martensitic structures that can be affected at as low as 100°C (Tylecote and Black 1980). It is also possible that silicate phases may be highly soluble in alkaline subcritical conditions resulting in removal of silicate slag inclusions exposed to the treatment solution. Further limitations of subcritical treatment to date have been cost, need for specialised equipment and training and the size of the objects which can be treated. Initial tests were done with treatment chambers of 600 ml volume or less. Larger systems up to 40 litres are currently being used at Clemson University and A-

Corros Expertise in France. Additional research on subcritical treatment of iron is being done in collaboration with CEA-Saclay, Paris (Bayle et al. 2016).

3.2.1.7 Hydrogen reduction

Hydrogen reduction is an example of an alternative approach to desalination that uses high temperatures to volatilize chloride rather than washing. It was first applied in Stockholm for treatment of iron cannon and other marine archaeological iron artefacts recovered from the 17th C Swedish warship *Wasa* (Barkman 1977). The method was further developed and utilised in Portsmouth, UK for artefacts from the *Mary Rose* (O'Shea et al. 1982; Barker 2003) and at the Western Australian Museum for iron from the *Batavia* and other vessels (North and Pearson 1977; North 1987, 227). Hydrogen reduction involves heating chloride-containing iron artefacts to high temperatures (between 400-800°C) in a closed furnace with a through stream of dry hydrogen gas that reduces corrosion products to magnetite and metallic iron. Chlorides are either sublimed or reduced to HCl and carried away from the object (Barker 2006). Hydrogen reduction is highly effective at removing chloride (Barkman 1977) but cost, health and safety, potential damage to the object due to thermal expansion/contraction and alteration of metallurgical structures at the high temperatures involved are concerns (Tylecote and Black 1980). Though loss of metallurgical information can be managed by pre-treatment sampling (O'Shea et al. 1982), it does not apply equally to all types of ferrous artefacts.

3.2.1.8 Plasma reduction

Gas plasma treatment of metal artefacts was first introduced in the UK (Daniels et al. 1979) and has seen considerable research and development, particularly at the Swiss

National Museum where it has been a part of the treatment strategy for archaeological iron since 1984 (Patscheider and Veprek, 1986; Schmidt-Ott 1997; Schmidt-Ott and Boissonnas 2002). Plasma reduction involves placing the artefact in an evacuated glass reaction vessel filled with a combination of gases, typically an inert gas and hydrogen. The gas mixture is excited into a plasma state by application of either DC current or RF (radio frequency) energy, causing reduction of corrosion products and potentially removal of chloride species. It was originally thought that plasma treatment would be highly effective at chloride removal at lower temperatures than those required by hydrogen reduction, but research showed that effective chloride removal did not always occur and that temperatures of 300-400°C are required to break down akaganeite and remove chlorides. These temperatures are unacceptable for the treatment of quenched martensitic structures as they cause alteration of the microstructure (Schmidt-Ott and Boissonnas 2002; Tylecote and Black 1980). More recently, plasma treatment at the Swiss National Museum has been used at lower temperatures (120°C) as a treatment step before desalination with alkaline sulphite. This pre-treatment aims to reduce corrosion products and create micro cracks in the corrosion layers to aid the desalination process (Schmidt Ott and Boissonnas 2002).

3.3 Alkaline Sulphite Washing

Alkaline sulphite washing has been found to be highly effective for desalination of archaeological iron and has been the subject of extensive study and refinement. As originally proposed for the treatment of marine recovered iron by North and Pearson (1975), it specified an alkaline treatment solution containing 0.5M NaOH and 0.5M Na₂SO₃ in stirred deionised water at 60°C, with or without a post treatment of 0.1M Ba(OH)₂ to precipitate and remove SO₃²⁻ afterwards. This aimed to increase porosity in

the corrosion products by chemically reducing ferric oxyhydroxides to magnetite (Fe_3O_4) whose smaller molar volume takes up less space than goethite, akaganeite or lepidocrocite, thereby increasing access to treatment solutions to diffuse chloride from the object. It has been adapted from a treatment for marine iron (North and Pearson 1975; North 1987, 222) for treatment of archaeological iron from terrestrial sites where it has been the subject of numerous studies (Rinuy and Schweizer 1981, 1982; Gilberg and Seeley 1982; Watkinson 1983, 1996; Selwyn and Logan 1993; Al-Zahrani 1999; Schmidt-Ott and Oswald 2006; Watkinson and Al Zahrani 2008; Rimmer 2010; Rimmer et al. 2012, 2013b; Schmutzler 2012; Watkinson and Rimmer 2014).

3.3.1 Previous evaluation of alkaline sulphite washing

Studies of the alkaline sulphite treatment have focused on investigation of the treatment mechanism and evaluation of desalination effectiveness, with some recent work examining post-treatment stability.

Investigation of the alkaline sulphite treatment mechanism (Gilberg and Seeley 1982) revealed that sodium sulphite scavenges oxygen to prevent corrosion of iron and oxidation of Fe^{2+} to Fe^{3+} ions according to the reaction:



This frees chloride from its counter ion role allowing it to diffuse out of the object (Turgoose 1982b, 1985, 1993; Watkinson and Al-Zahrani 2008) (Section 3.2.1.4-3.2.1.5).

It was originally proposed (North and Pearson 1975) that corrosion product porosity increased by reduction of iron oxyhydroxides to denser magnetite but Gilberg and Seeley (1982) showed this was not likely to occur and was not a major factor in treatment effectiveness.

Sodium sulphite is not solely responsible for the efficient extraction of chloride observed in alkaline sulphite treatments as it is a poor chloride extractor when used alone (Al-Zahrani 1999). The combination of de-oxygenation (by sodium sulphite or bubbling with gas) to prevent corrosion with OH^- to displace chloride ions results in high chloride extraction efficiencies (Watkinson and Al-Zahrani 2008).

Chloride release during aqueous desalination is a diffusion controlled process (North and Pearson 1978; Ouahman et al. 1997; Selwyn et al. 2001). In keeping with other

such processes its rate is affected by porosity, cracks and thickness of corrosion products as well as temperature, viscosity of the solution and mobility of Cl^- and OH^- ions. Diffusion of chloride in archaeological objects has been mathematically described in one of two ways. The 'uniform' model (North and Pearson 1978) assumed a uniform distribution of chloride ions in the CPLs and described chloride extraction as proportional to the square root of time. The 'abrupt' model (Selwyn et al. 2001) postulates that chloride is concentrated only at the metal/CPL interface and must migrate through the corrosion layers. The wash solution must also penetrate down to the metal surface, so abrupt models reflect a delay after placement of iron in a treatment solution before chloride extraction begins and a sigmoidal rather than linear graph of chloride release over the square root of time. The abrupt model better fits iron corrosion models and observations of chloride accumulation as a counter ion at metal/CPL interface. Diffusion models are difficult to apply directly to archaeological objects due to difficulties in measuring parameters such as corrosion layer morphology accurately (Selwyn et al. 2001) but have important implications for rate of chloride release during desalination and their modification by cracks and porosity in corrosion layers.

Lower solution concentrations than originally specified by North and Pearson (1975) such as 0.1M NaOH/0.05M Na_2SO_3 , still provide effective chloride removal (Schmidt-Ott and Oswald 2006; Rimmer 2010; Schmutzler 2012) and are recommended for reasons of economy and waste disposal requirements. Less concentrated solutions may also leave fewer chemical residues in objects after treatment.

Temperatures above 20°C may cause greater dissolution of iron compounds in alkaline conditions and expansion of iron metal and corrosion product layers (Selwyn and Argyropoulos 2005) which may result in more effective pathways for chloride extraction. Kinetic theory predicts that movement and diffusion of OH⁻ and Cl⁻ ions would be faster at higher temperatures such as 60°C as recommended by North and Pearson rather than at 20°C. It has been reported that heating alkaline sulphite solutions to 50°C speeds up desalination by a factor of 10X over treatments at 20°C (Schmidt-Ott and Oswald 2006). Rimmer (2010) found that alkaline sulphite desalination did proceed more rapidly to completion at 60°C than at 20°C in direct comparison tests, although chloride removal efficiency was approximately the same (Rimmer 2010; Rimmer et al. 2012). Temperature of alkaline desalination treatments also affects transformation of iron corrosion products from one form to another, which will be discussed further in Section 3.4.

Studies have also systematically evaluated alkaline sulphite treatment effectiveness in controlled tests. Amount of chloride extracted, chloride remaining after treatment, chloride extraction efficiency and more recently (Rimmer et al. 2013b) corrosion pre and post-treatment (Watkinson and Rimmer 2014) have been used to measure alkaline sulphite's effectiveness in general or in comparison with other methods.

Favourable desalination performance of alkaline sulphite treatment compared with sodium hydroxide washing alone has been demonstrated based on chloride extraction efficiency measurements which compare the amount of chloride extracted to total chloride originally present (Watkinson 1996; Watkinson and Al-Zahrani 2008).

Digestion of the sample to determine remaining chloride after treatment was used to

calculate the results. Sodium hydroxide solutions de-oxygenated by nitrogen gas performed equally well with alkaline sulphite (Rimmer et al. 2012) which is unsurprising given the de-oxygenating mechanism of sodium sulphite.

Not all research has indicated that alkaline sulphite performs as well or better than other desalination treatments. Wang et al. (2008) did not find an observable benefit to using it rather than NaOH alone, or of 0.5M concentration solutions versus 0.1M. The size of the test sample was however relatively small (≤ 5 samples per test vs. 10 for Watkinson and Al-Zahrani 2008) and method of determining remaining chloride limited to ion chromatography of a few flakes of corrosion layers, rather than complete digestion. For these reasons the results of this study are not directly comparable to Watkinson (1996) and Watkinson and Al-Zahrani (2008) and appear less conclusive.

Desalination effectiveness of alkaline sulphite and de-oxygenated alkaline washing were evaluated in comparison with washing in sodium hydroxide solutions without sulphite by Schmutzler (2012). Archaeological iron nails from two sites were treated and remaining chloride evaluated by acid digestion. This research aimed to evaluate whether alkaline sulphite is more effective at extracting chloride than other methods and if there is an advantage in using it or other de-oxygenated methods over NaOH alone. Evaluation was based mainly on remaining chloride content after treatment. Schmutzler (2012) found no statistical improvement in desalination performance due to sodium sulphite in alkaline solutions, unless the solution was also physically de-oxygenated by nitrogen or vacuum. Higher (0.5M) concentrations of sodium hydroxide were found to extract more chloride than lower (0.1M) concentration solutions.

Unheated 0.5M NaOH solutions without sulphite were recommended in the interests of economy as, though slower, they still extract reasonable amounts of chloride over time. Schmutzler's findings contradict those of other researchers who have seen significant advantages of alkaline sulphite solutions over simple washing for iron desalination (Watkinson 1996; Watkinson and Al-Zahrani 2008) but issues with methodology and interpretation of results make its main findings problematic.

Use of remaining chloride as the main metric for successful desalination must be approached with caution. Total chloride in iron objects before treatment varies and not all will reach the same low level of remaining salt after treatment. The form of remaining chloride, whether as FeCl_2 or akaganeite, or washed akaganeite is also not distinguished by this measurement. Washed akaganeite from which adsorbed chloride has been removed has been shown to pose much less risk of further corrosion to iron than unwashed akaganeite (Watkinson and Lewis 2005b; Watkinson and Emmerson 2016).

Perhaps a greater problem is that reported total chloride levels for most samples in Schmutzler's study before treatment are very low and normally less than 500ppm.

These chloride levels would already be considered extremely low by many conservators and such objects would be considered at low risk of corrosion. Reported treatment efficiencies of 50-80% are reductions of already small amounts of chloride and whether or not similar efficiencies could be obtained with samples containing more chloride is unknown.

Reported differences in remaining chloride for different treatment protocols are also very small, on the order of tens of parts per million between one sample and another.

While the data is interpreted by statistical ranking, these differences are within normal variation of remaining chloride results for a single treatment protocol applied to an assemblage of iron objects and do not appear great enough to support conclusions about relative efficacy of desalination methods.

A final point is that no quantitative means were used to assess stability of iron samples after the treatments applied, only limited visual assessments. Without measurement of corrosion rate post-treatment it is not possible to evaluate the importance of remaining chloride, comparisons between treatment protocols, or reduction in post-treatment corrosion after tested desalination methods have been applied.

Evidence that desalination of archaeological iron is rarely, if ever, 100% efficient leads to questions of what becomes of the chloride left in objects after treatment, where it is located and whether or not it is a factor in promoting further or 'reactivated' corrosion (Loeper-Attia 2007, 192).

SEM-EDS (energy dispersive spectroscopy) analysis detected freshly formed chlorine containing corrosion products, later identified as akaganeite by Raman spectroscopy, in deep pits around slag inclusions exposed in polished cross-sections of archaeological iron nails (Rimmer and Wang 2010). Fresh corrosion was more extensive in untreated samples compared to those treated with de-oxygenated alkaline washing. The location, form, and effect of remaining chloride after desalination treatment require further study. Apart from visual observations of corrosion occurring after desalination on cross sections or whole iron objects, evaluation of whether or not remaining chloride contributes to post-treatment corrosion requires an independent means of corrosion measurement.

3.3.2 Further research on alkaline sulphite washing of archaeological iron

Research outlined in Section 3.3.1 above has brought about evidence-based understanding of the use of alkaline sulphite washing to treat archaeological iron. The following areas require further research:

- Large scale evaluation of conservation treatment outcomes for archaeological iron by quantitative-statistical methods is relatively new. Additional datasets of material from varied archaeological sites are needed to collect further evidence for the behaviour of archaeological iron under treatment. This can be achieved by examining objects subjected to similar treatment protocols and recording their post-treatment corrosion rate.
- While alkaline sulphite washing removes significant amounts of chloride and reduces post-treatment corrosion rates (Rimmer 2010; Rimmer et al. 2012, 2013; Watkinson and Rimmer 2014), questions remain about location of residual chloride and how this relates to slag content and location. Slag inclusions may be sites of chloride accumulation in archaeological wrought iron (MacLeod et al. 2008) and it may be located in pits and CPLs after alkaline sulphite washing (Rimmer and Wang 2010). Microscopic examination of alkaline sulphite treated archaeological iron objects in cross section to determine their slag content, along with scanning electron microscopy and x-ray elemental microanalysis to detect the location of residual chlorine, will provide more data to explore these questions.
- The potential effects of NaOH, Na₂SO₃, Na₂SO₄, and NaCl residues left behind after alkaline sulphite washing, or of rinsing to remove them after treatment,

have been unclear in the conservation literature. Early protocols for alkaline sulphite washing included post treatment washing with 0.1M Ba(OH)₂ to convert residual sulphites to insoluble BaSO₃ or BaSO₄ (North and Pearson 1975; Bryce 1979). Later protocols omit this procedure but suggest rinsing out excess treatment reagents (North 1987, 222; Selwyn and Logan 1993; Schmidt-Ott and Oswald 2006). This involves rinsing to neutral pH during which excess chloride from the treatment bath will be removed along with excess OH⁻ ions to prevent them reacting with ferrous or ferric ions and the drying and precipitation of hygroscopic and unsightly chemical residues is prevented (Plenderleith and Werner 1971; Hamilton 1976; North 1987; Loeper-Attia and Weker 1997; Kergourlay et al. 2011; Argyropoulos et al. 2015). A potential concern for desalinated archaeological iron is that hygroscopic chemical residues will attract moisture to restart corrosion post treatment. These issues may potentially affect alkaline sulphite treated iron which has not been rinsed after treatment, but questions of whether or not there is a significant risk of further iron corrosion associated with omitting the rinsing step, and whether or not hygroscopicity of chemical residues is a major concern remain to be fully addressed.

- These questions have been partially answered by previous research in which precipitated residues of simulated alkaline sulphite washing treatments were studied. Precipitation produced residues containing NaSO₃, NaSO₄, FeSO₄, γ-FeOOH, Na₆(CO₃)(SO₄)₂ and testing the impact of these on iron powder at a range of RH values identified that the risk of corrosion due to residues was deemed to be low below 75% RH (Rimmer and Watkinson 2010). Considering

these results, the risk from deliquescence of residual compounds other than NaCl is not high except at very high humidities and the amount of NaCl in the residue would appear to be an important factor.

- Some recent studies (Rimmer et al. 2013b; Watkinson and Rimmer 2014) have shown reduced rates of iron corrosion post alkaline sulphite washing as compared with pre-treatment corrosion rates without rinsing. The impact of rinsing on post-treatment corrosion rate of alkaline sulphite treated archaeological iron has not been investigated using archaeological iron. It can be studied by comparing the oxygen consumption corrosion rate of significant numbers of rinsed and un-rinsed alkaline sulphite treated wrought iron samples.

3.4 Akaganeite Transformation During Storage and Conservation

Of particular interest for iron artefact conservation is the potential for akaganeite (β -FeOOH) to transform into other iron corrosion products, releasing chloride in the process. Its transformation in storage or during conservation treatment has received much attention from researchers (Stahl et al. 2003; Al-Zahrani 1999; Réguer et al. 2009; Rimmer 2010; Thickett 2012; Thickett and Odlyha 2014; Drews et al. 2013; Bayle et al. 2016).

Stahl et al. (2003) investigated the structure of synthetic akaganeite, confirmed its hollandite-like structure and reported that it did not break down or release occluded chloride below 200°C in atmospheric conditions and that adsorbed chloride could be washed from its surface. Temperatures >200°C caused transformation to hematite.

Réguer et al. (2009) studied the structure and chloride content of synthetic akaganeite

confirming most of its chloride is surface adsorbed and can be removed by washing, leaving only occluded chloride. Réguer suggests a benefit of desalination treatments is the removal of adsorbed chloride by washing as soon as possible after excavation (Réguer et al. 2009). Other researchers (Watkinson and Lewis 2005b; Watkinson and Emmerson 2016) have confirmed that adsorbed chloride can be rapidly washed from akaganeite reducing its ability to corrode iron.

Breakdown of akaganeite in room temperature storage of archaeological iron has been studied, as chloride released into iron objects in this manner would be available to promote corrosion. Akaganeite and lepidocrocite are less stable than goethite and change slowly into goethite (Knight 1982). Transformation of natural akaganeite to hematite has been shown to occur slowly at 20°C (Thickett 2012), with an estimated transformation of 0.22% by weight in 8 years. Faster transformation was observed in laboratory experiments with synthetic akaganeite at temperatures above 20°C which showed a 25.64% conversion to hematite at 180°C in 3 months (Thickett 2012).

Transformation experiments on natural and synthetic akaganeite in conditions of 20°C and a range of relative humidities found that β -FeOOH transforms partially to goethite with the depth of the transformation layer increasing with RH (Thickett and Odlyha 2014). Akaganeite formed naturally in displayed iron objects at an RH of 46-51% slowly transformed to goethite at a rate of 0.38 micrometres depth of the akaganeite-containing corrosion layer in 15 years. This slow rate of akaganeite transformation to release chloride may in part address some of the questions posed by Knight (1982).

Transformation of akaganeite will release occluded and surface adsorbed chloride into washing solutions, removing the threat of future transformation which may occur while iron objects are in storage. Akaganeite transformation is a desirable outcome of washing treatments, provided the newly free chloride is carried away and does not remain to promote corrosion in the object (Stahl et al. 2003; Rimmer 2010; Thickett and Odlyha 2014).

Some chloride removal techniques in Table 3.1, such as hydrogen reduction, transform or destroy akaganeite (Wagner et al. 2012). Plasma reduction is also capable of breaking down akaganeite and removing chloride at temperatures $\geq 400^{\circ}\text{C}$, but temperatures this high are not normally used in current plasma treatment of iron due to risk of metallographic alteration to the object (Schmidt-Ott and Boissonnas 2002). Subcritical water extraction at conditions of 0.5M NaOH, 50 bar pressure and 180°C transforms akaganeite to a hematite/goethite phase and akaganeite in the near surface corrosion layers of a cast iron object was also transformed to hematite/goethite (Drews et al. 2013). Transformation of akaganeite to hematite in subcritical conditions of 0.125 M NaOH, 160°C and 35 bar has recently been identified (Bayle et al. 2016).

Iron oxide transformations are perhaps unsurprising given that the extreme physical conditions of subcritical treatment are also conditions in which phase transformations occur (Cornell and Giovanoli 1990; Cornell and Schwertmann 2003). Elevated temperature in subcritical treatment conditions is most likely the important factor in iron corrosion product transformation (Bayle et al. 2016).

Considering washing techniques in less extreme physical conditions, Al-Zahrani (1999) examined effects of alkaline and non-alkaline washing treatments on samples of synthetic akaganeite and akaganeite/magnetite mixtures, measuring chloride extraction and changes to the corrosion products by semi-quantitative XRD. Synthetic akaganeite transformed to 100% goethite in both 0.5M NaOH and 0.5M NaOH/Na₂SO₃ solutions at 20°C over 4 months as measured by XRD, while non-alkaline aqueous solutions showed chloride extraction but no transformation. Washing with sodium sulphite solution alone did not result in transformation of akaganeite, indicating that the alkaline conditions were required. Partial transformation of up to 80% of the akaganeite to a mixture of 60-70% magnetite and 30-40% goethite occurred during heating to 70°C for 48 hrs and 100°C for 3 hours. Washing synthetic akaganeite/magnetite mixtures at variable alkaline pH detected that most transformation occurred at pH 10.5-11.

Rimmer (2010) examined transformation of synthetic akaganeite in alkaline solutions at concentrations of 0.1-1 M NaOH and from 0.05-0.5M Na₂SO₃ at temperatures of 20 and 60°C, both with and without sodium sulphite and seeding with 10 wt% goethite or magnetite. Synthetic akaganeite was produced using the same method as Al-Zahrani. Up to 50% of akaganeite transformed to goethite or goethite/hematite over 28 days, but hematite occurred only in the sulphite containing solutions heated to 60°C. No hematite was detected in samples seeded with goethite and magnetite. Seeding with magnetite retarded transformation to goethite in alkaline sulphite solutions (Rimmer 2010). Rimmer notes that the results differ in some respects from those predicted by the literature (Cornell and Giovanoli 1990) such as effect of alkaline concentration, as

well as from those obtained by Al-Zahrani (1999). Schmutzler (2012) used Raman spectroscopy to evaluate changes to synthetic akaganeite during immersion in 0.1, 0.5, and 2.0M NaOH solutions without sodium sulphite. She found that akaganeite transformed completely to goethite/hematite at 70°C over 21 days, and partially at 20°C over the same time period. Overall, predicting the likely outcome of environmental conditions on akaganeite transformation is fraught with inconsistencies.

3.4.1 Akaganeite transformation in heritage iron: further questions

A more complete understanding of the conditions in which akaganeite may transform and release chloride has been identified as an important research goal in archaeological iron conservation (Selwyn 2004b). It remains to be confirmed whether or not akaganeite consistently transforms to goethite and/or hematite in conditions prevalent during actual conservation treatments such as alkaline sulphite washing with 0.1M NaOH/0.05M Na₂SO₃ at 60°C in the relatively short time span of 30 days, and whether the results of Al-Zahrani (1999) or Rimmer (2010) are reproducible in this time frame using synthetic β-FeOOH produced by the same method. If transformation of akaganeite does occur, the extent of the transformation as measured by percentage phase change is also important to evaluate. Given that the first 15-30 days of alkaline sulphite treatment were identified by Rimmer (Rimmer 2010; Rimmer et al 2012) as the period in which the majority of chloride is removed from archaeological iron in an alkaline sulphite treatment, it is informative to know the extent of akaganeite transformation under these conditions and time periods. This has implications for whether chloride released through akaganeite breakdown contributes to the total release of chloride measured during desalination studies or whether chloride held in

the akaganeite structure is likely to remain there, and may only be detected by digestion of the samples.

3.5 Investigating the Impact of Slag on the Corrosion of Archaeological Wrought Iron and its Response to Alkaline Sulphite Treatment

3.5.1 Aims and Objectives

The following Aims and Objectives are addressed in this project:

Aims

- Explore whether there is a relationship between slag content of nails, their residual chloride and post-excavation corrosion rates by comparing patterns of slag within the nails to the amount of chloride within them; amount of chloride extracted by alkaline sulphite treatment; and the corrosion rate of nails before and after treatment.
- Explore relationships between slag content of archaeological iron and the effectiveness of chloride removal by the alkaline sulphite desalination both with and without post-treatment rinsing.
- Examine the impact of alkaline sulphite treatment on the corrosion rate of archaeological wrought iron in relation to its slag content.
- Examine the relationship between alkaline sulphite treatment at 60°C and transformation of β -FeOOH to other iron oxides.

Objectives

- Assess the corrosion rate of a statistically valid number of wrought iron nails from two different archaeological sites.
- Determine the distribution of slag in these nails and investigate the localisation of chloride relative to the slag.

- Treat these nails by the alkaline sulphite desalination technique and determine the amount of chloride removed from each nail as a function of its pre-treatment chloride content.
- Apply rinsed and non-rinsed protocols to equal, statistically valid numbers of alkaline sulphite treated archaeological wrought iron nails and determine their post-treatment corrosion rate. Assess the impact of post-treatment prolonged rinsing on corrosion rate.
- Synthesize β -FeOOH, assay, subject to alkaline sulphite washing at 60°C then determine composition using XRD.

4 Experimental Method

4.1 Research Method

The nature of the variables and use of non-reproducible and non-standardised archaeological objects meant that while the methodology is primarily quantitative, it was also necessary to employ a degree of qualitative assessment to deliver a mixed-methods approach (Reedy and Reedy 1988, 1992; Creswell 2014)

4.2 Experimental Variables

A large number of factors discussed in Chapters 1-3 affect the nature of archaeological wrought iron, its corrosion *in-situ* and post excavation, its response to conservation treatment by alkaline sulphite washing and corrosion post-treatment. The specific independent and dependent variables identified in this study are given in Table 4.1

Independent and Dependent Variables in the Study	
Independent	Dependent
Oxygen Consumption Measurement Conditions (80% RH 20°C)	Oxygen Consumption Rate Before/After Treatment
Site of Origin	Amount of Chloride Extracted
Sample	Remaining Chloride After Treatment
Weight	Presence/Absence of Chlorine (SEM EDS/WDS) (Qualitative)
Total Chloride	Amount of Chlorine (SEM EDS/WDS) (Quantitative)
Percent Area Slag	
Thickness of Corrosion Product Layers	
Presence/Absence of Microcracks	
Alkaline sulphite treatment Protocol	
Post Treatment Rinsing (Rinsed/Un-Rinsed)	Percentage Transformation of Synthetic β -FeOOH Powder
Synthetic β -FeOOH Production and Treatment Protocol	

Table 4.1 Independent and dependent variables used in the study

4.3 Method of Corrosion Measurement

A quantitative method for measuring the corrosion rate of wrought iron that relates to corrosion in storage environments was utilised in experimental work. Measurement of oxygen consumption as a proxy for metal corrosion processes has been well established by a number of recent studies (Matthiesen 2007; Matthiesen and Wonsyld 2010; Matthiesen and Stemann-Petersen 2014; Watkinson and Rimmer 2014; Emmerson and Watkinson 2014, 2016).

This technique measures all possible oxidation reactions occurring within the accuracy of the meter, not exclusively iron metal oxidation. Controls will be run for oxygen consumption by other factors such as plastic supports for the sample in the test jar. It is assumed that oxidation of existing corrosion products in metal samples that have experienced long term exposure to an oxygenated storage environment will not be significant. The majority of the oxygen consumed will be from the cathode reaction associated with iron corrosion at high RH. The oxygen consumption rate is therefore approximately proportional to the corrosion rate (Watkinson and Rimmer 2014). Evaluative studies have also shown that the measurements of metal corrosion by oxygen consumption have good reproducibility and correlate well with other methodologies such as weight loss (Matthiesen and Wonsyld 2010). The oxygen consumption rate under conditions of controlled temperature and relative humidity was therefore chosen as an appropriate proxy for corrosion of archaeological wrought iron in this study.

4.4 Experimental parameters: rationale

Tests were run in 80% relative humidity (RH) and 20°C temperature (T) as corrosion of iron is significant at this RH (Maréchal et al. 2007; Graedel and Frankenthal 1990).

These conditions also simulate the effect of placing iron in aggressive storage conditions (Rimmer et al. 2013a) where chloride contaminated iron will experience measurable corrosion in a relatively short period (Wang 2007b). Since iron has also been evaluated previously in these conditions using oxygen consumption (Watkinson and Rimmer 2014) this provides an opportunity to compare results.

Alkaline sulphite desalination is an effective treatment for archaeological iron and was employed due to the large database on its performance created by previous workers offering comparisons and aiding its refinement and evaluation (Rimmer et al. 2013b; Watkinson and Rimmer 2014). Consequently it was chosen to evaluate the effect of slag on the post-conservation outcomes of archaeological wrought iron.

Alkaline sulphite washing is not a 'single' treatment as it has previously been applied with variations of solution chemistry, temperature, and duration (Section 3.3). In this study, a 0.5M NaOH, 0.05M Na₂SO₃ solution at 60°C, similar to that used by the Swiss National Museum (Schmidt-Ott and Oswald 2006) that has also been tested in previous work at Cardiff University, will be used for desalination treatments. Since Rimmer (2010) showed heating the treatment solution to 60°C increases the rate of chloride extraction and shortens the treatment time, this temperature is used in the current study.

The samples chosen for these experiments were untreated archaeological wrought iron nails, which meant they varied considerably in size, shape, mass, volume,

corrosion profile, and chloride content, potentially making comparability of experimental results more challenging. While modern samples made from homogeneous ferrous metals offered advantages of greater reproducibility and standardisation, these advantages are outweighed by the inability to produce an analogue that mirrors naturally corroded archaeological wrought iron material which has deteriorated naturally over time (Watkinson et al. 2013). A sample set of 30 nails from each archaeological context was selected to provide suitable numbers for statistical analysis.

The samples met the following criteria:

- Not previously treated by a conservator
- Corroded with retention of a solid metal core
- Comparable size and mass
- Small enough to fit into experimental apparatus, ≤ 7 cm long
- Available for destructive analysis

Wrought iron nails are an ideal choice as they are frequently found in large numbers and available for analysis. Selection utilized screening with X-radiography to confirm retention of a metal core.

An additional criterion was that the samples should be from more than one archaeological site. This allows comparison of the nature and corrosion behavior of material of different origin and from different burial environments. Conducting the study on material across multiple sites allows for testing of whether or not there are

differences in composition, slag content, chloride content, oxygen consumption, and response to desalination treatment by site.

4.5 Akaganeite transformation

Ideally, *in situ* transformation of naturally formed corrosion product akaganeite occurring during alkaline sulphite washing of iron objects could have been investigated, but this would require specialised treatment cells and micro-Raman analysis (Kergourlay et al. 2010) not available for this study. Instead, experiments utilised synthetic akaganeite in 0.5M NaOH/0.05M Na₂SO₃ alkaline sulphite washing treatment at 60°C described in Section 4.7.11. Unwashed synthetic akaganeite is likely to have considerable surface-adsorbed chloride and was used to model freshly formed β-FeOOH on archaeological wrought iron post-excavation (Lewis 2009).

4.6 Sample material

Samples from two sites, Roman Caerleon and Colonial Williamsburg were selected for this study (Table 4.2, Sections 4.6.1-4.6.2) according to the criteria discussed in Section 4.4.

Site	Roman Caerleon	Colonial Williamsburg
Abbreviation	CAER	CW
Context	CPF08(001)	Basset Hall, Anderson Forge Brush Everard, Carter's Grove, Public Hospital, Anthony Hay Shop, Wetherburn's Tavern, Peyton Randolph and Tazwell Hall
Environment	Terrestrial	Terrestrial
Location	South Wales, UK	Virginia, USA
Date	1 st Century AD	17-19 th Century AD
# Samples	30	30
Excavated	2008	1960s-2001
Storage Post Ex	Stewart Box with silica gel	Polyethylene bags; uncontrolled environment prior to 2007. Post 2007 stored at 40% RH

Table 4.2 Source of archaeological wrought iron nail samples used in the study, with details of site, context, environment, location, date, number of samples, and post-excavation storage.

4.6.1 Roman Caerleon

Approximately 100 wrought iron nails were obtained from a secure 2nd C AD Roman period context at the ancient Fortress Isca Augusta at Caerleon, South Wales. The nails were excavated in 2008 and placed in dry storage maintained by desiccated silica gel from the time of their excavation until research commenced in 2012. These samples were in 'as excavated condition' with some residual soil cover and a voluminous iron corrosion layer. They were placed in desiccated storage at between 5-10% RH until experiments began. A photograph and scanning electron micrograph of a Caerleon nail can be seen in Figure 4.1



Figure 4.1 Digital photograph at 1.5X (top) and SEM-BSE image at 20X (bottom) of nail sample CAER_01 from Caerleon

4.6.2 Colonial Williamsburg

A second set of 100 wrought iron nails were obtained from the excavated archaeological collections of Colonial Williamsburg, a preserved 18th Century town and former capital of the Colony of Virginia. All samples from Colonial Williamsburg had been excavated from terrestrial sites and stored without conservation treatment. They were stored at Cardiff in sealed containers maintained at 5-10% RH maintained by

desiccated silica gel prior to testing. A photograph and SEM image of sample nail CW_09 from Colonial Williamsburg are shown in Figure 4.2.

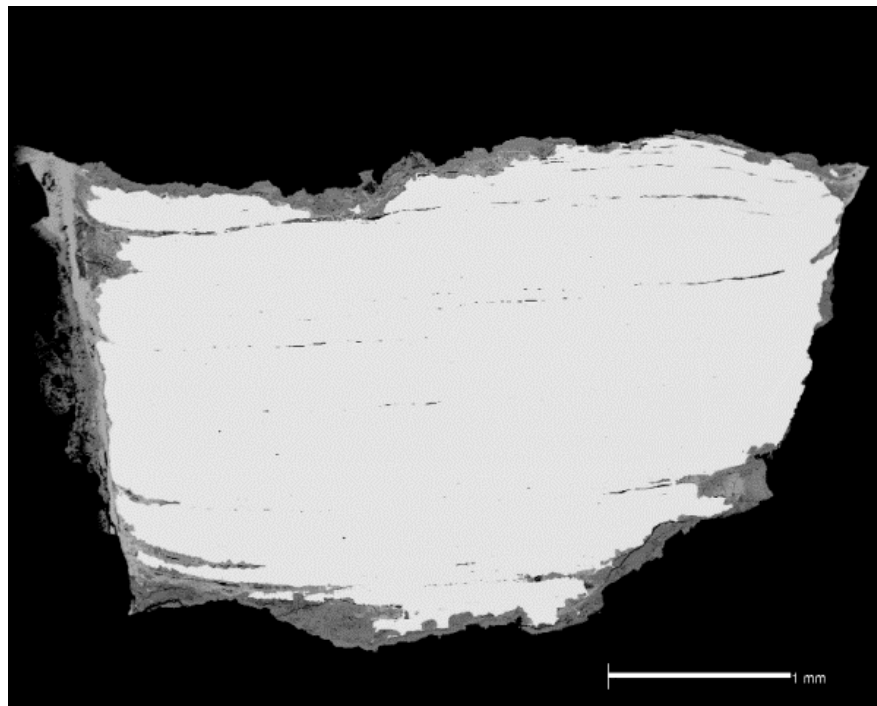


Figure 4.2 Digital photograph at 1.5X (top) and BSE-SEM image at 20X (bottom) of nail sample CW_09 from Colonial Williamsburg

4.7 Experimental Procedures

Experimental procedure is recorded in sections 4.7.1-4.7.12. Additional information is given in Appendices as indicated in the relevant sections below. All laboratory work

was carried out at Cardiff University following applicable Health and Safety guidelines according to UK Health and Safety Executive and Cardiff University regulations.

4.7.1 Sample selection, documentation, and preparation

Samples for the experiments were selected from the 100 nails available from each site described in Section 4.6 based on the criteria given in Section 4.4. X-radiography was used as a Pass/Fail test to verify the presence of a surviving wrought iron metal core. Thirty samples were selected from each site for corrosion testing and desalination treatment. Other samples were selected for analysis only (Table 4.3). At the outset all samples were documented using digital photography and a Mettler Toledo AX 504 analytical balance readable to 0.1 mg. These data provided a baseline reference point for comparison with the visual appearance and condition of the samples and any changes undergone by them throughout the experimental process. A list of all samples along with abbreviations used in this study is given for reference in Table 4.3. Digital photographs of all samples are provided in Appendix 8.6.

Sample				Analytical Record				
Sample	Designation	Mass (g)	PTR	X-Sect.	% Slag	SEM	EMPA/WDS	Total Chloride
CPF08_001_001	CAER_01	7.021	R	X	X	X		X
CPF08_001_002	CAER_02	2.236	R					X
CPF08_001_003	CAER_03	8.41	R					X
CPF08_001_004	CAER_04	4.197	R					X
CPF08_001_005	CAER_05	5.776	R					X
CPF08_001_006	CAER_06	17.754	R					X
CPF08_001_007	CAER_07	12.693	R	X	X	X		X
CPF08_001_008	CAER_08	8.094	R	X	X	X	X	X
CPF08_001_009	CAER_09	9.571	R					X
CPF08_001_010	CAER_10	13.191	R	X	X	X		X
CPF08_001_011	CAER_11	3.071	R					X

CPF08_001_012	CAER_12	3.191	R					X
CPF08_001_013	CAER_13	7.041	R	X	X	X		X
CPF08_001_014	CAER_14	7.468	R					X
CPF08_001_015	CAER_15	17.169	R					X
CPF08_001_016	CAER_16	23.482	NR					X
CPF08_001_017	CAER_17	11.177	NR					X
CPF08_001_018	CAER_18	6.588	NR	X	X	X		X
CPF08_001_019	CAER_19	5.701	NR	X	X	X		X
CPF08_001_020	CAER_20	2.394	NR					X
CPF08_001_021	CAER_21	5.405	NR	X	X	X		X
CPF08_001_022	CAER_22	4.413	NR	X	X	X		X
CPF08_001_023	CAER_23	4.665	NR					X
CPF08_001_024	CAER_24	1.886	NR					X
CPF08_001_025	CAER_25	1.595	NR					X
CPF08_001_026	CAER_26	3.655	NR					X
CPF08_001_027	CAER_27	1.957	NR	X	X	X		X
CPF08_001_028	CAER_28	3.268	NR					X
CPF08_001_029	CAER_29	34.502	NR					X
CPF08_001_030	CAER_30	29.597	NR			X	X	X
01AD-00031AK	CW_01	6.283	NR					X
10A-126	CW_02	8.275	NR					X
10F-38D	CW_03	12.271	NR	X	X	X		X
10F-35C	CW_04	9.625	R					X
10F-42D	CW_05	6.559	R	X	X	X		X
29F-614	CW_06	4.365	R					X
29F-617	CW_07	4.896	R	X	X	X		X
29F-894	CW_08	6.051	NR	X	X	X	X	X
01AD-00033AS	CW_09	5.073	R	X	X	X		X
Vepco Tr. Mon.	CW_10	6.904	R					X
CGER-164A-50AA	CW_11	7.935	NR					X
CGER-1740A	CW_12	3.721	NR					X
CGER-1755B	CW_13	5.382	R					X
CGER-1773F	CW_14	6.239	NR	X	X	X	X	X
CGER-1902	CW_15	9.649	NR	X	X	X		X
ER-1712E-4C	CW_16	6.641	R	X	X	X		X
ER-243L-28D	CW_17	3.814	NR					X

ER-364B-28D-1	CW_18	5.565	R					X
ER-364B-28D-2	CW_19	7.625	NR	X	X	X		X
ER-1009Q-9NA	CW_20	5.756	NR					X
ER-1069-9NA	CW_21	3.811	NR					X
ER-1215R-31AA	CW_22	4.307	NR					X
ER-1712A-4CA	CW_23	3.641	R					X
ER-1712B-4C	CW_24	6.621	R					X
ER-1720-4CA	CW_25	6.957	R					X
ER-2334A-4C	CW_26	5.867	R					X
ER-2531P-4C	CW_27	4.419	R					X
ER-2534A-4C	CW_28	7.361	NR					X
28G-783R	CW_29	4.989	R	X	X	X		X
44B-473	CW_30	16.680	NR					X
CPF08_300_MG1	CAER_31	20.415					X	
CPF08_300_MG2	CAER_32	23.288				X	X	
CGER1761C_L1	CW_31	6.055					X	
TAZ44B363_L3	CW_32	30.562					X	
29F-818_L1	CW_33	18.412					X	
CPF08-EN-1	CAER_EN1	6.74						X
CPF08-EN-2	CAER_EN2	6.19						X
CPF08-EN-3	CAER_EN3	7.37						X
CPF08-EN-4	CAER_EN4	6.34						X
CPF08-EN-5	CAER_EN5	2.72						X
29F-807	CW_35	3.92						X
10-120-AF	CW_36	3.35						X
ER-2533A-4C	CW_37	4.76						X
50HA-CGER-4059A	CW_38	3.23						X
CGER-191A-50M	CW_39	4.19						X

Table 4.3 List of samples studied from Caerleon (CAER) and Colonial Williamsburg (CW) with information on provenance, experimental procedures and analysis performed. Legend: PTR= Post Treatment Rinsing, R=rinsed, NR=not rinsed, X-section indicates mounted and polished transverse cross section prepared from this sample, % Slag = Percent Area Slag Measured, SEM=Scanning Electron Microscopy/Analysis, EPMA/WDS=Electron Probe Microanalysis/Wavelength Dispersive Spectroscopy.

4.7.2 Workflow

Each group of 30 samples (Section 4.7.1) was measured for oxygen consumption (corrosion rate) at 80% RH, treated by alkaline sulphite washing at 60° C, and re-measured for oxygen consumption at 80% RH. Each group of 30 samples was further divided into two groups of 15 samples, 15 of which were rinsed and 15 unrinsed following alkaline sulphite treatment (Table 4.3, Section 4.7.5). Five rinsed and five unrinsed treated samples from each site (20 in total) were studied in cross section to determine their amount of slag and distribution of chloride post-treatment. All samples were digested post-treatment in nitric acid to determine their residual chloride and this was used to calculate content. Workflow and order of procedures for the experiments is set out in Figure 4.3.

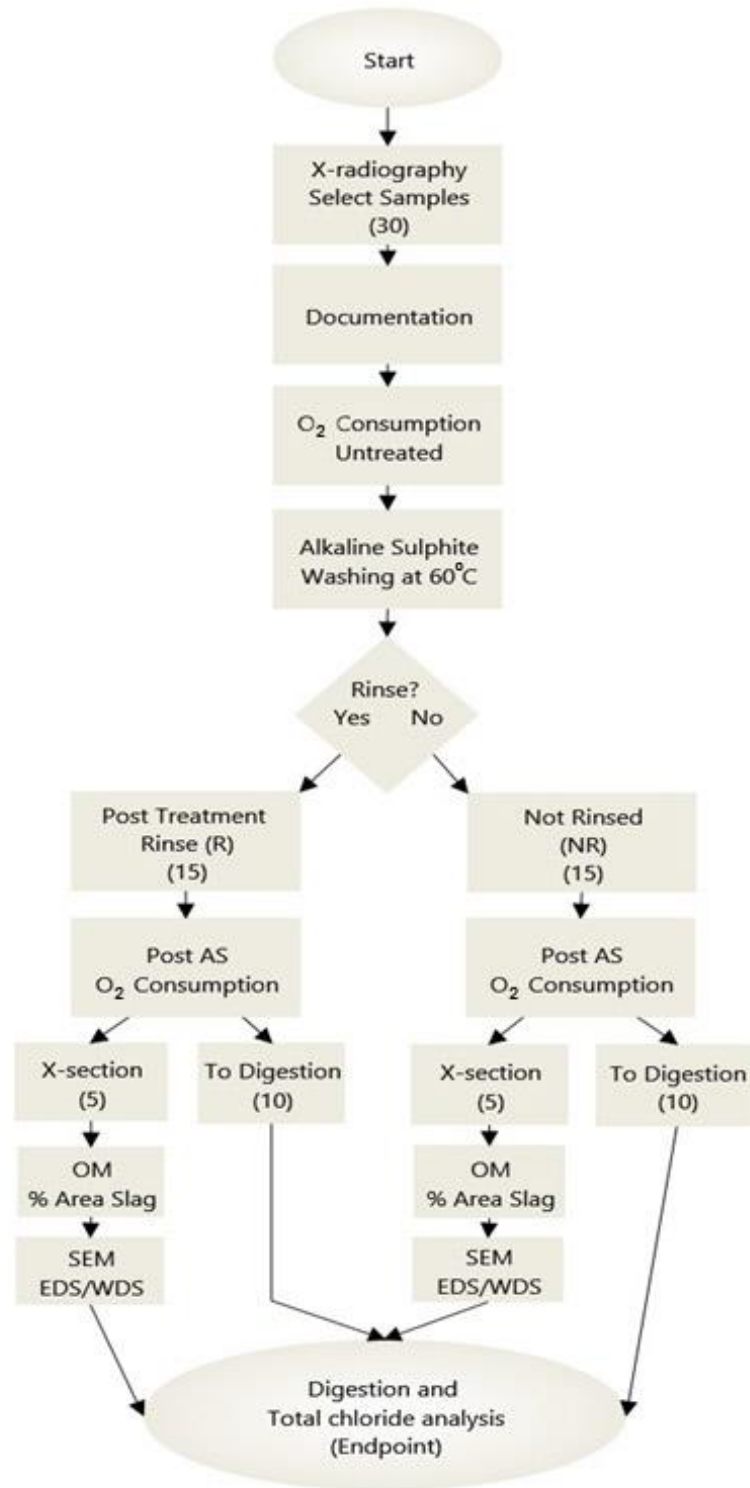


Figure 4.3 Workflow for experimental procedures applied to wrought iron nail samples from each archaeological site. Numbers in parentheses are number of samples involved in given experimental step.

4.7.3 Measurement of oxygen consumption

The oxygen consumption of the samples was measured as a proxy for corrosion rate both before and after alkaline sulphite washing treatment. Each sample to be measured was placed separately in a 250ml glass 'Kilner' jar with a gas-tight metal screw-top lid equipped with a rubber seal along with 160 g of silica gel pre-conditioned to the target RH (80%). The mass of conditioned silica gel required was empirically determined in previous studies (Watkinson and Rimmer 2014). The sample was supported and separated from the silica gel by a polystyrene weighing boat, the composition of which was confirmed by FTIR analysis. Constant temperature of 20°C was maintained throughout the experiment by placing the sealed jar in a Binder KBF240 climatic chamber. RH and temperature values are monitored during the experiment by a Madgetech RH/Temp 101A data logger included in the jar. The level of oxygen is monitored by a PSt3 sensor spot (WPI part#503090) containing an oxygen sensitive compound mounted on the inside of the glass jar with Radio Spares RTV silicone rubber compound. The sensor spot fluoresces when exposed to green light from a fibre optic probe attached to either a WPI Oxymini AOT or PreSens Fibox 4 oxygen meter (both types of meter were used during the course of the experiments). The sensor requires darkness to operate, which is provided by the enclosure of the sample jar and fibre optic probe in the climatic chamber during measurement. The fluorescence of the spot when exposed to light is quenched (reduced) by the presence of oxygen with less attenuation as oxygen is consumed, allowing calibration of the meter to read the partial pressure of oxygen in the reaction vessel.

Recording the change in pressure over time allows the amount of oxygen consumed in oxidation reactions in the sample to be measured. The partial pressure of oxygen in

millibars (mbar) is recorded via software over a period of 4 minutes for each measurement yielding approximately 20 data points. Initial pressure readings are normally in the range of 200-220 mbar and drop over the course of the test, in some cases to 0 mbar. The data are imported into Microsoft Excel and the mean and standard deviation of the data are calculated. Oxygen measurements are taken for each sample on a regular schedule and successive mean O₂ readings plotted to give an oxygen consumption curve versus time and to calculate the corrosion rate of each sample. Differences in the mass of the nails were also accounted for in the oxygen consumption rate calculations.

4.7.4 Chloride measurement

Chloride removed from each nail during alkaline sulphite washing was measured and the total chloride in each object was determined by digestion at the end of treatment. The sum of these values provides the total chloride in each object. Chloride measurement employed a Radiometer Analytical PHM250 Specific Ion Meter, REF621 Hg/HgSO₄ reference electrode, and ISE25Cl chloride ion specific electrode which have a detection limit of 0.5ppm and an accuracy of +/-10% (Rimmer et al. 2012). The specific ion meter was calibrated before each use according to procedures in Appendix 8.1.1 and samples analysed according to procedures in Appendix 8.1.2. Solution pH was measured before chloride determination with a Kent Electronic Instruments Model 7605 pH/millivolt meter and VWR 662-1759 gel filled pH electrode calibrated with pH 4.0, 7.0 and 9.2 buffers and was adjusted to between pH 5.5-7.0 by addition of 5M HNO₃ or 3M NaOH as needed. Some samples required additional preparation before chloride measurement. Details of these procedures are given in Appendices 8.1.3 and 8.1.4.

4.7.5 Alkaline Sulphite washing treatment

The group of 30 objects from each site was treated with alkaline sulphite washing at 60°C according to the following protocol. A treatment solution of 0.1M NaOH/0.05M Na₂SO₃ in deionised water was used. Solution volumes were between 100-125ml depending on the displacement of the object. Sample and solution were contained in standardized 125ml air-tight LDPE plastic screw-top containers to ensure de-oxygenation by the sodium sulphite and guard against ingress of air oxidising the sulphite. Tests were run at 60°C in a lab oven. The alkaline sulphite washing solution was changed every 14 days. Jars were rinsed with deionised water prior to adding fresh 0.1MNaOH/0.05M Na₂SO₃ to prevent carryover of chlorides from one solution to the next. Solutions were analysed for their chloride content.

The alkaline sulphite washing method can be considered to be complete when the chloride levels in the solution are less than or equal to 5 ppm (mg/L) +/-10% as measured by the chloride ion specific electrode (Rimmer et al. 2012). In the current study, samples were given 4 alkaline sulphite treatment baths to extract as much chloride as possible within an 8 week time frame, although the final chloride level of 5 ppm was only reached for some of the nails. Final chloride concentrations in treatment solutions are given in Table 5.10.

Following treatment all samples were given a quick wash for a few seconds under a stream of deionised water. Half the total number of nails (15 out of 30 for each site) were then processed according to a 'rinsed' post-treatment protocol consisting of soaking in baths of deionised water to remove residual NaOH/Na₂SO₃ and soluble chloride. Baths were changed weekly until the rinse water remained at pH 7.0. This normally required 5-6 weeks. The other half of the treated nails were processed

according to an 'un-rinsed' protocol in which they were dried in a 10% RH atmosphere maintained by desiccated silica gel. Both rinsed and unrinsed groups of nails were stored in a desiccator at 10% RH after their post-treatment protocol prior to oxygen consumption measurements.

4.7.6 Preparation of metallographic samples

Samples for metallographic analysis were prepared by cutting 2mm thick transverse cross sections from the midpoint of the nail shafts using a Struers Minitom slow speed metallographic saw with Struers high-density CBN (cubic boro-nitride) or Kemet high-density diamond blade. Oil based lubrication (Buehler Lapping Oil) was used to prevent loss of soluble chloride. The possibility of chloride contamination from the lubricant was eliminated by testing with FT-IR/ATR (see Appendix 8.3). Cross sections were mounted in Struers Epotek epoxy cold mounting resin and ground/polished from 320 to 0.25 micron grits. Lapping oil and oil-based diamond suspensions were used to prevent chloride loss. Metallographic samples were not normally etched for this study, as etching was not necessary and may have caused interference with the image analysis techniques employed (see Section 4.7.7). One sample from each of the two archaeological sites was etched with Nital, (100ml ethanol (C₂H₅OH) + 2ml nitric acid (HNO₃) (Scott 1991, Petzow 1999) to reveal its grain structure for characterisation purposes.

4.7.7 Measurement of slag content

Polished metallographic samples were imaged at 50X using reflected light brightfield optical microscopy (OM) on a Nikon Eclipse ME600 microscope with Diagnostic Instruments Spot 25.4 digital camera and software. Multiple captures at slightly

different focus points were digitally combined using the EDF (Extended Depth of Field) software tool in Struers Scentis VI image analysis software package. The minimum magnification of 50X did not capture the complete cross section in one frame, so multiple images of different regions were acquired and composited into single images of the complete sample using Adobe Photoshop CS 6.

The percentage area of slag in cross sectional images of the samples was determined using Struers Scentis VI image analysis software and Percent Area analysis module. A greyscale range representing slag was discriminated from the greyscale values of the rest of the image to deliver percentage slag. Percentage area of slag and metal in entire cross-sections of samples were recorded at 50X and percentage area slag calculated:

$$\% \text{ Area Slag} = \text{Area of Slag} / \text{Area of Metal}$$

A pre-processing step using Adobe Photoshop CS 6 was performed on images in which corrosion layers external to the preserved metal surface were digitally removed. This left metal cores as lighter greyscale regions easily distinguishable from the darker slag inclusions. This was done to prevent inaccurate determination of percent area slag where corrosion layers were approximately the same greyscale value as the slag inclusions. Inclusions other than slag, such as cementite and other carbonaceous structures, and grain boundaries might also potentially interfere with percent area measurement of slag due to similar greyscale values. Since these were not apparent in the un-etched samples, this was not of concern for the study.

Measurement of complete cross sections required an additional step due to the need to distinguish between total area of the sample and total area of the field of view in the digital photomicrograph. This was accomplished by identifying two 'phases' in Scenitis: the slag inclusions and the entire cross section excluding the corrosion product layers. The percent area slag measurement process is given in Figure 4.4.

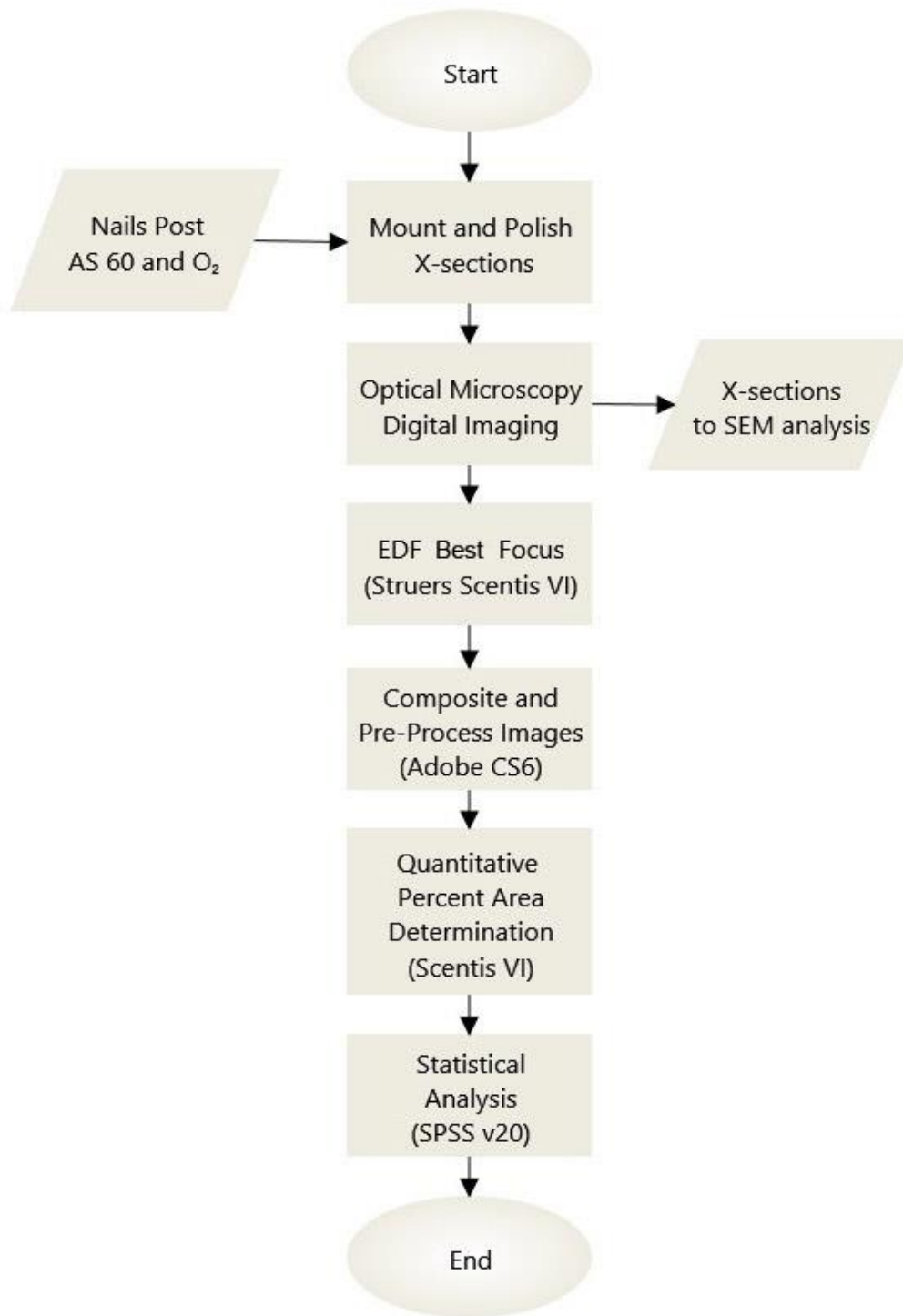


Figure 4.4 Flow chart of percent area slag measurement procedures

4.7.8 EPMA microanalysis

Four samples of untreated wrought iron nails representing the archaeological sites under study were examined by Electron Probe Micro Analysis (EPMA) (Table 4.4). Transverse cross sections of untreated nails not used in washing experiments were prepared as described in 4.2.5 and analysed with a Cameca SX-100 Electron Microprobe. Metallic and slag regions of the samples were analysed using 1 μm^2 spot and line scans across features. Accelerating voltage was 15kV with a current of 15 nA calibrated for elements Na, Mg, Al, Si, P, S, K, Ca, Ti, Cr, Mn, Fe, Co, and Ni using certified micro analytical standards before use. TAP, LIF, LTAP, LLIF, LPET crystals were utilised in the analyses. EPMA analysis was performed with the assistance of Dr. Joseph Boesenberg of the Department of Earth, Environmental and Planetary Sciences, Brown University in Providence, Rhode Island, USA. Results of analyses are given in Section 5.1.

EMPA Sample	Provenance
CAER_31	Caerleon-CPF08(001)
CW_31	Colonial Williamsburg-Carters Grove
CW_32	Colonial Williamsburg-Tazwell Hall
CW_33	Colonial Williamsburg-Brush Everard

Table 4.4 Sample nails analysed by EPMA at Brown University

4.7.9 SEM imaging and microanalysis of treated samples

A CamScan MaXim 2040 Scanning Electron Microscope (SEM) was used to image the polished cross sections of the wrought iron samples in both Secondary Electron (SEI) and Backscattered Electron (BEI) modes with high-vacuum and an accelerating voltage of 20kV. An analytical suite comprising an Oxford Instruments Model 5518 Energy Dispersive Spectrometer (EDS) with liquid nitrogen cooled silicon detector,

Oxford/Microspec WDX 400 Wavelength Dispersive Spectrometer (WDS), and Oxford Instruments INCA 1.0 software was used for X-ray microanalysis of treated and untreated nails in the study. Samples were imaged and analysed with EDS in point, line scan, and elemental mapping modes. The EDS spectrometer was standardised on pure cobalt wire before each analysis. Detection limits for EDS are nominally in the order of 0.2 wt%, which was sufficient for analysis of elements at this concentration or greater. However, EDS analysis did not produce spatially well resolved elemental maps for chlorine. This problem has been noted by other researchers (Logan 2016) who recommend WDS mapping as an effective alternative. A comparison of EDS and WDS chloride mapping results can be seen in Figure 4.5. Detection limits for well-calibrated WDS analyses are typically in the order of 200 ppm (0.02 wt%), or 10 times lower than for EDS (Goldstein et al. 2003). The use of WDS therefore allows for better spatial resolution in elemental mapping and detection of small quantities of chlorine which cannot be done by EDS alone.

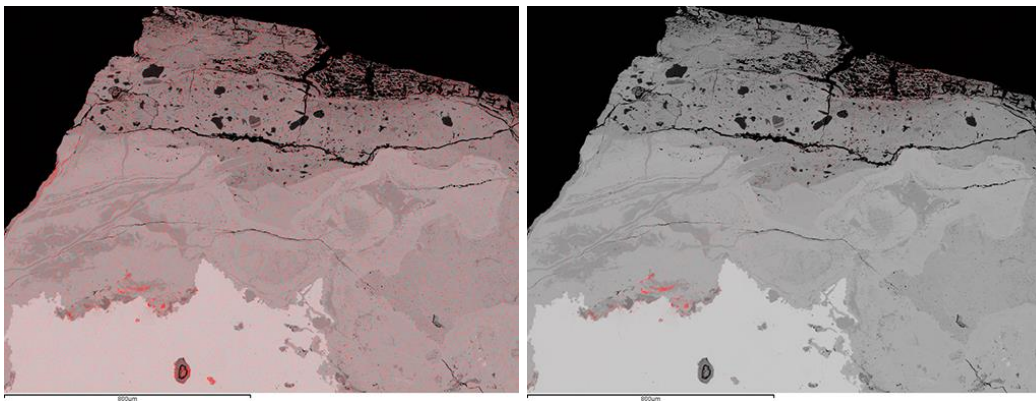


Figure 4.5 Comparison of SEM elemental mapping for chloride using EDS (left) and WDS (right) of a region of sample CAER_01 at 70X. Plots indicating detected chloride are shown in red pixels overlaid on a BSE base image.

SEM EDS/WDS mapping used 20kV and a higher beam current of 20 nA to provide adequate count rates. Beam current stability was verified using a Faraday cup before each map. The WDS spectrometer with PET (pentaerythritol) crystal was calibrated for chlorine using a NaCl standard (Micro Analytical Consultants Standard Block #4629) and the EDS detector standardised on cobalt. Elemental mapping was done using WDS for chloride maps and EDS for all other elements. EDS/WDS elemental maps were post processed with Oxford INCA Quantmap software to produce colour coded maps of elemental concentration in wt%.

A minimum of two EDS/WDS maps and one EDS line scan of each alkaline sulphite treated nail representing the corrosion product layers (CPLs) and slag inclusions near the metal/CPL interface and deeper in the metal structure were recorded to determine the presence or absence of chloride in these regions after treatment. In addition to chlorine mapping and detection, microanalysis of 8 additional samples was carried out using the SEM-WDS at Cardiff University in order to supplement EMPA compositional data (Section 4.7.8). WDS parameters and operating conditions were the same as for chloride analysis. Calibration for elements Na, Mg, Al, Si, P, S, K, Ca, Ti, Mn, Fe, Co, and Ni was carried out using Micro Analytical Consultants Standard Block #4629.

Calibration and analysis utilised PET, LIF crystals. Five spots on slag inclusions and five on the ferrite matrix were analysed for each sample. Samples analysed for composition by SEM-WDS are listed in Table 4.5 and results are given along with EPMA analysis in Section 5.1.

SEM-WDS Sample	Provenance
CAER_01	Caerleon-CPF08(001)
CAER_08	Caerleon-CPF08(001)
CAER_27	Caerleon-CPF08(001)
CAER_30	Caerleon-CPF08(001)
CAER_32	Caerleon-CPF08(001)
CW_08	Colonial Williamsburg-Brush Everard
CW_14	Colonial Williamsburg-Carters Grove
CW_34	Colonial Williamsburg-Carters Grove

Table 4.5 Sample nails analysed for elemental composition of metal and slag by SEM-WDS.

4.7.10 Digestion of samples to determine total remaining chloride

Nails were digested in 5M nitric acid at ambient temperature (20°C) over 2-3 months.

This involved weighing samples, placing them in clean LDPE 125ml screw-top sample vials with 50-100ml of 5M HNO₃. Variations in solution volumes were accounted for during chloride analysis. Vials were capped loosely to allow acid fumes and gases produced by dissolution of the iron nails to escape while preventing contamination and loss of chloride into the surrounding atmosphere, an issue highlighted by Schmutzler (2012; Schmutzler and Eggert 2010). Most nails were completely dissolved during the process but it was not possible to effect complete digestion of some samples. The minimum criterion used for nails to be considered sufficiently digested was that of digestion of the corrosion product layers and complete etching of the metal core.

Digestion solutions had low pH (≤ 2) and contained significant concentrations of iron ions. A procedure of neutralisation to slightly alkaline pH produced iron oxyhydroxide precipitates that were washed to expel Cl⁻ and prepare solutions for chloride measurement (Appendix 8.1.4).

4.7.11 Akaganeite transformation

Synthetic akaganeite (β -FeOOH) was produced according to the method previously used at Cardiff University by Al-Zahrani, Lewis, and Rimmer (Al-Zahrani 1998; Lewis 2009; Rimmer 2010). Equal parts (25g each) of fine iron powder and ferrous chloride tetrahydrate ($\text{FeCl}_2 \cdot 4 \text{H}_2\text{O}$) both Analar grade, were thoroughly mixed for 5 minutes in an agate mortar. Composition of both reactants was verified by X-ray powder diffraction before mixing. The mixture (50g) was placed in a sealed desiccating cabinet for 3 months at 92% (+/- 5%) RH maintained by a saturated salt solution of sodium carbonate (Na_2CO_3). The cabinet was opened weekly to stir the reactants and allow air into the chamber, preventing formation of magnetite rather than akaganeite due to oxygen depletion (Rimmer 2010). Production of akaganeite powder was verified by XRD analysis using a Panalytical X'pert Pro X-ray Diffractometer with PanAlytical HiScore software with International Centre for Diffraction Data (ICDD) 2005 Database (Appendix 8.2). A Perkin-Elmer Spectrum One FT-IR Spectrometer with Attenuated Total Reflectance (ATR) was used as a secondary analytical technique (Appendix 8.3).

The experimental procedure for investigating the transformation of akaganeite in alkaline sulphite treatment (outlined in Figure 4.6) was as follows. Ten LDPE 125ml screw-top bottles were thoroughly cleaned and rinsed with deionised water before being filled with 100ml of 0.5M NaOH/0.05 NaSO₃ solution made up in deionised water. The solution was prepared in a covered beaker with minimal headspace to minimize the oxidation of the sodium sulphite by ambient air. A mass of 5g synthetic β -FeOOH powder, previously analysed by XRD and FT-IR, was added to each bottle which was then tightly capped to achieve an airtight seal. The bottles were placed in an SNOL laboratory oven at 60°C. Samples were agitated by shaking every 5 days and left in the

oven for 30 days treatment time. The duration of the test was chosen to reflect the average treatment times which have been found to extract a significant amount of chloride from archaeological objects in previous studies (Rimmer 2010). The bottles were then removed from the oven, allowed to cool, and opened. The iron oxide powder was recovered by filtration and a sample of the treatment solution was taken for chloride analysis. The powder samples were rinsed in deionised water and allowed to dry in a sealed box maintained at low RH by desiccated silica gel for 1 week, by which time no further weight loss was detected. The dried powder was then re-analysed with XRD and FT-IR to evaluate any changes to the synthetic akaganeite which may have taken place. A flow chart outlining the procedure for production of synthetic akaganeite and the transformation experiment is given in Figure 4.6.

Semi quantitative XRD percentage phase analysis using Relative Intensity Ratings (RIRs) (Jenkins and Snyder 1996; Ermrich and Opper 2013) was used to determine relative amounts of corrosion phases before and after alkaline sulphite washing with approximately +/-10% accuracy. Accuracy was determined by a test of synthetic akaganeite vs. iron mineral powders reported in Appendix 8.2.

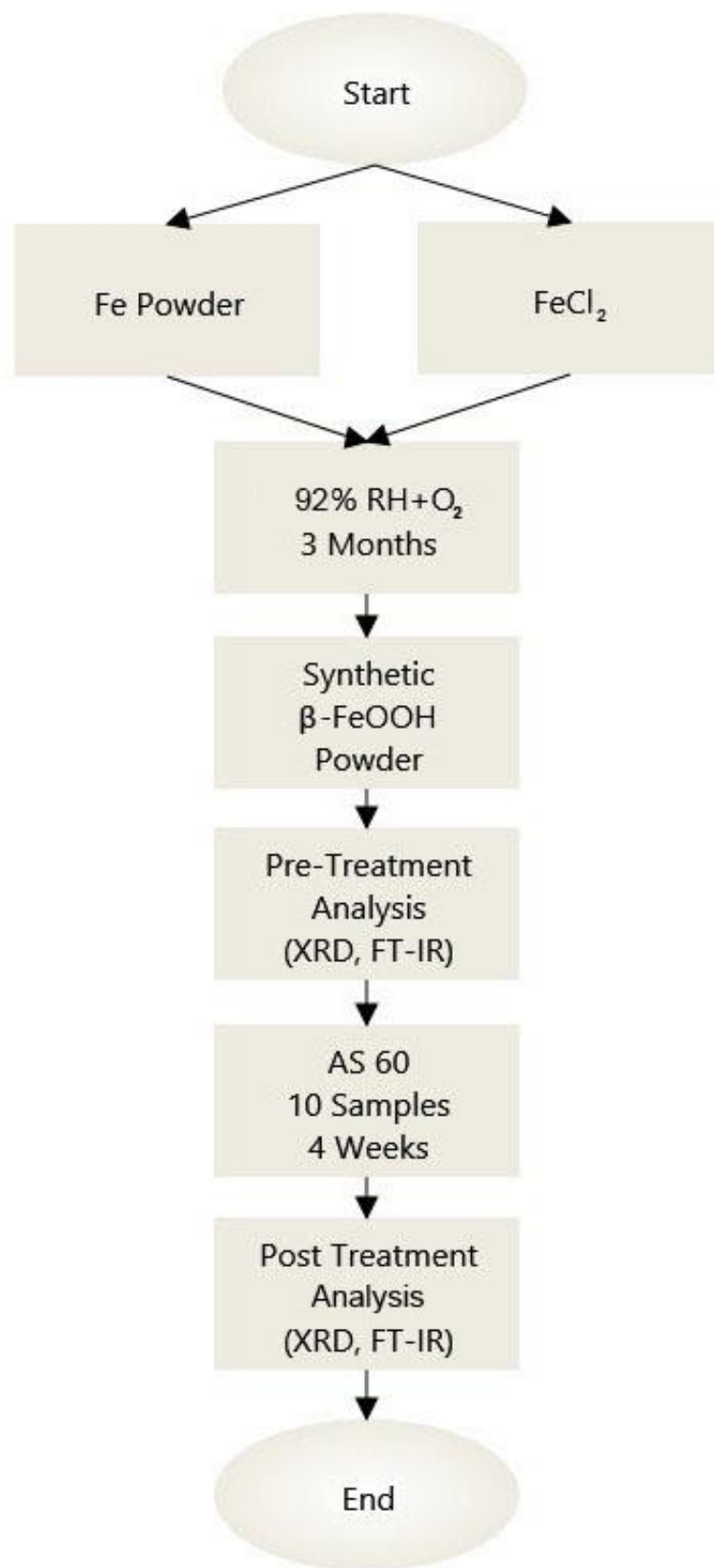


Figure 4.6 Flowchart of the procedures used for production of synthetic akaganeite (β -FeOOH) and the transformation experiment in alkaline sulphite solution (AS 60).

4.7.12 Data handling and statistical procedures

Data from the experiments were examined and presented in two principal ways, processing in Microsoft Excel and statistical analysis using SPSS. Data were also imported into SPSS (IBM SPSS Statistics v20) to allow the application of descriptive and inferential statistics. Statistical procedures utilised included means, tests of normal distribution, Pearson and Spearman Correlations. SPSS was also used to produce additional data outputs such as tables, boxplots, and scatter plots.

5 Results

5.1 Characterisation of Sample Material

X-radiography and microscopy of cross sections showed all of the samples examined contained a metallic core of wrought iron covered by corrosion product layers (CPL). (Figures 5.1 and 5.2, Appendix 8.6). There was significant variation in the thickness of the corrosion product layers (CPLs) and the amount of metal preserved. Optical microscopy and SEM revealed some nails had small regions of metal surrounded by a matrix of corrosion layers as a result of the stochastic nature of iron corrosion processes (Dillmann et al. 2014).



Figure 5.1 Digital photo at 1:1 scale (top) and SEM-BEI cross-sectional image (bottom) of CAER_10 a wrought iron nail from Caerleon. Voluminous corrosion product layers of varying thickness and degrees of cracking can be seen. Scale bar=1mm.

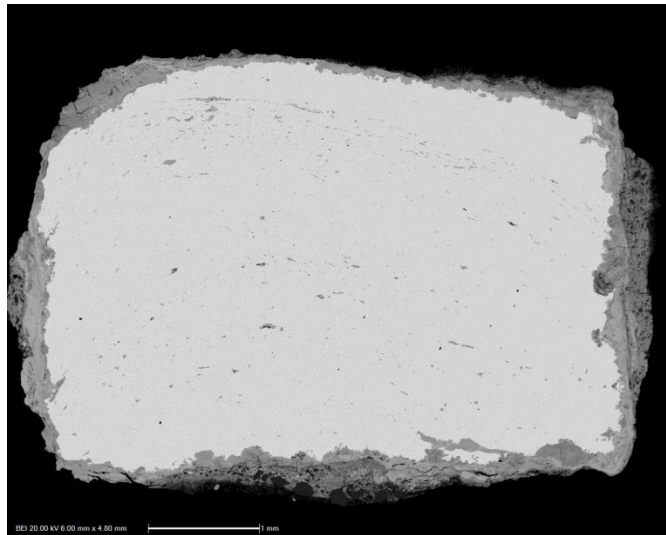


Figure 5.2 Digital photo at 1:1 scale (top) and SEM-BEI cross-sectional image (bottom) of CW_19, a wrought iron nail from Colonial Williamsburg. Corrosion product layers are thinner compared with those on CAER_01, and the amount of slag greater. Slag stringers reveal forging direction. SEM Scale bar=1mm

Elements of slag were surrounded by or incorporated into corrosion layers or pits, particularly when located within the first 1-200 micrometres below the metal/CPL interface (Figure 5.3). Assessing slag inclusions and their interaction with corrosion through examination of two dimensional cross sections presents challenges as they are 3D structures. The nature of slag inclusions and their potential effect on corrosion behaviour will be discussed in Chapter 6.

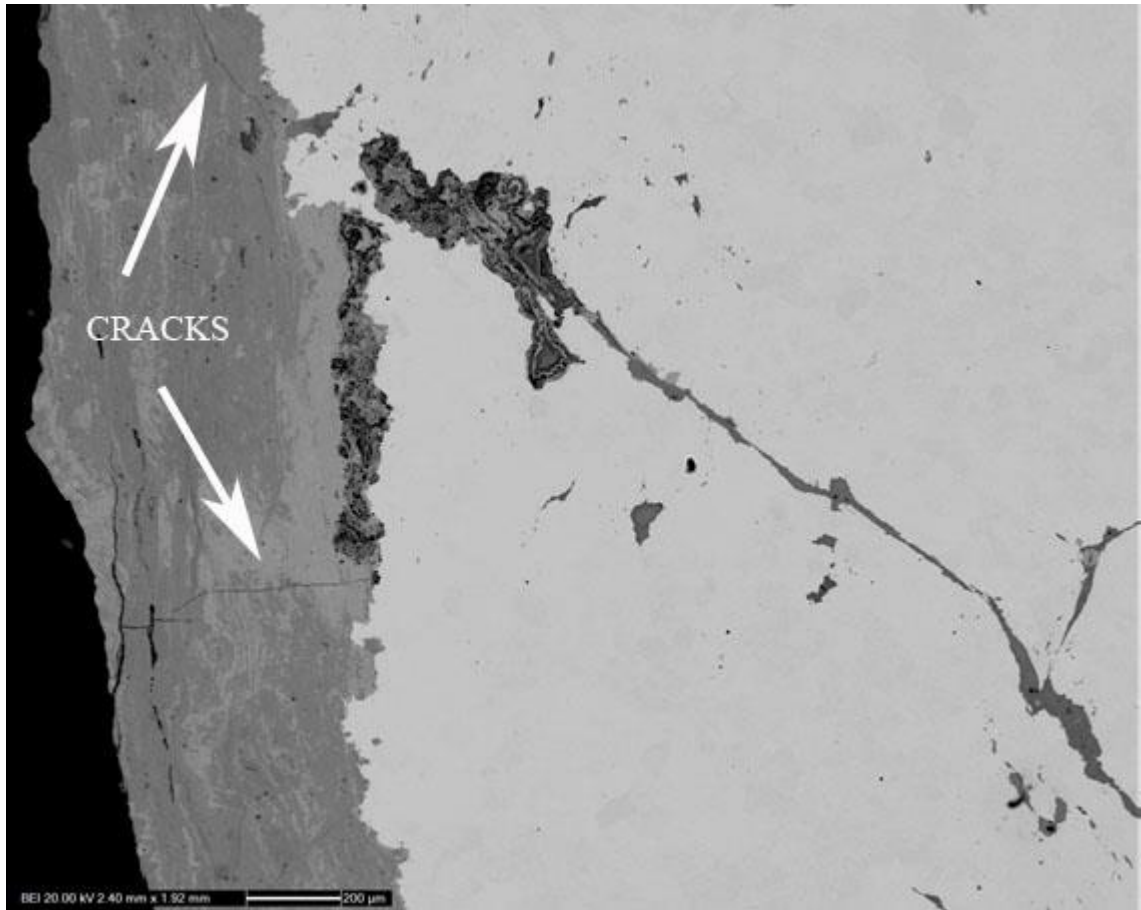


Figure 5.3 SEM-BEI micrograph of sample CAER_08 from Caerleon in polished cross section at 50X magnification (Scale bar=200 μ m). The ferrite core of the nail is rendered in light grey and the slag and corrosion products in darker grey tones. A long stringer of slag can be seen stretching from bottom right to top left, the top portion of which has been overtaken by a corrosion pit intersecting it from another plane. Longitudinal and radial cracks can also be seen in the corrosion product layers.

Thickness of corrosion product layers differed between the two archaeological sites.

On average, the thickness of corrosion on nails from Caerleon was double that of

Colonial Williamsburg (Figures 5.4, 5.5 and Table 5.1). The coverage of Colonial

Williamsburg nails by CPLs was also less complete than for Caerleon (Figures 5.6-5.9).

Sample	Max CPL Thickness (µm)	Min CPL Thickness (µm)
CAER_01	2390	116
CAER_07	3393	781
CAER_08	741	28
CAER_10	1763	76
CAER_13	2615	236
CAER_18	1926	87
CAER_19	1245	36
CAER_21	1118	43
CAER_22	1368	99
CAER_27	1947	165
CW_29	858	42
CW_14	178	26
CW_26	1012	34
CW_09	932	62
CW_05	959	52
CW_07	388	20
CW_16	1994	32
CW_19	537	69
CW_08	1752	41
CW_15	550	45

Table 5.1 Maximum and minimum thickness (µm) of CPLs of 10 nails each from Caerleon and Colonial Williamsburg as measured by calibrated image analysis of polished sections imaged by SEM-BSE.

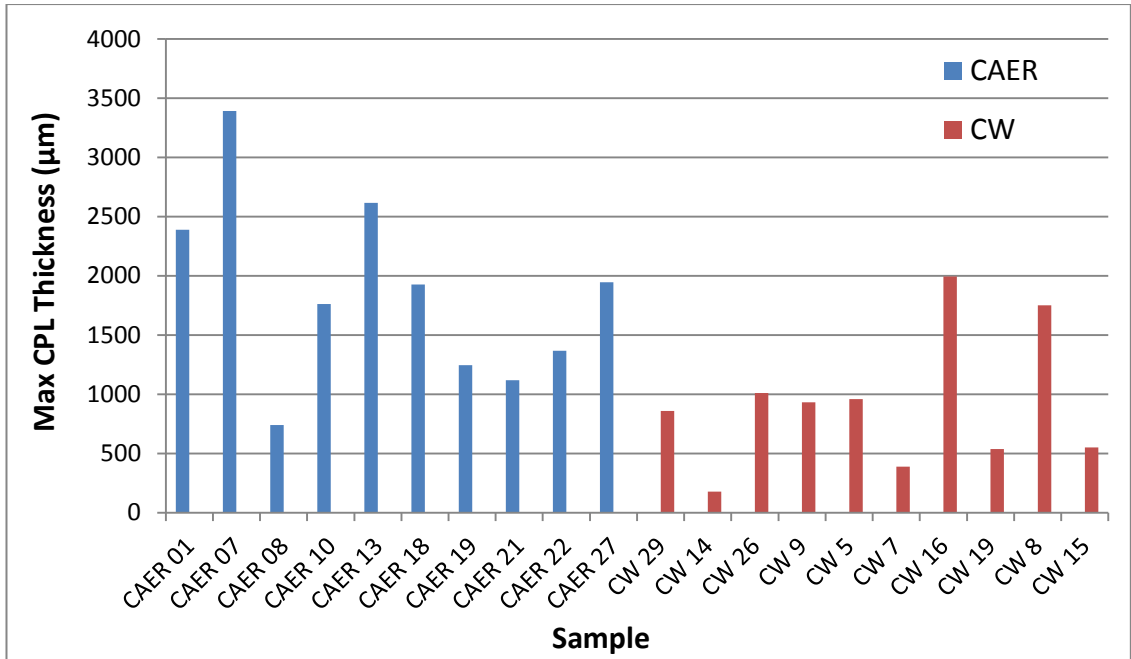


Figure 5.4 Maximum thickness (in μm) of corrosion product layers (CPLs) on 10 wrought iron nails each from Caerleon and Colonial Williamsburg as measured by calibrated image analysis of polished sections imaged by SEM-BSE.

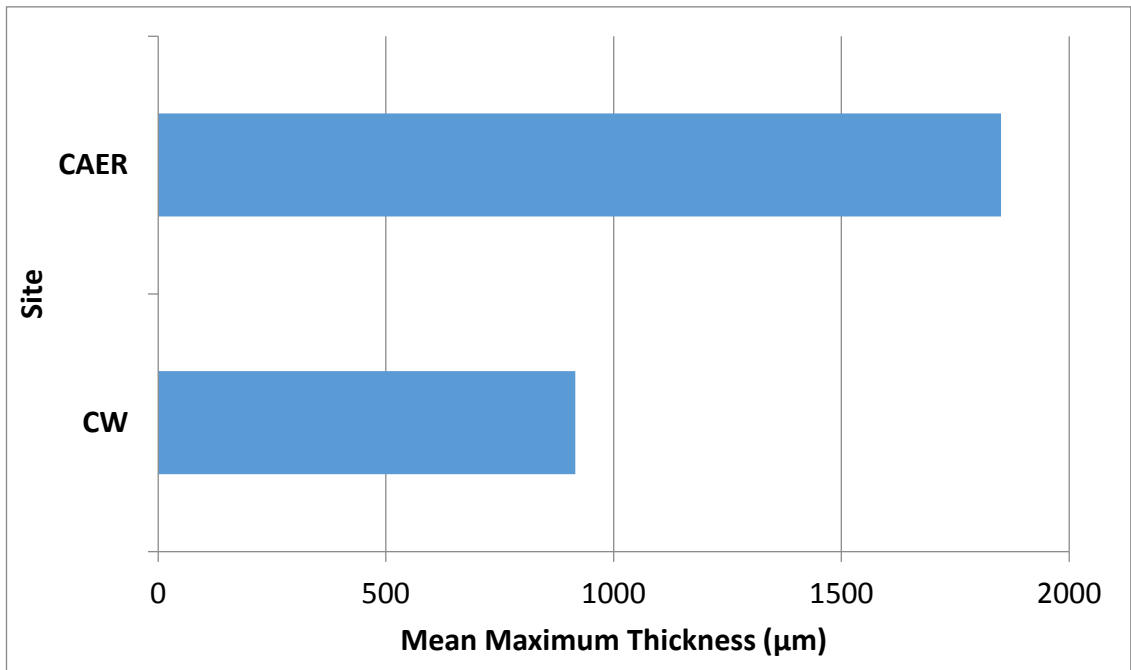


Figure 5.5 Mean maximum corrosion product layer thickness (μm) of 10 nails each from the sites of Caerleon and Colonial Williamsburg as measured by calibrated image analysis of polished sections imaged by SEM-BSE.



Figure 5.6 SEM-BSE image of Caerleon nail CAER_13 post alkaline sulphite treatment in polished cross-section at 13X magnification showing metal core, corrosion pits, thick DPL of up to 2615 μm , TM and extensive concentric and radial cracking. Scale bar=1mm

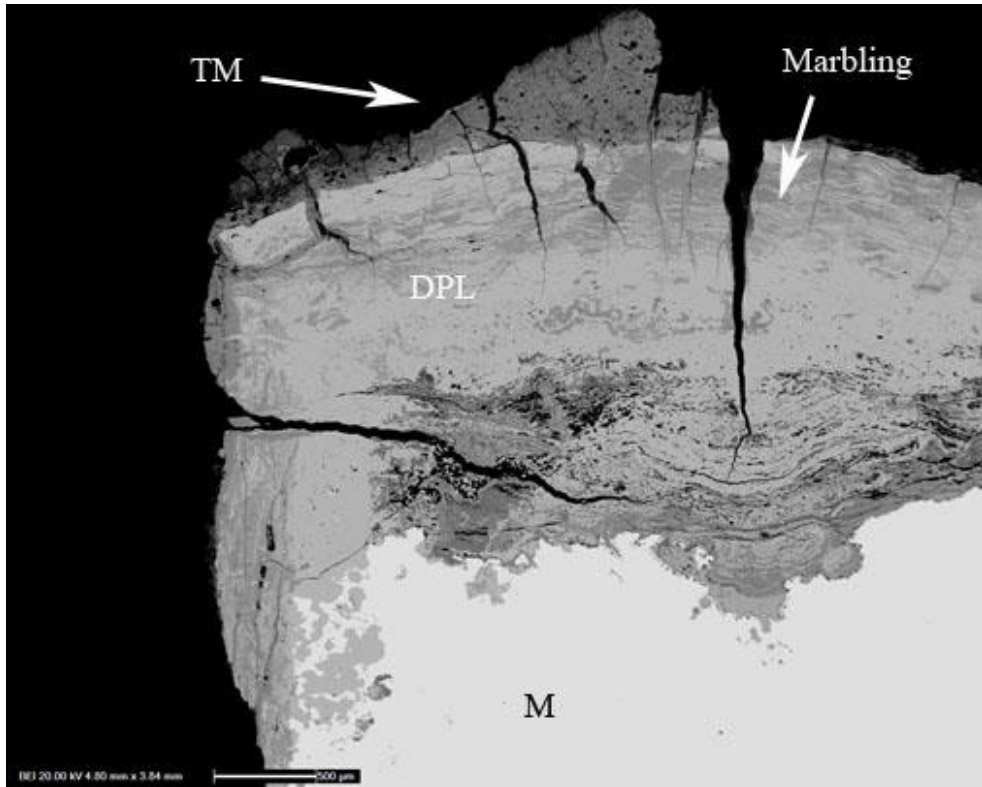


Figure 5.7 SEM-BSE image of nail CAER_13 post alkaline sulphite treatment at 25X showing metal core (M), wide radial cracking through TM and DPL corrosion layers and significant marbling in the DPL. Scale bar=500μm

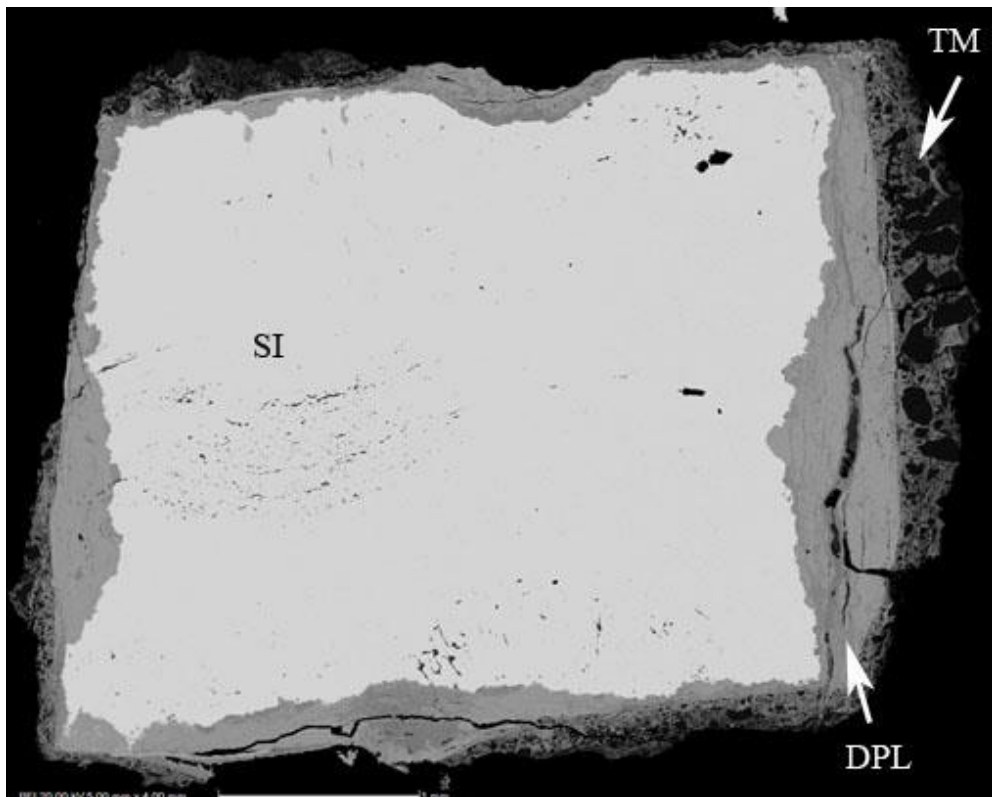


Figure 5.8 SEM-BSE image of nail CW_05 post alkaline sulphite treatment at 24X showing thinner DPL and TM corrosion layers up to 959 μm and significant marbling in the DPL. Cracks, primarily concentric, can be seen as well as the inhomogeneity of the slag inclusion (SI) distribution. Scale bar=1mm

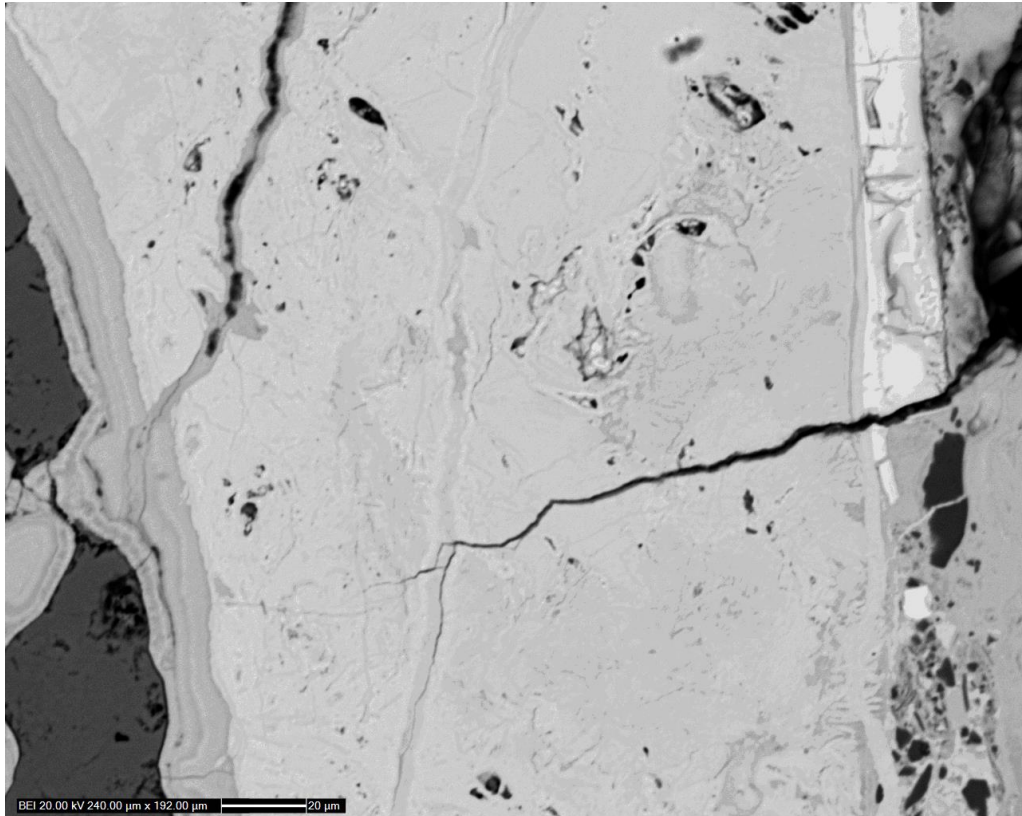


Figure 5.9 SEM-BSE image of nail CW_05 post alkaline sulphite treatment at 500X showing small radial crack from outer edge of DPL (right) towards the inner edge. Inclusions within the DPL can be seen as darker areas at the left. Scale bar=20μm

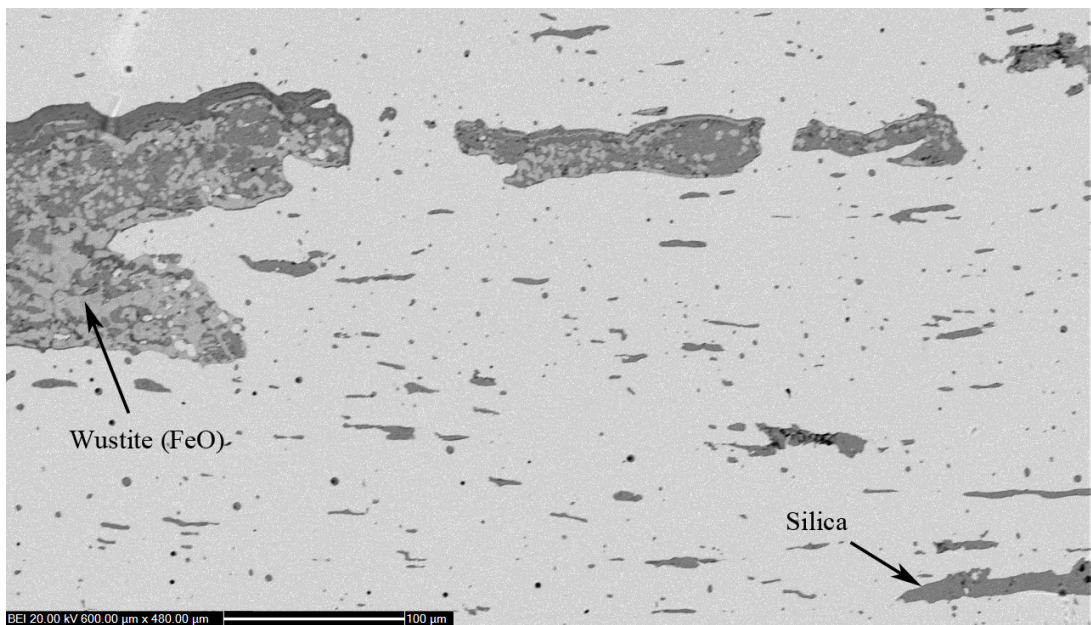


Figure 5.10 SEM-BSE image of slag inclusions in sample CW_16. Dark grey areas in inclusions are primarily composed of silica. Light grey regions within the slag are wüstite (FeO). Scale bar=100μm.

The elemental composition of samples from both archaeological sites was determined by Electron Probe Microanalysis (EPMA) as described in 4.2.8. Analyses of the metal (Table 5.2) and slag (Table 5.3) phases were performed as line scans. These provide the mean wt % values for each element or oxide. Linescans sometimes intersected areas of elevated concentrations of a given element, resulting in higher mean values overall. Carbon was not analysed, as it is difficult to detect accurately using EPMA (Boesenberg 2006). The EPMA data were supplemented by additional WDS data acquired by SEM (Tables 5.2 and 5.3). Results show the metallic (ferrite) phase of all samples contained low levels of elements in solid solution apart from phosphorus in four Colonial Williamsburg samples and one from Caerleon, manganese in one Williamsburg sample and nickel in another. Analysis of the slag phases showed varying amounts of SiO₂ and FeO depending on whether the slag inclusions were primarily silicate glass or contained significant wüstite (FeO). Figure 5.10 shows the appearance of SiO₂ and FeO in SEM-BSE imaging. Results of EPMA and SEM-WDS compositional analysis of slag inclusions in 12 sample nails as a scatterplot of wt % P₂O₅ vs wt % of MgO+Al₂O₃+K₂O/FeO are given in Figure 5.11

Elemental Composition of the Metallic Phase of 12 Wrought Iron Nail Samples by EPMA and SEM/WDS in wt%											
Sample	Si	P	S	Ca	Ti	Cr	Mn	Fe	Ni	Co	Total
CAER_01	0.07	0.06	nd	nd	nd	nd	nd	99.75	0.01	0.11	100.00
CAER_08	0.27	0.10	nd	nd	nd	nd	nd	99.51	nd	0.14	100.00
CAER_27	0.08	0.02	nd	nd	nd	nd	nd	99.76	0.01	0.13	100.00
CAER_30	0.09	0.01	nd	nd	nd	nd	nd	99.79	nd	0.15	100.00
CAER_32	0.05	0.04	nd	nd	nd	nd	nd	99.79	0.02	0.12	100.00
CAER_31	0.02	0.03	nd	nd	nd	nd	nd	99.68	0.04	nd	99.78
CW_08	0.23	0.29	nd	nd	nd	nd	nd	99.34	0.03	0.13	100.00
CW_34	1.23	0.01	nd	nd	nd	nd	nd	98.64	nd	0.12	100.00
CW_14	0.18	0.21	nd	nd	nd	nd	nd	99.50	nd	0.13	100.00
CW_31	0.03	0.33	0.03	nd	nd	nd	nd	99.62	0.04	0.02	100.06
CW_32	0.03	nd	nd	nd	nd	nd	2.36	94.16	0.02	nd	96.57
CW_33	0.15	0.23	0.01	nd	nd	nd	0.02	98.63	0.15	0.06	99.24

Table 5.2 Mean values (in wt %) for elemental composition of iron metal (ferrite) phase of 12 wrought iron nail samples (6 each) from Caerleon (CAER) and Colonial Williamsburg (CW) analysed by EPMA (shaded in grey) and SEM-WDS (unshaded). Each value is the mean of 5 analysis spots. nd=element analysed for but not detected.

Elemental Composition of Slag Inclusions in 12 Wrought Iron Nail Samples by EPMA and SEM/WDS in wt%													
Sample	Na ₂ O	MgO	Al ₂ O ₃	SiO ₂	SO ₂	K ₂ O	CaO	TiO ₂	MnO	FeO	NiO	P ₂ O ₅	Total
CAER_01	0.03	0.39	1.48	26.95	0.01	0.62	0.75	0.10	0.10	28.47	nd	0.06	100
CAER_08	0.05	0.29	1.57	29.13	0.01	0.88	0.60	0.11	0.08	24.74	nd	0.06	100
CAER_27	0.04	0.23	2.45	35.66	nd	0.77	0.85	0.23	0.31	12.20	nd	nd	100
CAER_30	0.08	1.01	2.89	37.93	nd	3.28	1.86	0.16	0.12	3.60	nd	nd	100
CAER_32	0.04	0.24	1.04	25.34	0.01	0.45	0.44	0.07	0.06	32.37	nd	0.14	100
CAER_31	0.15	0.77	2.60	34.27	0.24	0.96	1.23	0.12	0.31	59.27	nd	0.29	100.22
CW_08	0.02	0.07	0.35	9.72	0.02	0.10	0.41	0.02	0.24	59.80	nd	0.17	100
CW_14	0.01	0.19	0.35	14.00	0.08	0.40	2.28	0.02	0.71	47.33	nd	1.51	100
CW_34	0.03	0.47	1.67	19.38	0.01	0.75	6.04	1.12	0.29	33.48	nd	0.04	100
CW_31	0.14	0.23	0.99	11.04	1.04	0.20	0.64	0.18	1.02	72.97	0.01	10.92	99.38
CW_32	0.27	1.66	2.51	31.84	1.47	0.65	7.40	0.09	18.09	36.46	nd	0.94	101.37
CW_33	0.02	0.21	0.41	13.51	0.80	0.05	0.68	0.12	3.22	71.14	nd	9.98	100.16

Table 5.3 Mean values (in wt%) for elemental composition of silicate slag regions of 12 wrought iron nail samples (6 each) from Caerleon (CAER) and Colonial Williamsburg (CW) analysed by EPMA (shaded in grey) and SEM-WDS (unshaded). Each value is the mean of 5 analysis spots. nd=element analysed for but not detected.

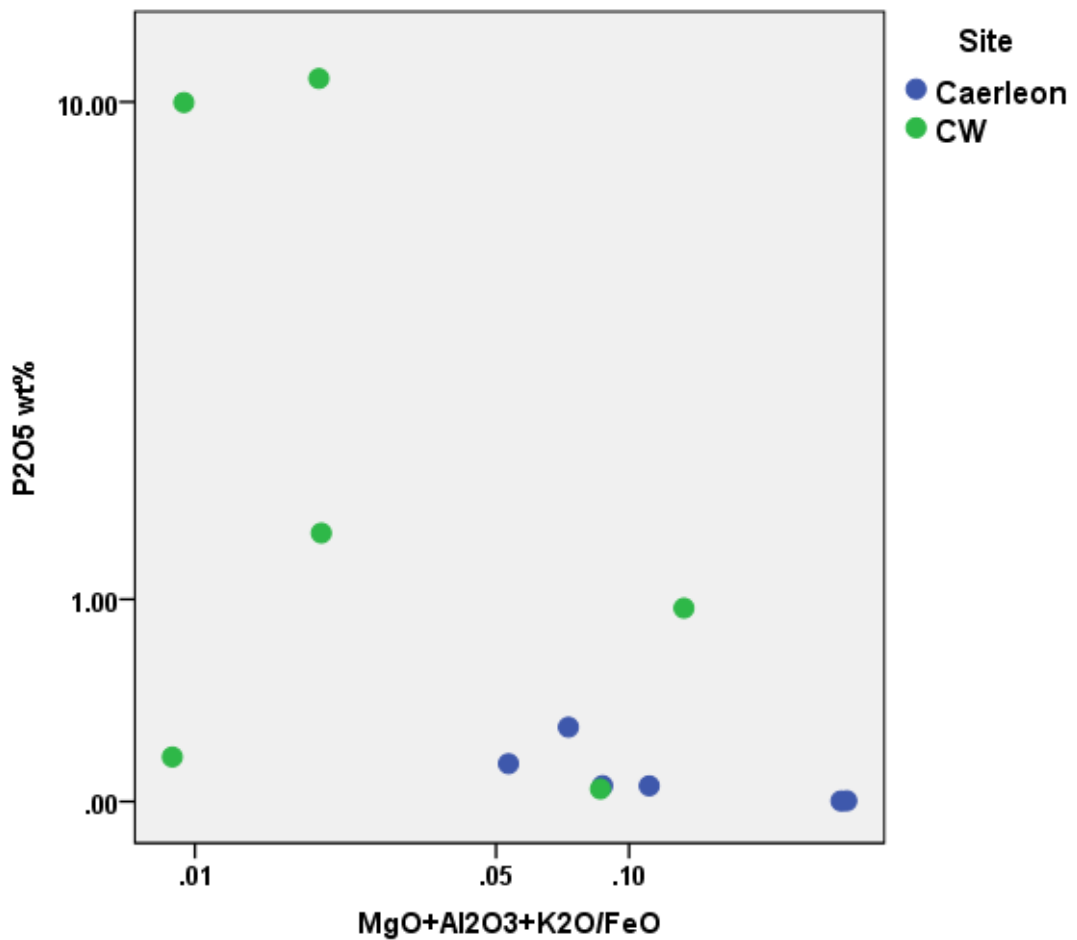


Figure 5.11 Scatterplot showing ratio of wt % of P₂O₅ to wt % of MgO+Al₂O₃+K₂O/FeO as analysed by EPMA and SEM/WDS for samples from Caerleon and Colonial Williamsburg. Logarithmic scales to show point separation more clearly. (Format after Birch and Martín-Torres 2015)

5.1.1 Chloride content

Prior to experiments, the chloride content of five untreated samples from each archaeological site was determined by nitric acid digestion according to the method described in section 4.7.10 (Figure 5.12, Table 5.4). Mean chloride content of Roman Caerleon was, on average, almost 2 times higher than those from Colonial Williamsburg.

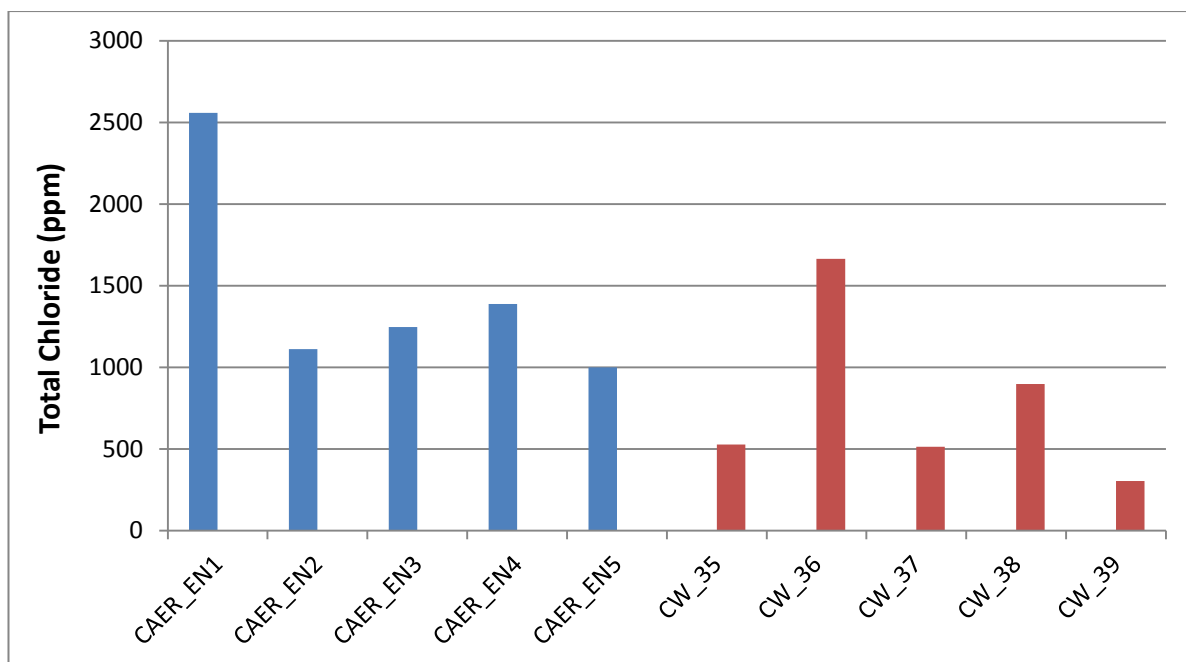


Figure 5.12 Total chloride content of 10 wrought iron nails, 5 each from the sites of Roman Caerleon (CAER) and Colonial Williamsburg (CW).

Sample	Site	Mass (grams)
CAER_EN1	Caerleon	6.74
CAER_EN2	Caerleon	6.19
CAER_EN3	Caerleon	7.37
CAER_EN4	Caerleon	6.34
CAER_EN5	Caerleon	2.72
CW_35	Colonial Williamsburg	3.92
CW_36	Colonial Williamsburg	3.35
CW_37	Colonial Williamsburg	4.76
CW_38	Colonial Williamsburg	3.23
CW_39	Colonial Williamsburg	4.19

Table 5.4 Untreated wrought iron nails digested and analysed for total chloride.

5.1.2 Mass of samples

The mass distributions of 30 sample nails each from Caerleon and Colonial Williamsburg were assessed (Figures 5.13 and 5.14). Calculated Shapiro-Wilk test of normality and skewness (deviation from normal distribution) results are given in (Table 5.5). Shapiro-Wilk significance is less than .05 for both sites, indicating that mass is not normally distributed. Skewness values from both sites are non-zero and positive, also indicating that they are skewed right and the mass values are not normally distributed.

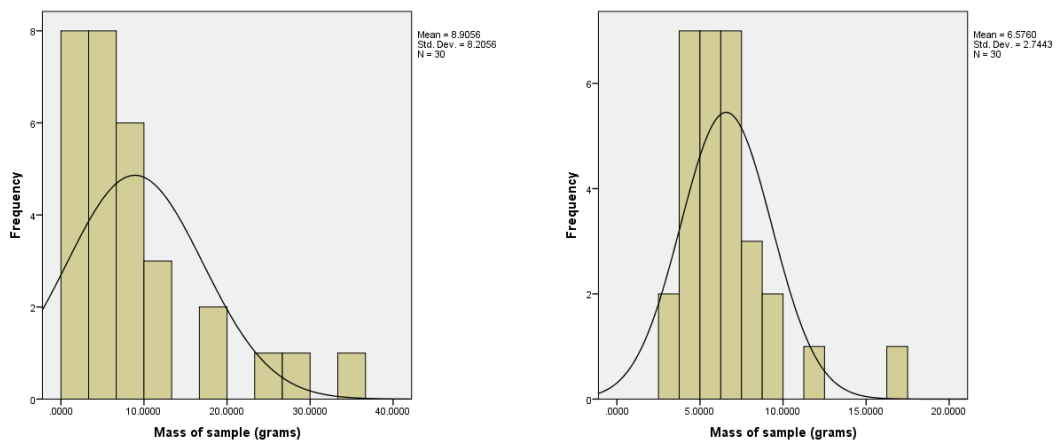


Figure 5.13 Histograms of the distribution of 30 samples of wrought iron nails each from the sites of Roman Caerleon (left) and Colonial Williamsburg (right) by mass. A curve indicating normal distribution is plotted in black.

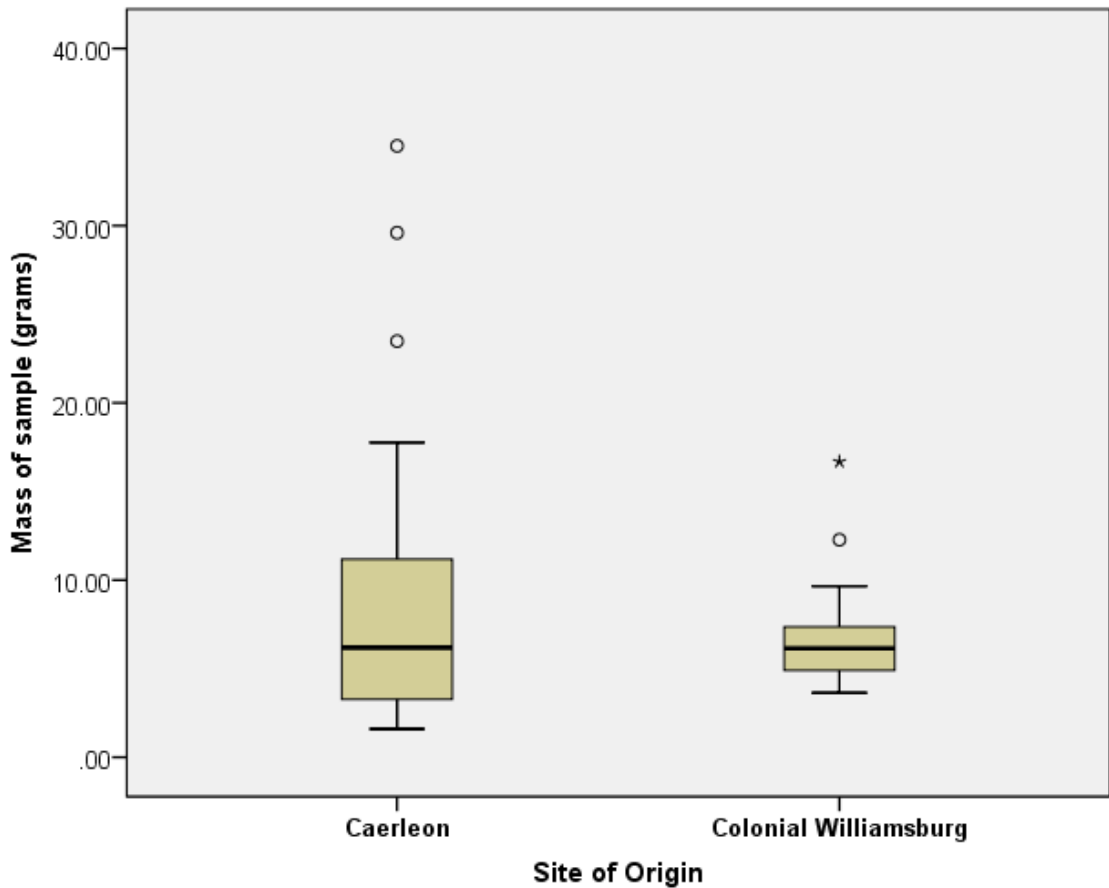


Figure 5.14 Boxplot of mass of sample nails (grams) by site of origin. The boxes in this and subsequent boxplots describe the region between the upper and lower quartile values. Horizontal lines within boxes indicate median values. Minimum and maximum values are indicated by 'whiskers' (horizontal bars above or below boxes). Outliers 1.5- 3 times the interquartile range above or below the quartile are shown by a circle, or greater than 3 times the inter-quartile range by a star (Field 2009).

Site	Shapiro-Wilk	Shapiro-Wilk Significance	Skewness
Caerleon	.657	.00	1.83
Colonial Williamsburg	.910	.00	2.04

Table 5.5 Shapiro-Wilk test of normality and skewness (measure of deviation from normal distribution) results of the mass in grams 60 wrought iron sample nails, 30 each from the sites of Caerleon, and Colonial Williamsburg. Shapiro-Wilk significance values and positive non-zero Skewness values indicated that the mass of the samples is not normally distributed.

5.1.3 Slag content

The slag content of 10 sectioned and polished samples from each site was measured after alkaline sulphite treatment using computer image analysis at 50X magnification using procedures described in section 4.7.7 (Table 5.6). Digital photomicrographs of the 20 samples reported in Table 5.6 are given in Figures 5.15-5.34. Table 5.7 lists mean percent area slag for each site along with results of Shapiro-Wilk tests of normal distribution and skewness values. The alpha value threshold for the Shapiro-Wilk test was .05. All skewness values are non-zero and positive indicating these data are skewed right and are not normally distributed. However, the percent area slag data for Colonial Williamsburg are nearly normally distributed as indicated by a Shapiro-Wilk significance of $> .05$ and a low skewness of .568. The cross sectional percentage area of slag ranged from 0.22–7.93% across both sites and Caerleon and Colonial Williamsburg nails are compared in Figure 5.35. Percentage area slag data and measurement methodology is explored further in Chapter 6.

Sample	Percent Area Slag (50X Total Area)
CAER_01	0.68
CAER_07	3.30
CAER_08	0.90
CAER_10	0.27
CAER_13	0.63
CAER_18	0.64
CAER_19	7.93
CAER_21	1.48
CAER_22	0.22
CAER_27	1.46
CW_05	0.68
CW_07	0.28
CW_08	1.32
CW_09	1.02
CW_14	1.96
CW_15	3.82
CW_16	2.03
CW_19	1.99
CW_26	4.11
CW_29	4.69

Table 5.6 Percent area of slag inclusions measured by computer image analysis of polished transverse sections of wrought iron nails from Roman Caerleon (CAER) and Colonial Williamsburg (CW) as imaged by optical microscopy at 50X magnification. The entire area of the preserved metal core was measured.

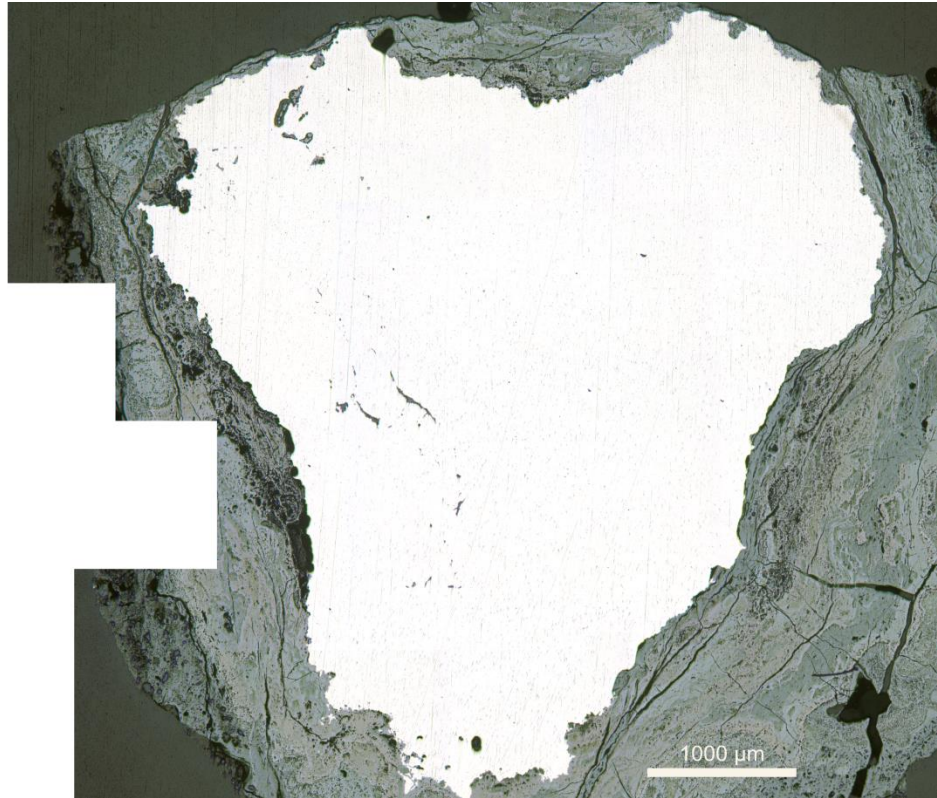


Figure 5.15 Composite digital photomicrograph of sample CAER_01 in polished cross-section at 50X magnification.

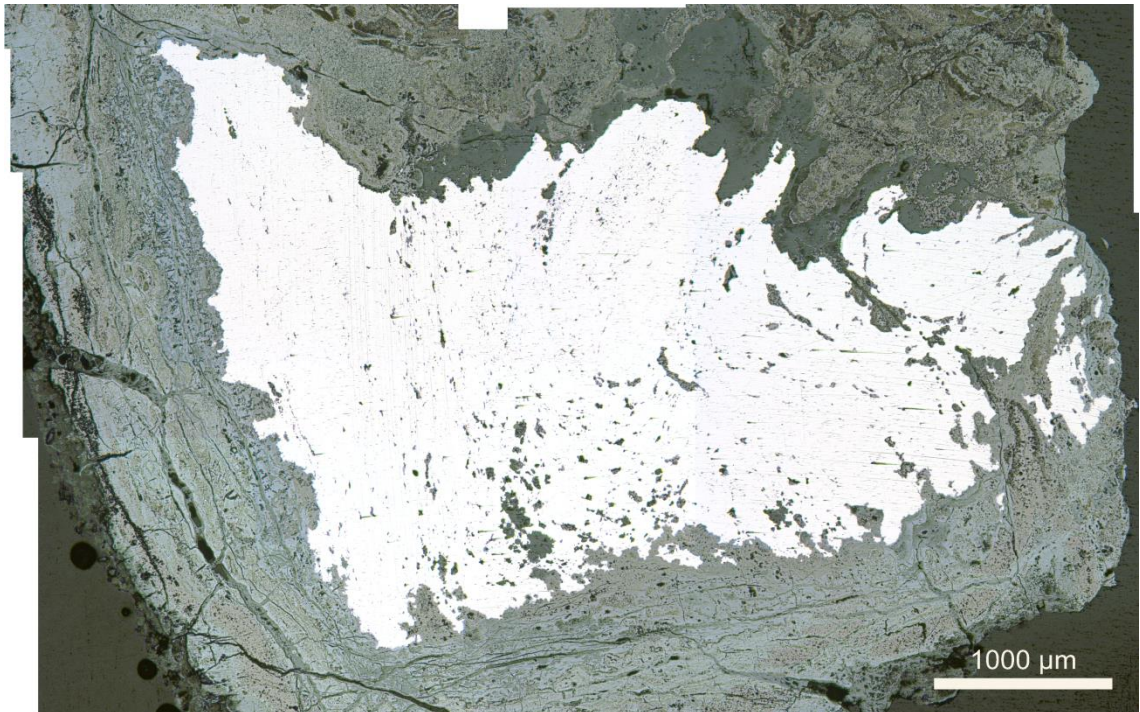


Figure 5.16 Composite digital photomicrograph of sample CAER_07 in polished cross-section at 50X magnification.

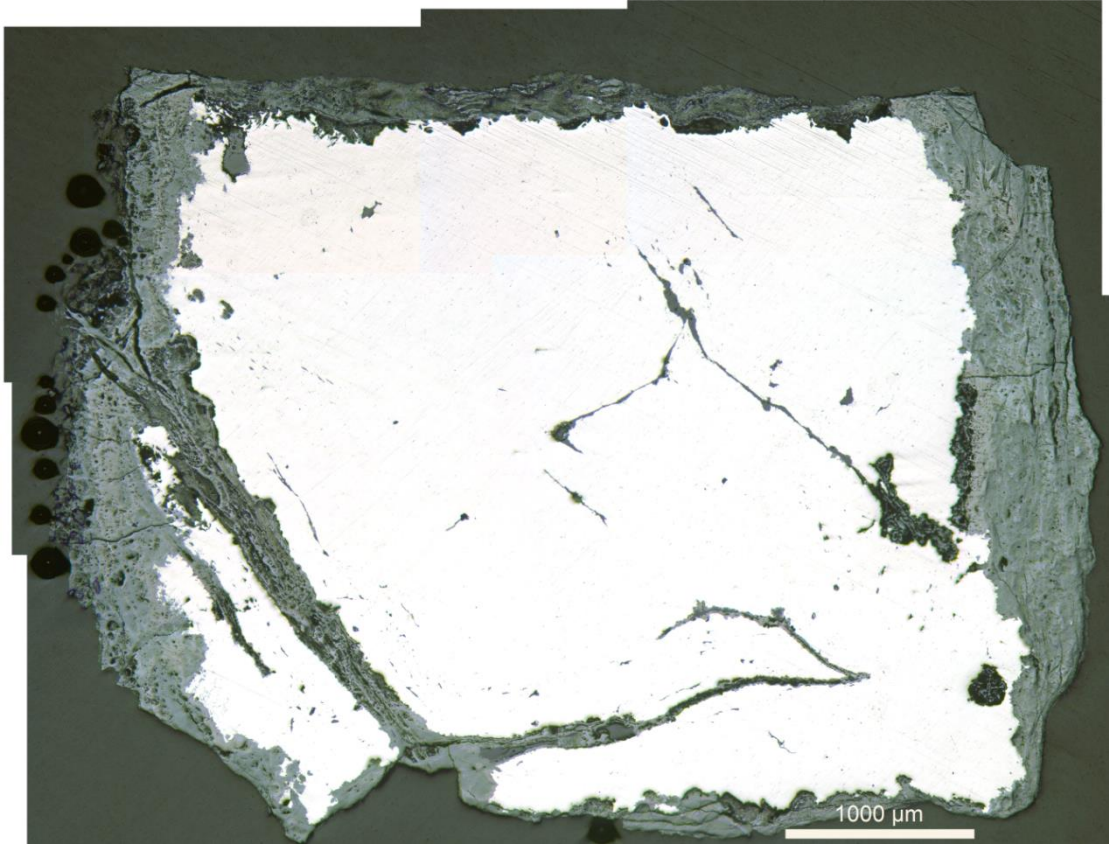


Figure 5.17 Composite digital photomicrograph of sample CAER_08 in polished cross-section at 50X magnification.

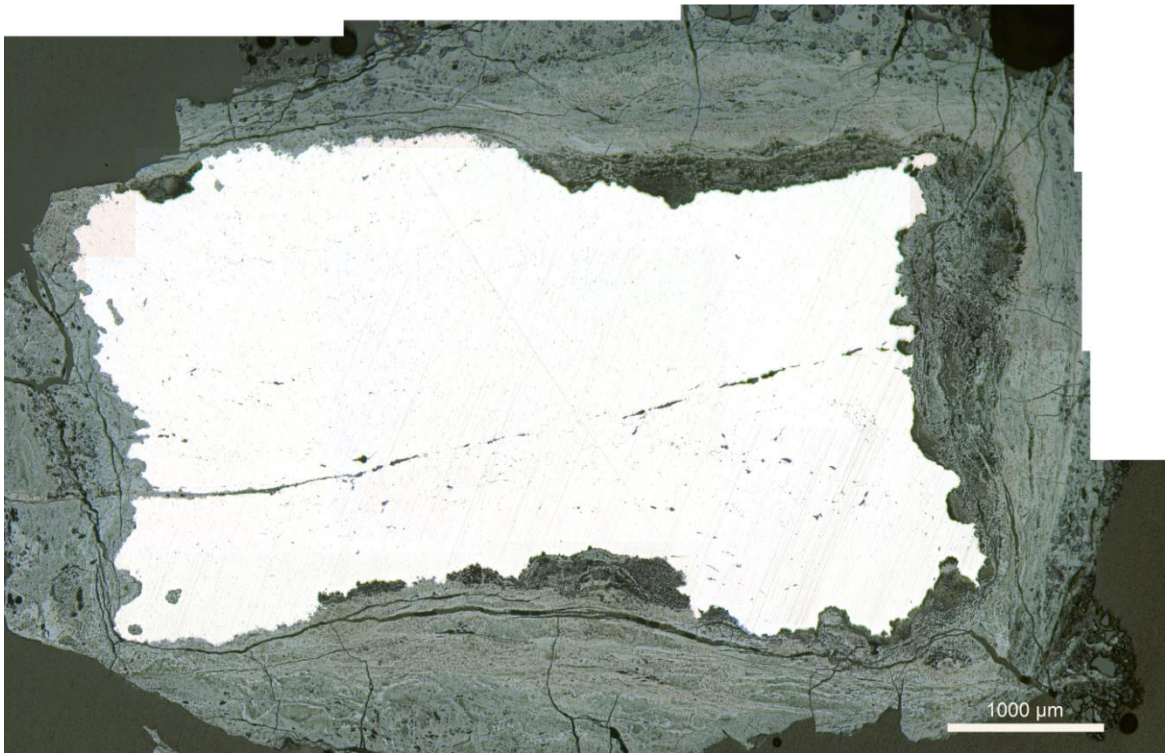


Figure 5.18 Composite digital photomicrograph of sample CAER_10 in polished cross-section at 50X magnification.



Figure 5.19 Composite digital photomicrograph of sample CAER_13 in polished cross-section at 50X magnification

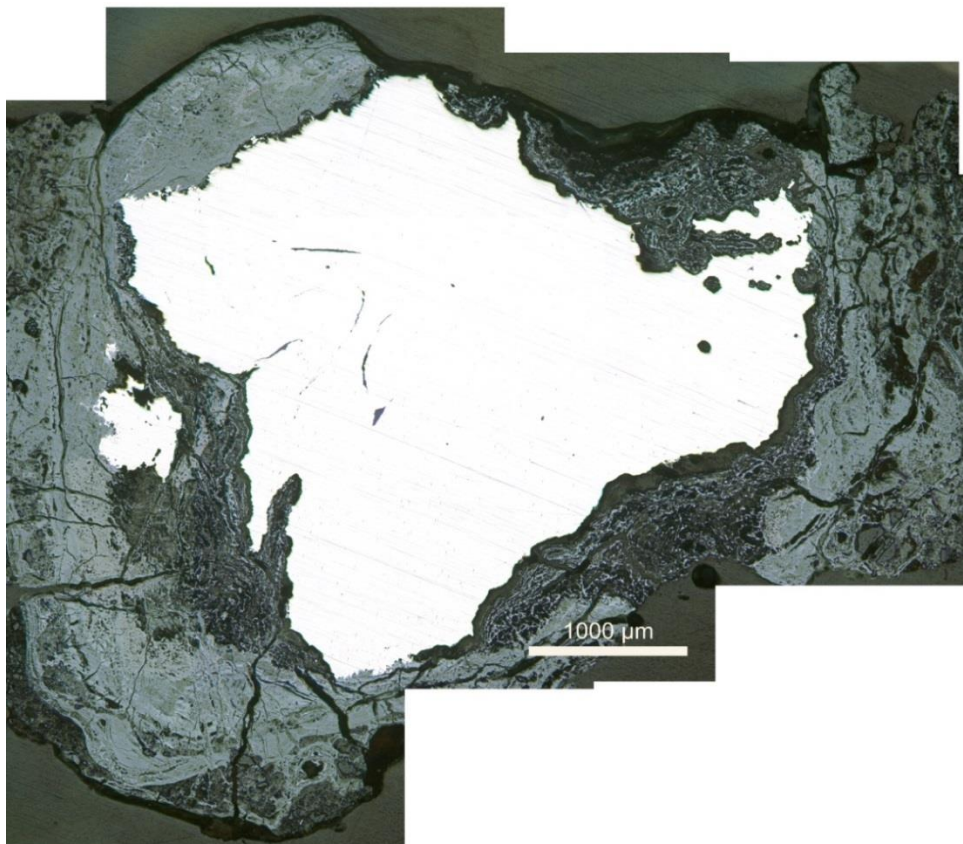


Figure 5.20 Composite digital photomicrograph of sample CAER_18 in polished cross-section at 50X magnification.

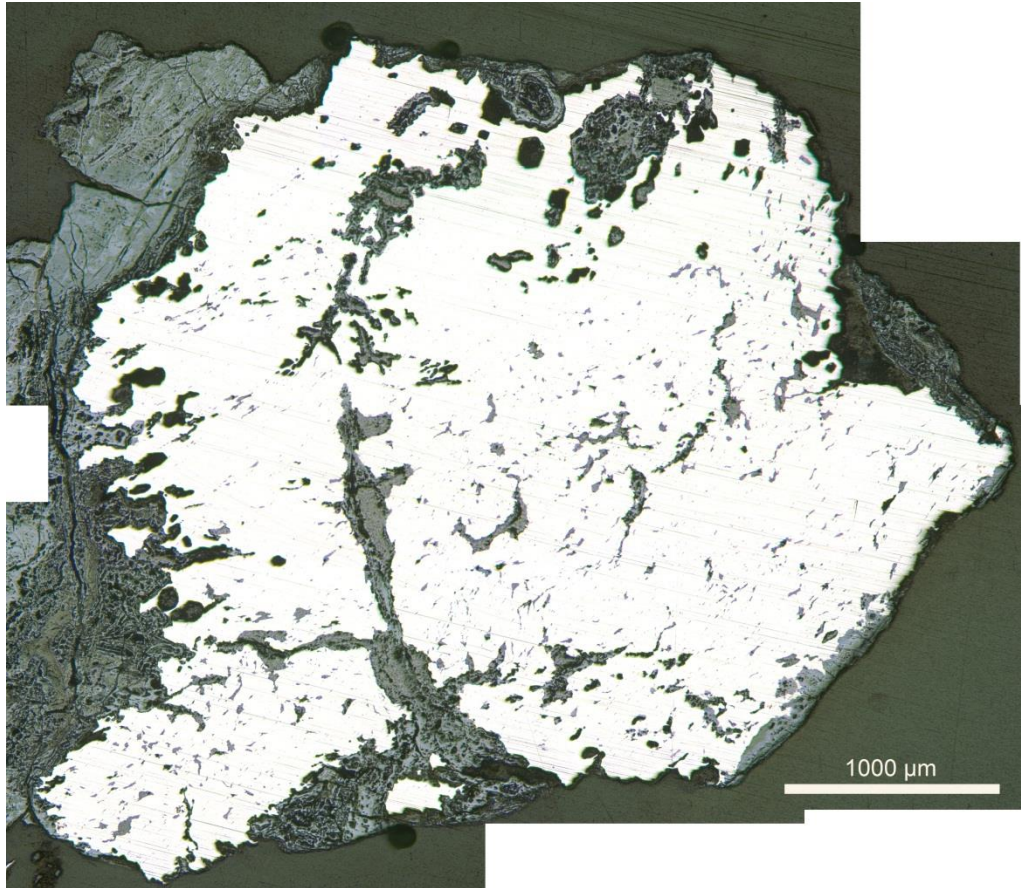


Figure 5.21 Composite digital photomicrograph of sample CAER_19 in polished cross-section at 50X magnification.

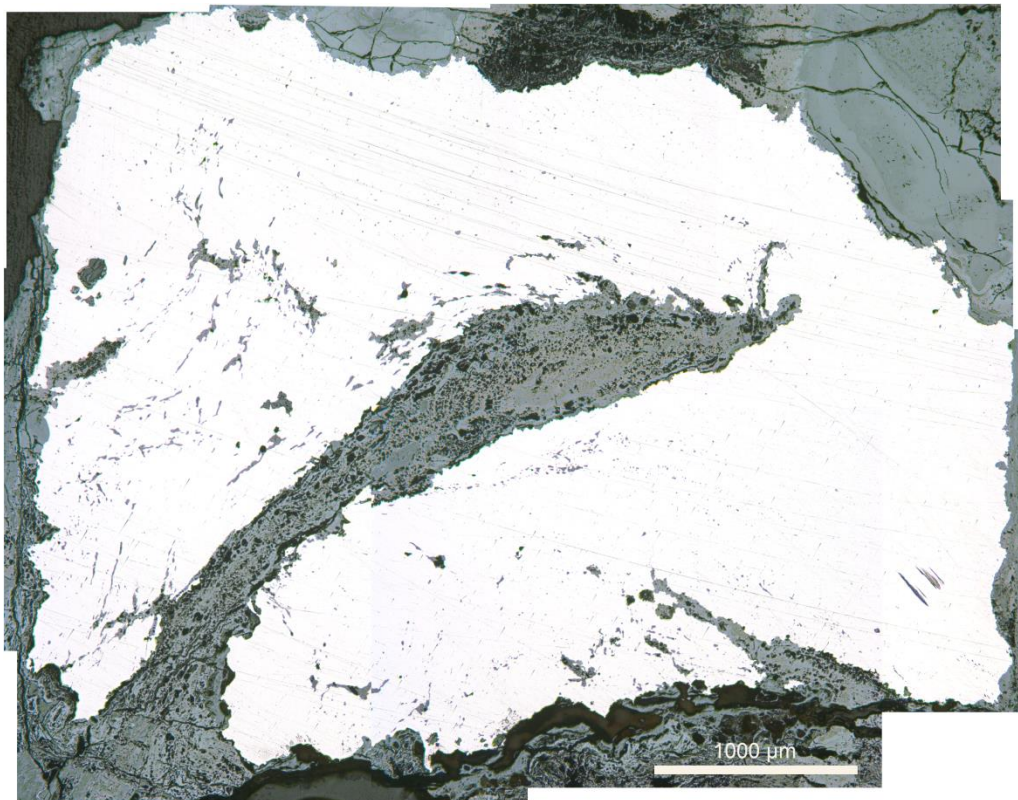


Figure 5.22 Composite digital photomicrograph of sample CAER_21 in polished cross-section at 50X magnification.

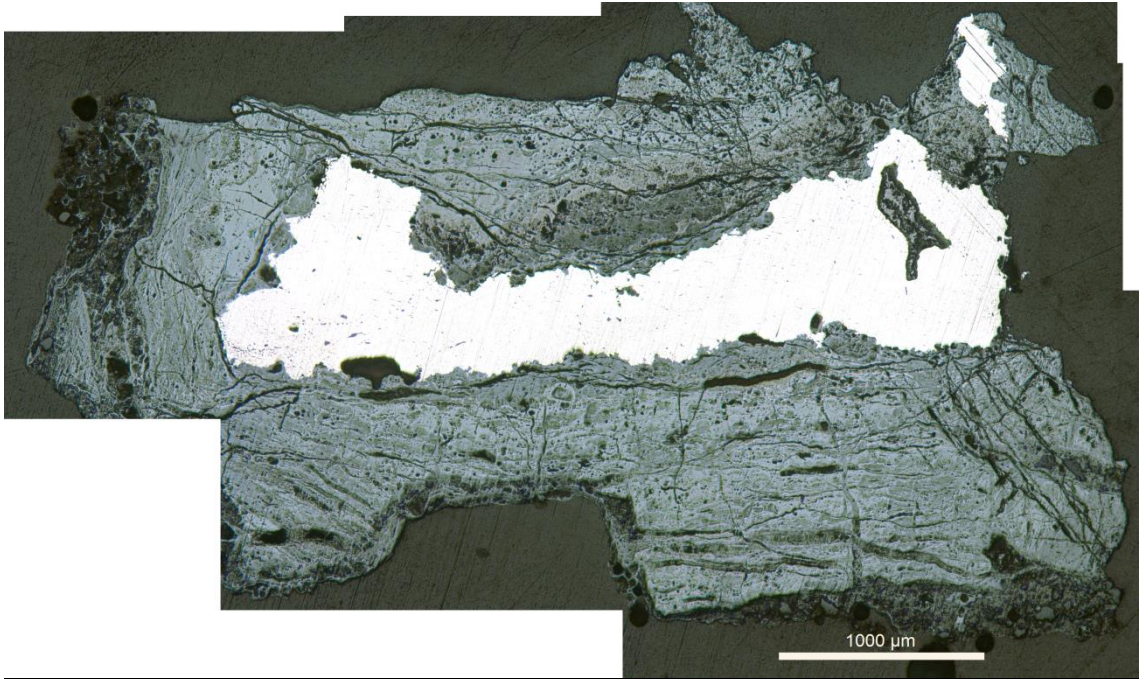


Figure 5.23 Composite digital photomicrograph of sample CAER_22 in polished cross-section at 50X magnification.

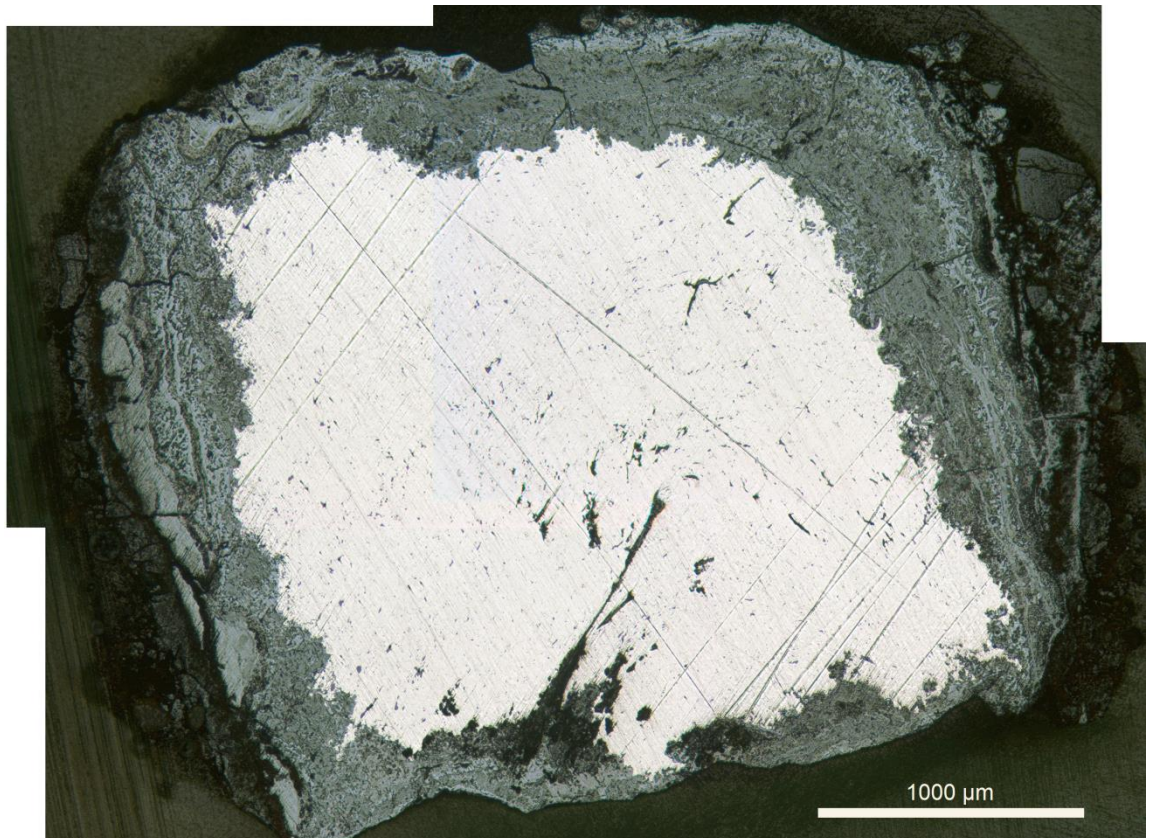


Figure 5.24 Composite digital photomicrograph of sample CAER_27 in polished cross-section at 50X magnification.

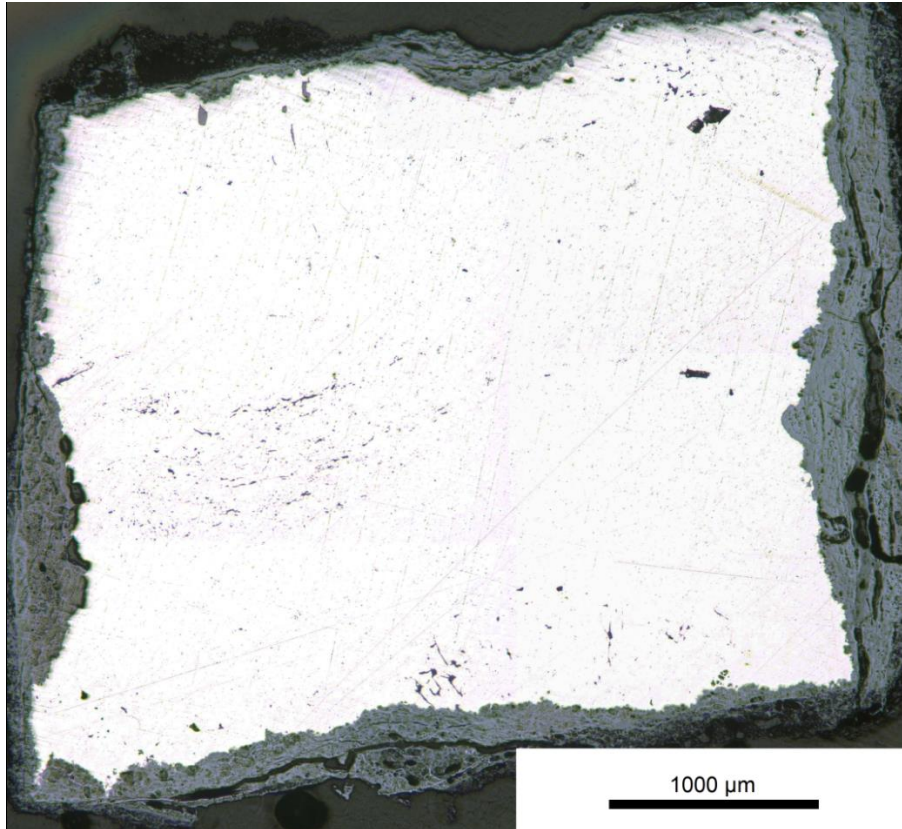


Figure 5.25 Composite digital photomicrograph of sample CW_05 in polished cross-section at 50X magnification.

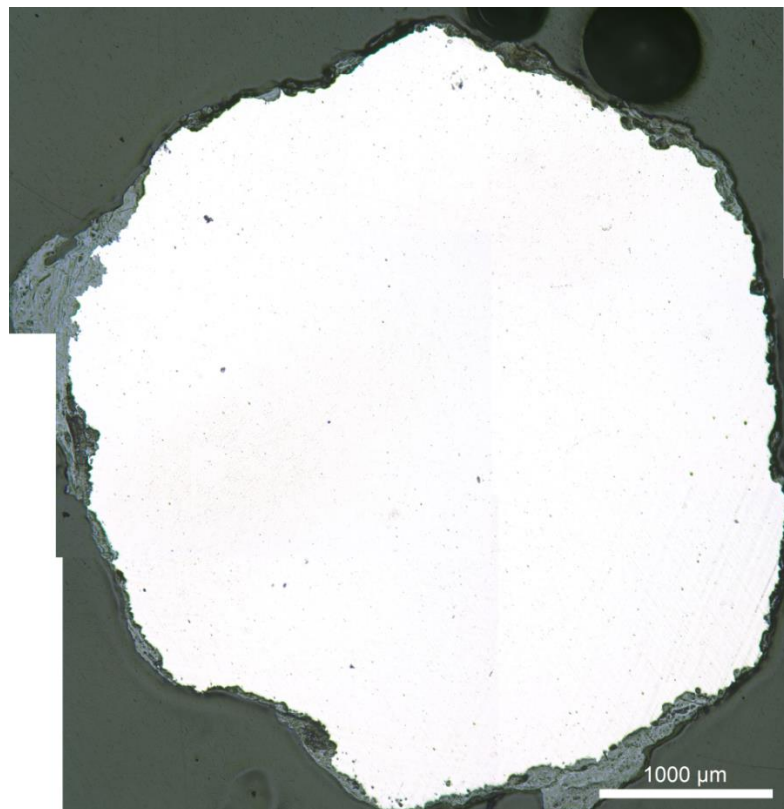


Figure 5.26 Composite digital photomicrograph of sample CW_07 in polished cross-section at 50X magnification.

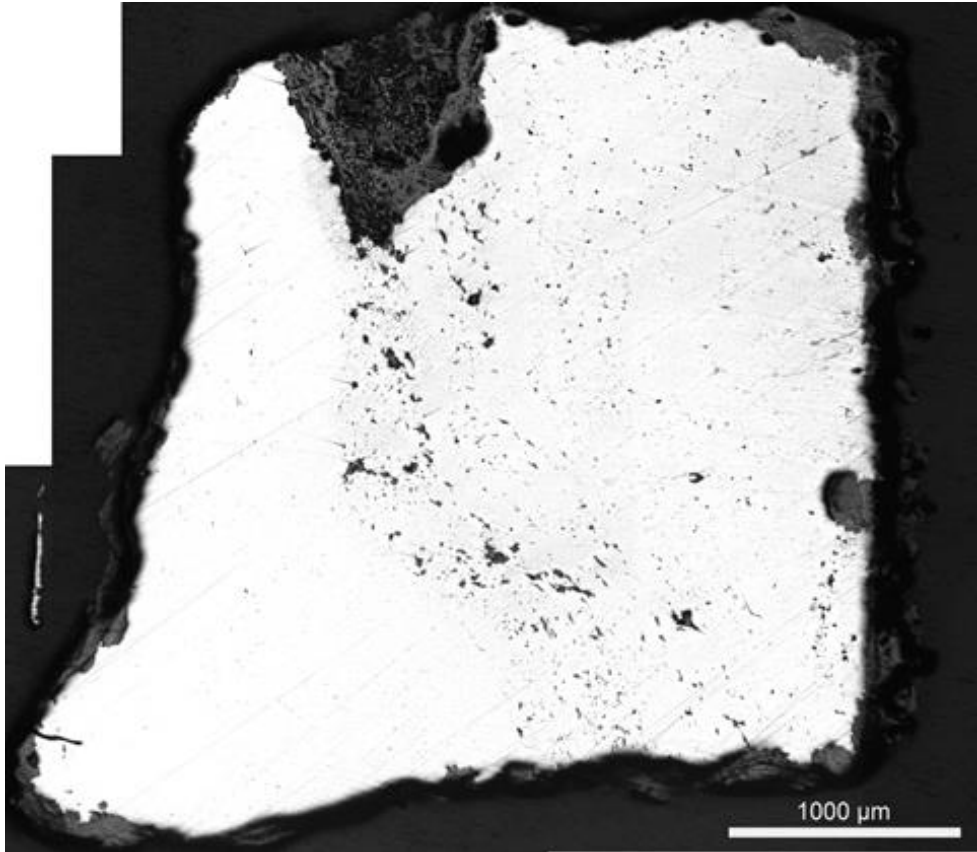


Figure 5.27 Composite digital photomicrograph of sample CW_08 in polished cross-section at 50X magnification.

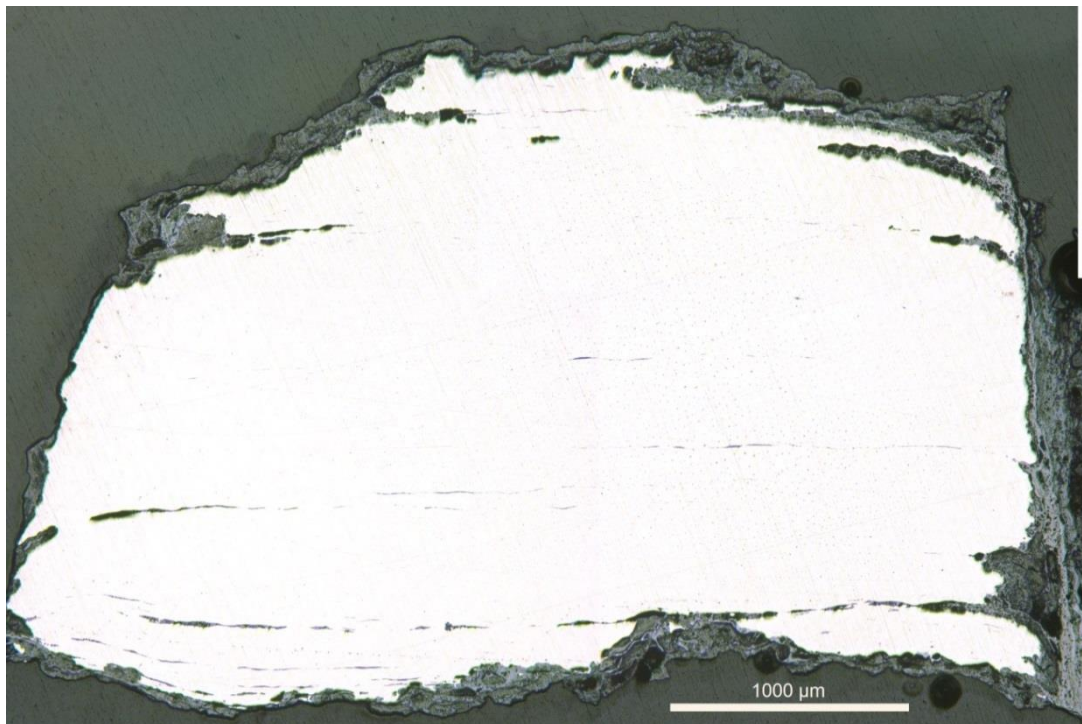


Figure 5.28 Composite digital photomicrograph of sample CW_09 in polished cross-section at 50X magnification.

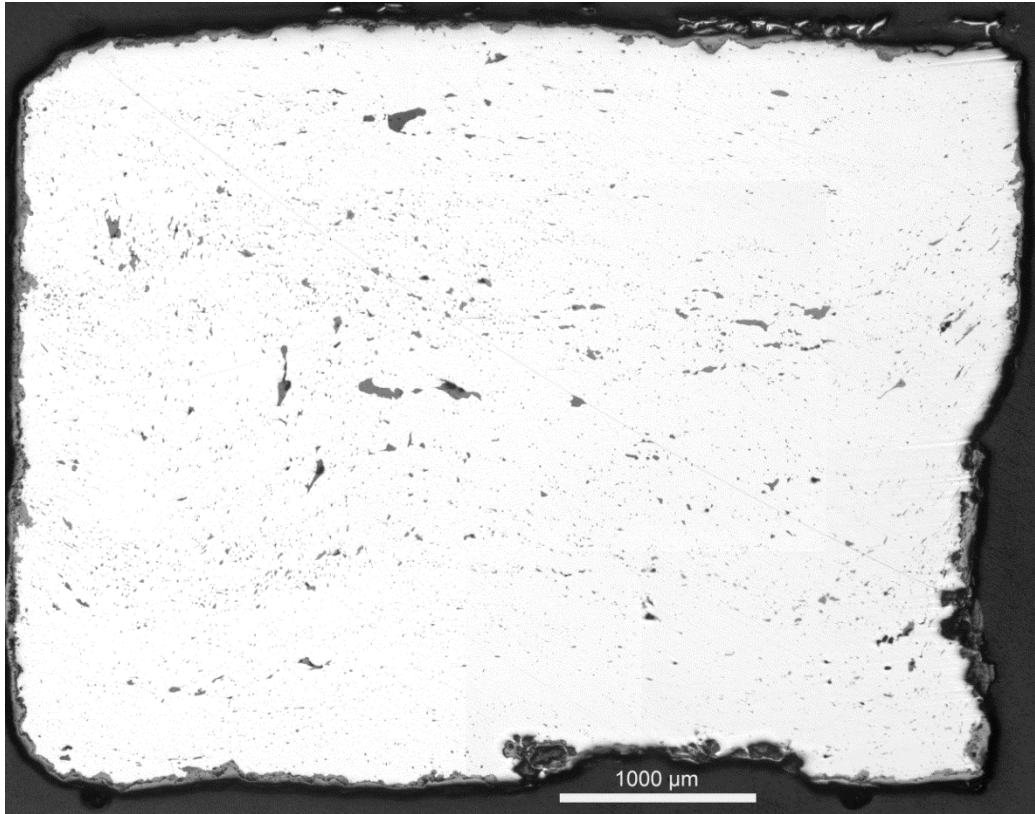


Figure 5.29 Composite digital photomicrograph of sample CW_14 in polished cross-section at 50X magnification.

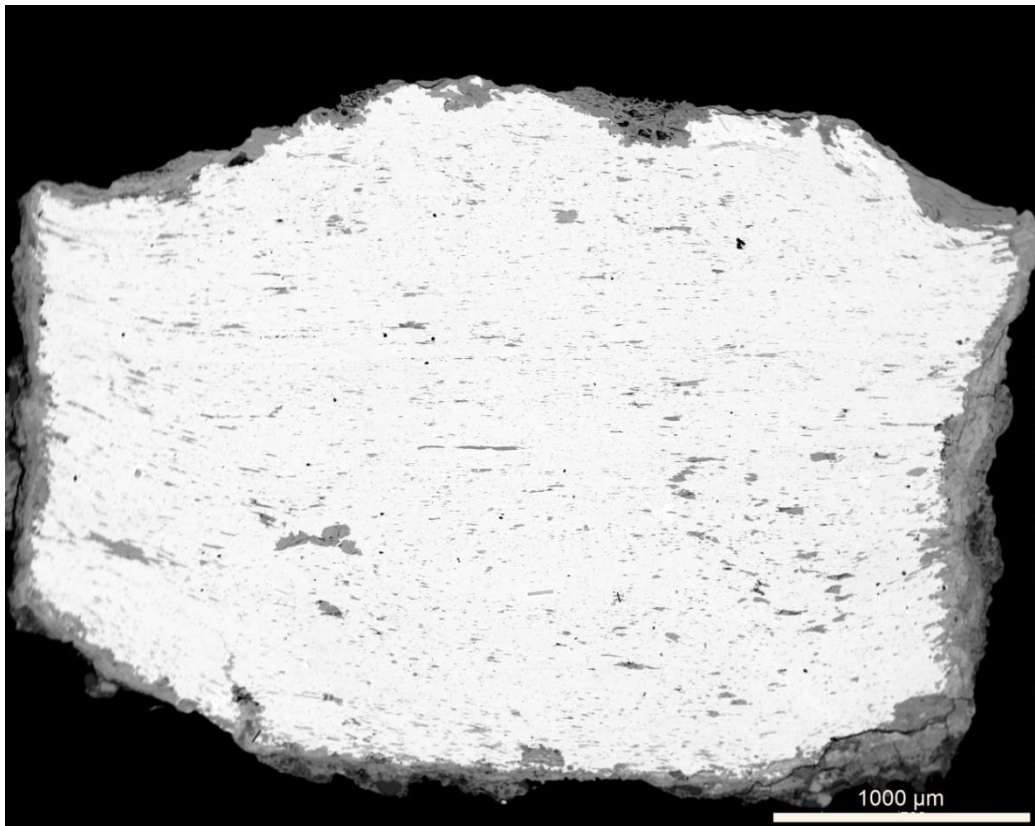


Figure 5.30 Composite digital photomicrograph of sample CW_15 in polished cross-section at 50X magnification.

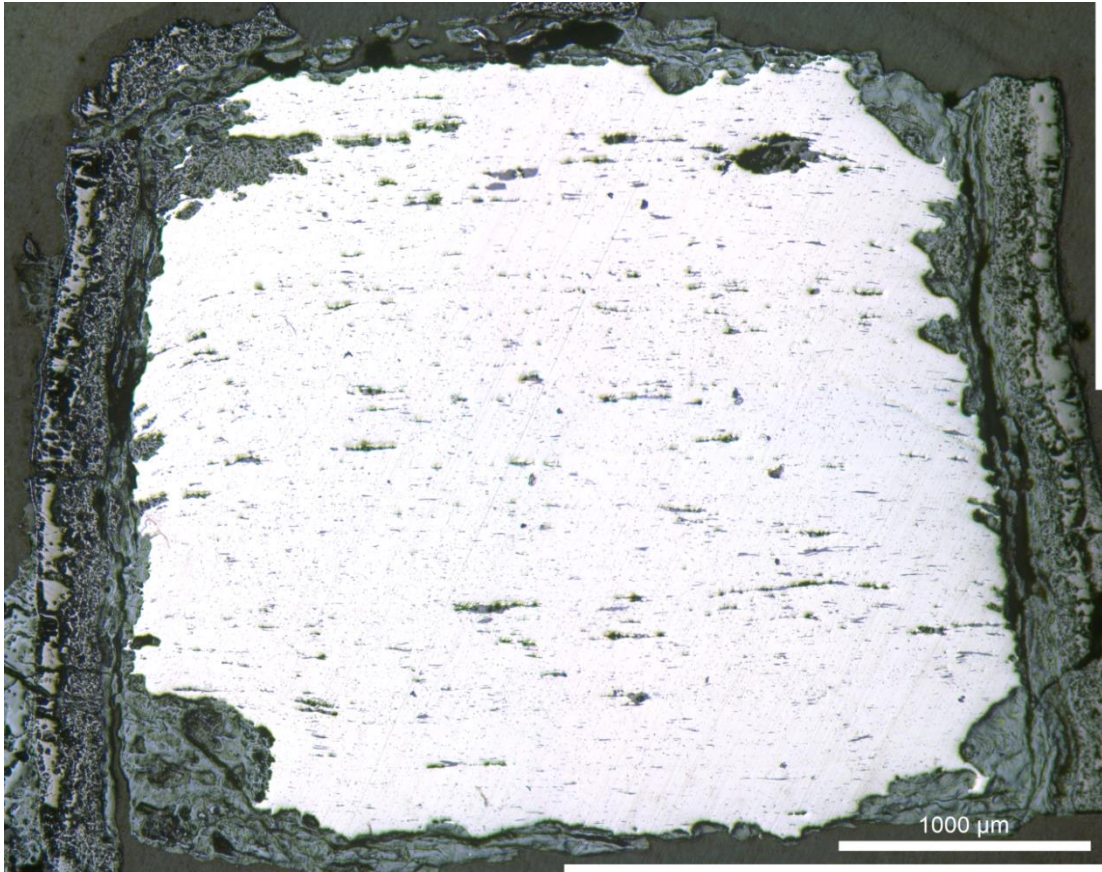


Figure 5.31 Composite digital photomicrograph of sample CW_16 in polished cross-section at 50X magnification.

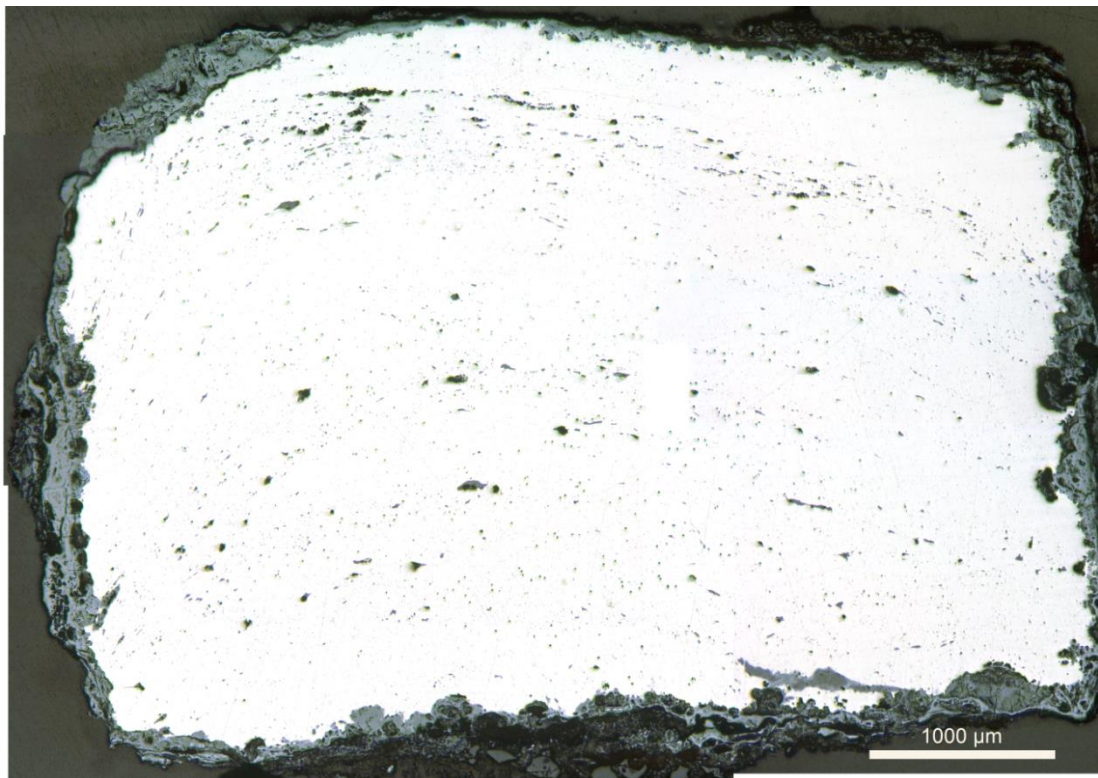


Figure 5.32 Composite digital photomicrograph of sample CW_19 in polished cross-section at 50X magnification.

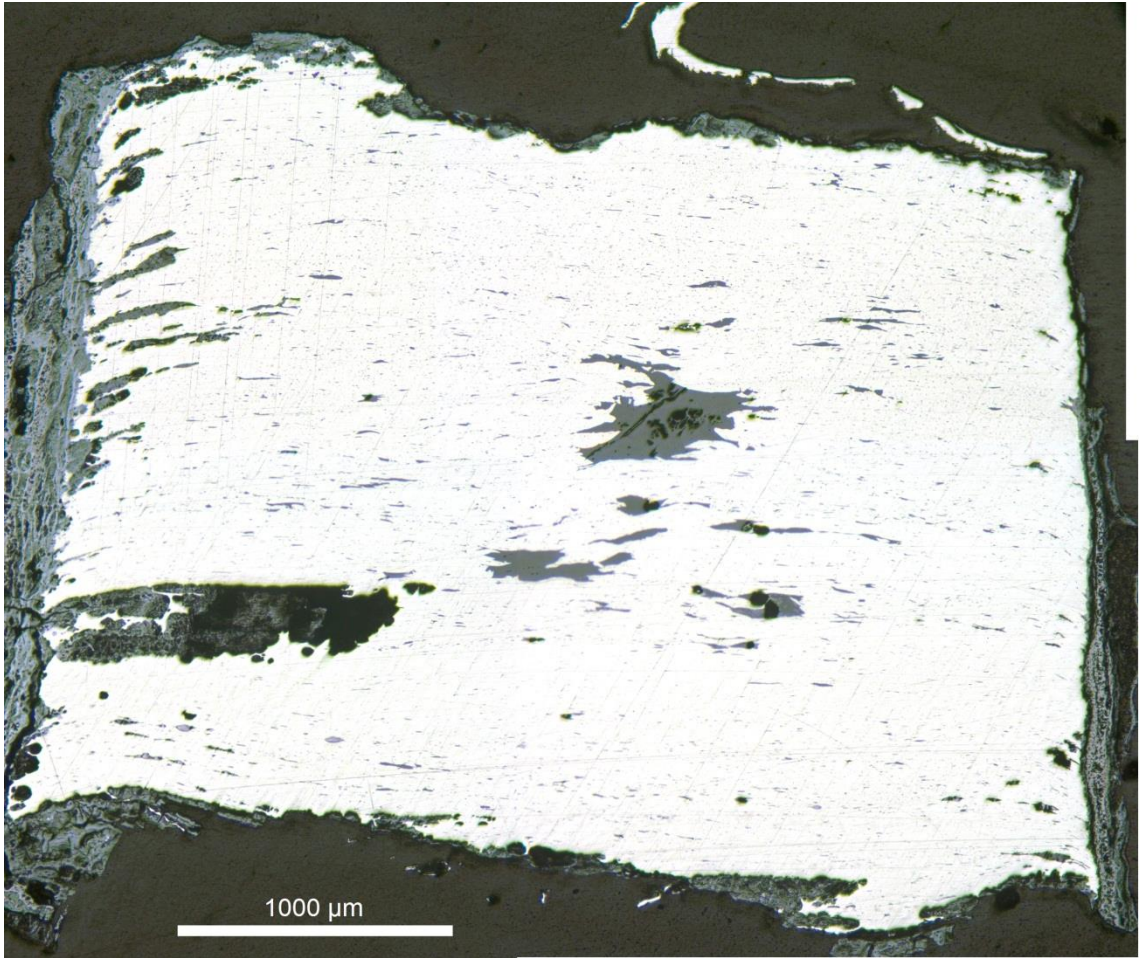


Figure 5.33 Composite digital photomicrograph of sample CW_26 in polished cross-section at 50X magnification.

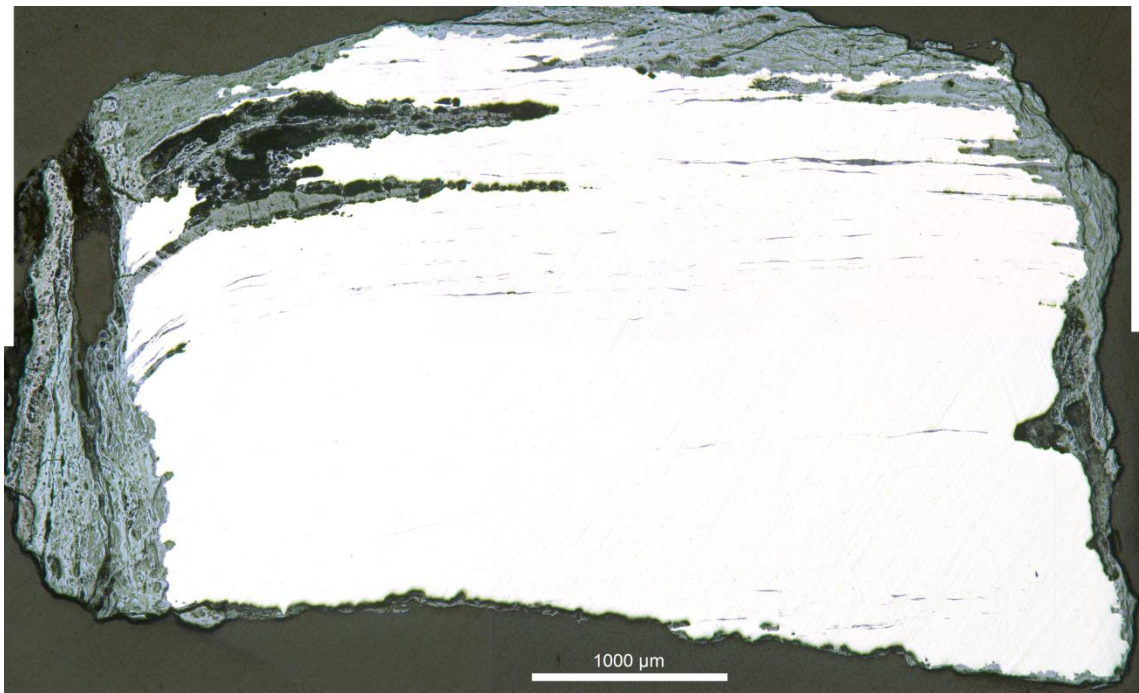


Figure 5.34 Composite digital photomicrograph of sample CW_29 in polished cross-section at 50X magnification.

Site of Origin/Statistic	Percent Area Slag at 50X
Caerleon	1.75
Shapiro-Wilk	.657 (p-value .00)
Skewness	2.45
Colonial Williamsburg	2.19
Shapiro-Wilk	.910 (p-value .28)
Skewness (CW)	.57

Table 5.7 Mean percent area slag as determined by computer image analysis of 10 sections of wrought iron nails each from Roman Caerleon and Colonial Williamsburg imaged at 50X by optical microscopy. Shapiro-Wilk test results and skewness values for each site are also given. The alpha value (significance threshold) is .05.

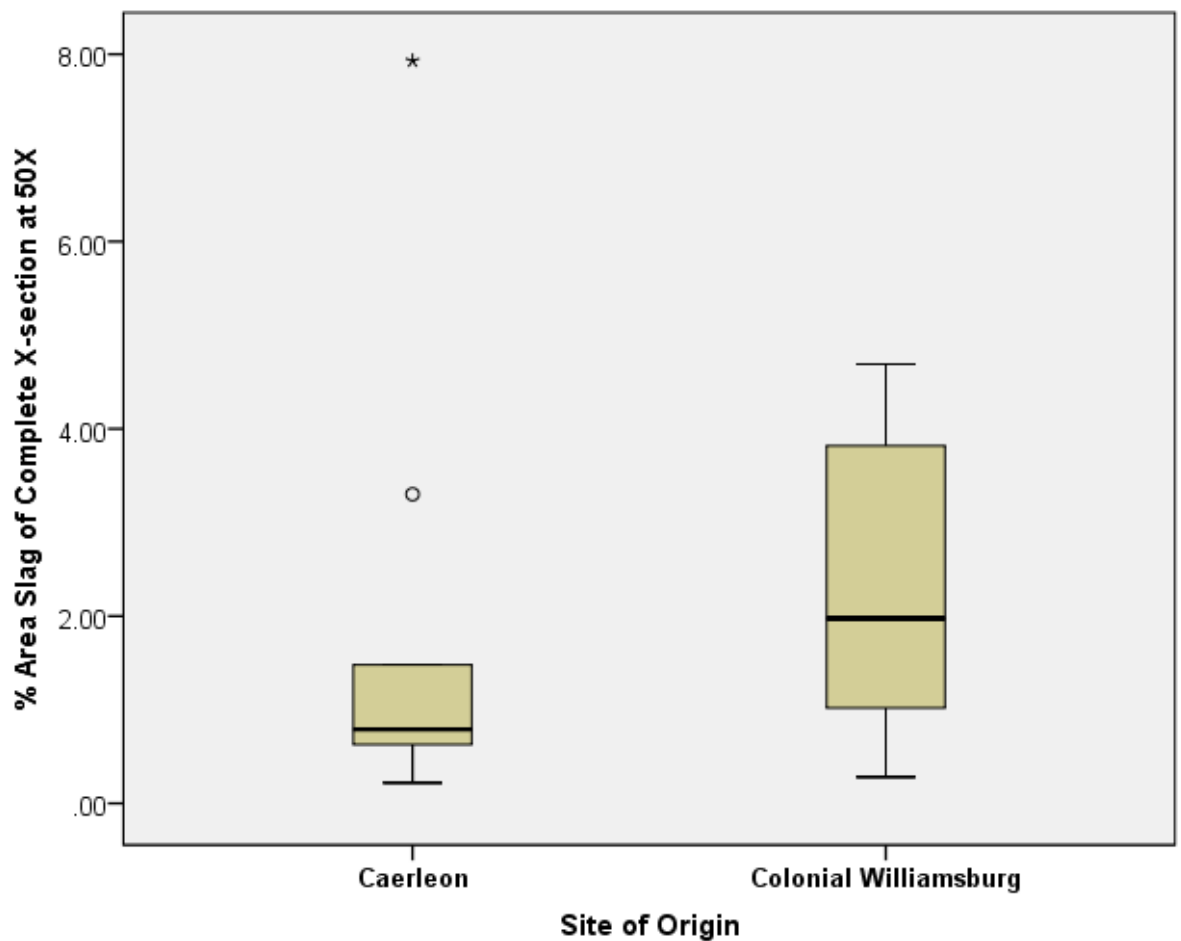


Figure 5.35 Boxplot of percent area slag values for 10 wrought iron nails each from Caerleon and Colonial Williamsburg measured at 50X magnification across the total area of the metal core. In this and following boxplots, outliers 1.5- 3 times the interquartile range above or below the quartile are shown by a circle, or greater than 3 times the inter-quartile range by a star (Field 2009).

5.2 Oxygen consumption rate

5.2.1 Untreated samples

Oxygen consumption (mbar) is recorded as a function of time to offer rate data (Figures 5.36-5.37). Figures 5.38 and 5.39 relate oxygen consumption per day to the mass of sample as mbar/day/gram for Caerleon and Colonial Williamsburg over 18 days as bar and boxplots. Figures 5.40-5.41 compare the mass of sample with oxygen consumption rate per day per gram for untreated samples from each of the two sites. Non-parametric tests of correlation (Spearman rho) are given in Table 5.8. There are no correlations between these factors significant at the .05 level or above.

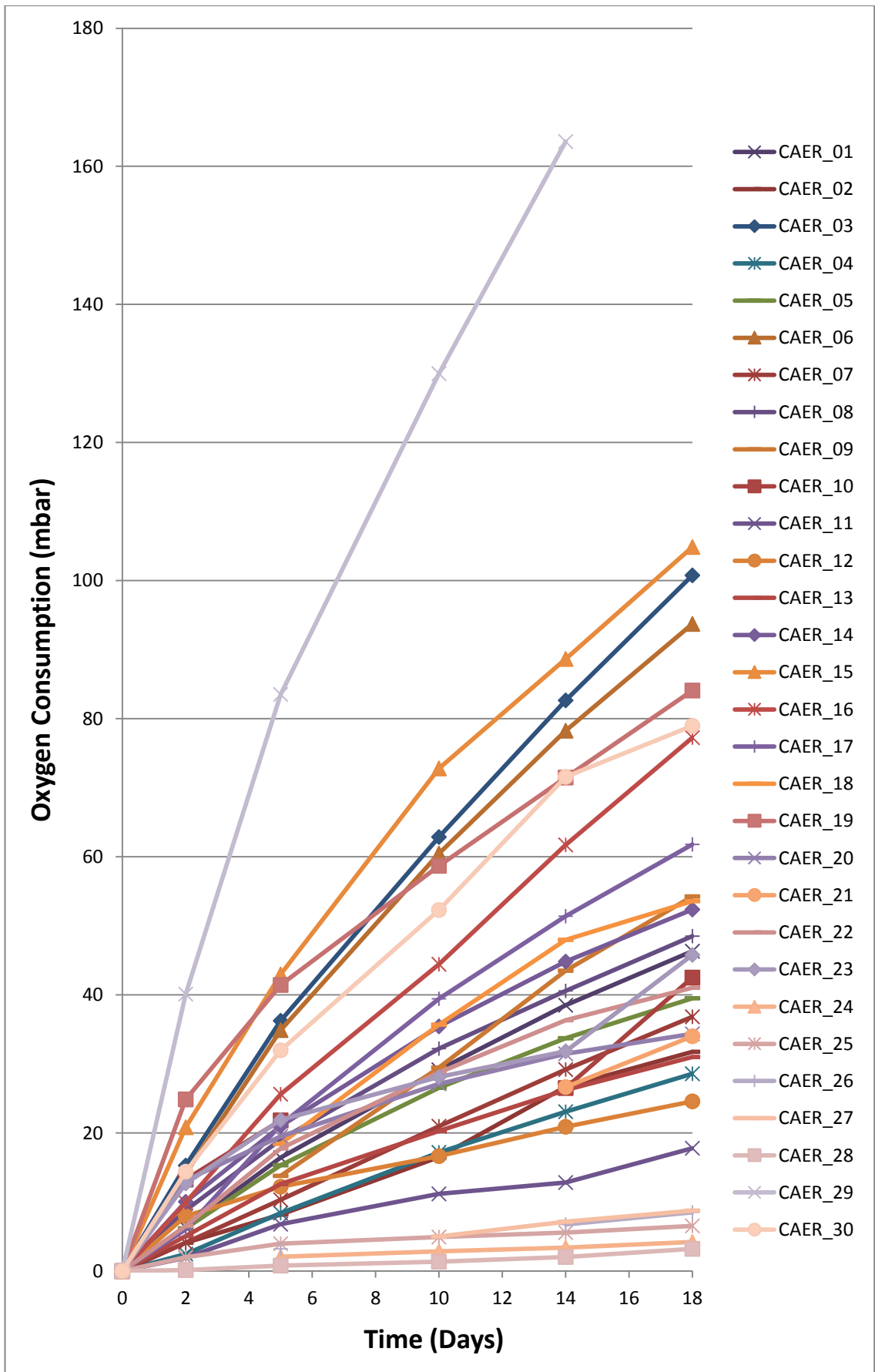


Figure 5.36 Oxygen consumption in millibars (+/- 2 mbar) of 30 untreated wrought iron nails within the first 18 days from the site of Roman Caerleon in conditions of 80% RH and 20°C.

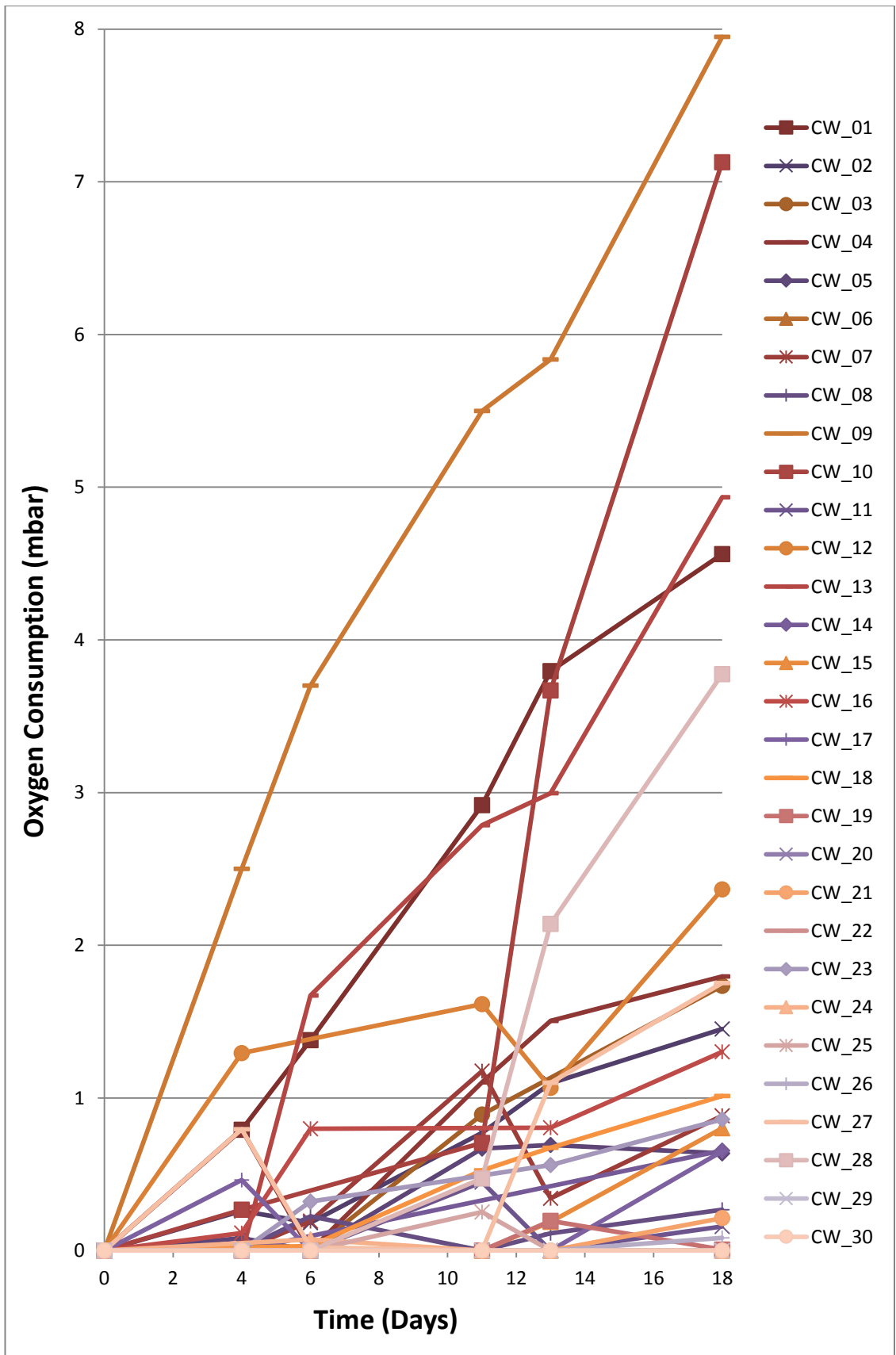


Figure 5.37 Oxygen consumption in millibars (+/- mbar) of 30 untreated wrought iron nails from the site of Colonial Williamsburg in conditions of 80% RH and 20°C.

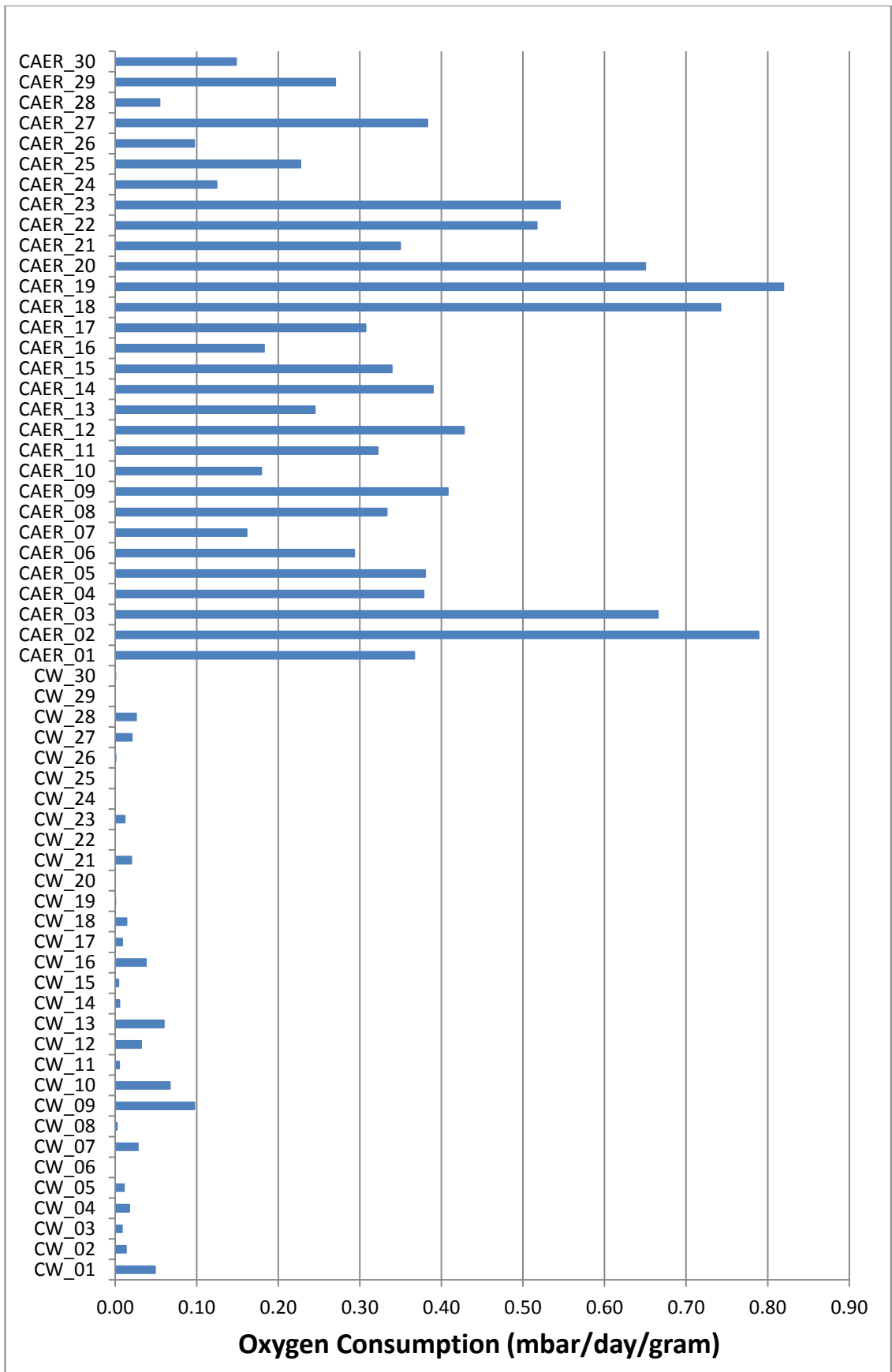


Figure 5.38 Comparison of oxygen consumption rate over 18 days in mbar/day/gram for untreated wrought iron nails from the sites of Caerleon and Colonial Williamsburg. Oxygen measurements subject to +/- 2 mbar error.

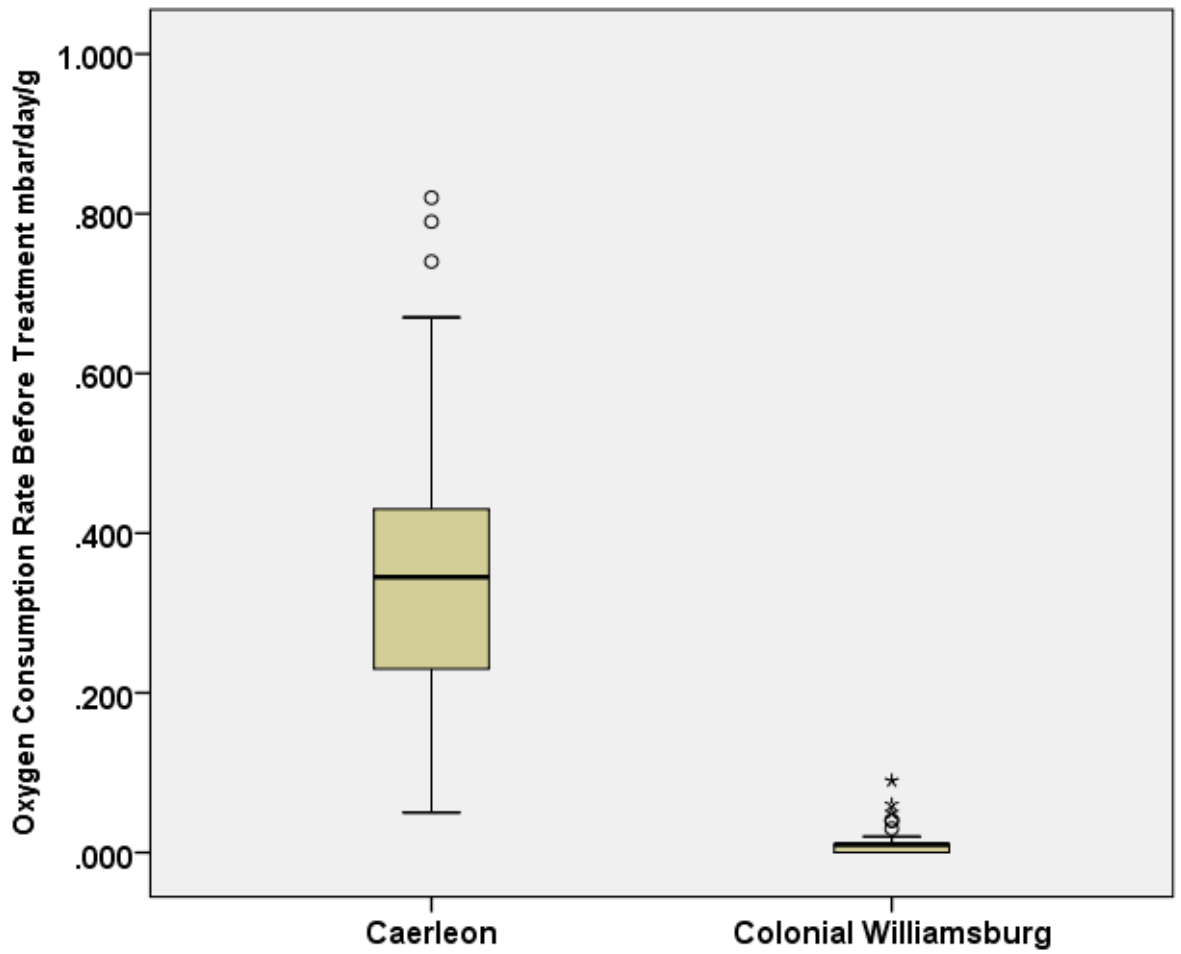


Figure 5.39 Boxplot of oxygen consumption rate in mbar/day/gram for untreated wrought iron nails over 18 days for the sites of Roman Caerleon and Colonial Williamsburg.

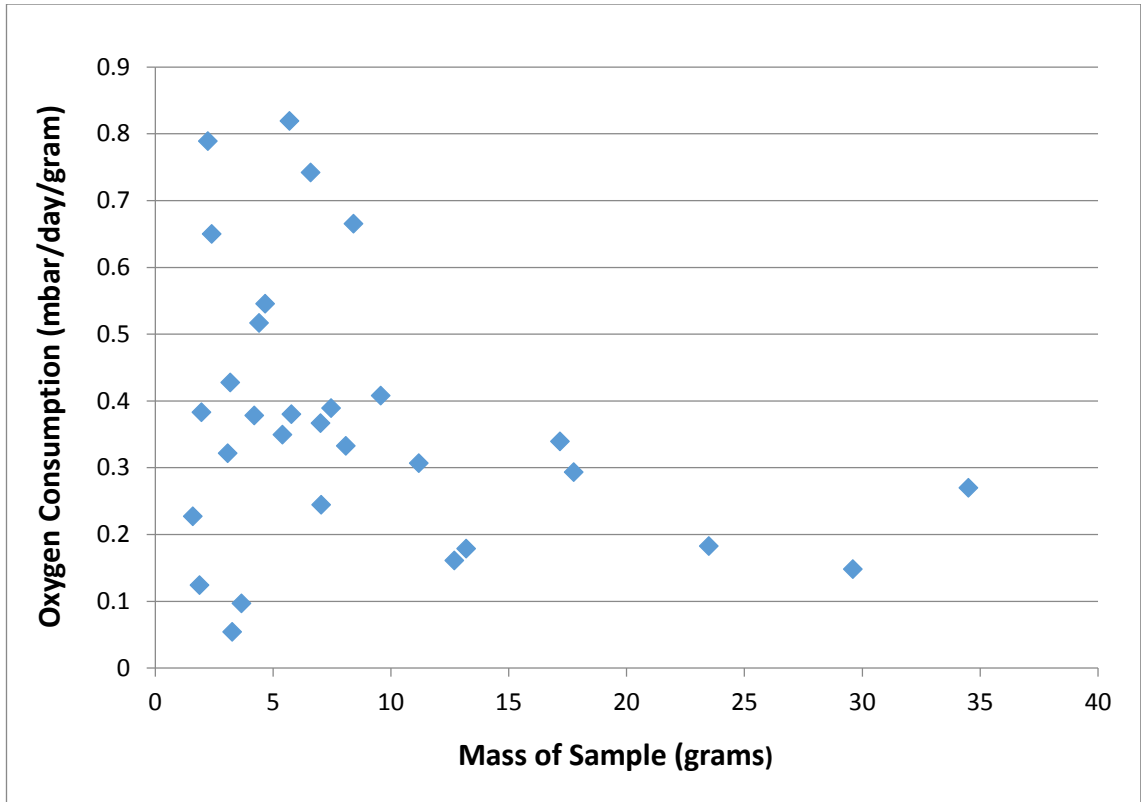


Figure 5.40 Oxygen consumption as a function of mass of sample over 18 days for 30 untreated samples from Caerleon.

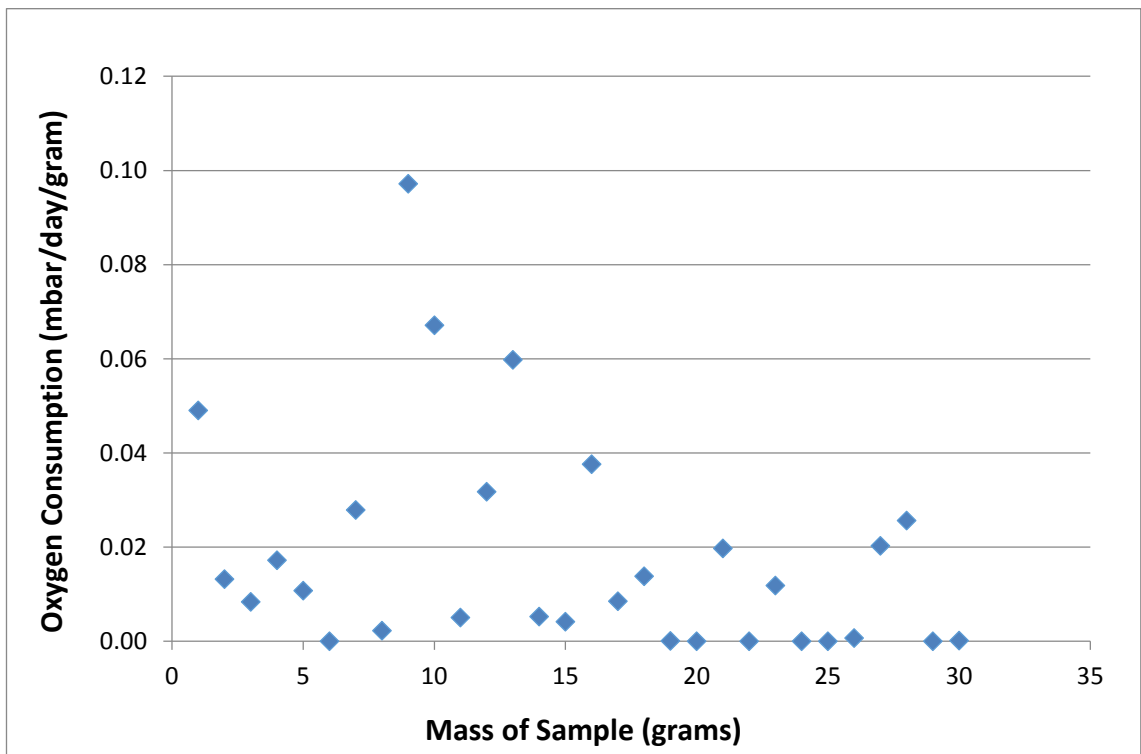


Figure 5.41 Oxygen consumption as a function of mass of sample over 18 days for 30 untreated samples from Colonial Williamsburg.

Variables	Number of Samples	Test	Correlation Coefficient	Significance	Significance Level
Mass of Sample/O ₂ Consumption/day/gram of sample (Untreated)	30 (Caerleon)	Spearman rho	-.216	.251	N/S
Mass of Sample/O ₂ Consumption/day/gram of sample (Untreated)	30 (Colonial Williamsburg)	Spearman rho	-.130	.493	N/S

Table 5.8 Non-parametric tests of correlation (Spearman rho) for mass of sample and oxygen consumption/day/gram of sample for 30 untreated nails each for Caerleon and Colonial Williamsburg, including correlation coefficient, significance and significance level. N/S (not significant) indicates that the correlation is not significant at the .05 level or above.

5.2.2 Samples treated by alkaline sulphite washing at 60° C

Following oxygen consumption measurement of the untreated wrought iron nails, they were desalinated by alkaline sodium sulphite washing (0.1M NaOH/0.05M Na₂SO₃) according to the method described in 4.7.5. Oxygen consumption results for the rinsed (R) and unrinsed (NR) samples for each site are plotted in Figures 5.42-5.49. A comparison of oxygen consumption after treatment by site is given in Figure 5.50. Figure 5.51 plots post-treatment oxygen consumption by site and rinsing protocol.

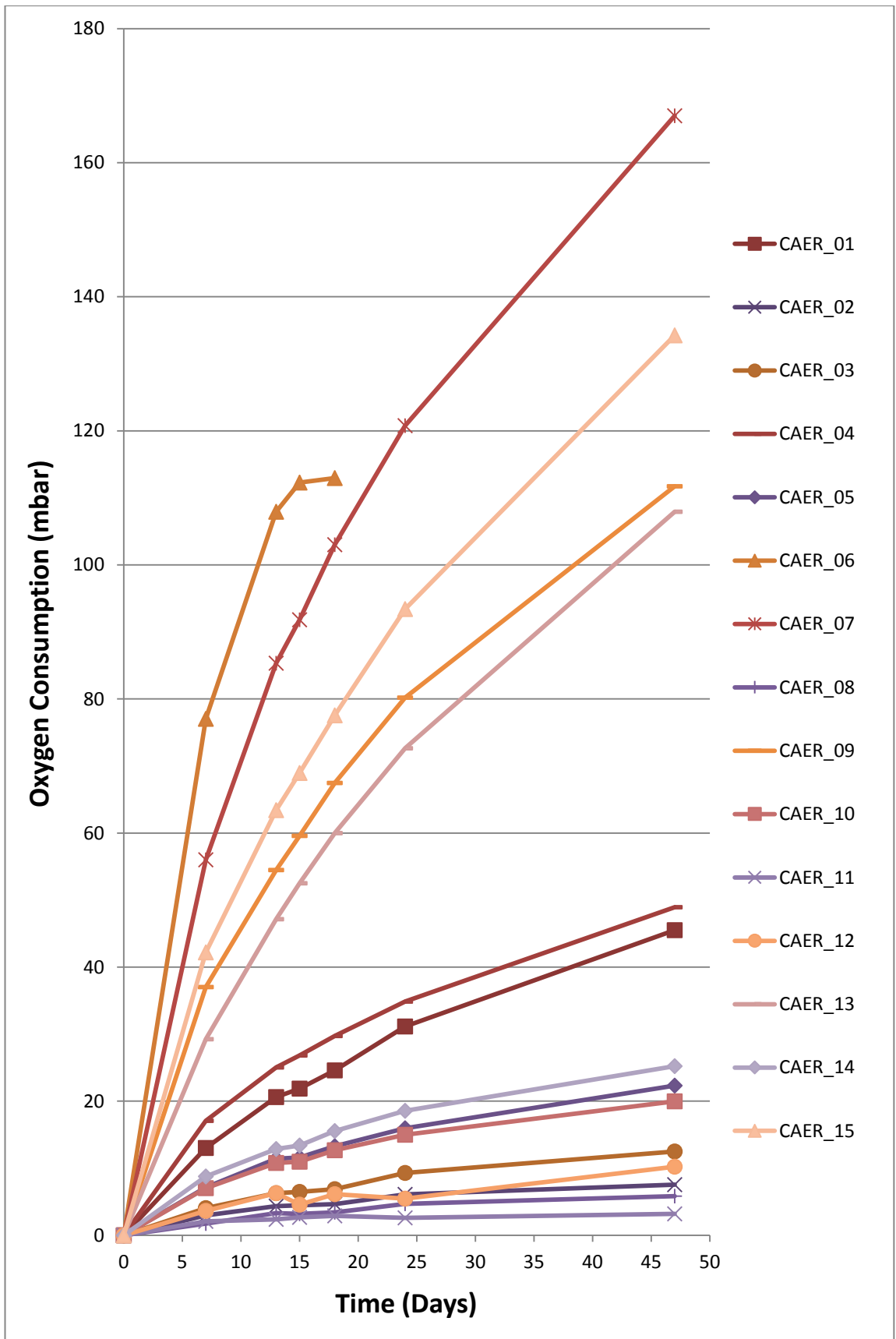


Figure 5.42 Oxygen consumption in millibars (+/-2 mbar) of 15 wrought iron nails from the site of Roman Caerleon treated by alkaline sulphite washing at 60°C and rinsed in deionised water to pH 7. Oxygen consumption measured in conditions of 80% RH and 20°C. Measurement stopped for sample CAER_06 after 18 days as all oxygen had been consumed.

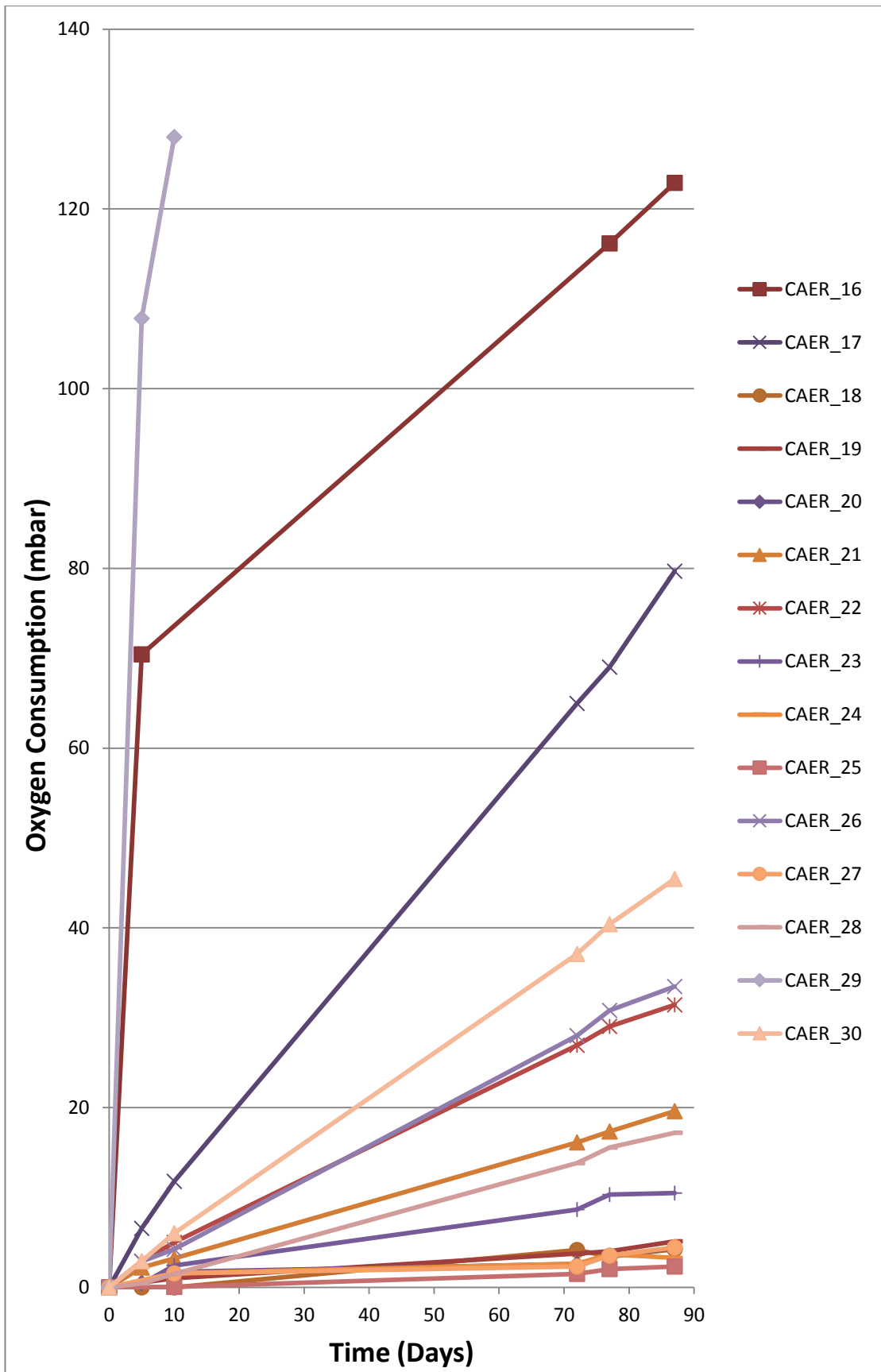


Figure 5.43 Oxygen consumption in millibars (+/- 2 mbar) of 15 wrought iron nails from the site of Roman Caerleon treated by alkaline sulphite washing at 60°C and left unrinsed following treatment. Oxygen consumption measured in conditions of 80% RH and 20°C.

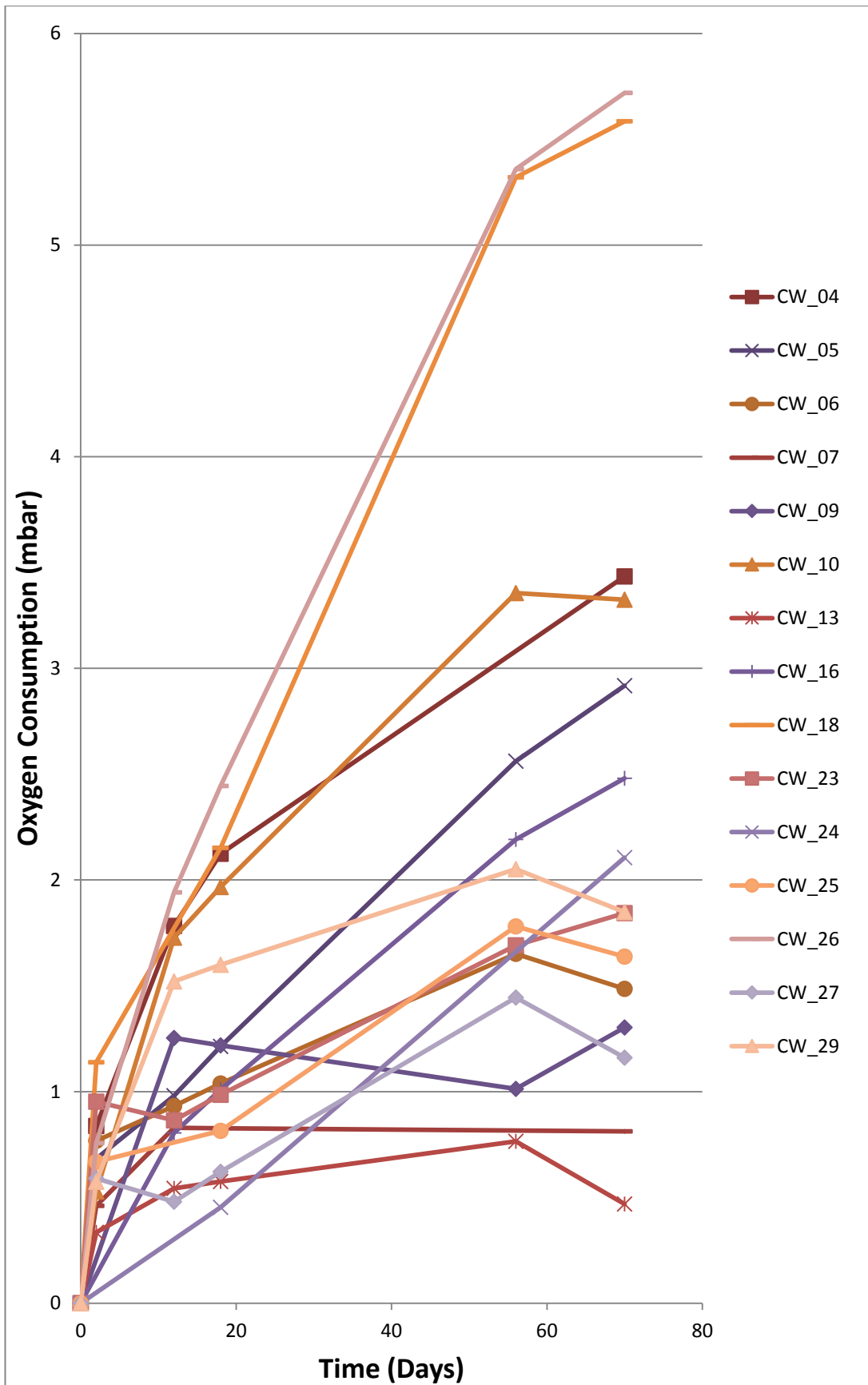


Figure 5.44 Oxygen consumption in millibars (+/-2 mbar) of 15 wrought iron nails from the site of Colonial Williamsburg treated by alkaline sulphite washing at 60°C and rinsed in deionised water to pH 7. Oxygen consumption measured in conditions of 80% RH and 20°C

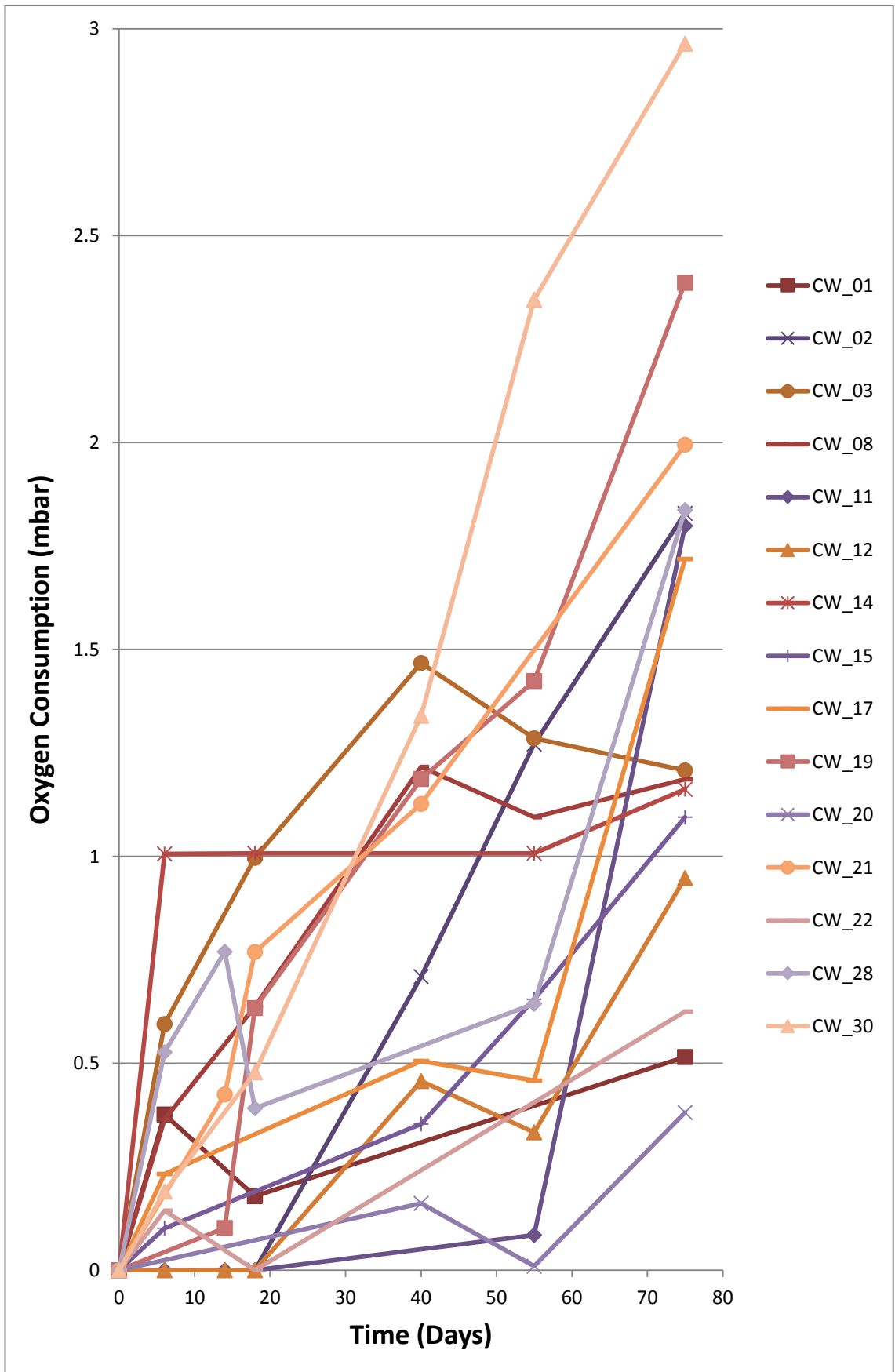


Figure 5.45 Oxygen consumption in millibars (+/-2 mbar) of 15 wrought iron nails from the site of Colonial Williamsburg treated by alkaline sulphite washing at 60°C and not rinsed following treatment. Oxygen consumption measured in conditions of 80% RH and 20°C

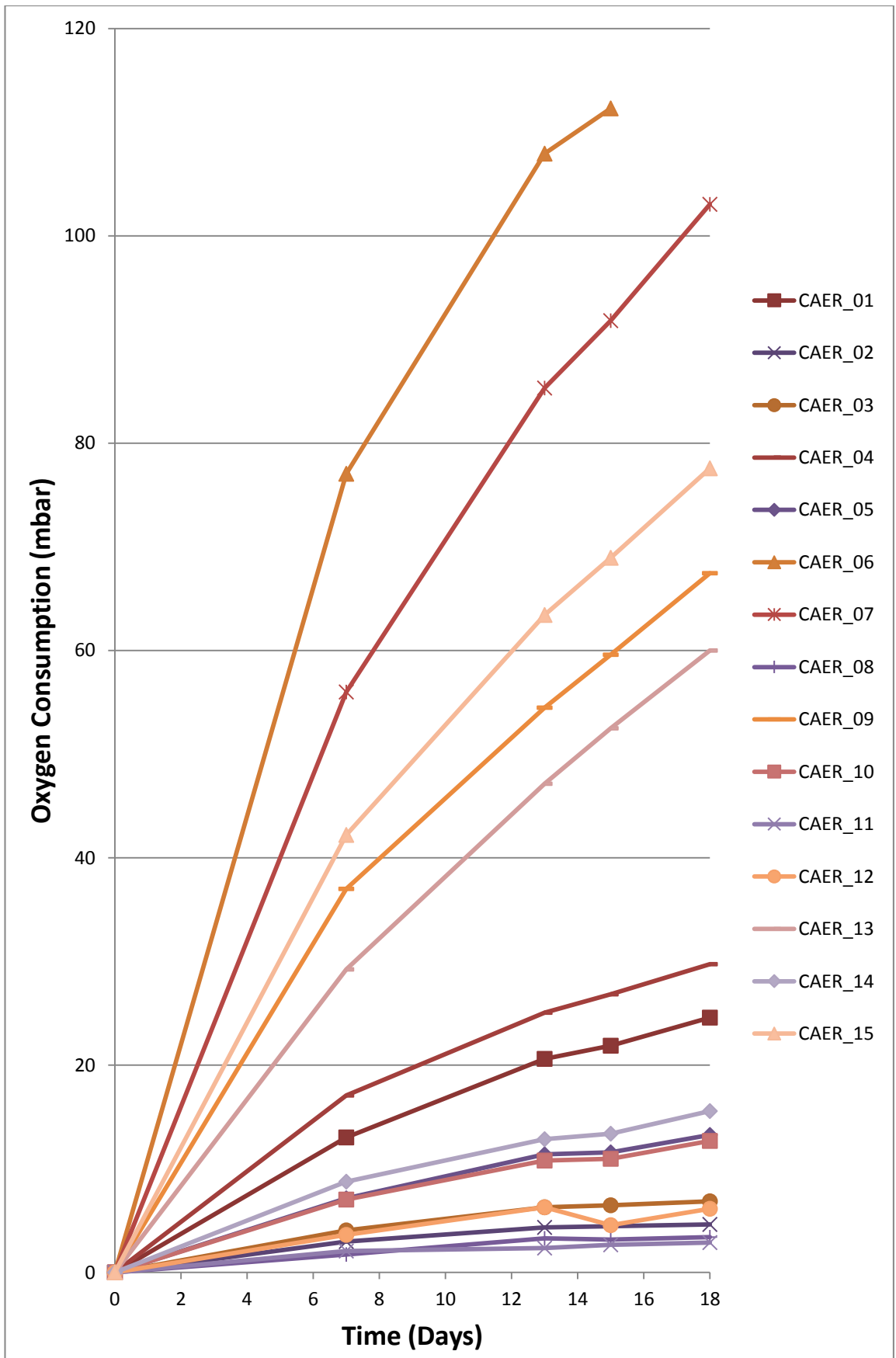


Figure 5.46 Oxygen consumption in millibars (+/-2 mbar) of 15 wrought iron nails from the site of Roman Caerleon treated by alkaline sulphite washing at 60°C and rinsed in deionised water to pH 7. Oxygen consumption measured in conditions of 80% RH and 20°C.

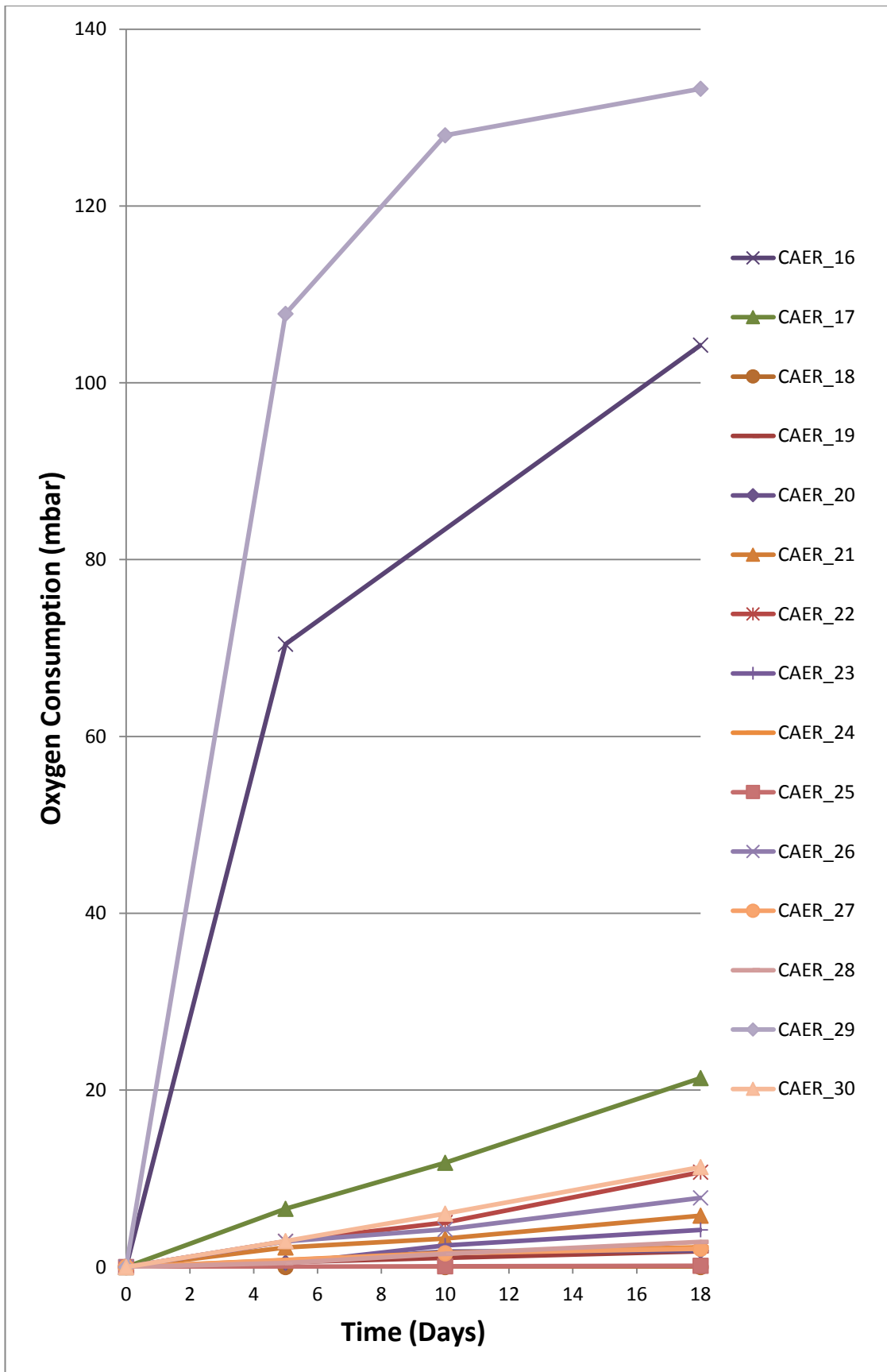


Figure 5.47 Oxygen consumption in millibars (+/-2 mbar) of 15 wrought iron nails from the site of Roman Caerleon treated by alkaline sulphite washing at 60°C and left unrinsed after treatment. Oxygen consumption measured in conditions of 80% RH and 20°C.

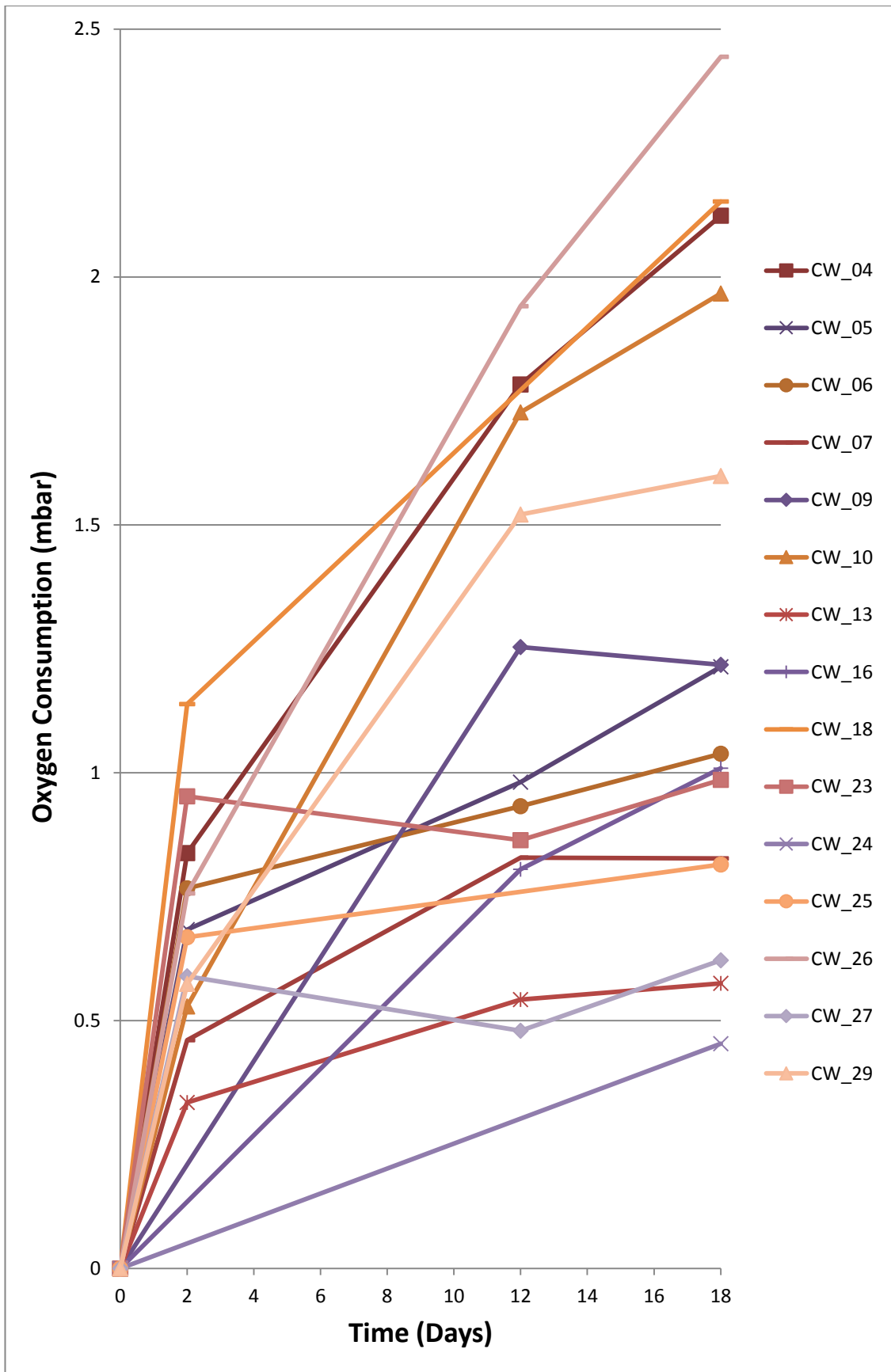


Figure 5.48 Oxygen consumption in millibars (+/-2 mbar) of 15 wrought iron nails from the site of Colonial Williamsburg treated by alkaline sulphite washing at 60°C and rinsed in deionised water to pH 7. Oxygen consumption measured in conditions of 80% RH and 20°C.

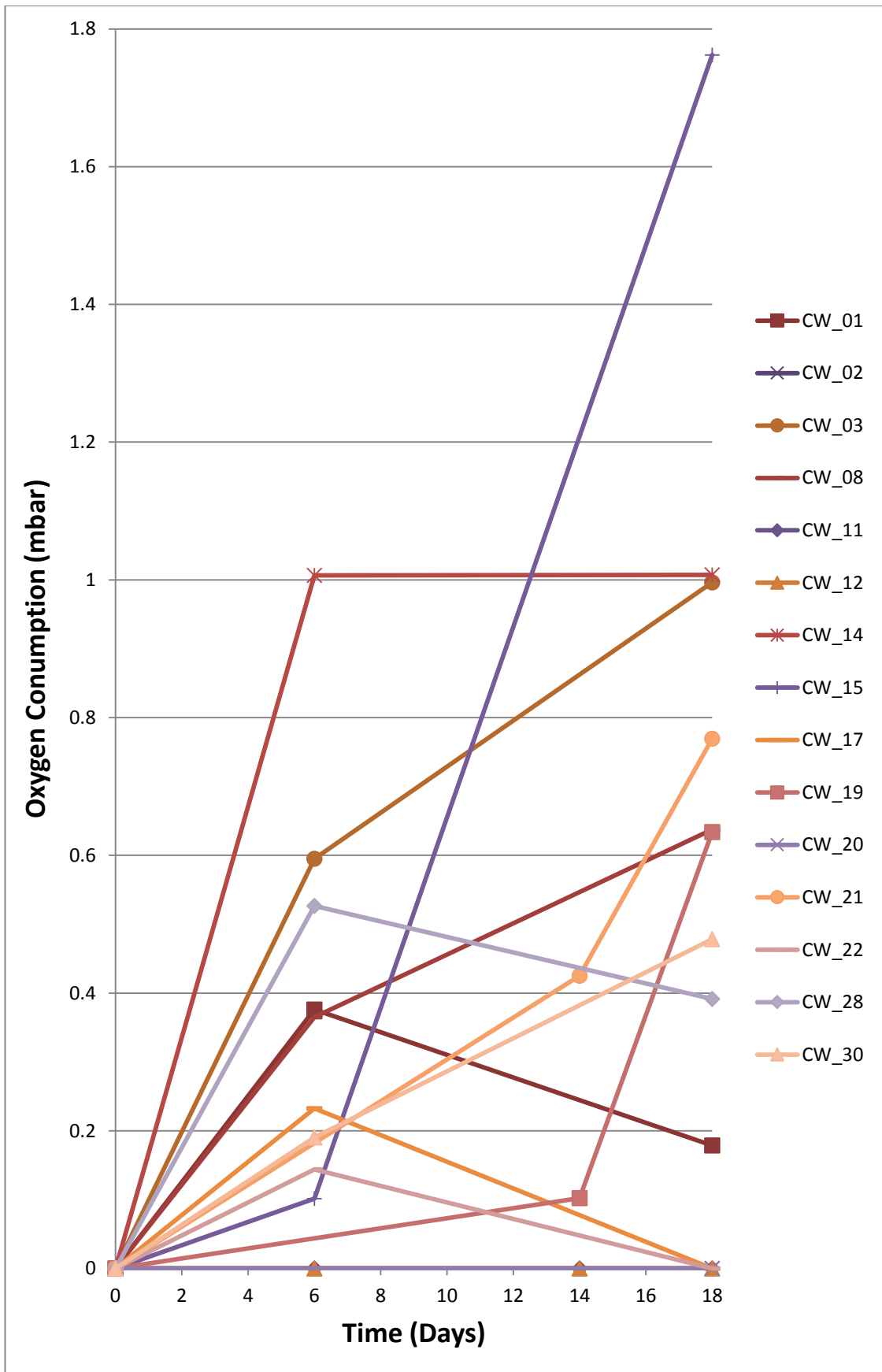


Figure 5.49 Oxygen consumption in millibars (+/- 2 mbar) of 15 wrought iron nails from the site of Colonial Williamsburg treated by alkaline sulphite washing at 60°C and left unrinsed after treatment. Oxygen consumption measured in conditions of 80% RH and 20°C.

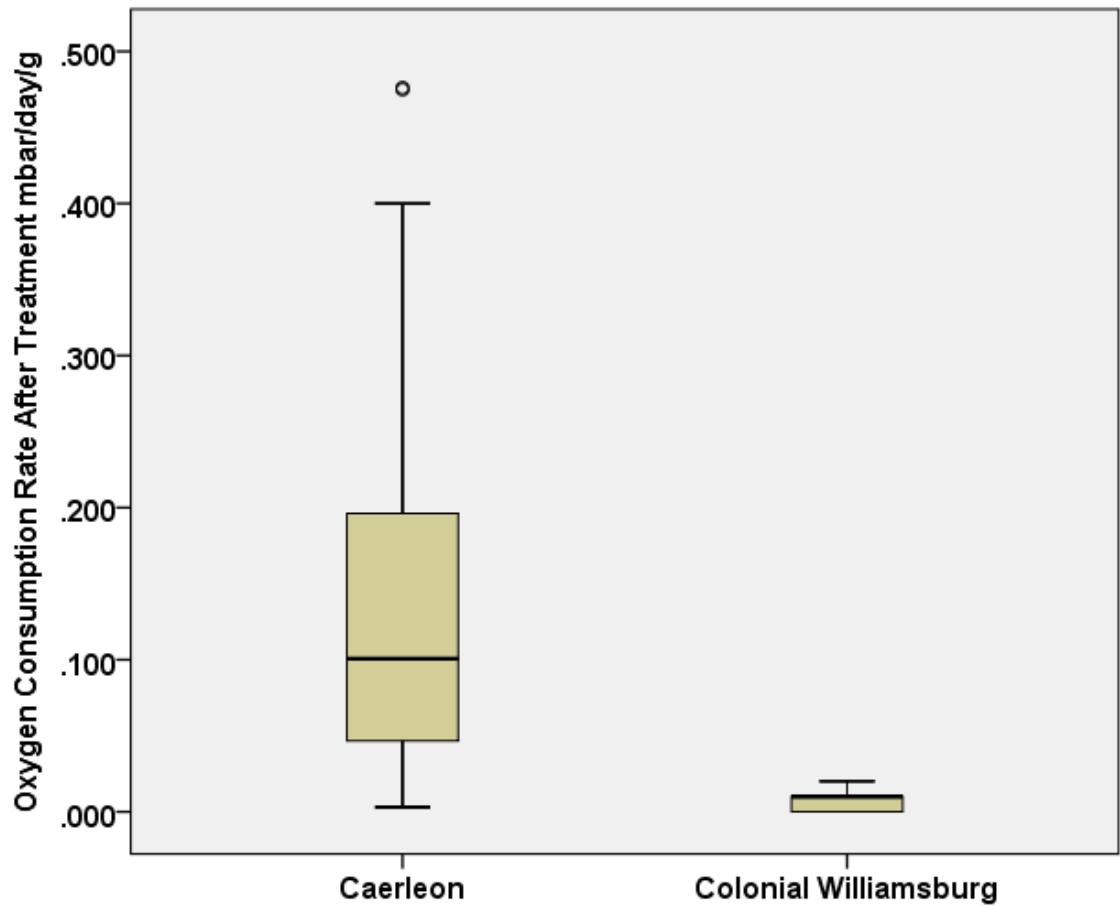


Figure 5.50 Boxplot of oxygen consumption rate over 18 days for wrought iron nails for the sites of Roman Caerleon and Colonial Williamsburg treated by alkaline sulphite washing at 60°C. All samples, both rinsed and un-rinsed, are plotted.

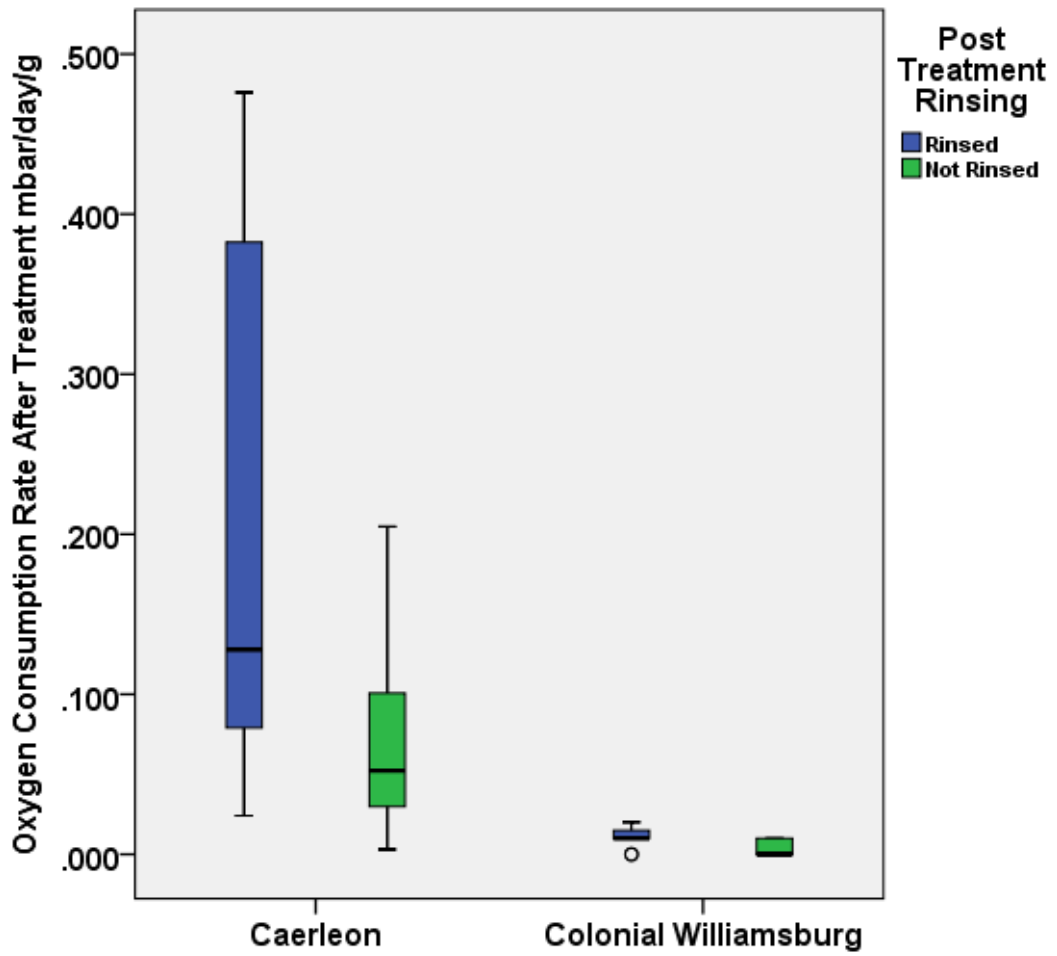


Figure 5.51 Boxplot of oxygen consumption rate over 18 days for wrought iron nails for the sites of Roman Caerleon and Colonial Williamsburg treated by alkaline sulphite washing at 60°C. Samples rinsed after treatment (Blue) and Not Rinsed (Green) are plotted separately for both sites.

5.2.3 Change in oxygen consumption rate

Comparing oxygen consumption rate of untreated and treated samples following both rinsed and unrinsed post treatment protocols shows differences between untreated and treated samples and also between rinsed and unrinsed samples (Figures 5.52-5.55). Figures 5.56 and 5.57 record the effect of rinsing by comparing the post-treatment oxygen consumption of rinsed and unrinsed samples from Caerleon and Colonial Williamsburg respectively. Mean oxygen consumption values for nails from each site, before and after treatment with and without rinsing, are given in Table 5.9.

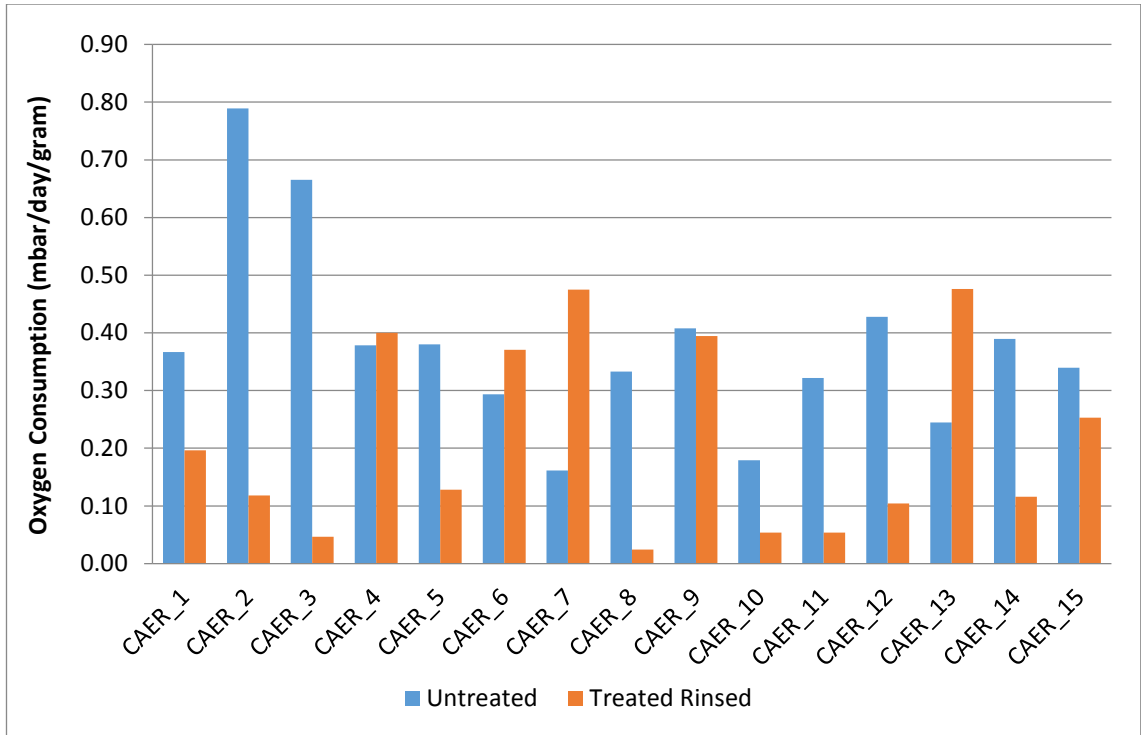


Figure 5.52 Oxygen consumption rate of 15 wrought iron nails from Caerleon in untreated, and treated rinsed state and conditions of 80% RH and 20°C. Rates reflect consumption within the first 18 days of oxygen measurement, subject to oxygen consumption measurement error of +/- 2 mbar.

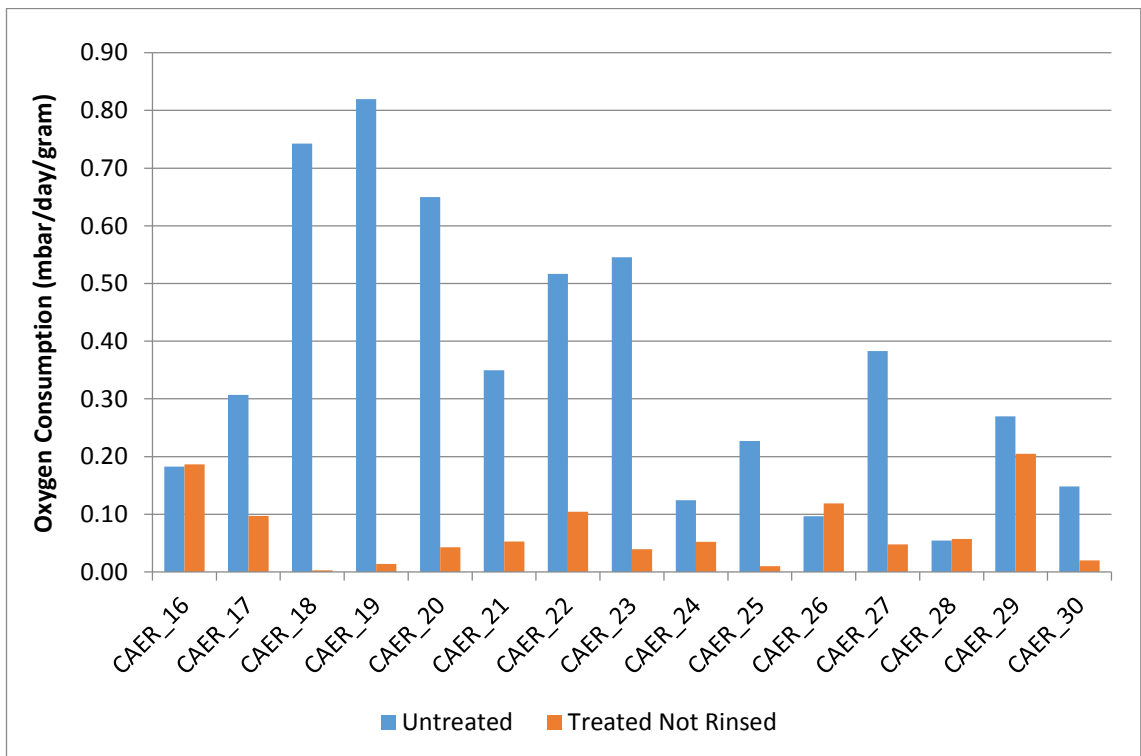


Figure 5.53 Oxygen consumption rate of 15 wrought iron nails from Caerleon in untreated, and Treated un rinsed state and conditions of 80% RH and 20°C. Rates reflect consumption within the first 18 days of oxygen measurement, subject to oxygen consumption measurement error of +/- 2 mbar.

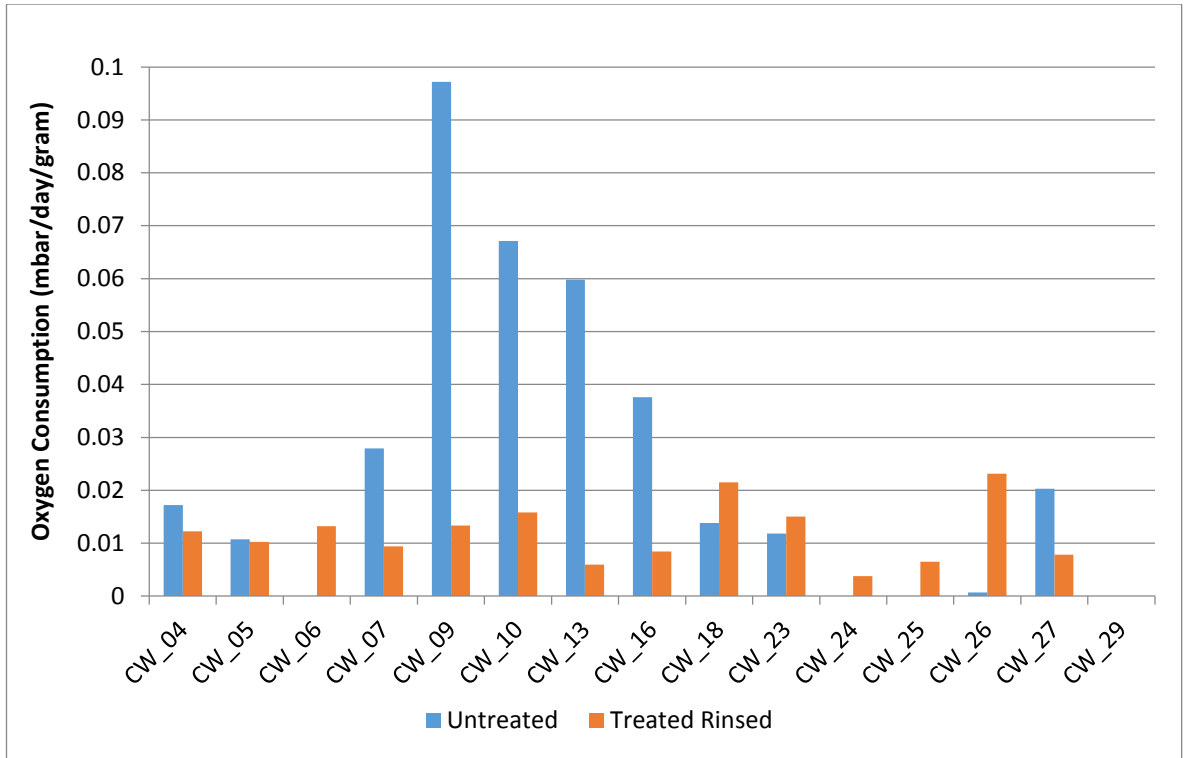


Figure 5.54 Oxygen consumption rate of 15 wrought iron nails from Colonial Williamsburg in untreated, and treated rinsed state and conditions of 80% RH and 20°C. Rates reflect consumption within the first 18 days of oxygen measurement, subject to oxygen consumption measurement error of +/-2 mbar.

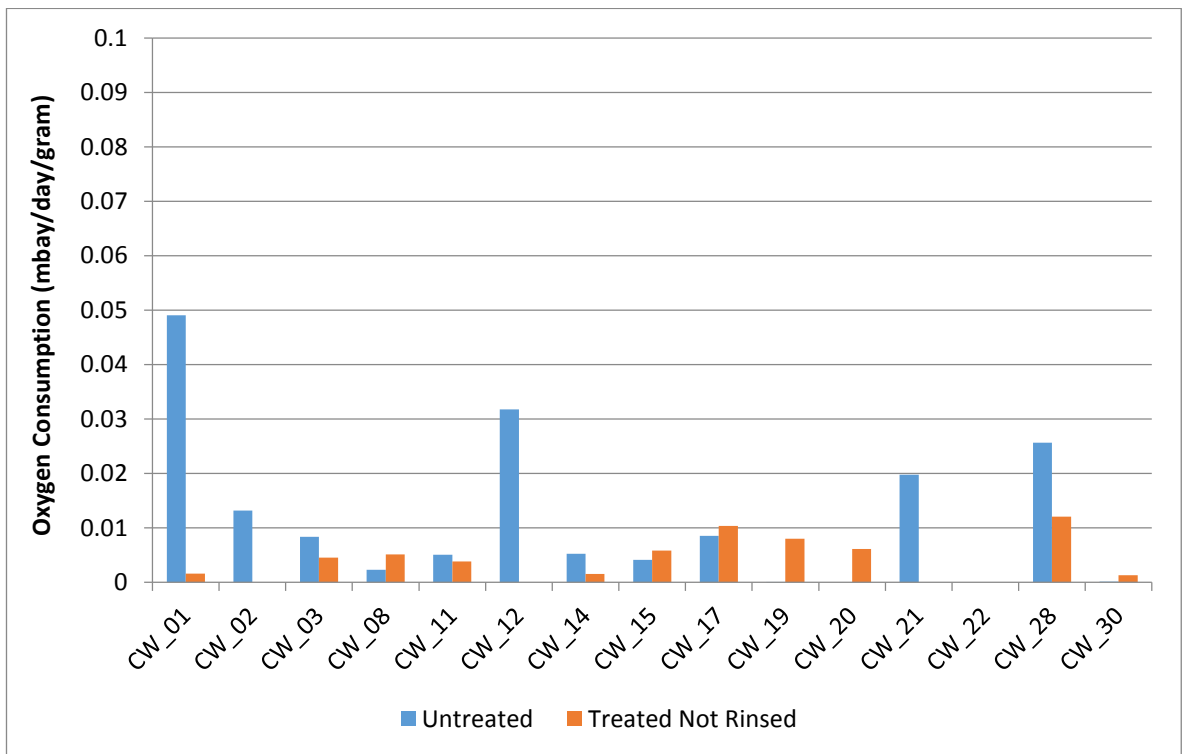


Figure 5.55 Oxygen consumption rate of 15 wrought iron nails from Colonial Williamsburg in untreated, and treated not-rinsed state and conditions of 80% RH and 20°C. Rates reflect consumption within the first 18 days of oxygen measurement, subject to oxygen consumption measurement error of +/-2 mbar.

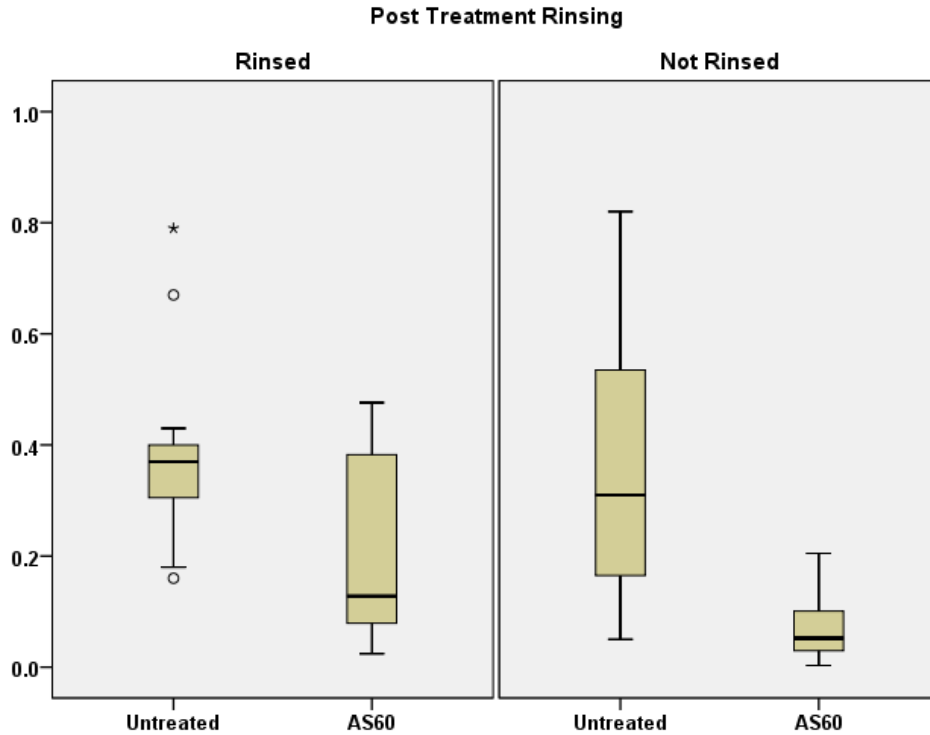


Figure 5.56 Comparison of oxygen consumption rate of wrought iron nails from Caerleon over 18 days in untreated and post AS60 conditions. Oxygen consumption rates are further compared between samples given rinsed and not rinsed post-treatment protocols. Plotted values for untreated nails differ as they represent 2 different subgroups of 15 samples each in the experiments.

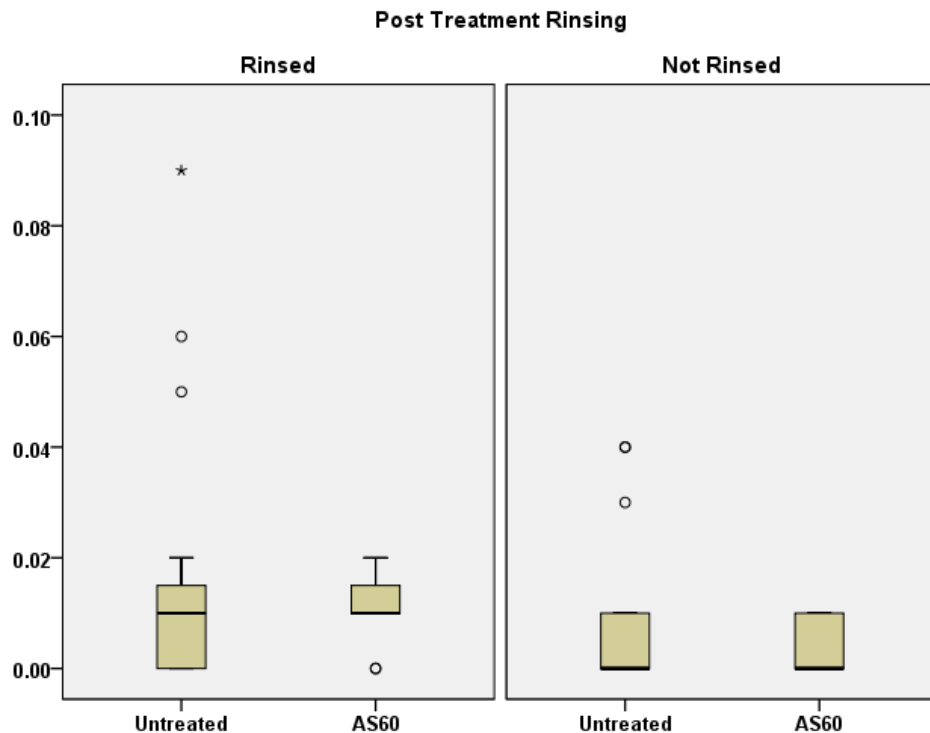


Figure 5.57 Comparison of oxygen consumption rate of wrought iron nails from Colonial Williamsburg over 18 days in untreated and post AS60 conditions. Oxygen consumption rates are further compared between samples given rinsed and not rinsed post-treatment protocols. Plotted values for untreated nails differ as they represent 2 different subgroups of 15 samples each in the experiments.

Site	Rinsing Protocol	Mean O ₂ Consumption Untreated mbar/day/gram	Mean O ₂ Consumption Treated AS 60	Mean Difference in O ₂ Consumption	Mean % Change by Rinsing Protocol	Mean % Change Combined
CAER	Rinsed	0.38	0.21	(-)0.17	-45%	-62%
	Not Rinsed	0.36	0.07	(-)0.29	-81%	
CW	Rinsed	0.02	0.01	(+)0.01	0%	0%
	Not Rinsed	0.01	0.00	(-)0.01	0%	

Table 5.9 Mean O₂ consumption over 18 days of wrought iron nail samples from Caerleon and Colonial Williamsburg, untreated, and treated with alkaline sulphite washing at 60°C in mbar/day/gram. Mean untreated and AS60 treated O₂ consumption values for rinsed and unrinsed samples and the mean change in O₂ consumption after treatment separated by rinsing protocol are also given.

5.2.4 Chloride extraction treatment efficiency

The chloride extraction treatment efficiency for an iron object is calculated by dividing the amount of chloride extracted into treatment solutions (Cl_e) by the total amount of chloride present, calculated as chloride extracted during treatment plus the amount remaining in the object after treatment as determined by digestion (Cl_r).

$$\text{Chloride Extraction Efficiency (E}_{ce}\text{)} = \frac{Cl_e}{Cl_e + Cl_r} \times 100$$

(Where Cl_e is extracted Cl^- and Cl_r is residual Cl^- in the object, both in ppm related to mass of object.)

Chloride concentration for treatments and digestion, as well as chloride extraction efficiencies, are given in Table 5.10. Figure 5.58 compares post-treatment remaining chloride (ppm) for samples from each site and Figure 5.59 compares total and remaining chloride across sites, with 5.60 and 5.61 recording the percentage of the total chloride remaining after alkaline sulphite treatment for both sites. Remaining chloride subdivided by post treatment rinsing protocol (rinsed or not rinsed) from each site is shown in Figures 5.62 and 5.63, while total and remaining chloride are shown as a function of rinsing protocol in Figure 5.64 and 5.65.

Sample	Post-Treatment Rinsing Protocol	Mass (g)	Extracted chloride (ppm)	Remaining chloride (ppm)	Total chloride (ppm)	Chloride extraction efficiency (%)	Final chloride in treatment solution (ppm)
CAER_01	R	7.02	3009	372	3381	89	25
CAER_02	R	2.24	6735	2923	9658	70	12
CAER_03	R	8.41	6187	300	6487	95	39
CAER_04	R	4.20	4663	605	5268	89	26
CAER_05	R	5.78	3601	1736	5337	67	7
CAER_06	R	17.75	2312	1359	3671	63	42
CAER_07	R	12.69	2941	215	3156	93	1
CAER_08	R	8.09	3283	319	3602	91	20
CAER_09	R	9.57	4032	922	4954	81	39
CAER_10	R	13.19	2337	28	2365	99	44
CAER_11	R	3.07	4696	1176	5872	80	11
CAER_12	R	3.19	3131	1210	4341	72	11
CAER_13	R	7.04	3076	885	3961	78	31
CAER_14	R	7.47	4524	995	5519	82	36
CAER_15	R	17.17	3609	397	4006	90	238
CAER_16	NR	23.48	1607	518	2125	76	35
CAER_17	NR	11.18	2165	367	2532	86	22
CAER_18	NR	6.59	6924	756	7680	90	50
CAER_19	NR	5.70	7490	212	7702	97	29
CAER_20	NR	2.39	11815	753	12568	94	51
CAER_21	NR	5.41	5685	541	6226	91	50
CAER_22	NR	4.41	4970	718	5688	87	18
CAER_23	NR	4.67	8073	291	8364	97	44
CAER_24	NR	1.89	4934	1425	6359	78	13
CAER_25	NR	1.60	7404	829	8233	90	29
CAER_26	NR	3.66	5463	1499	6962	78	10
CAER_27	NR	1.96	3288	791	4079	81	15
CAER_28	NR	3.27	2783	1032	3815	73	19
CAER_29	NR	34.50	3149	198	3347	94	361
CAER_30	NR	29.60	2692	252	2944	91	117
CAER(Mean)		8.91	4553	787	5340	85	48
CW_01	NR	6.28	1858	237	2095	89	75
CW_02	NR	8.28	2673	2024	4697	57	100
CW_03	NR	12.27	1146	1349	2495	46	47
CW_04	R	9.63	2116	695	2811	75	122
CW_05	R	6.56	1943	1043	2986	65	74
CW_06	R	4.37	2463	554	3017	82	17
CW_07	R	4.90	3548	940	4488	79	96
CW_08	NR	6.05	2006	218	2224	90	47
CW_09	R	5.07	3712	846	4558	81	75
CW_10	R	6.90	1480	905	2385	62	46
CW_11	NR	7.94	1238	589	1827	68	33
CW_12	NR	3.72	2958	990	3948	75	86
CW_13	R	5.38	5501	1439	6940	79	161
CW_14	NR	6.24	4683	717	5400	87	173

CW_15	NR	9.65	1671	709	2380	70	65
CW_16	R	6.64	1242	391	1633	76	48
CW_17	NR	3.81	1573	652	2225	71	18
CW_18	R	5.57	3939	412	4351	91	105
CW_19	NR	7.63	443	819	1262	35	13
CW_20	NR	5.76	2588	672	3260	79	42
CW_21	NR	3.81	6862	366	7228	95	118
CW_22	NR	4.31	2305	381	2686	86	31
CW_23	R	3.64	2715	606	3321	82	56
CW_24	R	6.62	4947	256	5203	95	160
CW_25	R	6.96	442	2401	2843	16	10
CW_26	R	5.87	8107	593	8700	93	318
CW_27	R	4.42	7622	276	7898	97	156
CW_28	NR	7.36	2731	666	3397	80	74
CW_29	R	4.99	4882	488	5370	91	76
CW_30	NR	16.68	507	221	728	70	44
CW(Mean)		6.58	2997	749	3745	75	83

Table 5.10 Chloride extracted during alkaline sulphite treatment of 60 wrought iron nails, together with post-treatment rinsing protocol: rinsed(R) or not rinsed (NR), mass, chloride extracted by alkaline sulphite treatment, remaining in the objects as determined by nitric acid digestion given in ppm (mass of chloride vs. mass of object in micrograms gram^{-1} , total chloride measured and chloride extraction efficiency as a percentage. Concentration of chloride measured in the final desalination bath is given in the last column.

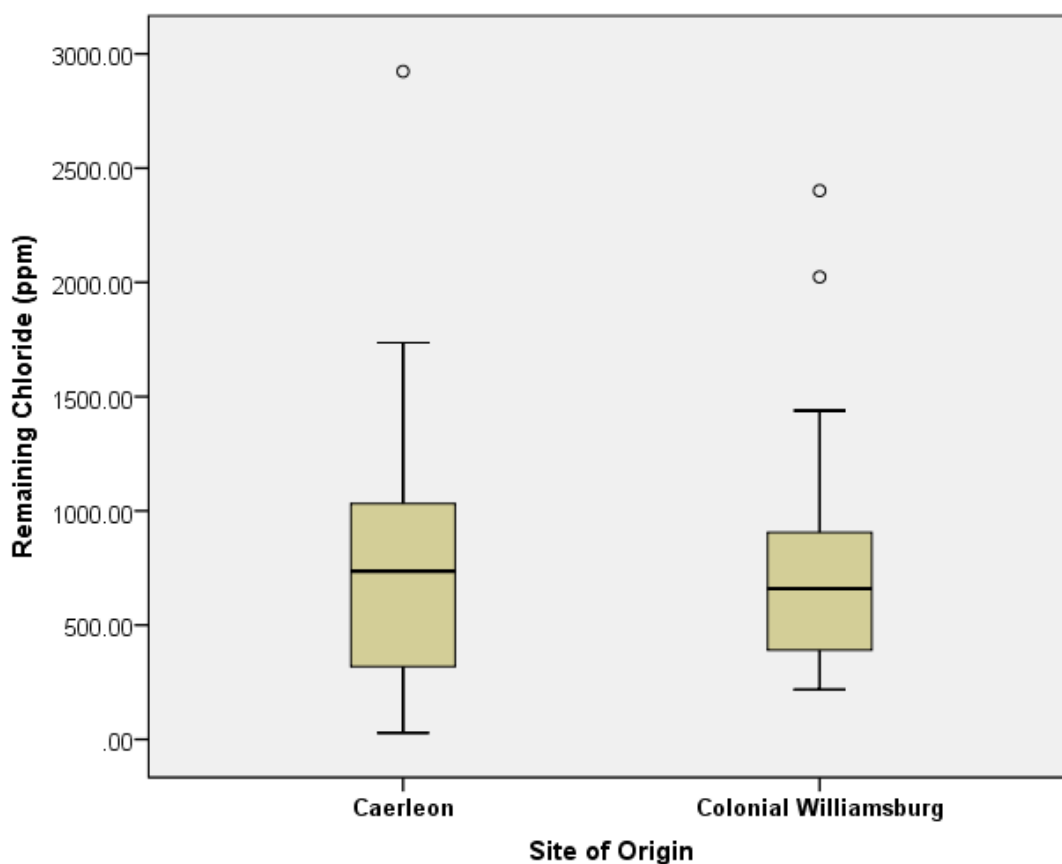


Figure 5.58 Remaining chloride in samples from Caerleon and Colonial Williamsburg after desalination with alkaline sulphite treatment at 60°C in ppm as measured by digestion in 5M nitric acid.

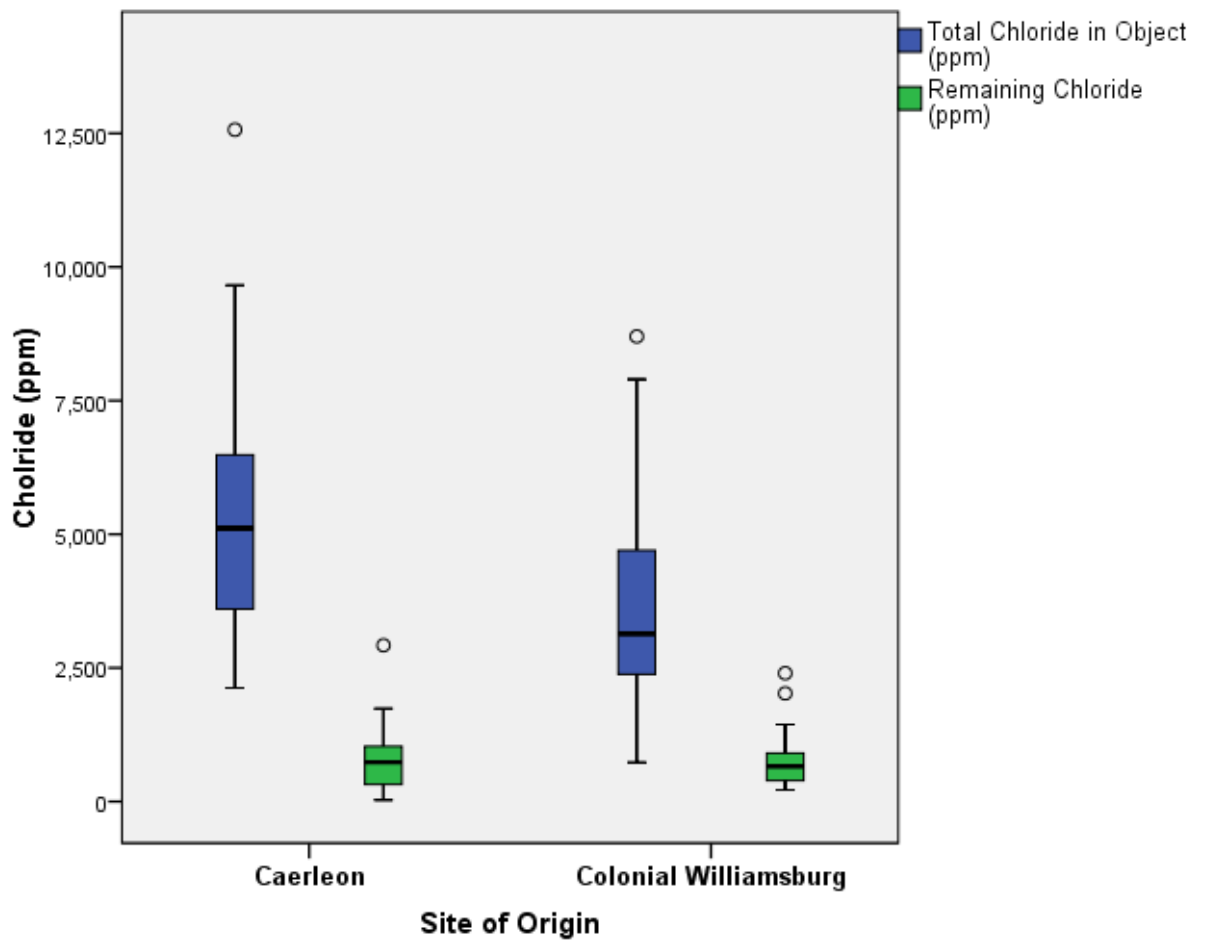


Figure 5.59 Comparison of total chloride and remaining chloride after alkaline sulphite treatment at 60°C for 30 wrought iron nails each from Caerleon and Colonial Williamsburg.

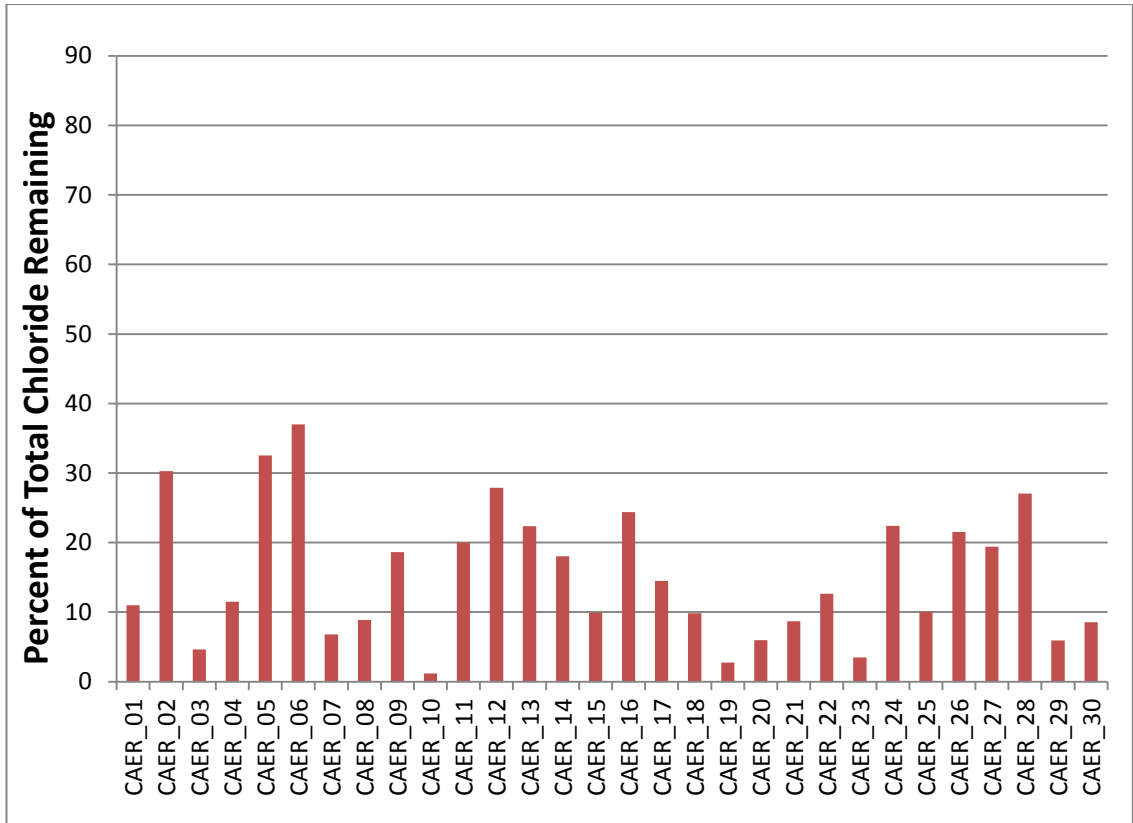


Figure 5.60 Remaining chloride in 30 nails from Caerleon after alkaline sulphite treatment as a percentage of the total chloride measured in each sample.

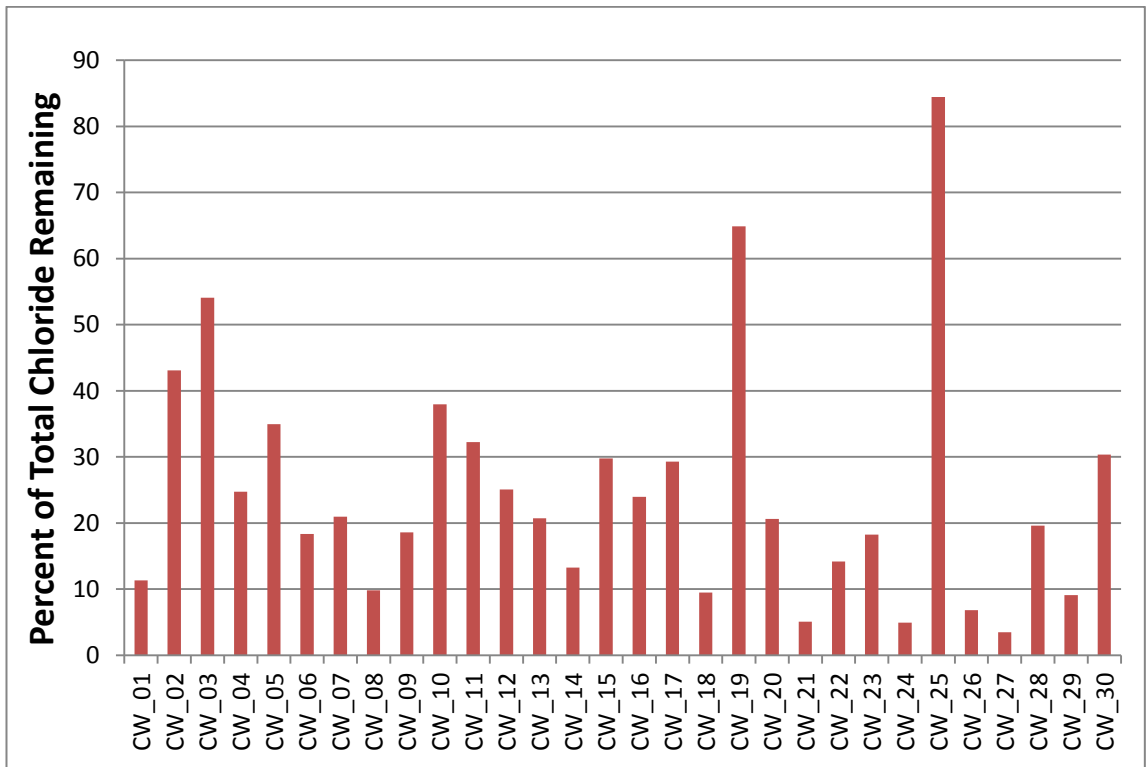


Figure 5.61 Remaining chloride in 30 nails from Colonial Williamsburg after alkaline sulphite treatment as a percentage of the total chloride measured in each sample.

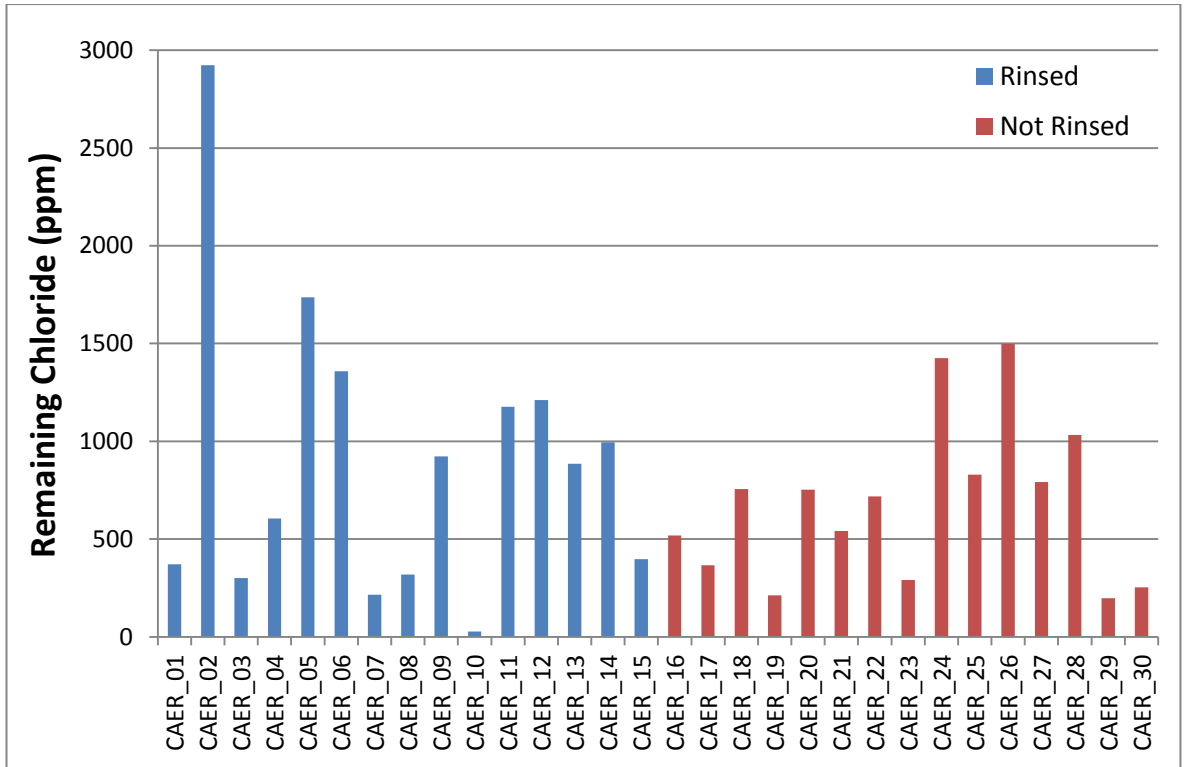


Figure 5.62 Total remaining chloride (ppm) in 30 samples from Caerleon after alkaline sulphite treatment: comparison of rinsed and not rinsed post-treatment protocols

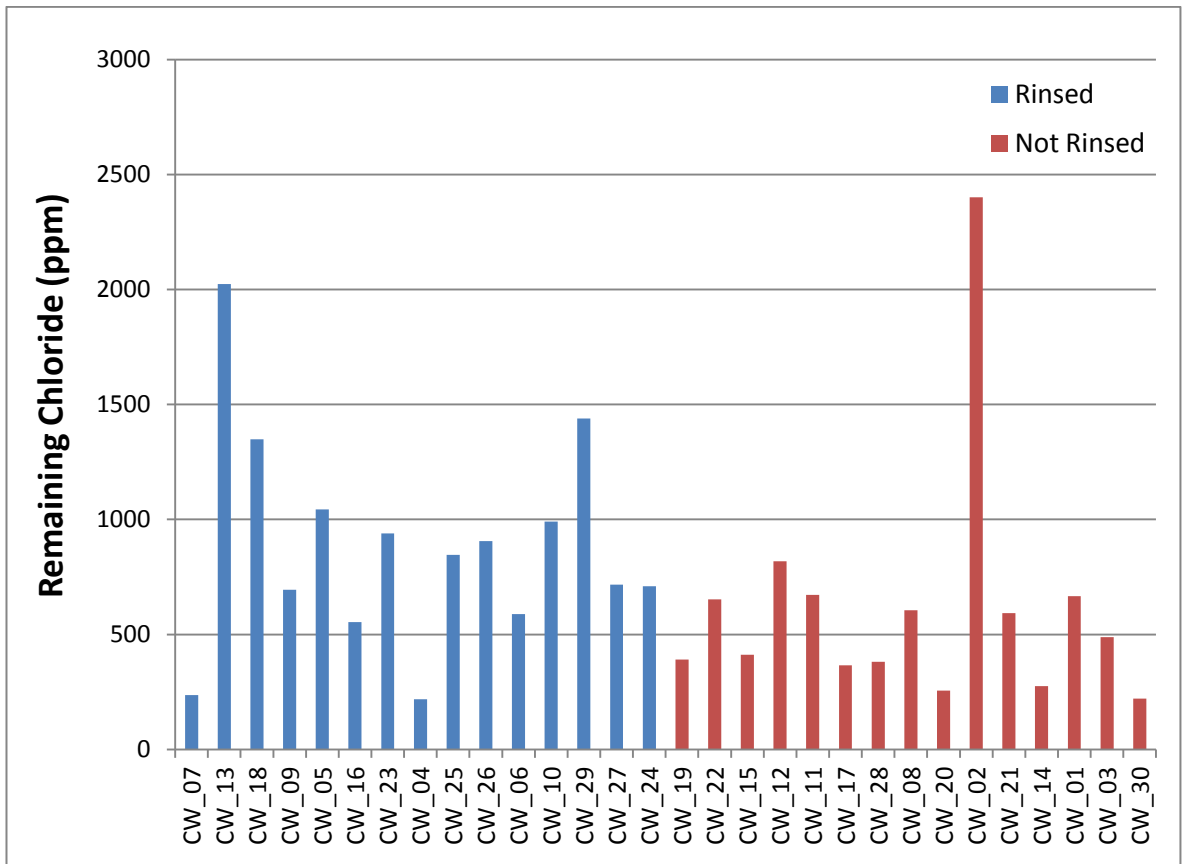


Figure 5.63 Total remaining chloride (ppm) in 30 samples from Colonial Williamsburg after alkaline sulphite treatment: comparison of rinsed and not rinsed post-treatment protocols.

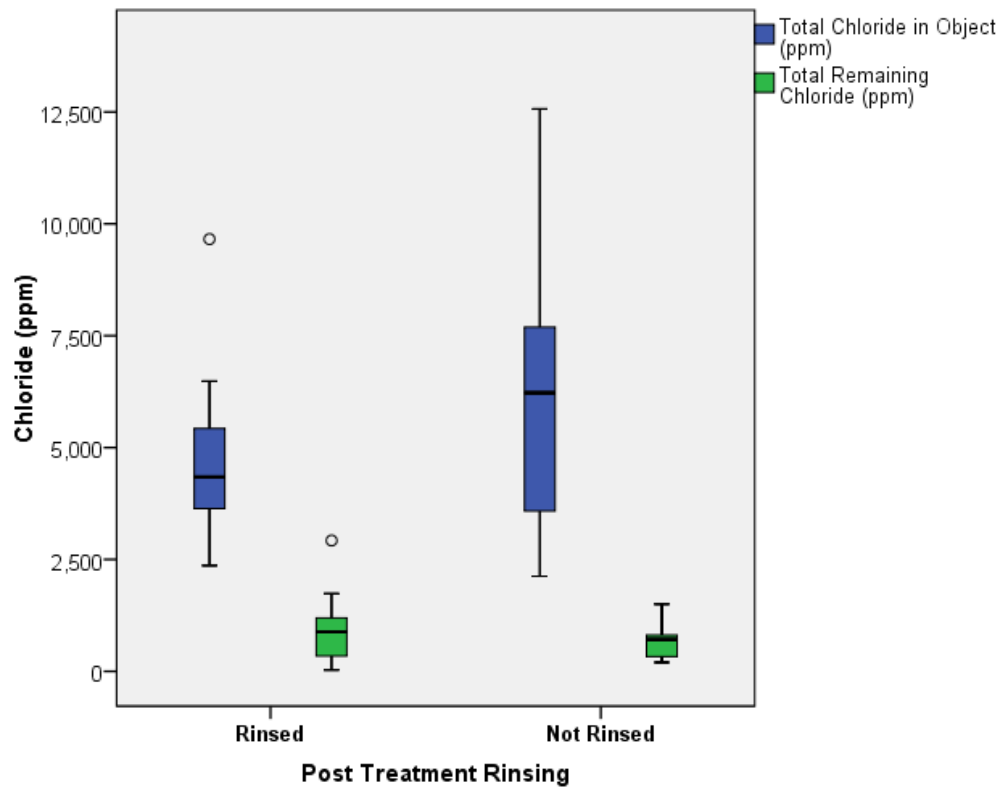


Figure 5.64 Comparison of total chloride and remaining chloride (ppm) measured for 30 nails from Caerleon with their assignment to rinsed or not rinsed protocols.

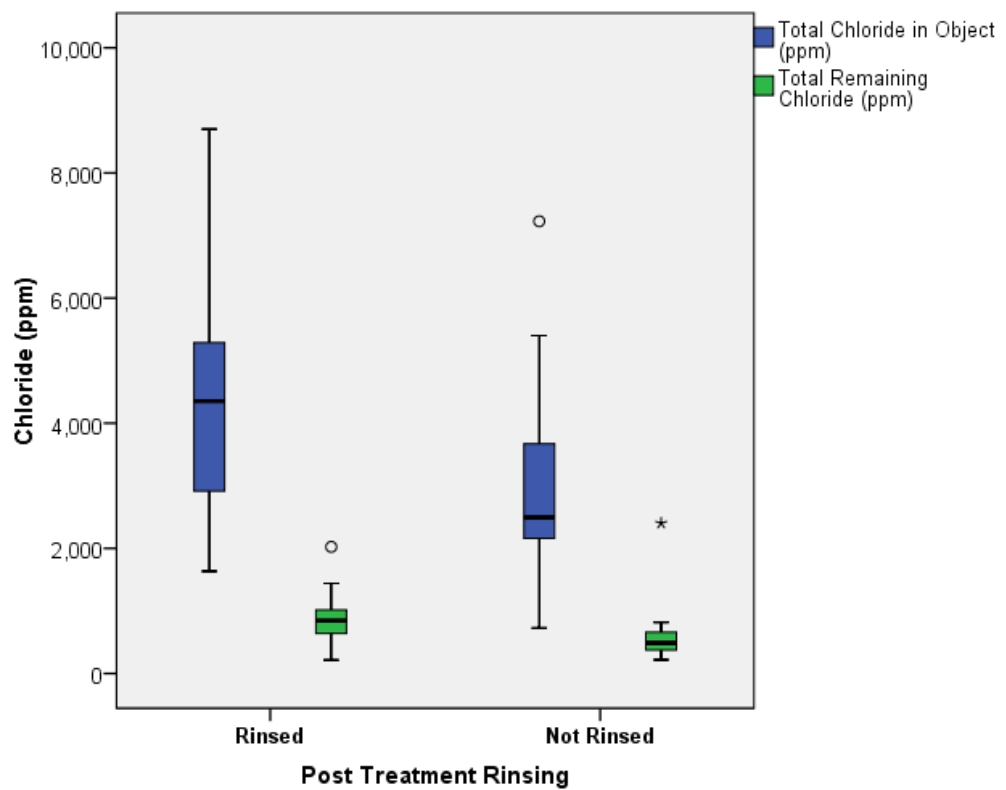


Figure 5.65 Comparison of total chloride and remaining chloride (ppm) measured for 30 nails from Colonial Williamsburg with their assignment to rinsed or not rinsed protocols.

5.2.5 Chloride content compared with oxygen consumption

The oxygen consumption rate of untreated nails from both sites is plotted against total chloride in Figure 5.66, and oxygen consumption of treated nails versus remaining chloride is plotted in Figure 5.67. Non-parametric tests of correlation are given in Table 5.11. Significant correlations of .05 or above are indicated, along with the level of significance, on the right side of the table.

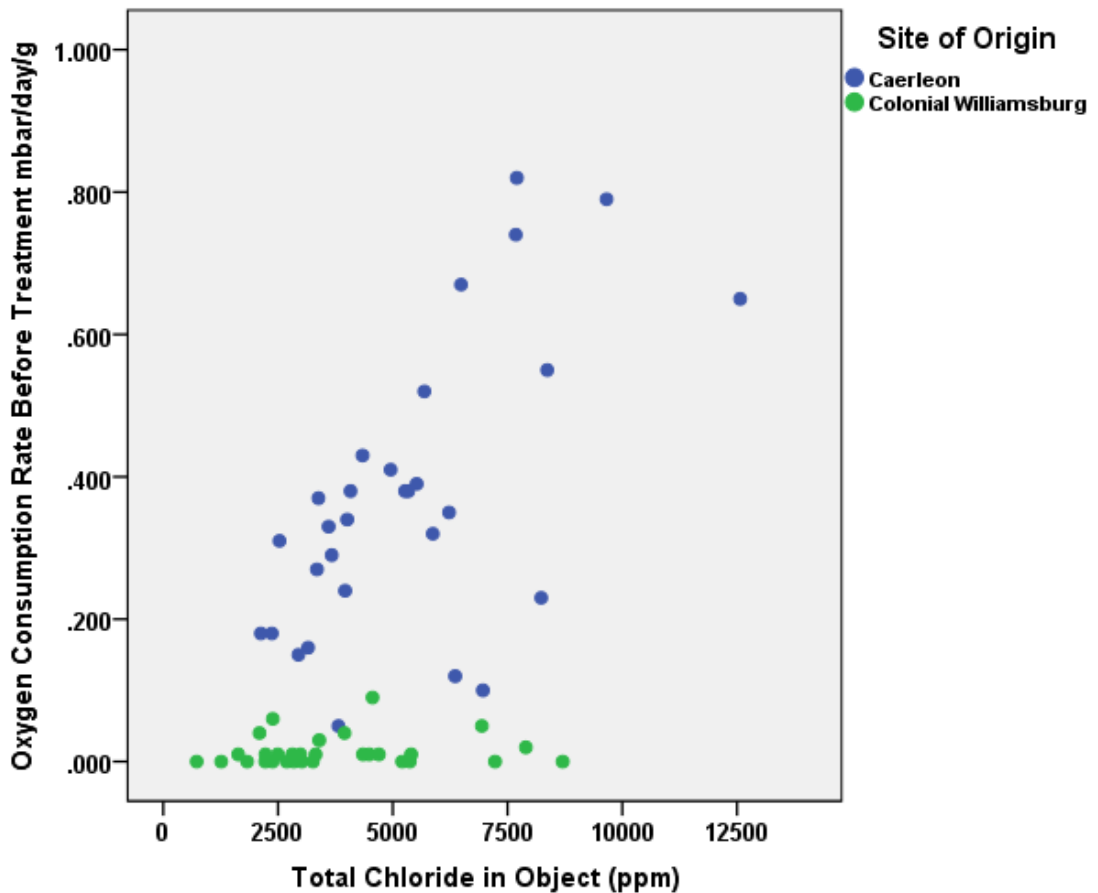


Figure 5.66 Oxygen consumption rate in mbar/day/gram over 18 days of 30 untreated samples each from Caerleon and Colonial Williamsburg (60 in total) as a function of total chloride in ppm measured by extraction and digestion.

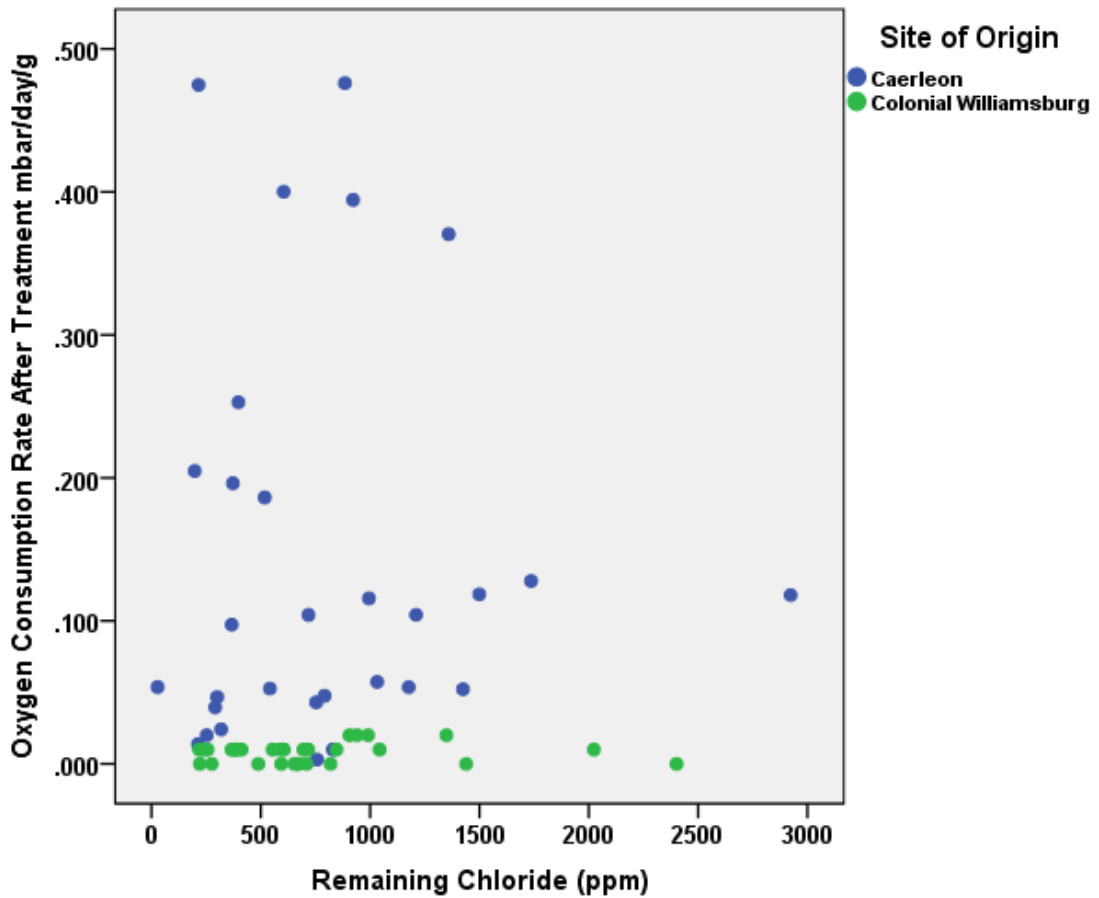


Figure 5.67 Oxygen consumption rate in mbar/day/gram over 18 days of 30 treated nails each from the sites of Caerleon and Colonial Williamsburg (60 in total) after alkaline sulphite treatment as a function of chloride remaining in ppm after treatment as determined by digestion.

Tests of Correlation Between Oxygen Consumption Corrosion Rate and Chloride Content					
Variables	Number Samples	Nonparametric Test	Correlation Coefficient	Significance	Significance Level
Oxygen consumption before treatment/total chloride	30 (CAER)	Spearman rho	.568	.00	.01
Oxygen consumption before treatment/total chloride	30 (CW)	Spearman rho	.172	.36	N/S
Oxygen consumption after treatment/remaining chloride	30 (CAER)	Spearman rho	.321	.19	N/S
Oxygen consumption after treatment/remaining chloride	30 (CW)	Spearman rho	.137	.47	N/S

Table 5.11 Non-parametric (Spearman-rho) tests of correlation between oxygen consumption rates before and after alkaline sulphite treatment and total and remaining chloride for the sites of Caerleon and Colonial Williamsburg. Significance values are given for correlations significant to the .05 level or above. N/S indicates that the correlation is not significant to the .05 level.

5.2.6 Chloride compared with Percent Area Slag

Post treatment chloride is related to percentage area slag as determined by image analysis of complete cross sections of sample nails at 50X magnification (Figure 5.68).

Non-parametric Spearman-rho tests of correlation between remaining chloride and percentage area slag showed no significant correlations (Table 5.12).

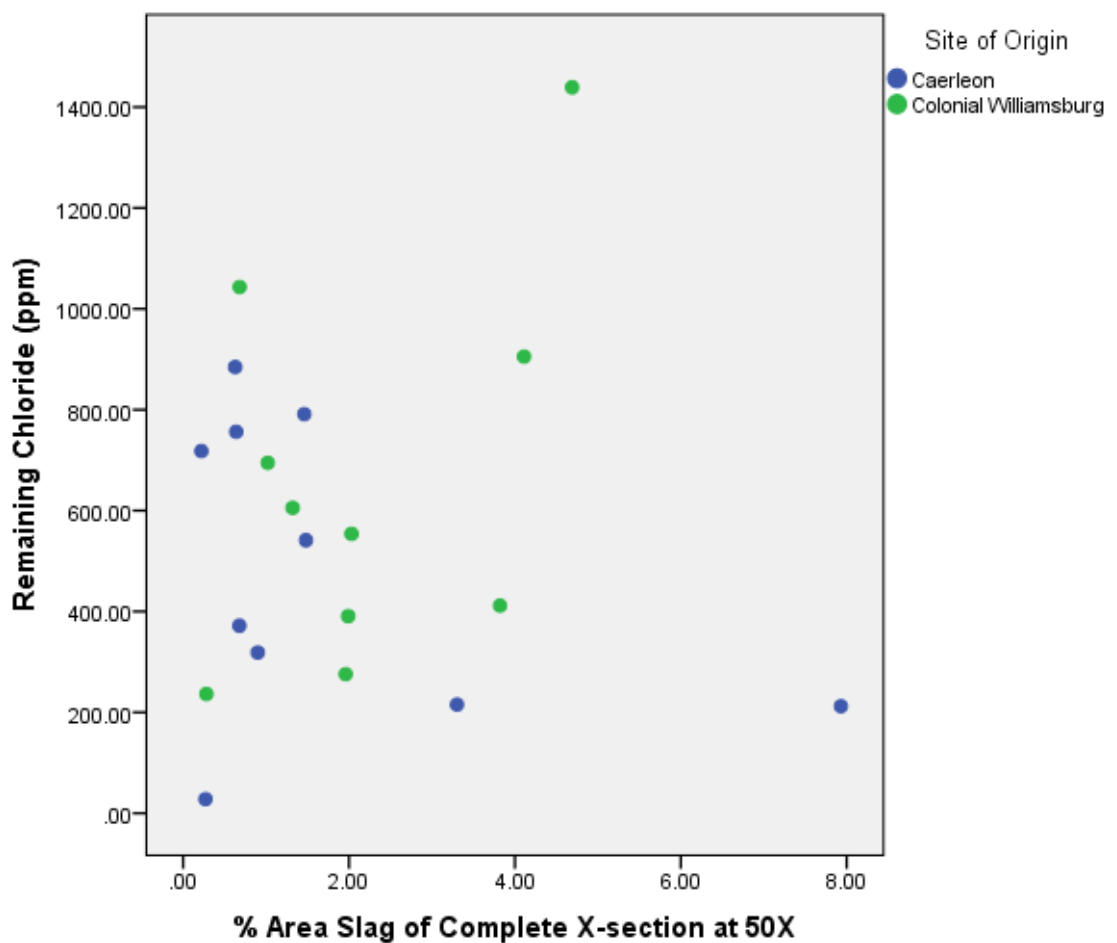


Figure 5.68 Scatterplot of remaining chloride in ppm vs percent area slag at 50X magnification in 20 wrought iron nails, 10 each from the sites of Caerleon and Colonial Williamsburg, treated by alkaline sulphite washing at 60°C.

Variables	Site	N	Test	Correlation Coefficient	Significance	Significance Level
Remaining Chloride/Percent Area Slag	CAER	10	Spearman	.30	.41	N/S
Remaining Chloride/Percent Area Slag	CW	10	Spearman	.35	.33	N/S

Table 5.12 Non-parametric (Spearman rho) correlation tests between remaining chloride in 30 sample nails treated by alkaline sulphite (10 samples per site) and percent area slag content as measured by image analysis at 50X magnification. Correlation Coefficients and significance values are given. N=Number of Samples, NS=not significant at the .05 level or below.

5.2.7 Chloride in cross sections of treated objects

Twenty cross sections of nails were analysed by SEM-EDS/WDS after alkaline sulphite treatment using elemental mapping, point, and linescan techniques (Section 4.7.9). An example is given for sample CAER_07 in Figures 5.69, 5.70 and Table 5.13. Complete SEM analytical data is given in Appendix 8.4, Sections 8.4.2-8.4.3. These techniques measure the presence of elements rather than ions, so the following discussion will relate to chlorine rather than chloride. The WDS chlorine map for this sample shows some chlorine in the range of 0-1 wt% (in dark blue) in the area of corrosion pits penetrating the sample plane. In the iron map, these corroded regions show diminished Fe content (~50 wt% in yellow) compared with the ferritic regions (purple-white). The lighter-coloured speckled region around the outside of the CPLs and within cracks records the epoxy mounting resin. The EDS lines (Figure 5.70) show a small amount of chlorine around a slag inclusion and at the outer edge of the CPLs but the level of chlorine is otherwise below EDS detection limits. Table 5.14 lists the results of elemental microanalyses for chlorine, indicating: the location where chlorine was detected (corrosion product layer (CPL) or slag inclusion (SI)); method used (mapping

or linescan); and maximum concentration detected in wt%. Additional notes about the location where chlorine was detected are given in parentheses.

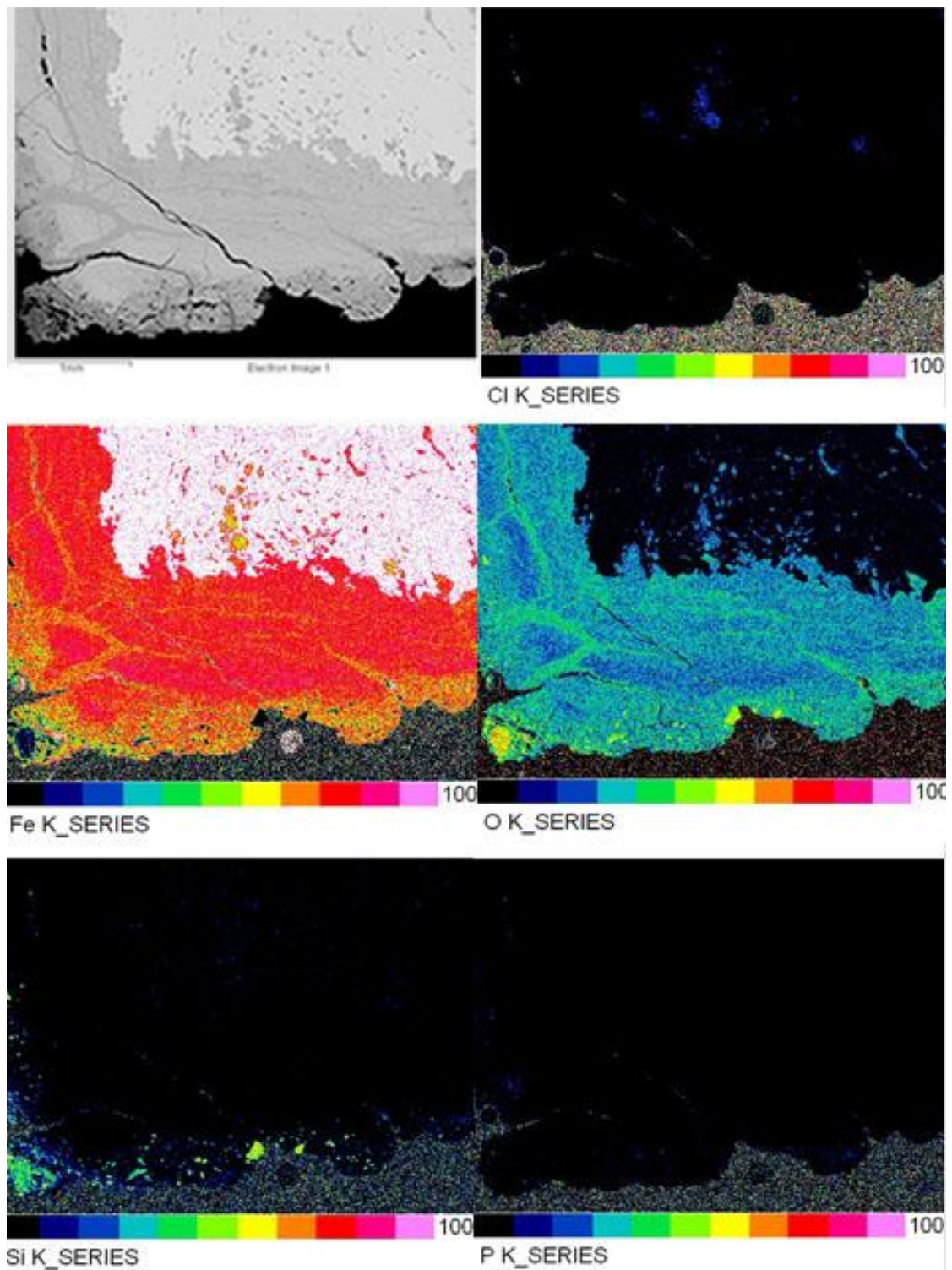


Figure 5.69 SEM (BEI) image (upper left) of Caerleon sample CAER_07 showing iron metal (ferrite), slag inclusions, and dense corrosion product layers, along with SEM-WDS quantitative elemental map for chlorine (top right), and SEM-EDS quantitative maps for Fe, O, Si, and P. All maps acquired for 2 hours (25 frames).

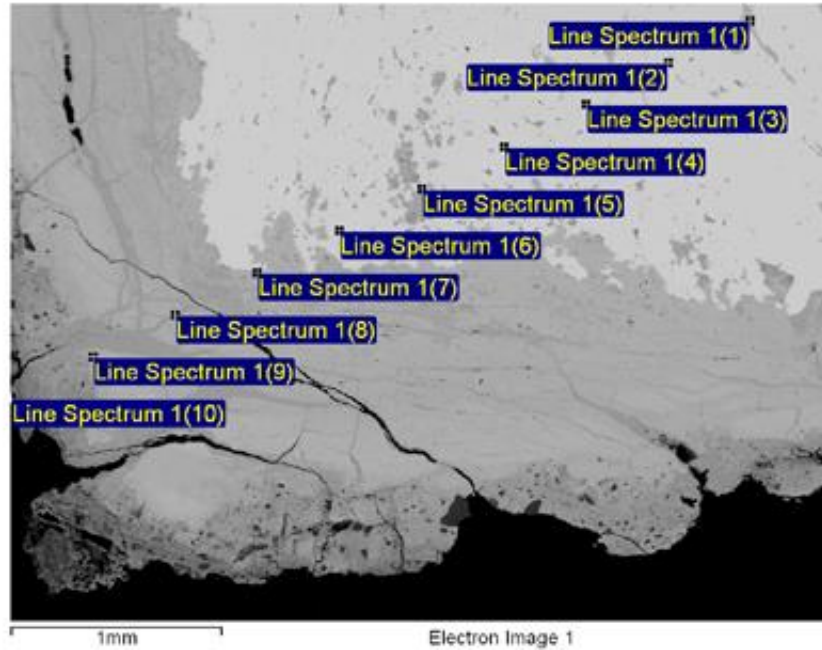


Figure 5.70 SEM (BEI) image of Caerleon sample CAER_07 with location of EDS line scan (10 data points from upper right to lower left) across a section of the sample from an interior slag inclusion to the outer CPL edge. Results of the analysis are given in Table 5.13 below.

CAER_07 EDS Line scan (Concentration in wt% - normalized)						
Spectrum	O	Si	P	Cl	Fe	Total
Line Spectrum 1(1)	25.53	2.91	0.03	0.21	71.32	100.00
Line Spectrum 1(2)	0.49	0.06	0.00	0.02	99.43	100.00
Line Spectrum 1(3)	0.06	0.07	-0.05	0.03	99.90	100.00
Line Spectrum 1(4)	0.14	0.05	-0.06	0.07	99.80	100.00
Line Spectrum 1(5)	-0.04	0.05	-0.06	0.07	99.97	100.00
Line Spectrum 1(6)	0.12	0.09	-0.05	0.04	99.80	100.00
Line Spectrum 1(7)	24.57	0.29	0.06	0.07	75.01	100.00
Line Spectrum 1(7)	24.57	0.29	0.06	0.07	75.01	100.00
Line Spectrum 1(9)	27.41	1.16	0.76	0.04	70.63	100.00
Line Spectrum 1(10)	25.56	10.15	0.33	0.45	63.51	100.00
Mean	13.82	1.55	0.14	0.13	84.36	100.00
Max.	31.53	10.15	0.76	0.45	99.97	
Min.	-0.04	0.05	-0.06	0.02	63.51	

Table 5.13 SEM-EDS line scan results for Caerleon sample CAER_07 along the 10 data points indicated in Figure 23 above. EDS spectrometer standardised on cobalt before analysis, all points analysed for 30 seconds. Elemental concentrations given in wt % (data normalised to 100%).

Sample	Mapping: Corrosion Product Layers	Mapping: Slag Inclusions	Line Scan: Corrosion Product Layers	Line scan: Slag Inclusions
CAER_01	10.0 (pit)	0	0	3.67
CAER_07	0-10 (pit)	0	15.56 (pit around slag)	0.21
CAER_08	0	0	0.24 (pit)	1.02
CAER_10	10.0 (metal/CPL)	0	0	0.17
CAER_13	10-20 (pit)	0	0.92(outside CPL)	0.47
CAER_18	10-20 (metal/CPL)	0	1.1 (pit)	0
CAER_19	0	0	5.24 (outside CPL)	0.32
CAER_21	10 (pit)	10	0.19 (pit)	0.22
CAER_22	1-10(metal/CPL)	10	0.65 (outside CPL)	9.13 (pit)
CAER_27	0	20 (spot)	0.65 (outside CPL)	21.24
CW_05	0	0	0.41 (inside CPL crack)	0
CW_07	0	0	6.05 (outside CPL)	0
CW_08	0	0	0	0.19
CW_09	0	0	0	0.67
CW_14	0	0	0	0
CW_15	0	0	0.28 (outside CPL)	0.18
CW_16	0	0	0.46 (pit)	0
CW_19	0	0	0.17 (inside CPLs)	0
CW_26	0	0	0.14 (metal/CPL)	0
CW_29	10 (pit)	10	3.23 (pit)	0

Table 5.14 Results of SEM microanalyses for chlorine indicating the sample, method (mapping or linescan) location (Corrosion Product Layer-CPL, or Slag Inclusion-SI), and approximate maximum chlorine concentration in normalised wt% based on analysis of a minimum of 2 sites of interest for each sample. Additional notes on location of detected chlorine are given in parentheses.

5.3 Akaganeite transformation

Samples of synthetic akaganeite were assayed by powder XRD and FT-IR for the akaganeite transformation experiments (Figures 5.71 and 5.72). XRD returned akaganeite and some goethite in the samples before alkaline sulphite treatment. XRD diffractograms matched monoclinic akaganeite (0-042-1315) and synthetic goethite (01-081-0464) in the ICDD (2005) database. Five XRD analyses of one batch of synthetic akaganeite powder with semi-quantitative RIR phase determinations gave percentages of 87-100% and 0-13% (+/- 10%) for akaganeite and goethite respectively. These results are shown in Table 5.15. FT-IR analysis (Figure 5.72) of the same samples show a clear absorption band at 840 wavenumbers (cm^{-1}) which has been identified as characteristic of the hollandite structure of $\beta\text{-FeOOH}$ (Murad and Bishop 2000).

XRD Analysis	% akaganeite ($\beta\text{-FeOOH}$)	% goethite ($\alpha\text{-FeOOH}$)
1	100	0
2	100	0
3	87	13
4	90	10
5	91	9

Table 5.15 Five XRD-RIR analyses of synthetic akaganeite before experimental alkaline sulphite treatment. Percent phase determinations subject to +/- 10% error

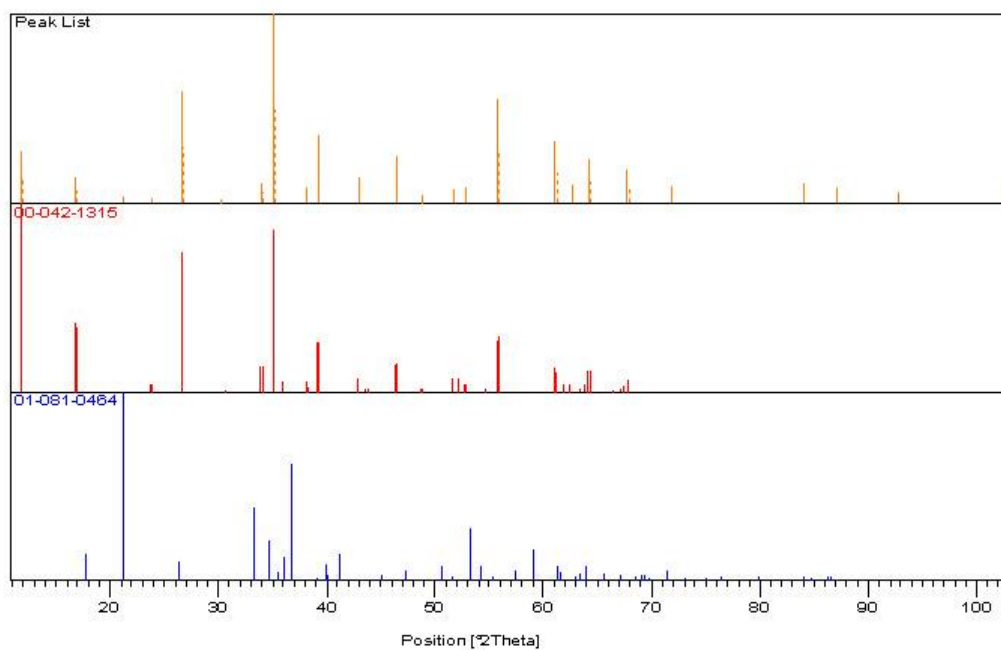
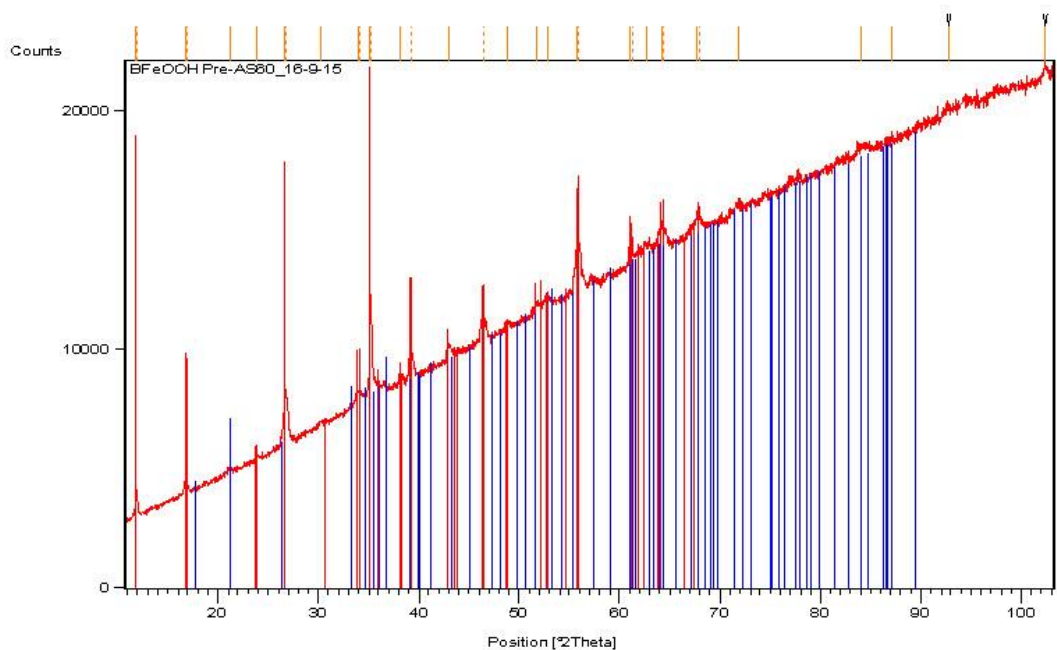


Figure 5.71 X-ray Diffractogram (top) of synthetic β -FeOOH powder before alkaline sulphite treatment and stick plot (bottom) showing sample pattern (top band) and matching compounds akaganeite-M (00-042-1315) (middle) and goethite (01-081-0464)(bottom).

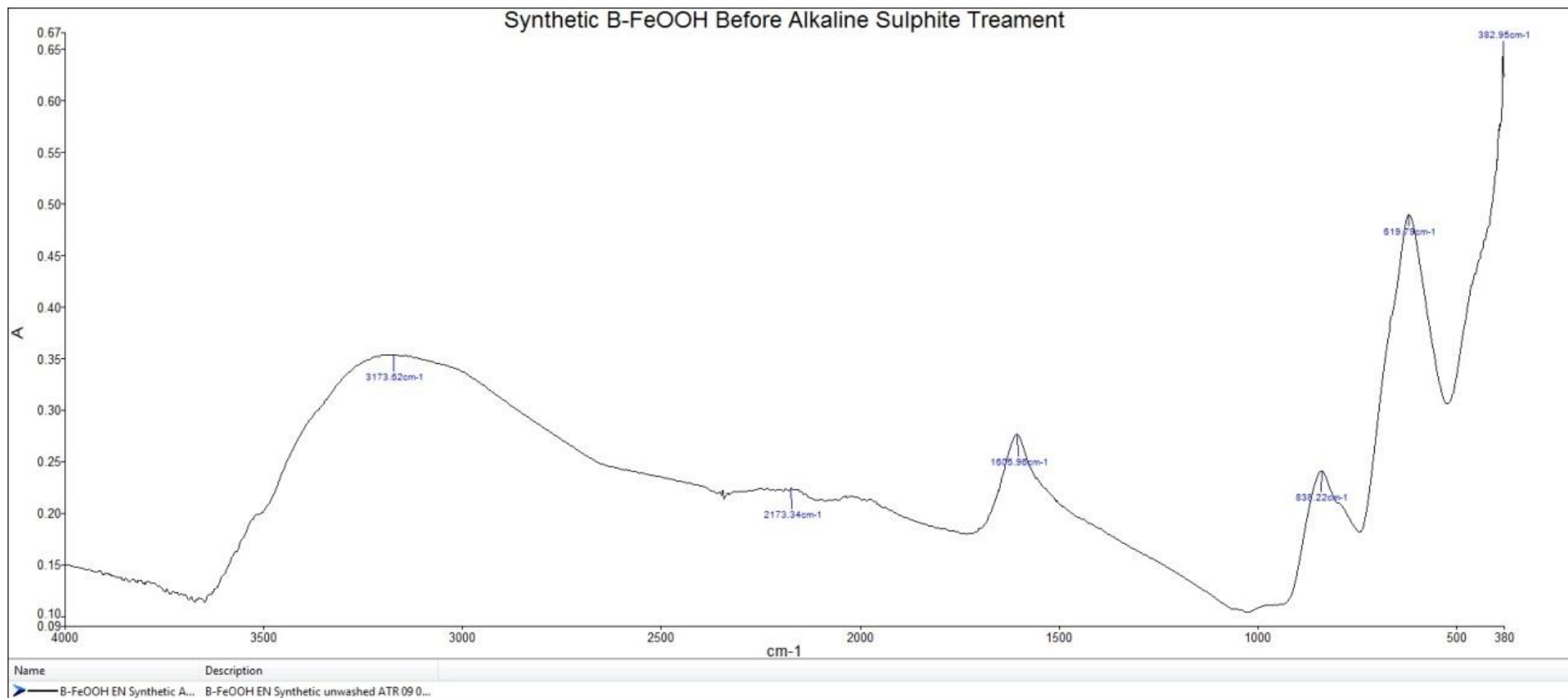


Figure 5.72 Absorbance FT-IR spectrum of untreated synthetic β -FeOOH sample 1 before alkaline sulphite transformation experiment.

Analysis of synthetic akaganeite samples β -FeOOH AS60 1-10 after alkaline sulphite washing at 60°C for 1 month showed a different XRD and FT-IR pattern (Figures 5.73-5.74, Appendix 8.4.4). XRD-RIR results from analysis of sample β -FeOOH AS60 1 showed that akaganeite was no longer present and that the powder was composed of a 72/28% ratio of goethite to hematite. XRD results for samples β -FeOOH AS60 1-10 are given in Table 5.16. FT-IR absorbance spectra of the alkaline sulphite treated samples are given in Figure 5.74 with the untreated spectrum shown for comparison. The band at 840 wavenumbers is no longer present, but peaks can be seen at 792 and 887, characteristic of goethite. Library searching returned a 75% match to goethite (IMP00188 GOETHITE, MARQUETTE CO., MI, US, SI-NMNH, #93710) in the IRUG database in all ten samples.

Sample	% akaganeite	% goethite	% hematite
β -FeOOH AS60 1	0	72	28
β -FeOOH AS60 2	0	73	27
β -FeOOH AS60 3	0	72	28
β -FeOOH AS60 4	0	74	26
β -FeOOH AS60 5	0	74	26
β -FeOOH AS60 6	0	67	33
β -FeOOH AS60 7	0	63	37
β -FeOOH AS60 8	0	65	35
β -FeOOH AS60 9	0	66	34
β -FeOOH AS60 10	0	62	38
Mean	0	69	31

Table 5.16 Percentage iron phases present after alkaline sulphite washing of 10 samples of synthetic β -FeOOH for 30 days, as analysed semi-quantitatively by XRD-RIR. Percentages given are +/- 10%

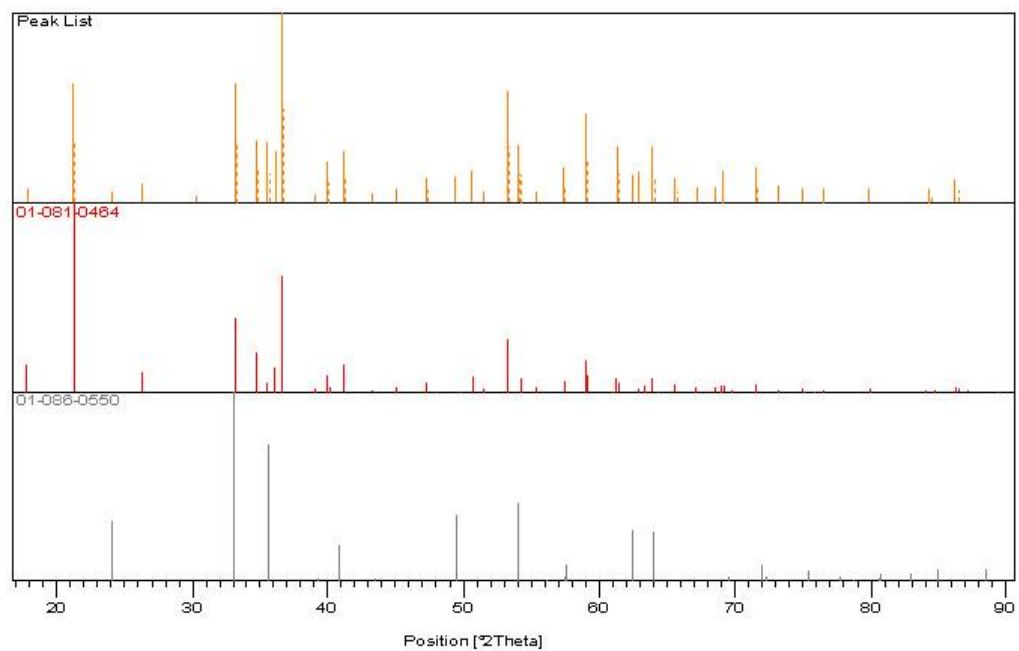
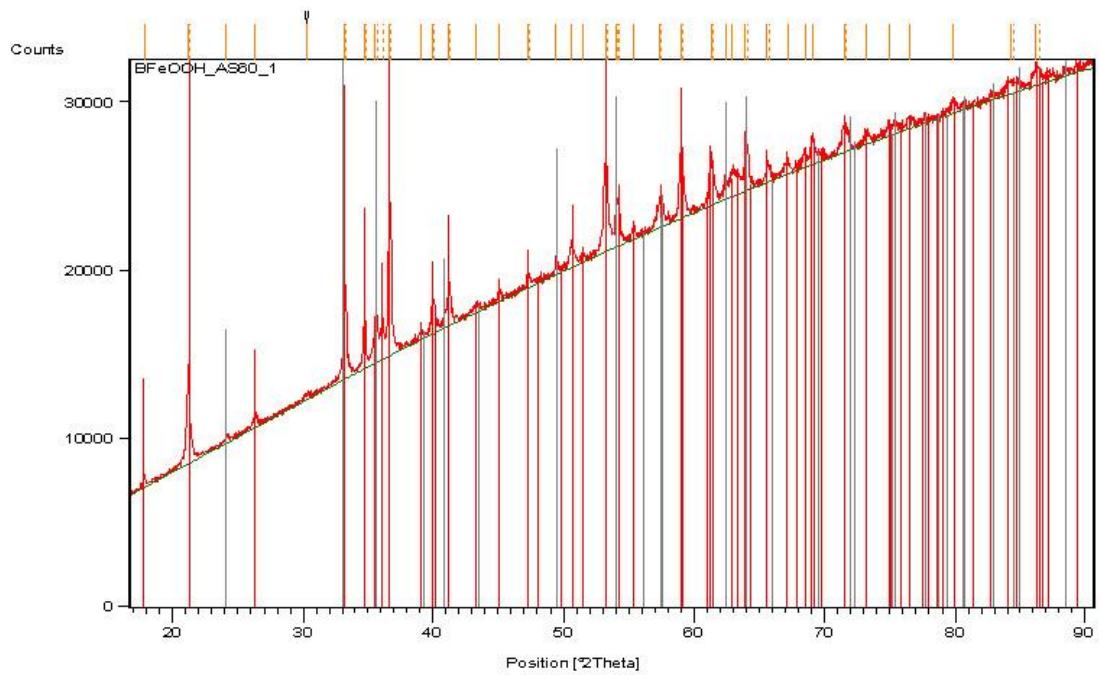


Figure 5.73 X-ray Diffractogram (top) of synthetic akaganeite powder sample β -FeOOH AS1 after alkaline sulphite treatment for 30 days, and stick plot (bottom) showing diffraction pattern (top) and matching compounds goethite (01-081-0464)(middle) hematite α -Fe₂O₃(01-086-0550)(bottom).

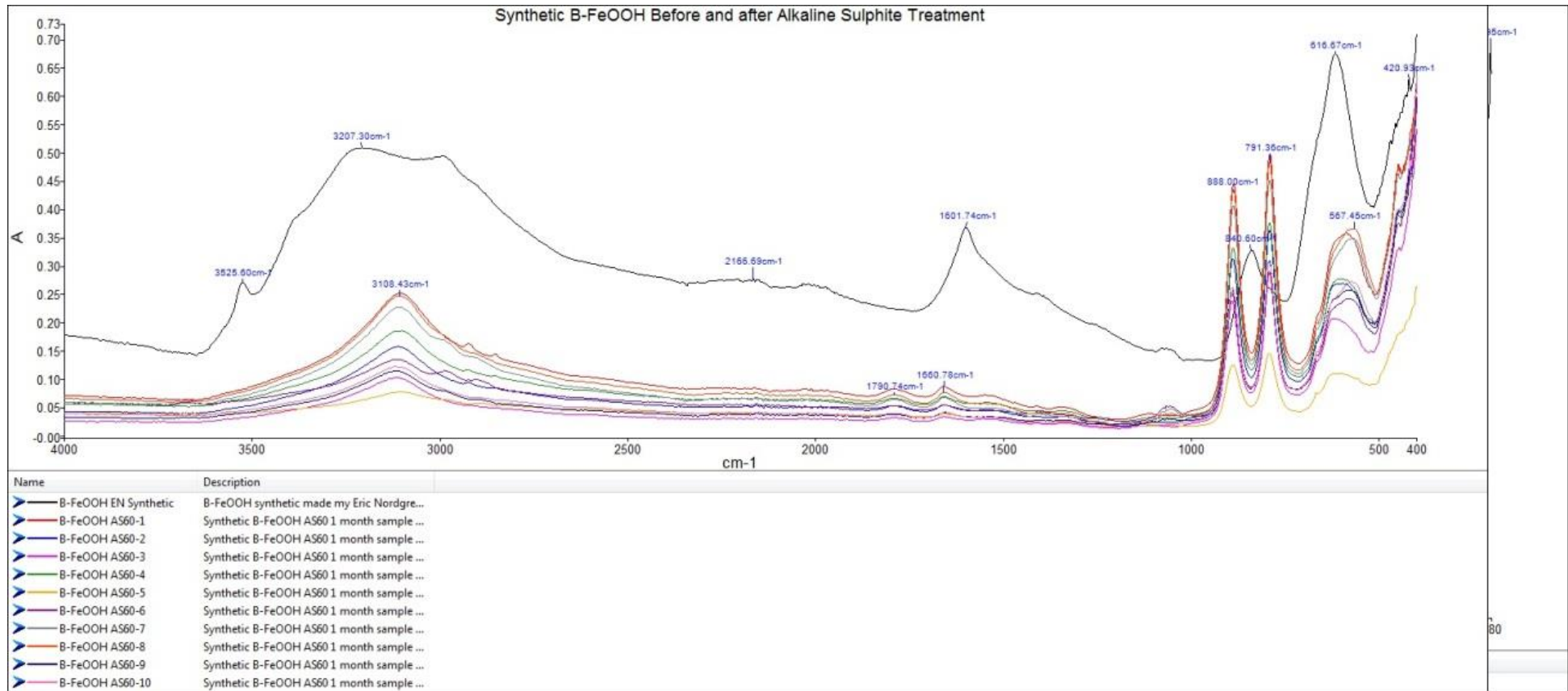


Figure 5.74 FT-IR absorbance spectra of 10 alkaline sulphite treated samples of synthetic akaganeite (bottom) with the untreated synthetic akaganeite spectrum shown for comparison (top).

6 Discussion

6.1 Composition and Production Technique of Nails

6.1.1 Composition

EMPA and SEM-WDS analysis of the metal matrix of six sample nails from each site show the metallic (ferrite) phase of all samples contained low levels of elements in solid solution, apart from phosphorus (primarily in Colonial Williamsburg samples), manganese in one Williamsburg nail and nickel in another (Tables 5.2 and 5.3). The high amount of silicon in solution in CW_34 is attributed to silicate slag in close proximity. Sulphur was not found in the majority of samples and only seen at the edge of EMPA detection limits in two Williamsburg samples. Ca, Ti, and Cr were not detected at all. Phosphorus levels of between 0.21 and 0.33 wt% for CW_08, 14, 31 and 33 classify them as high phosphorus wrought irons. Carbon was not analysed for as it is difficult to detect reliably by EPMA or SEM-WDS (Boesenberg 2006). However, it will be present and may be in solid solution or precipitated at grain boundaries as cementite (Fe_3C).

Analysis of slag phases showed varying amounts of SiO_2 and FeO depending on whether slag inclusions were primarily silicate glass or contained significant wüstite (FeO) (Figure 5.10). Most nails contained higher amounts of either SiO_2 or FeO . Caerleon nails contained more silicate inclusions without wüstite and Colonial Williamsburg samples contained more slag with high wüstite levels.

The thermodynamic and physico-chemical conditions present during iron smelting have an effect on the chemistry of the wrought iron they produce which can be seen

particularly well in the slag inclusions. Recent work on large sample sets (Birch and Martín-Torres 2015; Dillmann and L'Héritier 2007) has found that ratios of wt% phosphorus pentoxide (P_2O_5) to the sum of wt % of MgO, Al_2O_3 , and K_2O divided by wt% FeO present in slag inclusions are a good indicator of whether wrought iron was produced by the direct (bloomery) or indirect (blast furnace and finery/puddling) smelting process.

Results for these ratios as analysed for six samples each from Caerleon and Colonial Williamsburg are plotted in Figure 5.11. Based on the above criteria, the samples from Caerleon were produced by the direct bloomery process and a majority of those from Colonial Williamsburg were made by an indirect process as indicated by their higher P_2O_5 /alkali ratios. Two of the Williamsburg samples CW_32 and CW_34 have low ratios more typical of direct process wrought iron manufacture, therefore bloomery production cannot be ruled out using this method of analysis. This fits the known archaeological provenance of the nails. Some of the iron produced in the American Colonial period was made by what is termed the 'American' bloomery process (Gordon 1996, 57) which could account for the CW_32 and CW_34 results, but these may also be due to limitations of this analysis method as a predictor, since even the larger studies cited above exhibit a range of results, not all of which clearly fall into the 'direct' or 'indirect' category. These differences in production may have a bearing on past and present corrosion behaviour of the sample nails in this study.

6.1.2 Slag

Silicate slag content of wrought iron nails from Caerleon and Colonial Williamsburg was evaluated in polished cross sections to examine the potential effect of slag on

corrosion of archaeological iron. Slag content of the 10 samples examined from each site varied considerably by sample (Figures 5.15-5.34). All nails contained slag but there were low levels in CAER_01, 10, 13, and 18 and CW_05 and 07. Sample CW_05 in Figure 5.26 may be a post 18th C type of nail formed from drawn iron wire rather than forged, with its low slag content a composition closer to low-carbon steel rather than a true wrought iron. Others nails such as CAER_07 and 19 and CW_15 and 26 have visibly significant amounts of slag that can be seen both visually and in percent area slag data (Table 5.6).

Colonial Williamsburg samples had a higher percent area slag than Caerleon samples (Figure 5.35) except for CAER_19 (Figure 5.21) which had the highest percent area slag (7.9%) of all samples. Lower amounts of slag in Caerleon nails (0.27-3.30%) may be due to their production method involving smelting in a slag-tapping bloomery furnace, followed by smithing to remove excess slag in the finished product. It is possible that the amount of slag in many of the Caerleon samples was underestimated to some degree due to issues discussed in Section 6.1.2.1.

Percentage area slag of Colonial Williamsburg nails was measured at 0.28-4.69% with considerable variation in inclusion density and morphology. This is likely due to the fact that samples are from distinct archaeological sites in the Williamsburg area, and thus have more varied local provenance, production methods and age than Caerleon samples.

Slag inclusion size, morphology, and distribution vary between samples from the two sites. These factors are influenced by production techniques and can result in widely differing microstructures. Slag inclusions were observed in lengths (or diameters if

spherical) from ≤ 1 to 500 μm . Slag size is determined by whether manufacture employed bloomery or blast furnace process, silica content and cooling rate with crystalline phases such as wüstite (FeO) growing larger when iron is cooled more slowly (Abbaschian et al. 2010). Slag size and also morphology are influenced by smithing technique (Boesenberg 2006), with orientation indicating the direction of forging (Figures 5.16, 5.25, 5.28, and 5.34) and distribution reflecting the working process (Ryzewski and Gordon 2008). Thoroughly smithed high-quality wrought iron will have a nearly homogeneous distribution of slag of fairly uniform size and morphology throughout its structure (Aston and Story 1939). Samples CAER_13 and 18, and CW_07, 14 and 15 come closest to this ideal. Homogeneity is not always achieved and samples such as CAER_21, CW_08 and CW_26 are often found, where slag distribution is biased towards one region of the structure, or inclusion density is particularly heavy near the original surface or the centre of the object.

Slag inclusions at and near the original surface are reached as corrosion pits progress into the metal structure using slag as a cathode site (Figure 5.21). As a result, chloride collects and corrosion extends deep into the metal core (Figure 5.22, 5.28, 5.33, 5.34). Since slag plays a role in the mechanical properties of wrought iron, this corrosion will affect its physical structure and contribute to breakup of wrought iron objects.

6.1.2.1 Limitations of slag measurement methodology

Measurement of percent area slag by image analysis had limitations. Accurately discriminating slag inclusions from corrosion pits and layers was challenging. The Scenitis image analysis software separated phases provided there were significant differences in grayscale, which was easy for medium to dark-grey slag visible against

light grey ferrite without corrosion products of similar greyscale. Distinguishing slag was difficult when thick CPLs or deep corrosion pits were present alongside inclusions (Figures 5.16, 5.21, 5.22, 5.33). While corrosion pits with morphology distinct from slag were removed in pre-processing, confusing small pits with small slag inclusions remained a risk and may have produced slight over estimation of slag content in some objects.

In most Caerleon and some Colonial Williamsburg nails (CW_26, 29 in Figures 5.34), slag has become incorporated into DPLs as the corrosion horizon has progressed down into the metal. Since the image analysis method cannot distinguish similar greyscale values of CPLs from slag contained within them, only slag contained within the ferrite matrix was measured, which could produce under-reporting of percent area slag that would have been present in the uncorroded object. Caerleon samples will be more affected by this bias, as their thicker corrosion layers have significantly progressed below the original surface. This may be partly responsible for the lower percent area slag measurements for Caerleon compared to Colonial Williamsburg (Figure 5.35). Caerleon nails were expected to have less slag than those from Colonial Williamsburg based on manufacturing process, but the true difference may be less than was recorded.

The limits of slag measurement relate to the size of slag inclusions that can be distinguished and measured, which depends on the magnification, optical and digital resolution of the microscope and digital image capture system. Slag inclusions can vary greatly in size from $\leq 1 \mu\text{m}$ to several hundred μm across. Images were captured at 50X magnification, which allows features of $1 \mu\text{m}$ in diameter to be distinguished. It was

difficult to resolve such small inclusions clearly in digital images at this magnification and imaging at higher magnification and resolution would detect the smallest slag inclusions and increase accuracy of percent area slag determinations.

Since measurements of slag must be 2D for what are 3D microstructures, percent area slag will always be a relative, rather than an absolute, as it does not account for volume of slag. The majority of slag is contained in the form of elongated stringers oriented parallel to the longitudinal axis of the nail (Figures 5.30, 5.31, 5.32, 5.34, 5.35).

6.2 Condition of Nails

Corrosion was more voluminous on Caerleon samples than on most Colonial Williamsburg nails which was confirmed by X-radiography (Figures 5.1-5.2, Appendix 8.6). The presence of chloride (0-2500ppm) was verified by acid digestion of a small sample of 5 untreated nails from each site (Figure 5.12). CPLs of 20 wrought iron nails examined in cross section with OM and SEM-BEI (Figures 5.6-5.9) exhibited morphologies similar to those reported in previous studies (Bertholon 2000, 2007; Neff et al. 2003, 2004). Ferrite metal cores were surmounted by a dense product layer, over which a transformed medium including external markers such as sand grains was often present. Slag inclusions were visible in the ferrite matrix and in many cases also in the dense product layer.

A variegated or 'marbled' appearance was apparent in the DPL as dark grey veins (Figure 5.7). It is supposed that marbling is potentially important for the transfer of electrons through otherwise less-conductive regions of CPLs during corrosion reactions *in situ* (Réguer et al. 2007a) and in atmospheric conditions (Monnier et al. 2011).

General indications of compounds likely to be present are based on analyses of archaeological iron corrosion products from other sites (Neff et al. 2005, 2006a; Réguer et al. 2007a; Chitty et al. 2007, 117). Lighter grey regions are most likely goethite (α -FeOOH), lepidocrocite (γ -FeOOH), or akaganeite (β -FeOOH) and the darker marblings maghemite (γ -Fe₂O₃) and or magnetite (Fe₃O₄) (Chitty et al. 2007) or lepidocrocite and ferrihydrite (Fe₅HO₈·9H₂O) (Monnier et al. 2011). Comparing CPL thickness between Caerleon and Colonial Williamsburg (Figure 5.4, Figure 5.5 Table 5.1) indicates that corrosion layers are thicker in Caerleon nails than for those from Colonial Williamsburg, which may have implications for post-excavation corrosion rates. Mechanisms and rates of corrosion for archaeological iron *in situ* have been the subject of considerable recent research (Neff et al. 2005; 2006b, 2007; Vega et al. 2007). Neff et al. (2005) measured DPL and TM corrosion layers in 54 archaeological wrought iron nails from Glinet, France and found that all samples had a corrosion rate of $\leq 4 \mu\text{m}/\text{year}$, $1.3 \mu\text{m}$ on average, based on a parabolic model of corrosion. This relatively high rate is quite similar to average rates of corrosion of 1.02 and 2.90 $\mu\text{m}/\text{year}$ obtained for Caerleon and Colonial Williamsburg nails based on dividing CPL thickness by approximate age since burial in an archaeological context.

Comparative research (Vega et al. 2007, 106) on Glinet nails based on sodium iodide and ¹⁸O isotope studies of oxygen transport through corrosion layers arrived at much lower rates of corrosion between 0.07 and 0.59 $\mu\text{m}/\text{year}$. Since these two related studies concluded oxygen transport through CPLs to the metal/CPL interface is the rate limiting factor in corrosion rate, the lower values (Vega et al. op. cit.) are much more realistic when CPLs of significant thickness are present. The parabolic model is less

likely to be correct, as it is probable that initial corrosion proceeds more rapidly following a linear model and that events such as cracking of the CPLs may cause 'kinetic breaks' temporarily increasing corrosion rate by providing greater access to dissolved oxygen (Vega et al. 2007, 107). This identifies corrosion morphology and cracking as important factors for determining corrosion rate.

The amount of time an iron artefact has been buried in soil is one factor in past growth of CPLs, but there is no direct relationship between time and CPL thickness as rates of corrosion during burial depend on many environmental factors (Watkinson et al. 2013, 408). Access to oxygen has been shown to be important in the corrosion process and will influence prevalent corrosion reactions (Chapter 2). The thickness, density, porosity, and physical integrity of CPL layers will influence post excavation oxygen access. If oxygen is capable of reaching the site of cathodic reactions the chloride content of the iron object becomes important (Turgoose 1982b).

Microcracks are often present in CPLs of archaeological wrought iron objects (Neff et al. 2005). They may form as a result of impact, freeze-thaw and thermal shock damage while in context, and as a result of post excavation corrosion processes that cause stress on CPLs, leading to fracture. Much of this stress results from increased relative molar volume of ferric oxyhydroxide corrosion products (akaganeite, goethite) as compared with iron metal or ferrous precursors (Selwyn 2004b; Neff et al. 2005; Jegdić et al. 2011). Cracks forming during burial may become marbled regions composed of magnetite or maghemite or be filled with deposits of exogenous elements such as Ca or Si (Neff et al. 2005) that act as markers for pre-excavation cracking events. Other

cracks form during rapid post-excavation corrosion particularly when the chloride results in akaganeite formation.

Microcracks were visible in all samples examined in the current study, but are not present to the same extent and in the same orientation in each nail. It was generally observed that radial cracks extending from the outer CPLs down nearly to the level of the metal/CPL interface were present in samples from Caerleon (Figures 5.6 and 5.7). Such cracks run perpendicular to the surface of the preserved metal core and provide a connection between the core and the outside environment (Figure 6.1).

Another type of cracking, 'concentric cracking', runs in parallel to the metal surface at various levels within CPLs and does not normally reach the level of the metal core or the outer edge of the corrosion crust (Figure 6.2). Sample CW_05 exhibits this concentric cracking, as well as some partial radial cracking which does not reach the metal core (Figure 5.8).

Nails from Colonial Williamsburg generally exhibited concentric cracking and some radial cracking that did not extend throughout the whole thickness of the CPLs (Figure 5.9). Additional SEM images of the samples evaluated for cracking are given in Appendix 8.4.1.

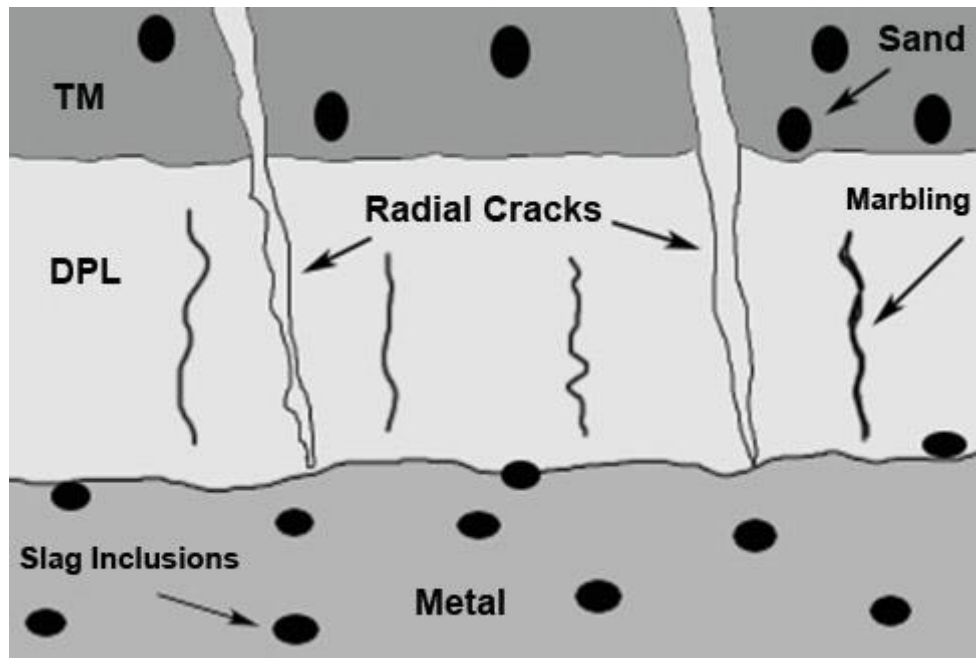


Figure 6.1 Schematic representation of radial cracks present in corrosion product layers of the majority of 10 nails from Caerleon examined in cross-section.

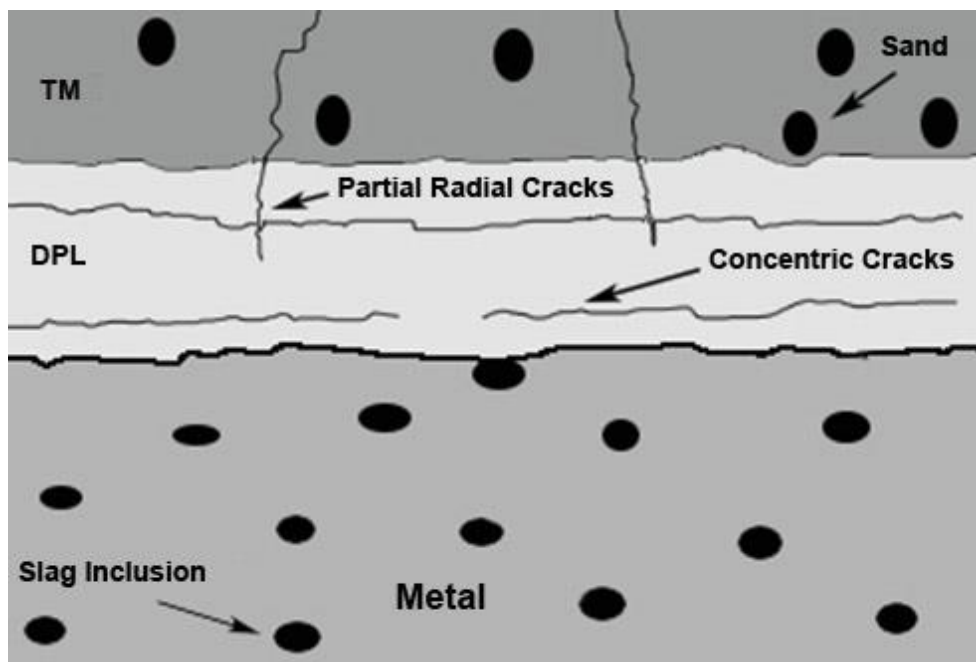


Figure 6.2 Schematic representation of concentric cracks and partial radial cracks present in corrosion product layers of the majority of 10 nails from Colonial Williamsburg examined in cross-section.

Another cause of cracking in treated nails may be from aqueous rinsing to pH 7.0 over several weeks following alkaline sulphite washing at pH 11-12, as the iron was not protected from new corrosion by an anoxic solution or elevated pH during rinsing. Pressure on CPLs caused by corrosion during rinsing may result in radial cracking leading to faster post-treatment atmospheric corrosion rates.

6.3 Corrosion in Atmosphere

Prior to treatment there are significant differences in oxygen consumption behaviour between the two sites (Figures 5.36-5.39). Consumption for Caerleon exceeded Colonial Williamsburg with 16 of 30 samples consuming 40 mbar or more. Many of the samples were still consuming oxygen steadily at day 18, while a few CAER_24, 25, 27, 28 reacted slowly and consumed only 10 mbar O₂ by the end of the test. In contrast Colonial Williamsburg samples (Figure 5.37) consumed much less oxygen over the same period of time than those from Caerleon. The highest consuming sample CW_09, recorded 7.9 mbar over 18 days, less than 5% of the highest consuming Caerleon sample (CAER_29, 163 mbar). The majority of the 30 Colonial Williamsburg samples tested consumed much less than this, with 24 under 2mbar in 18 days (Figure 5.38). When the oxygen measurement error of +/- 2mbar is considered, it can be seen that much of the variance in values for Colonial Williamsburg is within experimental error, with only 2 samples exceeding this error margin. Comparing untreated corrosion rates, Caerleon nails clearly corrode at a faster rate than those from Colonial Williamsburg, many of which do not corrode at all (Figures 5.38 and 5.39). There is also significant variation in rate within sites. Boxplots show the much higher median rate value for Caerleon, but the bottom whisker representing the lowest Caerleon values reaches down to the upper range of Colonial Williamsburg samples (Figure 5.39).

6.3.1 Oxygen consumption in relation to slag and mass

Slag content, microcracks in CPLs and mass of samples can all influence corrosion rate. If the percent area of slag inclusions in wrought iron is a significant factor in atmospheric corrosion, a relationship should be apparent in the data. Plotting oxygen consumption rate as a function of percent area slag for both sites shows no clear pattern (Figure 6.3). Spearman correlation tests (Table 6.1) show a coefficient of $-.389$ at a significance level of $.09$, a slight negative correlation, but not significant to the $.05$ level. There is no clear relationship between amount of slag and atmospheric corrosion rate as measured in this study.

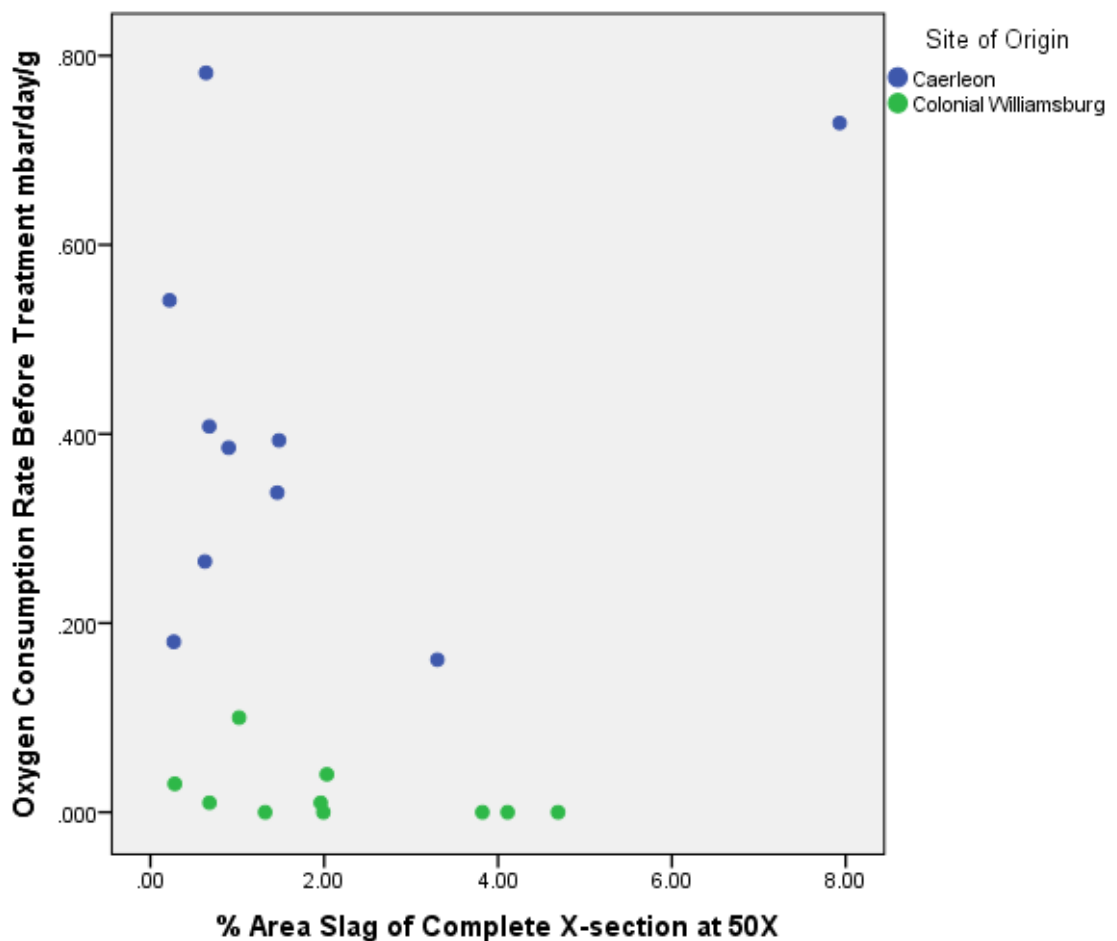


Figure 6.3 Plot of untreated oxygen consumption rate in mbar/day/gram as a function of percent area slag for 10 samples each from the sites of Caerleon and Colonial Williamsburg.

Variables	N	Test	Correlation Coefficient	Significance	Significance Level
Untreated Oxygen Corrosion Rate/Percent Area Slag	20	Spearman	-.389	.09	N/S

Table 6.1 Spearman tests of correlation between pre-treatment oxygen corrosion rate and percent area slag (as determined by OM and SEM-BEI imaging in 10 samples each from Caerleon and Colonial Williamsburg).

Examining oxygen consumption rates of untreated nails as a function of their mass (Figures 5.40 and 5.41) showed no discernible pattern other than clustering based on median oxygen consumption rate (Caerleon) or mass of sample (Williamsburg). The lack of a significant correlation between mass and oxygen consumption rate is confirmed by Spearman statistical tests, which did not indicate correlation significant to the .05 level (Table 5.8). The Spearman non-parametric test of correlation was selected as mass data for the sample nails were not normally distributed (Figure 5.13, Table 5.5). Oxygen consumption corrosion rate measurements are not significantly influenced by mass of the sample nails.

6.4 Alkaline Sulphite Treatment

Total chloride present, chloride extracted during alkaline sulphite treatment, remaining chloride, chloride extraction efficiency and rinsing were related to pre and post-treatment atmospheric corrosion rates and the results are related to observed slag and corrosion product layers.

6.4.1 Chloride Extraction treatment efficiency

Chloride removal by 0.1M NaOH/0.05M Na₂SO₃ desalination at 60°C was significant and efficient for most samples (Table 5.10). Mean extraction efficiency was slightly higher for Caerleon nails which started with more chloride than samples from Williamsburg. Total chloride values for Caerleon and Colonial Williamsburg nails are between 2,125 and 12,568 ppm and 728 and 8,700 ppm respectively (Table 5.10). Alkaline sulphite treatment removed a substantial amount of chloride, between 1,607 and 11,815 ppm for Caerleon samples (mean: 4,553) and 442-8,107 ppm (mean: 2,997) for Williamsburg (Table 5.10). Remaining chloride in the treated nails ranged from 28-

2923ppm (mean: 787ppm) for Caerleon and 218-2401 ppm (mean: 749ppm) for Colonial Williamsburg (Figures 5.60-5.61). Remaining chloride for samples from both sites shows similar mean and median chloride levels (Figure 5.58).

Chloride extraction efficiencies (Remaining Cl^- / Total Cl^- X 100 %) for the two sites ranged from 63-99% for Caerleon and 16-97% for Colonial Williamsburg although the two lowest efficiencies, 16% and 35% for CW_25 and CW_19 can be regarded as outliers (seen as circles in Figure 6.4). The high treatment efficiency of most samples is in line with previous results for alkaline sulphite treatment at 60°C (Rimmer et al. 2012) although the low efficiencies for a few of the Colonial Williamsburg samples are difficult to explain beyond the issue of variation between samples. Although the maximum extraction efficiency is similar for both sites, median and minimum values for Williamsburg are somewhat lower than for Caerleon (Figure 6.4). The lower amount of chloride in Williamsburg samples before treatment is also reflected in this data

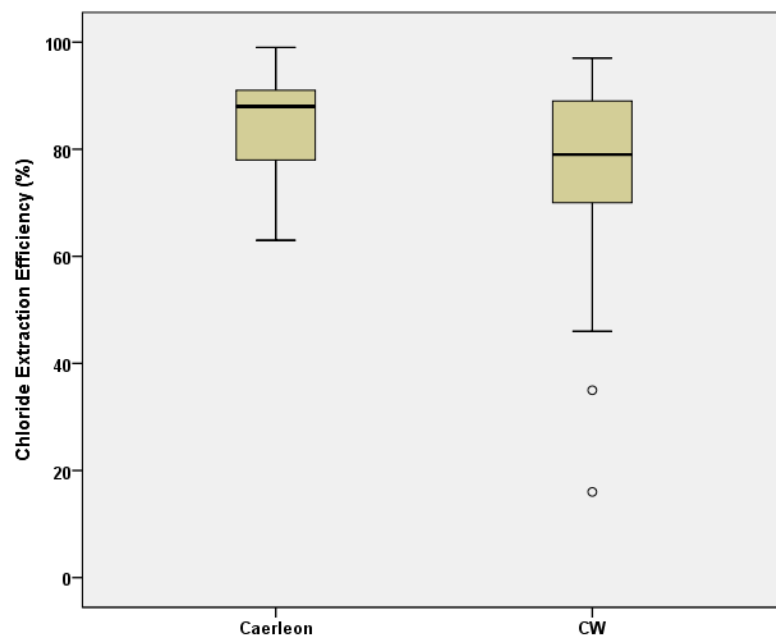


Figure 6.4 Chloride extraction efficiencies (in percent) of 30 samples each from the sites of Caerleon and Colonial Williamsburg treated by alkaline sulphite washing at 60°C

The effect on chloride extraction of including or omitting rinsing to pH 7 following alkaline sulphite washing on remaining chloride content was minimal (Figures 5.62-5.63 and 5.64-5.65). For Caerleon samples the median and range of values is similar between rinsed and unrinsed samples (Figure 5.64). Colonial Williamsburg samples also show variation in remaining chloride and generally lower values for unrinsed samples. Looking at broad trends, there is lower median remaining chloride for unrinsed samples than for rinsed samples from Colonial Williamsburg (Figure 5.65).

Consideration of the effects of rinsing must also take into account the range of total chloride in objects before desalination treatment. This is only possible for the Caerleon samples as the ranges of total and remaining chloride do not overlap, and it can be seen that there is no significant difference in the range of remaining chloride between rinsed and unrinsed samples (Figure 5.64). Based on this data, there is no indication that applying an additional post-treatment rinsing to pH 7 results in significantly lower remaining chloride levels than washing in deionised water for a few seconds following alkaline sulphite treatment of archaeological iron objects.

6.4.2 Post Treatment atmospheric corrosion rate

Post-treatment corrosion rates for Caerleon nails show lower values for most nails, as well as a general trend towards lower consumption in unrinsed compared with rinsed samples (Figures 5.42 and 5.43). Comparisons between untreated and treated (rinsed and unrinsed) samples showed surprising results for individual nails such as CAER_06 which consumed more oxygen in 18 days after treatment than it did in the same amount of time before treatment despite removal of 2312 ppm chloride (Figures 5.46 and 5.47). Differences between untreated and post-treatment oxygen consumption for

Colonial Williamsburg are essentially negligible irrespective of whether they were rinsed or unrinsed (Figures 5.44-5.55 and 5.48-5.49). A reduction in oxygen consumption can be seen in most nails, as well as a general trend towards lower consumption in samples that were unrinsed compared with those that were rinsed. Samples CW_09 and CW_10 were the highest consuming before treatment at 7.9 and 7.1 mbar respectively but consumed 1.2 and 1.9 mbar in the same amount of time and 1.3 and 3.3 mbar during further testing up to 70 days, which indicates no or very little corrosion taking account of meter error (Figure 5.44). Most Colonial Williamsburg samples reached a plateau within 5 days of exposure. The trend is of lower oxygen consumption by unrinsed samples compared to rinsed, that is particularly apparent over the first 18 days, but the amount of oxygen consumed by Colonial Williamsburg samples remains very low in all cases.

Comparing post-treatment oxygen consumption (Figure 5.50) with consumption untreated (Figure 5.39) shows approximately the same relative difference in consumption by site as occurred prior to treatment. Caerleon samples consume more oxygen than those from Colonial Williamsburg both before and after treatment.

Although the majority of Caerleon samples consumed less after treatment than before treatment, their post-treatment consumption rates are spread over a broader range of values. Not all individual samples had significantly reduced rates, and the rate of one outlier (CAER_06) was actually higher after treatment. Rinsed samples consume oxygen at a higher rate than unrinsed samples (Figure 5.51). This effect is much bigger for Caerleon nails but is also evident for Williamsburg.

6.4.3 Effect of chloride content

The well-documented role of chloride ions in post-excavation archaeological iron corrosion (Turgoose 1982b; Réguer et al. 2007a) would suggest that chloride content and oxygen consumption should be related and that lowering chloride through desalination will reduce oxygen consumption. Relating oxygen consumption to total chloride for Caerleon samples before treatment is mainly linear although there are some outliers. In contrast, Colonial Williamsburg samples are clustered at very low levels of oxygen consumption irrespective of their chloride content (Figure 5.66).

Relating post-treatment oxygen consumption to remaining chloride (Figure 5.67) shows Caerleon samples have generally lower oxygen consumption and chloride content than they did before treatment, with a tendency towards a linear relationship, although this is not entirely predictive as samples consuming different levels of oxygen can contain the same amount of chloride. Oxygen consumption and chloride content are strongly positively correlated at the .01 level for Caerleon samples before desalination treatment, but not after treatment (Table 5.11). The two factors are not significantly correlated for Colonial Williamsburg nails before treatment, but although they appear to correlate at the .05 level after treatment, the low level of oxygen consumption must be taken into account. The significant correlation of pre-treatment Caerleon samples is consistent with the model of higher chloride levels resulting in higher oxygen consumption, but the non-significant relationship after treatment is less easy to explain. The lack of clear relationship after the nails were treated may be due to the increased importance of other factors in relation to chloride content.

A significant correlation between low chloride content and low oxygen consumption for Colonial Williamsburg nails after desalination is explicable by a chloride-focused model of corrosion rate but the lack of relationship before treatment is not. This leads to the conclusion that the low chloride and low oxygen values for treated Colonial Williamsburg samples are a coincidence caused by the fact that they consumed almost no oxygen either before or after desalination.

6.4.4 Effect of microcracks and post treatment rinsing

Visual assessment of cracking of nails in cross-section (Figures 5.15-5.34 and Appendix 8.4.1) was used to provide the dataset for Table 6.2. Objects with radial cracks progressing from outer CPLs down to the metal/CPL interface were designated as 'positive' for radial cracking, while samples with only concentric cracking were not. Corrosion layers assessed for cracking in cross-section after alkaline sulphite washing and their relationship with post-treatment oxygen consumption was explored. Mean oxygen consumption rates for radially cracked and un-cracked samples were .09 and .02 mbar/gram/day respectively. Higher median as well as upper quartile maximum oxygen consumption for radially cracked samples are apparent (Figure 6.3), indicating that radial microcracks influence oxygen consumption corrosion rates.

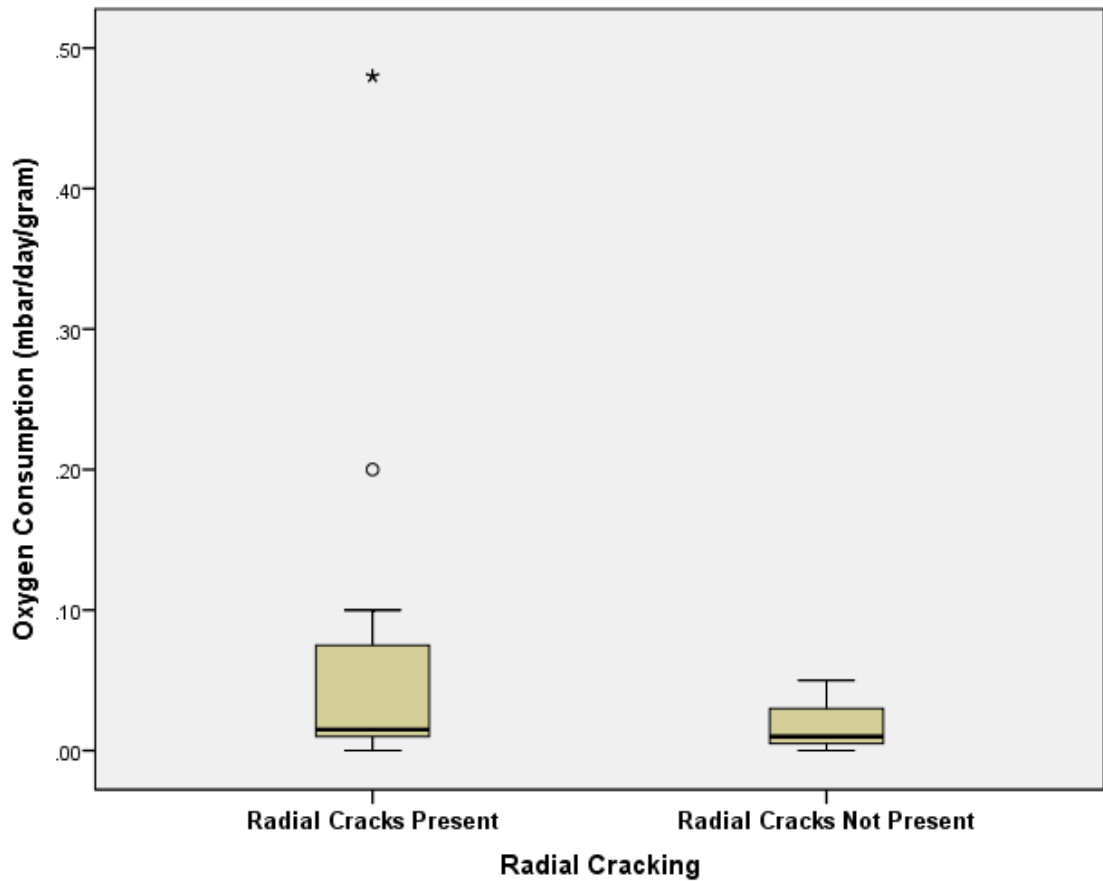


Figure 6.3 Post-treatment oxygen consumption rate as a function of presence or absence of radial cracks observed in cross-sections of 10 nails each for Caerleon and Colonial Williamsburg after alkaline sulphite treatment.

Relating post-treatment remaining chloride to radial cracking reveals the median remaining chloride (500-550 ppm) is nearly the same for both categories of cracking, but chloride values for radially cracked samples extend over a greater range (Figure 6.4). This data does not show the amount of chloride remaining is preferentially associated with presence of radial cracks, but neither does it show the opposite. This may be partially explained by a lack of co-location of radial cracks and chloride in some samples.

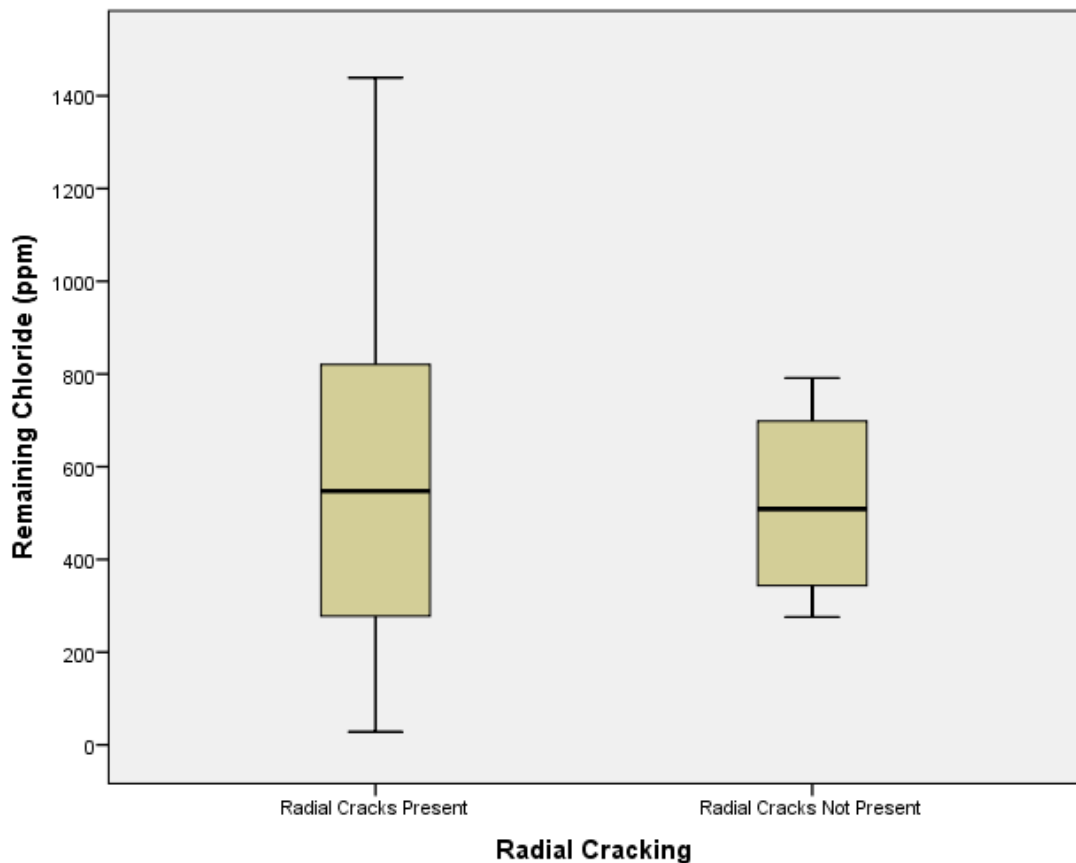


Figure 6.4 Remaining chloride after alkaline sulphite treatment as a function of presence or absence of radial cracks observed in cross-sections of 10 nails each for Caerleon and Colonial Williamsburg after alkaline sulphite treatment.

Four of 15 rinsed Caerleon samples had a higher oxygen consumption rate after treatment than before (Figures 5.52-5.53) which is unexpected as washing had removed a significant amount of chloride. Thirteen out of 15 unrinsed samples had significantly lower oxygen consumption rates than rinsed samples.

Post-treatment oxygen consumption of Colonial Williamsburg nails show a more varied picture, but few conclusions can be drawn from this data as the differences between individual samples are small and in some cases within experimental error of +/- 2 mbar O₂ (Figures 5.54-5.55). Some rinsed samples such as CW_09, CW_10 and CW_13 show a clear drop in consumption, while others (CW_06, CW_24, CW_25) have nearly zero consumption before treatment and positive consumption afterwards. While unrinsed

Colonial Williamsburg samples have lower post-treatment oxygen consumption than rinsed samples, nothing can be inferred from the data due to the very small changes recorded and the meter error range (Figure 5.55).

Untreated oxygen consumption rates of groups subjected to either rinsed or unrinsed protocols were not the same for either site (Figure 5.56 and Table 5.9). This may be due to non-uniformity of the archaeological samples, or just the absence of one sample with high or low chloride which would alter the range within the boxplot (Section 3.6.4). Compared to untreated rates, oxygen consumption was reduced to a greater extent in unrinsed Caerleon samples while rinsing shifted the range of corrosion rates slightly higher in Williamsburg samples (Figure 5.57, Table 5.9).

No rinsed samples were without radial cracks and irrespective of site origin, post-treatment oxygen consumption is higher for samples with radial microcracks than those without them (Table 6.2 and Figure 6.5). There is significant correlation between the presence of radial microcracks and rinsing of samples after alkaline sulphite treatment (Table 6.3), and between higher oxygen consumption rate after treatment and post treatment rinsing of Caerleon samples (Figure 6.5, Table 6.3), This suggests that radial cracks likely result from corrosion during uninhibited aqueous rinsing.

Sample	Rinsing Protocol R=Rinsed UR= Unrinsed	Figure: OM/SEM Image	Radial Cracking Yes/No	Post-Treatment Corrosion Rate (mbar/gram/day)
CAER_01	R	5.15/8.1	Yes	.20
CAER_07	R	5.16/8.2	Yes	.48
CAER_08	R	5.17/8.3	Yes	.02
CAER_10	R	5.18/8.4	Yes	.05
CAER_13	R	5.19/8.5	Yes	.48
CAER_18	UR	5.20/8.6	Yes	.00
CAER_19	UR	5.21/8.7	Yes	.01
CAER_21	UR	5.22/8.8	Yes	.05
CAER_22	UR	5.23/8.9	Yes	.10
CAER_27	UR	5.24/8.10	No	.05
CW_05	R	5.25/8.11	Yes	.01
CW_07	R	5.26/8.12	Yes	.01
CW_08	NR	5.27/8.13	No	.01
CW_09	R	5.28/8.14	Yes	.01
CW_14	UR	5.29/8.15	No	.00
CW_15	UR	5.30/8.16	No	.01
CW_16	R	5.31/8.17	Yes	.01
CW_19	R	5.32/8.18	Yes	.01
CW_26	R	5.33/8.19	Yes	.02
CW_29	R	5.34/8.20	Yes	.00

Table 6.2 Post treatment rinsing protocol Rinsed (R) or Unrinsed (UR) applied to 20 samples of wrought iron nails from the sites of Caerleon and Colonial Williamsburg, together with Figure reference for OM/SEM-BSE image, presence or absence of radial cracks penetrating through the corrosion layers and post alkaline sulphite treatment oxygen consumption in mbar/g/day.

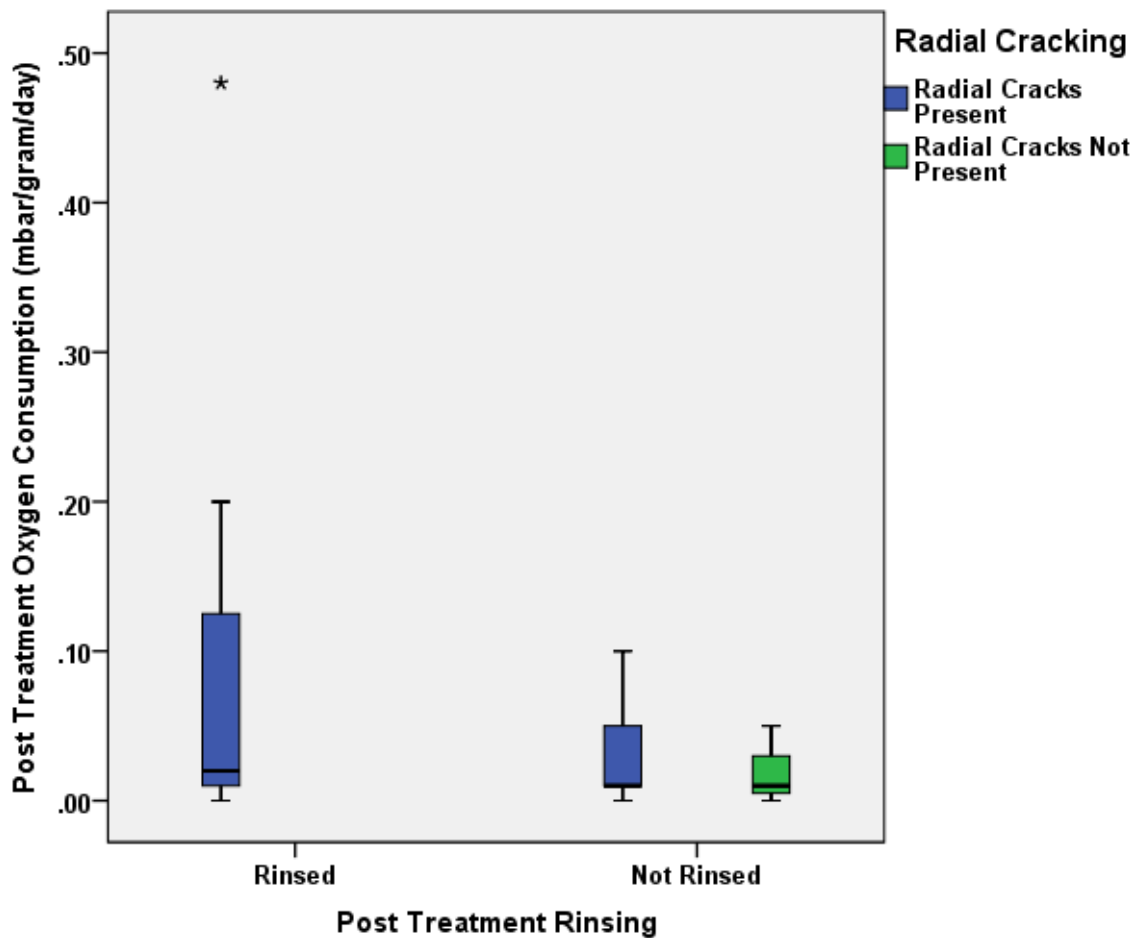


Figure 6.5 Post-treatment oxygen consumption of all samples as a function of rinsing protocol and presence or absence of radial cracks in the samples.

Factors Compared	Samples/(N)	Correlation Test	Correlation Coefficient	Significance
Radial Cracking/Post Treatment Rinsing	CAER (10) CW (10)	Pearson	.553	.011
Change in Oxygen Consumption Rate/Post Treatment Rinsing	CAER (30)	Spearman	.803	.005

Table 6.3 Results of Pearson test of correlation for presence of radial cracking with post treatment rinsing protocol for 10 samples each from Caerleon and Colonial Williamsburg, and Spearman tests of correlation for post-treatment oxygen consumption with post treatment rinsing for 30 samples from Caerleon and Colonial Williamsburg. Significance level was .05. Non-parametric Spearman tests used for values incorporating non-normally distributed mass data.

6.4.5 Effect of percent area slag

No clear pattern or relationship between remaining chloride and percent area slag is apparent for either site (Figure 5.72). Caerleon samples are randomly distributed with different amounts of chloride present in nails that have the same percent area slag. Only three of the Colonial Williamsburg samples show a trend of increasing chloride with percent area slag and values for the rest of the samples from the site appear random. Overall, there is no evidence of a significant correlation between chloride content and percent area slag in archaeological wrought iron as investigated in this study (Table 5.12).

Lack of correlation between percent area slag and chloride content may be due to methodological issues with slag measurement (Section 6.1.2) or that they are only significantly related in specific objects. Also, chloride can be present for other reasons apart from its association with slag and slag is not necessarily accessible to chloride. A large amount of slag at the metal surface will favour chloride concentration at the anode sites that will develop with slag acting as the cathode. The resulting pits will further concentrate chloride, influencing the chloride to slag ratio. Thus a large amount of slag within the body of an object coupled with a low surface concentration may produce a different ratio to one with less slag in the bulk of the metal but a greater amount accessible to chloride at its surface.

6.5 Microanalysis of treated samples

The presence of chloride in wrought iron nails after treatment and its potential relationship to other variables were also evaluated by SEM-WDS mapping and SEM-EDS linescan analysis of alkaline sulphite treated samples (Figures 5.69-5.70, Tables 5.13-5.14 and Appendices 8.4.2-8.4.3). These microanalytical techniques are subject to some limitations. Nails were examined in only one transverse plane, and it was not possible to analyse them in entire cross sections. The random sampling strategy may or may not have sampled areas with Cl⁻ after treatment as chloride is not evenly distributed and treatment seeks to remove it from the metal-CPL interface. Uneven distribution of chloride in different regions of the metal/CPL interface has been seen in previous studies (Réguer et al. 2007a).

6.5.1 Location and concentration of chlorine in treated nails

SEM-WDS mapping detected limited residual chlorine in corrosion product layers and very little around slag inclusions (Figure 5.69, Appendix 8.4.2, Table 5.14). Chlorine that was detected was found at the metal/CPL interface or in deep pits, which is expected as these are areas where it collects due to corrosion mechanisms (Section 2.3.2).

Chlorine was more evident in samples from Caerleon than from Colonial Williamsburg, which likely testifies to the random sampling procedure limitations, since both sites retained similar ranges of chloride post-treatment (5.62-5.65). SEM-EDS linescans detected chlorine in CPLs in a greater number of the samples than SEM-WDS but some results were below or on the edge of reliable EDS detection limits. Overall, chlorine was detected in pits and at metal/CPL interfaces, inside cracks in the DPL, and on the outside surface of the CPLs. SEM-EDS detected chlorine in slag inclusions in only 8 out of 20 samples not associated with corrosion pits. The localisation of chloride could

contribute to the differences in corrosion rate for smaller amounts of chloride present in nails post-treatment.

More residual chlorine is present in sampled CPLs and around slag inclusions in nails from Caerleon than from Colonial Williamsburg. Chlorine is still present at the metal/CPL interface of some nails, indicating incomplete chloride removal. Chlorine in the DPLs and outside the CPLs of some samples is likely present as a result of incomplete diffusion from the metal/CPL interface. This seems to be supported by four out of seven unrinsed samples in which chlorine was detected on the outer surface of CPLs. While the rinsing procedure may have removed the chloride from the metal/CPL interface and DPL layers which was en-route to the surface of the corrosion layers, the evidence for this is not statistically significant. Chloride on the outer surface of the CPLs does not offer greater risk of post-treatment corrosion as it is physically separated from the metal/CPL interface where iron must provide anode sites for corrosion reactions to occur. Any increased risk from chloride on the outside of CPLs is likely to be primarily due to hygroscopicity of NaCl at $\geq 75\%$ RH (Rimmer and Watkinson 2010). Data on oxygen consumption rates of rinsed and unrinsed alkaline sulphite treated iron samples instead indicates that at 80% RH, rinsed iron objects are likely to corrode faster than those left unrinsed. This is likely due to their extensive radial cracking offering access to the metal/CPL interface.

6.6 Akaganeite Transformation

The results of the akaganeite transformation experiments differ from some previous studies that centred on alkaline washing solutions used when treating archaeological iron (Figures 5.71-5.74, Table 5.16-5.17 and Appendix 8.4.4). All 10 samples of

synthetic akaganeite did not retain akaganeite after 30 days in alkaline sulphite treatment at 60°C. In the same conditions, Rimmer (2010) reported partial transformation of β -FeOOH (Table 6.4). Akaganeite placed in 0.1M NaOH produced results consistent with Cornell and Giovanoli (1990), who recorded transformation to a mixture of goethite and hematite at pH 11-15 and $\text{OH}^- < 0.5\text{M}$ or $> 2\text{M}$. Within the 0.5-2M range akaganeite transformation produced only goethite (Table 6.4).

The mean percentage of goethite and hematite determined by XRD-RIR for 10 alkaline sulphite treated akaganeite samples was 69% and 31% (Table 5.18). Percentage hematite fell in between the values of 20% and 55% obtained by Cornell and Giovanoli for somatoidal akaganeite crystals immersed respectively in 0.1 and 0.01M OH^- solutions. Their data also indicated that transformation to 31% hematite will occur if rod shaped akaganeite crystals are present (Cornell and Giovanoli 1990).

Results of tests here align with those for 2 samples tested by Schmutzler (2012), who observed complete transformation of akaganeite powder to hematite and goethite using 0.1 M concentration of OH^- without sodium sulphite at 70°C for a maximum of 21 days. This mirrors the results of Al-Zahrani who confirmed that it is the hydroxyl ions that are important for transformation of akaganeite in aqueous solutions (Al-Zahrani 1999).

Study	Conditions	Result
Cornell and Giovanoli 1990	< 0.5 >2M OH ⁻ 0.5 - 2M OH ⁻	akaganeite→goethite+hematite akaganeite→goethite
Al-Zaharani 1999	0.5M NaOH 20°C 120 days	akaganeite→goethite (complete)
Rimmer 2010	0.1-1M NaOH 20°C 0.1-1M NaOH 60°C 28 days	akaganeite→goethite akaganite→goethite+hematite (partial)
Schmutzler 2012	0.1M NaOH 70°C 21 days	akaganeite→goethite + hematite (complete)
Bayle et al. 2016	Subcritical 0.125M NaOH 160°C, 35 bar 3-4 hours	akaganeite→hematite (complete)

Table 6.4 Results of previous studies on the transformation of synthetic akaganeite in alkaline solutions.

Results of the current study are significant as the complete transformation of akaganeite in 0.1M NaOH/0.5M Na₂SO₃ over a 30 day period at 60°C was achieved at significantly lower temperatures and pressures than were present for complete or near complete akaganeite transformation during alkaline desalination in other studies (Drews et al. 2014; Bayle et al. 2016). These results show breakdown of akaganeite and release of occluded chloride during heated alkaline sulphite washing treatments is a realistic possibility.

Results here (Section 5.4) are for synthetic akaganeite powder. The greater surface area of this finely divided akaganeite powder, as compared with the solid akaganeite in CPLs means that transformation is likely to have been faster and more complete than it might have been in solid CPLs, where porosity and access to the treatment solution is limited. This corrosion product morphology will influence whether akaganeite transformation occurs and the rate of change given it is normally next to the metal surface.

Using akaganeite prepared by solid-state reaction between iron powder and FeCl_2 at > 90% RH may also have influenced the transformation results. A number of different synthetic akaganeite crystal morphologies have been observed depending on how they were prepared. Somatoidal or 'cigar shaped' crystals result from hydrolysis of FeCl_3 solution at pH 1.2 or rod-shaped crystals if this solution is partially neutralized with NaOH first (Cornell and Schwertmann 2000). Synthetic akaganeite produced by this method has been used in most akaganeite studies (Stahl et al. 2003; Schmutzler 2012; Bayle et al. 2016), while the solid state FeCl_2 -iron powder reaction has been used by Al-Zahrani (1999), Lewis (2009), Rimmer (2010), and in the current study. The crystal morphology of synthetic β - FeOOH produced by the solid state reaction method has not been determined. The possibility that different morphological types of synthetic akaganeite crystals transform in different ways must be considered. The current experiments should only be directly compared to studies which have used the solid-state powder method listed above.

The differences in behaviour of synthetic iron corrosion products and naturally formed products means researchers have questioned whether synthetic iron compounds should be used in archaeological conservation research (Rimmer 2010; Bayle et al. 2016). This parallels justification for using archaeological iron objects rather than modern analogues in conservation research (Section 4.4). While standardization presents challenges, naturally formed products and corrosion layers are likely to give a more accurate picture of how archaeological objects respond.

6.7 Discussion Summary

6.7.1 Oxygen consumption rate and chloride content of Caerleon nails

The relationship between oxygen consumption and chloride content is significantly correlated and approximately linear for Caerleon samples before treatment, but not after treatment. This pattern recorded for Caerleon nails may be due to the nature of the samples studied, which may be anomalous in some respect. However, a similar pattern was observed for a group of 10 nails from Billingsgate, London (Watkinson and Rimmer 2014) in which a significant correlation between oxygen consumption rate and chloride was found before treatment but not after alkaline sulphite desalination, indicating the results for Caerleon are not unique.

Higher chloride concentrations present before desalination treatment result in more corrosion, consuming more oxygen and yielding an approximately linear relationship between chloride and oxygen consumption. The amount of chloride present may be the most influential corrosion variable in pre-treatment conditions, greater than the CPL morphology that determines oxygen and water transport to corrosion sites. When chloride levels are reduced, overall corrosion rates may be lower, but the relatively greater effect of other variables such as CPL morphology, porosity, and cracking and the location and accessibility of remaining chloride mean that the relationship between oxygen consumption and amount of chloride is not straightforward and no clear correlation between the two factors is evident. While this explanation would appear to fit current models of archaeological iron corrosion and the known variability of CPL morphology, conclusions can only be drawn for the objects tested. As always, it must be kept in mind that these trends were observed at a high RH of 80%, and may

not reflect the oxygen consumption patterns of wrought iron at lower RH, particularly at 20% and below where corrosion mechanisms based on the influence of $\text{FeCl}_2 \cdot 2\text{H}_2\text{O}$ and $\beta\text{-FeOOH}$ will dominate (Watkinson and Lewis 2005b; Lewis 2009).

6.7.2 Oxygen consumption and chloride content of Colonial Williamsburg nails

A surprising trend in the data was the extremely low oxygen consumption of nails from Colonial Williamsburg both before and after desalination treatment, despite removal of large amounts of chloride during treatment (Section 5.2.3, 5.3.2, 6.4.3). This contrasts with Caerleon samples where both oxygen consumption and chloride content are reduced post-treatment. Corrosion layers are thicker in the CPLs of Caerleon samples and exhibit many radial cracks extending to the metal/CPL interface (Figure 6.1), whereas the thinner CPLs on Colonial Williamsburg samples largely contain concentric or parallel cracks (Figure 6.2).

Recent corrosion models for archaeological iron indicate that oxygen and/or water vapour must diffuse down through pores and cracks in corrosion layers to the metal/CPL interface where both anodic and cathodic corrosion reactions take place (Vega et al. 2005, 2007, 107). Increased porosity or cracking would therefore facilitate oxygen penetration to increase rates of chloride-driven corrosion. Radial cracks allow large amounts of oxygen to reach the metal/CPL interface, replacing penetration through nanopores in the CPL structure as the controlling factor for oxygen delivery (Dillmann et al. 2004). This could explain the slow/no corrosion of Colonial Williamsburg nails despite them containing substantial amounts of chloride.

Retaining the integrity of the CPL post-treatment will also influence corrosion rate irrespective of the amount of chloride remaining in objects. A counter to this reasoning is that significant chloride was removed from Colonial Williamsburg samples during alkaline sulphite treatment. This required diffusion processes through the corrosion layer saturated with treatment solution. No clear rationale can explain this, particularly as an exemplar diffusion coefficient at 25°C for O₂ gas in water ($2.10 \times 10^{-5} \text{ cm}^2\text{s}^{-1}$) is higher than chloride diffusion in aqueous solution ($1.25 \times 10^{-5} \text{ cm}^2\text{s}^{-1}$) (Cussler 1997). Complete saturation of the CPL over the long treatment time period may partially influence this and the concentric cracking will contribute to improved diffusion rates through the CPL.

6.8 Conclusion

Nails from Roman Caerleon have thicker corrosion product layers than those from Colonial Williamsburg, and more extensive radial cracking. The composition profile of all of the Caerleon nails is consistent with bloomery smelting, while a majority of Williamsburg nails have compositions associated with blast furnace and finery/puddling production methods. The slag inclusion content of nails from Colonial Williamsburg was higher than for Caerleon. This is consistent with the iron working processes used for the two sites. Total chloride present in untreated nails from the two sites is of a similar range to other terrestrial archaeological iron objects. Oxygen consumption rates for untreated samples from Caerleon showed a linear relationship with chloride content, but those from Colonial Williamsburg did not and inexplicably consumed much less oxygen than expected, taking into consideration their chloride content. Many Williamsburg nails failed to register any oxygen consumption during the 18 day test.

Following alkaline sulphite washing, oxygen consumption of Caerleon samples was reduced by up to 62%, but was unchanged for Williamsburg samples attesting to the success of alkaline sulphite in reducing corrosion rate. The relationship between oxygen consumption and chloride content was less clear for Caerleon nails after treatment than before. In line with their stability before treatment, Colonial Williamsburg nails again showed negligible consumption with the result that meaningful correlation of chloride content with oxygen consumption rate was not possible. A significant difference between oxygen consumption of samples according to whether they were rinsed or unrinsed post-treatment offers useful information on the value of post-treatment rinsing following alkaline sulphite desalination. Rinsed samples consumed oxygen at a faster rate than unrinsed samples for both sites and significant radial microcracking of CPL layers coincided with higher post-treatment oxygen consumption and post-treatment rinsing protocol. These results suggest that any prolonged rinsing has to be a controlled process, during which iron is not able to corrode. Radial cracking may well result from rinsing protocols where corrosion can occur and this clearly aids post-treatment corrosion. Controlling corrosion during rinsing requires careful thought, as chemical inhibition will leave residues in objects when the goal of rinsing is to remove treatment chemical residues. Further, there was no evidence in this study that alkaline sulphite residues impact post-treatment corrosion rate, nor that rinsing improves chloride extraction efficiency.

There was no clear relationship or statistical correlation between percent area slag and post-treatment remaining chloride or oxygen consumption for the wrought iron samples studied. Much more work is required to overcome the limitations of the 2D

analysis of slag to assess its influence on corrosion rate post-excavation and the quantity of chloride in objects.

Regarding post-excavation management of archaeological iron, results show that chloride containing iron objects covered by intact voluminous corrosion layers may be less stable than those with thinner CPLs due to the presence of radial cracks and oxygen consumption measurements are needed to assess iron artefact stability (Matthiesen and Stemann-Petersen 2014). Outcomes of desalination treatments in terms of reduction in post-treatment corrosion rates, irrespective of amount of chloride released, may be unpredictable and require more study. Removal of occluded as well as surface adsorbed chloride through transformation of akaganeite in 60°C 0.1M NaOH/0.05M Na₂SO₃ desalination is realistic in a 30 day treatment and this can be utilised when designing treatment protocols. Extensive rinsing of archaeological iron to pH 7 following alkaline desalination treatments without protective measures may do more harm than good and should be reconsidered. Given the limited risk posed by alkaline sulphite residues promoting further corrosion (Rimmer and Watkinson 2010) and the benefit of not rinsing shown here it may be discouraged. It is also possible that NaOH remaining in unrinsed iron objects may inhibit further corrosion.

6.9 Further Work

A further study evaluating oxygen consumption of archaeological wrought iron treated by desalination methods such as electrolytic reduction or subcritical fluid extraction would allow parallel data to be gathered and build towards a more comprehensive and quantitative picture of the efficacy of available conservation treatments for

archaeological iron. Additional tests utilising alternative methods of slag measurement could be done to either support or disprove the hypothesis that slag is a significant factor in archaeological iron chloride retention and corrosion processes.

Samples from Colonial Williamsburg did not consume significant oxygen either before or after alkaline sulphite treatment, and consumption rates were not affected by the removal of chloride. This surprising result indicates that certain assemblages of wrought iron artifacts may behave unexpectedly, deviating from established patterns of chloride content, corrosion and oxygen consumption. Further study of Colonial Williamsburg iron should be undertaken to ascertain whether this is a reproducible outcome and to develop the theories on radial/concentric cracking put forward here.

Post-treatment rinsing aims to remove soluble chloride and treatment chemicals to prevent precipitation of visually obscuring and hygroscopic residues. Results indicating that post-treatment rinsing increases corrosion rates for alkaline sulphite treated iron should be investigated further on a larger scale with more analysis and different rinse periods.

Oxygen consumption rates of wrought iron nails with varying CPL morphologies and patterns of microcracking were shown to be different. A much larger study focusing on relationships between CPL morphology, cracking, and oxygen consumption corrosion rates of archaeological iron is needed to ascertain whether these effects are statistically significant.

7 References

Abbaschian, R., Abbaschian, L. and Reed-Hill, R. E. 2010. *Physical Metallurgy Principles*. 4th ed., SI Units ed. Stamford: Cengage Learning.

Allan Hamilton, W. 2000. Microbial Influenced Corrosion in the Context of Metal Microbe Interactions. In: Sequeria, C.A.C. ed. *Microbial Corrosion: Proceedings of the 4th International EFC Workshop*. Lisbon: European Federation of Corrosion/IOM Communications.

Alvarez, M. G. and Galvele, J. R. 2010. Pitting Corrosion. In: Cottis, R.A., et al. eds. *Shreir's Corrosion*. 4th ed. Vol. 2. Amsterdam: Elsevier.

Al-Zahrani, A. 1999. *Chloride ion removal from archaeological iron and β -FeOOH*. PhD Thesis, University of Wales Cardiff.

Angelini, E., Grassini, S. and Tusa, S. 2013. Underwater corrosion of metallic heritage artefacts. In: Watkinson, D. et al. eds. *Corrosion and conservation of cultural heritage metallic artefacts*. Cambridge: Woodhead, pp. 236-259.

Argo, J. 1982. The treatment of corrosion with amines. *Conservation News* (17), pp. 7-9.

Argyropoulos, V., Giannoulaki, M. and Charalambous, D., 2015. *The conservation of underwater metal shipwrecks and find from the Aegean: Manual of good practice (in Greek)*. Athens: Dionikos.

Askey, A., Lyon, S. B., Thompson, G. E., Johnson, J. B., Wood, G. C., Cooke, M. and Sage, P. 1993. The corrosion of iron and zinc by atmospheric hydrogen chloride. *Corrosion Science* (34), pp. 233-247.

Aston, J. and Story, E. B. 1939. *Wrought Iron Its Manufacture, Characteristics, and Applications*. 2nd ed. Pittsburgh: A. B. Byers Company.

Barker, D. 2003. Conservation of Metals. In: Jones, M. ed. *For Future Generations: Conservation of a Tudor Maritime Collection*. Portsmouth: The Mary Rose Trust Ltd., pp. 75-94.

Barker, D. 2006. Metals. In: May, E. and Jones, M. eds. *Conservation Science: Heritage Materials*. Cambridge: The Royal Society of Chemistry.

Barkman, L. 1977. Conservation of rusty iron objects by hydrogen reduction. In: Floyd-Brown, B. et al. eds. *Corrosion and metal artifacts-a dialogue between conservators and archaeologists and corrosion scientists*. Washington, DC: US Department of Commerce-National Bureau of Standards, pp. 155-166.

Bayle, M., de Viviés, P., Memet, J. B., Foy, E., Dillmann, P. and Neff, D. 2016. Corrosion product transformations in alkaline baths under pressure and temperature: the sub-critical stabilisation of marine iron artefacts stored under atmospheric conditions. *Materials and Corrosion* 67(2), pp. 190-199.

Beaudoin, A., Clerice, M.-C., Francoise, J., Labbe, J.-P., Loeper-Attia, M.-A. and Robbiola, L. 1997. Corrosion d'Objets Archéologiques en Fer après Dechloruration par la Methode au Sulfite Alcalin: Caracterisation Physico-Chimique et Retraitement Electrochimique. In: MacLeod, I.D. et al. eds. *Metal 95: Proceedings of the International Conference on Metal Conservation*. Semur en Auxois, 25-28 September 1995. London: James and James.

Bertholon, R. 2000. *La limite de la surface d'origine des objets metalliques archeologiques, caracterisation, localisation et approche de mecanismes de conservation*. PhD, Universite Paris 1 Pantheon-Sorbonne.

Bertholon, R. 2007. Archaeological metal artefacts and conservation issues: long-term corrosion studies. In: Dillmann, P. et al. eds. *Corrosion of metallic heritage artefacts: Investigation, conservation and prediction for long-term behaviour*. Cambridge: Woodhead and Boca Raton: CRC Press, pp. 31-40.

Birch, T. and Martín-Torres, M. 2015. Iron bars from the 'Gresham Ship': Employing multivariate statistics to further slag inclusion analyses of ferrous objects. *Historical Metallurgy* 48(1 and 2), pp. 69-78.

Boesenberg, J. S. 2006. Wrought Iron from the USS *Monitor*: Mineralogy, Petrology and Metallography. *Archaeometry* 48(4), pp. 613-631.

Book Archive 2012. *Principles of General Chemistry: Corrosion* [Online]. Available at: <http://2012books.lardbucket.org/books/principles-of-general-chemistry-v1.0/s23-06-corrosion.html> [Accessed: 5/6/2016].

Bowens, A. 2009. Archaeological conservation and first aid for finds. In: Bowens, A. ed. *Underwater Archaeology: The NAS Guide to Principles and Practice*. 2nd ed. Online: The Nautical Archaeology Society, pp. 148-162.

Bowles, J. F. W. Howie, R.A., Vaughan, D. J. and Zussman, J. 2011. *Non-Silicates: Oxides, Hydroxides, and Sulphides*. Second ed. London: The Geological Society.

Bryce, T. 1979. Alkaline sulphite treatment of iron at the National Museum of Antiquities of Scotland. In: Slater, E. and Tennant, N. eds. *The Conservation and Restoration of Metals*. Edinburgh: Scottish Society for Conservation and Restoration.

Buchwald, V. F. and Wivel, H. 1998. Slag Analysis as a Method for the Characterization and Provenancing of Ancient Iron Objects. *Materials Characterization* 40, pp. 71-96.

Campbell, F. C. ed. 2008. *Elements of Metallurgy and Engineering Alloys*. Materials Park: ASM International.

- Cain, J. R. 1924. Influence of Sulphur, Oxygen, Iron and Manganese on the Red-Shortness of Iron. In: Technologic Papers of the National Bureau of Standards. Washington: Government Printing Office.
- Caple, C. 2000. *Conservation Skills: Judgement, Method, and Decision Making*. London: Routledge.
- Chitty, W. J., Dillmann, P., L'Hostis, V. and Lombard, C. 2005. Long-term corrosion resistance of metallic reinforcements in concrete—a study of corrosion mechanisms based on archaeological artefacts. *Corrosion Science* 47(6), pp. 1555-1581.
- Chitty, W. J., Huet, B., Dillmann, P., L'Hostis, V., Beranger, G. and Idrissi, H. 2007. Long-term behaviour of iron embedded in concrete: from the characterisation of archaeological analogues to the verification of the oxygen reduction as the limiting step for corrosion rate. In: Dillmann, P. et al. eds. *Corrosion of metallic heritage artefacts*. Cambridge: Woodhead, pp. 109-130.
- Cornell, R. M. and Giovanoli, R. 1990. Transformation of Akaganeite into Goethite and Hematite in Alkaline Media. *Clays and Clay Minerals* 38(5), pp. 469-476.
- Cornell, R. M. and Schwertmann, U. 2000. *Iron Oxides in the Laboratory*. 2nd ed. Weinheim: Wiley-VCH.
- Cornell, R. M. and Schwertmann, U. 2003. *The Iron Oxides: Structure, Properties, Reactions, Occurrences and Uses*. 2nd ed. Weinheim: Wiley-VCH.
- Costain, C. G. 2000. Evaluation of Storage Solutions for Archaeological Iron. *Journal of the Canadian Association for Conservation* 25, pp. 11-20.
- Cotterell, T. 2015. Email communication Received 30/09/2015.
- Craddock, P. T. 2010. *Early Metal Mining and Production*. London: Archetype Publications.
- Creswell, J. W. 2014. *Research Design: Qualitative, quantitative, and mixed methods approaches*. 4th ed. London: Sage Publications.
- Cronyn, J. M. 1990. *The Elements of Archaeological Conservation*. London: Routledge.
- Cudennec, Y. and LeCerf, A. 2006. The transformation of ferrihydrite into goethite or hematite, revisited. *Journal of Solid State Chemistry* 179, pp. 716-722
- Cussler, E. L. 1997. *Diffusion: Mass Transfer in Fluid Systems*. 2nd ed. New York: Cambridge University Press.
- Daniels, V. D., Holland, L. and Pascoe, M. W. 1979. Gas plasma reactions for the conservation of antiquities. *Studies in Conservation* 24, pp. 85-92.

Dillmann, P. and L'Heritier, M. 2007. Slag inclusion analyses for studying ferrous alloys employed in French medieval buildings: supply of materials and diffusion of smelting processes. *Journal of Archaeological Science* 34(11), pp. 1810-1823.

Dillmann, P., Mazaudier, F. and Hœrlé, S. 2004. Advances in understanding atmospheric corrosion of iron. I. Rust characterisation of ancient ferrous artefacts exposed to indoor atmospheric corrosion. *Corrosion Science* 46(6), pp. 1401-1429.

Dillmann, P., Neff, D. and Feron, D. 2014. Archaeological analogues and corrosion prediction: from past to future: a review. *Corrosion Engineering, Science, and Technology* 49(6), pp. 567-576.

Drews, M., de Viviés, P., González, N. and Mardikian, P. 2004. A study of the analysis and removal of chloride in iron samples from the "Hunley". In: Ashton, J. and Hallam, D. eds. *Metal 2004: proceedings of the international conference on metals conservation*, Canberra, 4-8 October 2004. Canberra: National Museum of Australia, 247-60.

Drews, M., González-Pereyra, N. and Cook, D. 2014. The transformation of iron oxides, oxyhydroxides and corrosion products by subcritical water treatment. In: Hyslop, E., et al. eds. *Metal 2013: Interim Meeting of the ICOM-CC Metal Working Group*. Edinburgh, 16-20 September 2013. Edinburgh: Historic Scotland and International Council of Museums, pp. 111-118.

Drews, M., González-Pereyra, N. G., Mardikian, P. and de Viviés, P. 2013. The application of subcritical fluids for the stabilization of marine archaeological iron. *Studies in Conservation* 58(4), pp. 314-325.

Ehrenreich, R. M. and Strahan, K. 1987. The effects of boiling on the quenched steel structure of martensite. In: Black, J. ed. *Recent Advances in the Conservation and Analysis of Artefacts*. London: Summer Schools Press.

Emmerson, N. 2015. *Heritage wrought iron: towards the development of evidence based standards for coating*. PhD Thesis, Cardiff University.

Emmerson, N. and Watkinson, D. 2014. Protective coatings for historic wrought iron, qualitative assessment to produce evidence-based protocols. In: Hyslop, E., et al. eds. *Metal 2013: Interim Meeting of the ICOM-CC Metal Working Group*. Edinburgh, 16-20 September 2013. Edinburgh: Historic Scotland and International Council of Museums, pp. 119-127.

Emmerson, N. J. and Watkinson, D.E. 2016. Surface Preparation of historic wrought iron: Evidencing the requirement for standardisation. *Materials and Corrosion* 67(2), pp. 176-189.

Ermrich, M. and Opper, D. 2013. XRD for the analyst: Getting acquainted with the principles. *X-Ray Powder Diffraction*. Almelo: Panalytical.

Evans, U. R. 1960. *The Corrosion and Oxidation of Metals*. London: Edward Arnold.

Field, A. P. 2009. *Discovering statistics using SPSS*. 3rd ed. London: SAGE.

Gil, M. L. A., Santos, A., Bethencourt, M., Garcia, T., Fernandez-Bastero, S., Velo, A. and Gago-Duport, L. 2003. Use of X-ray and other techniques to analyse the phase transformation induced in archaeological cast iron after its stabilisation by the electrolytic method. *Analytica Chimica Acta* 494, pp. 245-254.

Gilberg, M. R. and Seeley, N. J. 1981. The Identity of Compounds Containing Chloride Ions in Marine Iron Corrosion Products: A Critical Review. *Studies in Conservation* 26, pp. 50-56.

Gilberg, M. R. and Seeley, N. J. 1982. The Alkaline Sodium Sulphite Reduction Process for Archaeological Iron: A Closer Look. *Studies in Conservation* 27, pp. 180-184.

Goldstein, J., Newbury, D. E., Joy, D. C., Lyman, C. E., Echlin, P., Lifschin, E., Sawyer, L. and Michael, J. R. 2003. *Scanning electron microscopy and X-ray microanalysis*. 3rd ed. New York: Springer.

González, N. G., Mardikian, P., Nasanen, L. and Drews, M. 2013. The use of subcritical fluids for the stabilisation of archaeological iron: an overview. In: Dillmann, P. et al. eds. *Corrosion and conservation of cultural heritage metallic artefacts*. Cambridge: Woodhead, pp. 434-465.

González-Pereyra, N., Brocard, T., Cretté, S., de Viviés, P., Drews, M. and Mardikian, P. 2010. The use of subcritical fluids for the stabilization of concreted iron artifacts. In: Mardikian, P. et al. eds. *Metal 2010: proceedings of the interim meeting of the ICOM-CC Metal Working Group*, Charleston October 11-15, 2010. Charleston: Clemson University, pp. 21-30

González-Pereyra, N., Nasanen, L. and Crette, S. 2014. From Rivets to Composites: Ten Years of Subcritical Research. In: Hyslop, E., et al. eds. *Metal 2013: Interim Meeting of the ICOM-CC Metal Working Group*. Edinburgh, 16-20 September 2013. Edinburgh: Historic Scotland and International Council of Museums, pp.197-202.

Gordon, R. B. 1988. Strength and structure of wrought iron. *Archaeomaterials* 2, pp. 109-137.

Gordon, R. B. 1996. *American Iron: 1607-1900*. Baltimore: Johns Hopkins University.

Graedel, T. E. and Frankenthal, R. P. 1990. Corrosion Mechanisms for Iron and Low Alloy Steels Exposed to the Atmosphere. *Journal of the Electrochemical Society* 137(8), pp. 2385-2394.

Groysman, A. 2010. *Corrosion for Everybody*. London: Springer.

Guest, P. and Gardner, A. 2008. *Caerleon: Excavations In Priory Field 2008: Interim Report*. Cardiff: Cardiff University.

Guilminot, E., Baron, G., Memet, J. B., Huet, B., Le Noc, E. and Roze, J. P. 2007. Electrolytic treatment of archaeological marine chloride impregnated iron objects by remote control. In: Degriigny, C. ed. *Metal 07: Interim meeting of the ICOM-CC Metal WG, Amsterdam, 17-21 September 2007*. Amsterdam.

Hack, H. 2010. Galvanic Corrosion. In: Cottis, R.A., et al. eds. *Shreir's Corrosion*. 4th ed., Vol. 2. Amsterdam: Elsevier. pp. 828-856.

Haisch, T., Mittenmeijer, E. J. and Schultze, J. W. 2002. On the influence of microstructure and carbide content of steels on the electrochemical dissolution process in aqueous NaCl electrolytes. *Materials and Corrosion* 53, pp. 740-755.

Hamilton, D. L. 1976. *Conservation of Metal Objects from Underwater Sites: A Study in Methods*. Austin: Texas Memorial Museum/Texas Antiquities Committee.

Henderson, M. A. 2002. The interaction of water with solid surfaces: fundamental aspects revisited. *Surface Science Reports* 46, pp. 1-308.

Hoërlé, S., Mazaudier, F., Dillmann, P. and Santarini, G. 2004. Advances in understanding atmospheric corrosion of iron. II. Mechanistic modelling of wet-dry cycles. *Corrosion Science* 46(6), pp. 1431-1465.

Hou, P. Y. 2010. Types of High Temperature Corrosion: Oxidation of Metals and Alloys. In: Cottis, R.A., et al. eds. *Shreir's Corrosion*. Vol. 1. Amsterdam: Elsevier, pp. 195-239.

Jegdić, B., Polic-Radovanović, S., Ristić, S. and Alil, A. 2011. Corrosion Processes, Nature and Composition of Corrosion Products on Iron Artefacts of Weaponry. *Scientific Technical Review* 61(2), pp. 50-56.

Jenkins, R. and Snyder, R. L. 1996. *Introduction to X-ray Powder Diffractometry*. New York: John Wiley and Sons.

Jones, D. A. 2014. *Principles and Prevention of Corrosion*. Harlow: Pearson.

Kergourlay, F., Guilminot, E., Neff, D., Rémazeilles, C., Réguer, S., Refait, P., Mirambet, F., Foy, E. and Dillmann, P. 2010. Influence of corrosion products nature on dechlorination treatment: case of wrought iron archaeological ingots stored 2 years in air before NaOH treatment. *Corrosion Engineering, Science, and Technology* 45(5), pp. 408-413.

Kergourlay, F., Rémazeilles, C., Neff, D., Foy, E., Conforto, E., Guilminot, E., Réguer, S., Dillmann, P., Nicot, F., Mielcarek, F., Rebière, J. and Refait, P. 2011. Mechanisms of the dechlorination of iron archaeological artefacts extracted from seawater. *Corrosion Science* 53(8), pp. 2474-2483.

- Knight, B. 1982. Why do some iron objects break up in store? In: Clarke, R.W. and Blackshaw, S.M. eds. *Conservation of Iron: Proceedings of the Symposium held at the National Maritime Museum*. Greenwich, 4th July 1980. Greenwich: Trustees of the National Maritime Museum, pp. 50-52.
- Knight, B. 1990. A review of Corrosion of Iron from Terrestrial Sites and the Problem of Post-Excavation Corrosion. *The Conservator* 14, pp. 37-43.
- Knight, B. 1997. The Stabilisation of Archaeological Iron, Past Present and Future. In: MacLeod, I.D. et al. eds. *Metal 95: Proceedings of the International Conference on Metal Conservation Held at Semur en Auxois, France, 25-28 September 1995*. London: James and James.
- Kreislova, K., Knotkova, D. and Geiplova, H. 2013. Atmospheric corrosion of historical industrial structures. In: Dillmann, P. et al. eds. *Corrosion and conservation of cultural heritage metallic artefacts*. Cambridge: Woodhead, pp. 311-342.
- Kuhn, C. and Eggert, G. 2010. Keep Cool? Deep Freeze Storage of Archaeological Iron. In: Mardikian, P. et al. eds. *Metal 2010: Interim meeting of the ICOM-CC Metal Working Group*. Charleston, October 11-15, 2010. Charleston: Clemson University, pp. 15-20.
- Laboratory of the Oriental Institute of the University of Chicago 2014. *Archaeological Iron Storage Research Project* [Online]. Chicago: The Oriental Institute of the University of Chicago. Available at: <https://oi.uchicago.edu/collections/archaeological-iron-storage-research-project> [Accessed: 19/5/2016].
- LaCoudre, N., Degriigny, C. and de Lavergne, E. 1991. *Electricité et Archéologie*. 3rd ed. St. Denis: Electricité de France.
- Lewis, M. R. T. 2009. *The Influence of Atmospheric Moisture on the Corrosion of Chloride-Contaminated Wrought Iron*. PhD Thesis, Cardiff University.
- Leygraf, C. and Graedel, T. E. 2000. *Atmospheric Corrosion*. New York: John Wiley and Sons.
- L'Heritier, M., Dillmann, P., Aumard, S. and Fluzin, P. 2013. Iron? Which Iron? Methodologies for metallographic and slag inclusion studies applied to ferrous reinforcements from Auxerre Cathedral. In: Humphris, J. and Rehren, T. eds. *The World of Iron*. London: Archetype.
- Lide, D. R. ed. 2005. *CRC handbook of chemistry and physics: a ready-reference book of chemical and physical data*. 86th ed. Boca Raton: CRC Press.
- Loeper-Attia, M. A. 2007. A proposal to describe reactivated corrosion of archaeological iron objects. In: Dillmann, P. et al. eds. *Corrosion of Metallic Heritage Artefacts*. Cambridge: Woodhead and Boca Raton: CRC Press, pp. 190-202.

- Loeper-Attia, M.-A. and Weker, W. 1997. Déchloruration d'Objets Archaeologiques en Fer par la Methode du Sulfite Alcalin a l'IRRAP. In: MacLeod, I.D. et al. eds. *Metal 95: Proceedings of the International Conference on Metal Conservation*. Semur en Auxois, 25-28 September 1995. London: James and James.
- Logan, R. G. 2016. The Graphitic Corrosion of Cast Iron: Aspects on the Deterioration of Trunk Main. PhD Thesis, University of Surrey.
- Lyon, S. B. 2010. Corrosion in Natural Waters. In: Cottis, R.A., et al. eds. *Shrier's Corrosion*. Vol. 2. Amsterdam: Elsevier, pp. 1094-1106.
- MacLeod, I. D. 1981. Shipwrecks and Applied Electrochemistry. *Journal of Electroanalytical Chemistry* 118, pp. 291-303.
- MacLeod, I. D. 2015. Change Management in Materials Conservation. In: Bammer, G. ed. *Change! Combining Analytic Approaches with Street Wisdom*. Acton: Australian National University Press, pp. 245-226.
- MacLeod, I. D., Cook, D. and Schindelholz, E. 2008. Corrosion and conservation of three elements of the American Civil War ironclad USS *Monitor* (1862). In: Bridgland, J. ed. *ICOM 15th Triennial Conference, New Delhi, 22-26 September 2008*. New Delhi. Allied Publishers.
- MacPhail, D., Lam, E. and Doyle, A. 2003. Heat Sealing of Escal Barrier Films. *The Conservator* (27), pp. 107-116.
- Maréchal, L., Perrin, P., Dillmann, P. and Santarini, G. 2007. Study of the atmospheric corrosion of iron by ageing historical artefacts and contemporary low-alloy steel in a climatic chamber: comparison with mechanistic modelling. In: Dillmann, P. et al. eds. *Corrosion of metallic heritage artefacts*. Cambridge: Woodhead and Boca Raton: CRC Press, pp. 131-167.
- Matthiesen, H. 2007. A novel method to determine oxidation rates of heritage materials in vivo and in situ. *Studies in Conservation* 52(4), pp. 271-280.
- Matthiesen, H., Hilbert, L.R. and Gregory, D.J. 2003. Siderite as a Corrosion Product on Archaeological Iron from a Waterlogged Environment. *Studies in Conservation* 48, pp. 183-194.
- Matthiesen, H. and Stemann-Petersen, K. 2014. A fast and non-destructive method to document and quantify the efficiency of metals conservation. In: Hyslop, E., et al. eds. *Metal 2013: Interim Meeting of the ICOM-CC Metal Working Group*. Edinburgh, 16-20 September 2013. Edinburgh: Historic Scotland and International Council of Museums, 175-180.

- Matthiesen, H. and Wonsyld, K. 2010. In situ measurement of oxygen consumption to estimate corrosion rates. *Corrosion, Engineering, Science and Technology* 45, pp. 350-356.
- Memet, J. B. 2007. The corrosion of metallic artefacts in seawater: descriptive analysis. In: Dillmann, P. et al. eds. *Corrosion of metallic heritage artefacts*. Cambridge: Woodhead and Boca Raton: CRC Press, pp. 152-167.
- Monnier, J., Burger, E., Berger, P., Neff, D., Guillot, I. and Dillmann, P. 2011. Localisation of oxygen reduction sites in the case of iron long term atmospheric corrosion. *Corrosion Science* 53(8), pp. 2468-2473.
- Munoz-Vinas, S. 2009. Minimal Intervention Revisited. In: Richmond, A. and Bracker, A. eds. *Conservation: Principles, Dilemmas, and Uncomfortable Truths*. London: Butterworth-Heinemann, pp. 47-59.
- Murad, E. and Bishop, J. L. 2000. The infrared spectrum of synthetic akaganeite, B-FeOOH. *American Mineralogist* 85, pp. 716-721.
- Neff, D., Bellot-Gurlet, L., Dillmann, P., Bertholon, R. 2003. Structural characterization of corrosion products on archaeological iron. An integrated analytical approach to establish corrosion typologies. In: *International Conference on the Application of Raman Spectroscopy in Art and Archaeology*. Ghent, 3-6 September 2003.
- Neff, D., Bellot-Gurlet, L., Dillmann, P., Réguer, S. and Legrand, L. 2006a. Raman imaging of ancient rust scales on archaeological iron artefacts for long-term atmospheric corrosion mechanisms study. *Journal of Raman Spectroscopy* 37(10), pp. 1228-1237.
- Neff, D., Dillmann, P., Bellot-Gurlet, L. and Beranger, G. 2005. Corrosion of iron archaeological artefacts in soil: characterisation of the corrosion system. *Corrosion Science* 47(2), pp. 515-535.
- Neff, D., Dillmann, P., Descostes, M. and Beranger, G. 2006b. Corrosion of iron archaeological artefacts in soil: Estimation of the average corrosion rates involving analytical techniques and thermodynamic calculations. *Corrosion Science* 48(10), pp. 2947-2970.
- Neff, D., Réguer, S., Bellot-Gurlet, L., Dillmann, P. and Bertholon, R. 2004. Structural characterization of corrosion products on archaeological iron: an integrated analytical approach to establish corrosion forms. *Journal of Raman Spectroscopy* 35(8-9), pp. 739-745.

- Neff, D., Vega, E., Dillmann, P. and Descostes, M. 2007. Contribution of iron archaeological artefacts to the estimation of average corrosion rates and the long-term corrosion mechanisms of low-carbon steel buried in soil. In: Dillmann, P. et al. eds. *Corrosion of metallic heritage artefacts*. Cambridge: Woodhead and Boca Raton: CRC Press, pp. 41-76.
- Noel-Hume, I. 1991. *A Guide to Artifacts of Colonial America*. New York: Vintage Books.
- North, N. A. 1976. Formation of coral concretions on marine iron. *International Journal of Nautical Archaeology and Underwater Exploration* 5(3), pp. 253-258.
- North, N. A. 1982. Corrosion Products on Marine Iron. *Studies in Conservation* 27, pp. 75-83.
- North, N. A. 1987. Conservation of metals. In: Pearson, C. ed. *Conservation of Marine Archaeological Objects*. London: Butterworth and Co., pp. 207-252.
- North, N. A. and MacLeod, I. D. 1987. Corrosion of metals. In: Pearson, C. ed. *Conservation of Marine Archaeological Objects*. London: Butterworth, pp. 68-98.
- North, N. A. and Pearson, C. 1975. Alkaline sulphite reduction treatment of marine iron. In: *Icom committee for conservation. 4th triennial meeting, Venice, 13-18 October*. Paris: ICOM.
- North, N. A. and Pearson, C. 1977. Thermal decomposition of FeOCl and marine cast iron corrosion products. *Studies in Conservation* 22, pp. 146-157.
- North, N. A. and Pearson, C. 1978. Washing methods for chloride removal from marine iron artefacts. *Studies in Conservation* 23, pp. 174-186.
- Oliveira, C.M. and Fonseca, I.T E. 2014. The efficiency of electrochemical methods for the removal of chloride ions from iron marine archaeological objects: A comparative study. *Materials and Corrosion* 65(1), pp. 38-44.
- O'Shea, C., Davies, B. and Kendell, K. 1982. The use of hydrogen reduction in stabilizing large items of iron recovered from the sea. In: Bromelle, N.S. and Thompson, G. eds. *Science and technology in the service of conservation: preprints of the contributions to the Washington congress, 3-9 September 1982*. Washington, DC. International Institute for the Conservation of Historic and Artistic Works.
- Ouahman, R., Rahouadj, R. and Fluzin, P. 1997. Traitement de stabilisation du fer par le sulfite alcalin: modélisation de la diffusion des ions Cl⁻. In: MacLeod, I.D. et al. eds. *Metal 95: Proceedings of the international conference on metals conservation*. Semur-en-Auxois, 25-28 September 1995. London: James and James.

- Paterakis, A. and Hickey-Friedman, L. 2011. Stabilization of Iron Artifacts from Kaman-Kalehoiuk: A Comparison of Chemical and Environmental Methods. *Studies in Conservation* 56, pp. 179-190.
- Paterakis, A. and Mariano, M. 2013. Oxygen Absorbers and Desiccants in the Protection of Archaeological Iron: Maintaining Some Control. In: Hyslop, E., et al. eds. *Metal 2013: Interim Meeting of the ICOM-CC Metal Working Group*. Edinburgh, 16-20 September 2013. Edinburgh: Historic Scotland and International Council of Museums, pp. 181-188.
- Patscheider, J. and Veprek, S. 1986. Application of low-pressure hydrogen plasma to the conservation of ancient iron artifacts. *Studies in Conservation* 31, pp. 29-37.
- Paynter, S. 2007. Innovations in bloomery smelting in Iron Age and Romano-British England. In: LaNiece, S. et al. eds. *Metals and Mines: Studies in Archaeometallurgy*. London: Archetype, pp. 202-210.
- Petzow, G. 1999. *Metallographic Etching; Techniques for Metallography, Ceramography, and Plastography*. 2nd ed. Materials Park, Ohio, USA: ASM International.
- Phull, B. 2010. Marine Corrosion. In: Cottis, R.A. et al. eds. *Shreir's Corrosion*. 4th ed. Vol. 2. Amsterdam: Elsevier, pp. 1107-1148.
- Plenderleith, H. J. and Werner, A. E. A. 1971. *The conservation of antiquities and works of art: treatment, repair and restoration*. 2nd ed. London: Oxford University Press.
- Pollack, H.W. 1998. *Materials Science and Metallurgy*. Reston, VA: Reston Publishing Company.
- Pourbaix, M. 1974. *Atlas of Electrochemical Equilibrium in Aqueous Solutions*. Houston: National Association of Corrosion Engineers.
- Procter, R.P.M. 2010. Outline of Structural Metallurgy Relevant to Corrosion. In: Cottis, R.A. et al. eds. *Shreir's Corrosion*. 4th ed. Vol. 1. Amsterdam: Elsevier, pp. 52-76.
- Rathgen, F. 1905. *The Preservation of Antiquities: a Handbook for Curators*. Auden, G.A. and Auden, H.A. translators. Cambridge: Cambridge University Press.
- Reedy, T. J. and Reedy, C. L. 1988. *Statistical Analysis in Art Conservation Research*. Marina del Rey: J. Paul Getty Trust.
- Reedy, T. J. and Reedy, C. L. 1992. *Principles of Experimental Design for Art Conservation Research*. Marina del Rey: Getty Conservation Institute.

Refait, P. and Génin, J.-M. R. 1997. The Mechanisms of Oxidation of Ferrous Hydroxychloride β -Fe₂(OH)₃Cl in Aqueous Solution: the Formation of Akaganeite vs Goethite. *Corrosion Science* 39(3), pp. 539-553.

Réguer, S., Dillmann, P. and Mirambet, F. 2007a. Buried iron archaeological artefacts: Corrosion mechanisms related to the presence of Cl⁻containing phases. *Corrosion Science* 49(6), pp. 2726-2744.

Réguer, S., Mirambet, F., Dooryhee, E., Hodeau, J. L., Dillmann, P. and Lagarde, P. 2009. Structural evidence for the desalination of akaganeite in the preservation of iron archaeological objects, using synchrotron X-ray powder diffraction and absorption spectroscopy. *Corrosion Science* 51(12), pp. 2795-2802.

Réguer, S., Mirambet, F., Rémazeilles, C., Vantelon, D., Kergourlay, F., Neff, D. and Dillmann, P. 2015. Iron corrosion in archaeological context: Structural refinement of the ferrous hydroxychloride Fe₂(OH)₃Cl. *Corrosion Science* 100, pp. 589-598.

Réguer, S., Neff, D., Bellot-Gurlet, L. and Dillmann, P. 2007b. Deterioration of iron archaeological artefacts: micro-Raman investigation on Cl-containing corrosion products. *Journal of Raman Spectroscopy* 38(4), pp. 389-397.

Rémazeilles, C., Dheilly, A., Sable, S., Lanneluc, I., Neff, D. and Refait, P. 2010a. Microbiologically influenced corrosion process of archaeological iron nails from the sixteenth century. *Corrosion Engineering, Science, and Technology* 45(5), pp. 388-394.

Rémazeilles, C., Neff, D., Kergourlay, F., Foy, E., Conforto, E., Guilminot, E., Réguer, S., Refait, P. and Dillmann, P. 2009. Mechanisms of long-term anaerobic corrosion of iron archaeological artefacts in seawater. *Corrosion Science* 51(12), pp. 2932-2941.

Rémazeilles, C. and Refait, P. 2007. On the formation of B-FeOOH (akaganeite) in chloride-containing environments. *Corrosion Science* 49, pp. 844-857.

Rémazeilles, C., Saheb, M., Neff, D., Guilminot, E., Tran, K., Bourdoiseau, J.-A., Sabot, R., Jeannin, M., Matthiesen, H., Dillmann, P. and Refait, P. 2010b. Microbiologically influenced corrosion of archaeological artefacts: characterisation of iron (II) sulfides by Raman spectroscopy. *Journal of Raman Spectroscopy* 41(11), pp. 1425-1433.

Rimmer, M. 2010. *Investigating the treatment of chloride-infested archaeological iron objects*. PhD Thesis, Cardiff University.

Rimmer, M., Thickett, D., Watkinson, D. and Ganiaris, H. 2013a. Guidelines for the Storage and Display of Archaeological Metalwork. English Heritage: Swindon.

Rimmer, M. and Wang, Q. 2010. Assessing the effects of alkaline desalination treatments for archaeological iron using scanning electron microscopy. *The British Museum Technical Research Bulletin* 4, pp. 79-86.

- Rimmer, M. and Watkinson, D. 2010. Residues of Alkaline Sulphite Treatment and Their Effects of the Corrosion of Archaeological Iron Objects. In: Mardikian, P. et al. eds. *Metal 2010:Proceedings of the interim meeting of the ICOM-CC Metal Working Group*, Charleston, October 11-15, 2010. Charleston: Clemson University, pp. 1-7.
- Rimmer, M., Watkinson, D. and Wang, Q. 2012. The efficiency of chloride extraction from archaeological iron objects using de-oxygenated alkaline solutions. *Studies in Conservation* 57(1), pp. 29-41.
- Rimmer, M., Watkinson, D. and Wang, Q. 2013b. The impact of chloride desalination on the corrosion rate of archaeological iron. *Studies in Conservation* 58(4), p. 326-337.
- Rinuy, A. and Schweizer, F. 1981. Méthodes de conservation d'objets de fouilles en fer. Etude quantitative comparée de l'élimination des chloreurs. *Studies in Conservation* 26, pp. 29-41.
- Rinuy, A. and Schweizer, F. 1982. Application of the alkaline sulphite treatment to archaeological ironwork: A comparative study of different desalination methods. In: Clarke, R.W. and Blackshaw, S.M. eds. *Conservation of Iron*. Greenwich: Trustees of the National Maritime Museum.
- Robinson, W. 1998. *First Aid for Underwater Finds*. London: Archetype.
- Ryzewski, K. and Gordon, R. 2008. Historical nail-making techniques revealed in metal structure. *Historical Metallurgy* 42(1), pp. 50-64.
- Schindelholz, E. and Kelly, R. G. 2012. Wetting phenomena and time of wetness in atmospheric corrosion: a review. *Corrosion Reviews* 30 (5/6), pp. 135-170.
- Schmidt, F. E. and Lucas, G. M. 2009. Analysis of historic circa 1863 Phoenix iron alloy. *Advanced Materials and Processes* (July), pp. 24-25.
- Schmidt-Ott, K. 1997. Applications of low-pressure plasma treatment at the Swiss National Museum and assessment of the results. *Zeitschrift für Schweizerische Archäologie und Kunstgeschichte* 54(4), pp. 45-50.
- Schmidt-Ott, K. and Boissonnas, V. 2002. Low-Pressure hydrogen plasma: An assessment of its application on archaeological iron. *Studies in Conservation* 47, pp. 81-87.
- Schmidt-Ott, K. and Oswald, N. 2006. Alkali-Sulfit-Entsalzung: Tipps und Tricks. *Beiträge zur Erhaltung von Kunst-und Kulturgut* 2, pp. 126-134.
- Schmutzler, B. 2012. *Rettung vor dem Rost; Die Weiterentwicklung der Eisenentsalzung nach der Alkali-Sulfit-Methode zur Erhaltung grosser Fundmengen*. Rahden: Verlag Marie Leidorf GmbH.

- Schmutzler, B. and Eggert, G. 2010. Chloride Calamities: Assessment of Residual Chloride Analysis to Compare Iron Desalination Methods. In: Mardikian, P. et al. eds. *Metal 2010: Proceedings of the interim meeting of the ICOM-CC Metal Working Group*. Charleston, October 11-15, 2010. Charleston: Clemson University, pp. 24-31.
- Schwartz, K. 2016. Email to Eric Nordgren, Received 16-2-2016.
- Scott, D. A. 1991. *The Metallography and Microstructure of Ancient and Historic Metals*. Marina Del Rey: The J. Paul Getty Trust in Association with Archetype Books.
- Scott, D. A. and Eggert, G. 2009. *Iron and Steel in Art*. London: Archetype.
- Scott, D. A. and Seeley, N. J. 1987. The Washing of Fragile Iron Artefacts. *Studies in Conservation* 32(2), pp. 73-76.
- Scully, J. C. 1990. *The Fundamentals of Corrosion*. 3rd ed. Oxford: Pergamon Press.
- Selwyn, L. S. 2004a. *Metals and Corrosion: A Handbook for the Conservation Professional*. Ottawa: Canadian Conservation Institute.
- Selwyn, L. S. 2004b. Overview of archaeological iron: the corrosion problem, key factors affecting treatment, and gaps in current knowledge. In: J., A. and D., H. eds. *Metal 2004: proceedings of the international conference on metals conservation*. Canberra, 4-8 October 2004. Canberra: National Museum of Australia, pp. 294-306.
- Selwyn, L. S. and Argyropoulos, V. 2005. Removal of Chloride and Iron Ions from Archaeological Wrought Iron with Sodium Hydroxide and Ethylenediamine Solutions. *Studies in Conservation* 50, pp. 81-100.
- Selwyn, L. S., Argyropoulos, V. and Logan, J. 1997. Developing a Conservation Treatment using Ethylenediamine as a Corrosion Inhibitor for Wrought Iron Objects Found at Terrestrial Archaeological Sites. In: MacLeod, I.D. et al. eds. *Metal 95: Proceedings of the International Conference on Metals Conservation Semur-en-Auxois, 25-28 September, 1995*. London: James and James.
- Selwyn, L. S. and Logan, J. 1993. Stability of treated iron: a comparison of treatment methods. In: Bridgland, J. ed. *ICOM Committee for Conservation tenth triennial meeting, Washington, DC, 22-27 August 1993: preprints*. Paris: International Council of Museums Committee for Conservation.
- Selwyn, L. S., McKinnon, W. R. and Argyropoulos, V. 2001. Models for Chloride Ion Diffusion in Archaeological Iron. *Studies in Conservation* 46, pp. 109-120.
- Selwyn, L. S., Sirois, P. J. and Argyropoulos, V. 1999. The Corrosion of Archaeological Iron with Details on Weeping and Akaganeite. *Studies in Conservation* 44(4), pp. 217-232.

- Shibaeva, T., Laurinavichyute, V. K., Tsirlina, G., Arsenkin, A. M. and Grigorovich, K. V. 2014. The effect of microstructure and non-metallic inclusions on corrosion behavior of low carbon steel in chloride containing solutions. *Corrosion Science* 80, pp. 299-308.
- Stahl, K., Nielsen, K., Jiang, J., Lebech, B., Hanson, J., Norby, P. and van Lanschot, J. 2003. On the akaganeite crystal structure, phase transformations and possible role in post-excavational corrosion of iron artifacts. *Corrosion Science* 45, pp. 2563-2575.
- Stratmann, M. 1990. The Atmospheric Corrosion of Iron — A Discussion of the Physico-Chemical Fundamentals of this Omnipresent Corrosion Process. *Berichte der Bunsengesellschaft für Physikalische Chemie* 94(6), pp. 629-639.
- Stratmann, M. and Hoffmann, K. 1989. In situ Mossbauer Spectroscopic Study of Reactions Within Rust Layers. *Corrosion Science* 29(11/12), pp. 1329-1352.
- Thickett, D. 2012. *Post Excavation Changes and Preventive Conservation of Archaeological Iron*. PhD Thesis, Birkbeck College-University of London.
- Thickett, D., Csefalvayova, L. and Strlic, M. 2011. Smart conservation: targeting controlled environments to improve sustainability. In: Bridgland, J. ed. *ICOM-CC 16th triennial conference Lisbon*. Lisbon: Criterio-Producao Grafica Lda.
- Thickett, D. and Odlyha, M. 2010. Assessment of Dry Storage Microenvironments for Archaeological Iron. In: Williams, E. and Peachey, C. eds. *The Conservation of Archaeological Materials: Current Trends and Future Directions*. Williamsburg, Virginia: Archaeopress.
- Thickett, D. and Odlyha, M. 2014. Formation and transformation of Akaganeite. In: Hyslop, E., et al. eds. *Metal 2013: Interim Meeting of the ICOM-CC Metal Working Group*. Edinburgh, 16-20 September 2013. Edinburgh: Historic Scotland and International Council of Museums, pp. 103-110.
- Thomson, G. 2003. *The Museum Environment*. 2nd ed. Amsterdam: Elsevier/Butterworth Heinemann.
- Tripathi, V. 2013. An ethno-archaeological survey of iron working in India. In: Humphris, J. and Rehren, T. eds. *The World of Iron*. London: Archetype.
- Turgoose, S. 1982a. The Nature of Surviving Iron Objects. In: Clark, R. and Blackshaw, S. eds. *Conservation of Iron: Proceedings of the Symposium held at the National Maritime Museum*. Greenwich. 4th July 1980. Greenwich: Trustees of the National Maritime Museum, pp. 1-7
- Turgoose, S. 1982b. Post Excavation Changes in Iron Antiquities. *Studies in Conservation* 27, pp. 97-101.

- Turgoose, S. 1985. The corrosion of archaeological iron during burial and treatment. *Studies in Conservation* 30, pp. 13-18.
- Turgoose, S. 1993. Structure, Composition and Deterioration of Unearthed Iron Objects. In: *Current Problems in the Conservation of Metal Antiquities*. Tokyo, 4-6 October 1989. Tokyo: Tokyo National Research Institute of Cultural Properties.
- Tylecote, R. F. 1962. *Metallurgy in archaeology: a prehistory of metallurgy in the British Isles*. London: Edward Arnold.
- Tylecote, R. F. 1992. *A History of Metallurgy*. 2nd ed. London: Institute of Materials.
- Tylecote, R. F. and Black, J. 1980. The effect of hydrogen reduction on the properties of ferrous materials. *Studies in Conservation* 25, pp. 87-96.
- University of California, Davis 2016. *Eh/pH (Pourbaix) diagram for Iron-Water system showing ions and compounds and thermodynamically predicted regions of corrosion, passivation, and protection* [Online]. Available at: UC Davis.edu via Commons:[http://chemwiki.ucdavis.edu/Textbook_Maps/Inorganic_Chemistry_Textbook_Maps/Map%3A_Inorganic_Chemistry_\(Wikibook\)/Chapter_04%3A_Redox_Stability_and_Redox_Reactions/4.5%3A_Pourbaix_diagrams](http://chemwiki.ucdavis.edu/Textbook_Maps/Inorganic_Chemistry_Textbook_Maps/Map%3A_Inorganic_Chemistry_(Wikibook)/Chapter_04%3A_Redox_Stability_and_Redox_Reactions/4.5%3A_Pourbaix_diagrams) [Accessed: 5-15-2016].
- Vega, E., Berger, P. and Dillmann, P. 2005. A study of transport phenomena in the corrosion products of ferrous archaeological artefacts using ^{18}O tracing and nuclear microprobe analysis. *Nuclear Methods in Physics Research* 240, pp. 554-558.
- Vega, E., Dillmann, P. and Berger, P. 2007. Species transport in the corrosion products of ferrous archaeological analogues: contribution to the modelling of long-term iron corrosion mechanisms. In: Dillmann, P. et al. eds. *Corrosion of metallic heritage artefacts*. Cambridge: Woodhead and Boca Raton, CRC Press, pp. 90-108.
- De Viviés, P., Cook, D., Drews, M., González, N., Mardikian, P. and Memet, J. B. 2007. Transformation of akaganeite in archaeological iron artefacts using subcritical treatment. In: Degriigny, C. ed. *Metal 2007: Interim meeting of the ICOM-CC Metal Working Group*. Amsterdam. ICOM-CC Metal Working Group.
- Wagner, U., Demoulin, T., Gebhard, R., Hausler, W., Mazzola, C., Meissner, I. and Wagner, F. 2012. The stabilization of archaeological iron objects: Mossbauer and XRD studies. *Hyperfine Interactions* 208, pp. 111-116.
- Walker, R. 2001. Instability of Iron sulfides on Recently Excavated Artifacts. *Studies in Conservation* 46, pp. 141-152.
- Wang, Q. 2007a. An Investigation of Deterioration of Archaeological Iron. *Studies in Conservation* 52, pp. 125-134.

- Wang, Q. 2007b. Effects of relative humidity on the corrosion of iron: an experimental view. *The British Museum Technical Research Bulletin* 1 pp. 65-73.
- Wang, Q., Dove, S., Shearman, F. and Smirniou, M. 2008. Evaluation of methods of chloride ion concentration determination and effectiveness of desalination treatments using sodium hydroxide and alkaline sulphite solutions. *The Conservator* 31, pp. 67-74.
- Watkinson, D. 1983. Degree of mineralization: its significance for the stability and treatment of excavated ironwork. *Studies in Conservation* 28(2), pp. 85-90.
- Watkinson, D. 1996. Chloride Extraction from Archaeological Iron: Comparative Treatment Efficiency. In: Roy, A. and Smith, P. eds. *Archaeological Conservation and its Consequences*. Copenhagen, 26-30 August 1996. Copenhagen: International Institute for Conservation, pp.208-212.
- Watkinson, D. 2010. Measuring effectiveness of washing methods for corrosion control of archaeological iron: problems and challenges. In: *Corrosion, Science, Engineering, and Technology* 45(5), pp. 400-406.
- Watkinson, D. and Al-Zahrani, A. 2008. Towards quantified assessment of aqueous chloride extraction methods for archaeological iron: de-oxygenated treatment environments. *The Conservator* 31, pp. 75-86.
- Watkinson, D. and Emmerson, N. 2016. The impact of aqueous washing on the ability of βFeOOH to corrode iron. *Environmental Science and Pollution Research International* (online) DOI: 10.1007/s11356-016-6749-3.
- Watkinson, D. and Lewis, M. R. T. 2004. SS Great Britain iron hull: modelling corrosion to define storage relative humidity. In: Ashton, J. and D., Hallam, D., eds. *Metal 2004: proceedings of the international conference on metals conservation*, Canberra, 4-8 October 2004. Canberra: National Museum of Australia, pp. 88-103.
- Watkinson, D. and Lewis, M. R. T. 2005a. Desiccated storage of chloride contaminated archaeological iron objects. *Studies in Conservation* 50(4), pp. 241-252.
- Watkinson, D. and Lewis, M. R. T. 2005b. The Role of $\beta\text{-FeOOH}$ in the Corrosion of Archaeological Iron. In: Vandiver, P.B. et al. eds. *Materials Issues in Art and Archaeology VII*. Boston, 30th November-3rd December 2004. Warrendale: Materials Research Society, pp. 103-114.
- Watkinson, D. and Lewis, M. R. T. 2008. Desiccated Storage of Chloride Contaminated Iron: A Study of the Effects of Loss of Environmental Control. In: May, E. et al. eds. *Heritage Microbiology and Science: Microbes, Monuments, and Maritime Marvels*. Cambridge: The Royal Society of Chemistry, pp. 279-292.
- Watkinson, D. and Neal, V. 1998. *First Aid For Finds*. 3rd ed. Hertford: UKIC/Rescue.

Watkinson, D. and Rimmer, M. 2013. Archaeological iron: Relating post-excavation corrosion rate to object longevity. In: Dechema, Eurocorr Congress Secretariat ed. *Eurocorr 2013: For a blue sky*. Estoril, 1-5 September 2013. Estoril: European Corrosion Federation.

Watkinson, D., Rimmer, M. B. and Kergourlay, F. 2013. Alkaline desalination techniques for archaeological iron. In: Dillmann, P. et al. eds. *Corrosion and conservation of cultural heritage metallic artefacts*. Oxford: Woodhead, pp. 407-433.

Watkinson, D. and Rimmer, M. 2014. Quantifying effectiveness of chloride desalination treatments for archaeological iron using oxygen measurement. In: Hyslop, E. et al. eds. *Metal 2013: Interim Meeting of the ICOM-CC Metal Working Group*. Edinburgh, 16-20 September, 2013. Edinburgh: Historic Scotland and International Council of Museums, pp. 95-102.

Wihr, R. 1975. Electrolytic desalination of archaeological iron. In: *Conservation in archaeology and the applied arts. Preprints of the contributions to the Stockholm Congress, 2-6 June 1975*. London: International Institute for the Conservation of Historic and Artistic Works.

www.substech.com 2016. *Simplified Pourbaix Diagram for Iron-Water at 25C* [Online]. Available at:
http://www.substech.com/dokuwiki/lib/exe/detail.php?id=pourbaix_diagrams&cache=cache&media=pourbaix_diagram.png [Accessed: 5/15/2016].

Young, T. 2014. Roman Military Control on Iron Making in South Wales. In: Cech, B., and Rehren, T. eds. *Early Iron in Europe*. Montagnac: Editions Monique Mergoïl, pp. 215-226.

8 Appendices

8.1 Appendix 1: Chloride Analysis

8.1.1 Specific Ion Meter Calibration Procedures

A Radiometer Analytical PHM250 Specific Ion Meter, REF621 Hg/HgSO₄ reference electrode, and ISE25Cl chloride ion specific electrode were used for chloride measurement during the experiments. Calibration of the meter before each measurement session was done as follows:

Ambient temperature in the lab was measured with a Fisher Scientific FB 70245 digital thermometer/hygrometer and programmed into the meter before calibration. Four calibration standards in concentrations of 7.088, 35.44, 172.2, and 354.4ppm chloride were prepared by dilution from a stock 0.1M (3544ppm) chloride standard purchased from Fisher Scientific. Standards were prepared by pipetting precise volumes of 0.1M Cl⁻ solution into volumetric flasks and diluting with de-ionised water. All solutions were kept covered with watch glasses after preparation to prevent contamination.

Standards and samples were buffered with 0.5M HN₄CH₃COO/CH₃COOH added in a 1/10 ratio as an ionic strength adjuster. The specific ion meter was calibrated taking into account the reduced concentrations due to the addition of the buffer. Calibration was tested against the standards at regular intervals and redone if found to deviate more than 10% off from the standards. All pipettes and glassware used in chloride measurement was rinsed three times with de-ionised water and dried thoroughly before use.

8.1.2 Specific Ion Meter Chloride Analysis Procedures

Procedures for analysis of chloride concentration in aqueous solutions were as follows:

A 10ml volume of the test solution was taken and the total volume of the solution recorded. The test sample was prepared for analysis by the addition of 0.5M $\text{NH}_4\text{CH}_3\text{COO}/\text{CH}_3\text{COOH}$ added in 1/10 ratio as an ionic strength adjuster. The chloride ion specific electrode and reference electrode of a previously calibrated Radiometer Analytical PHM250 Specific Ion Meter were then placed in the test solution which was stirred constantly during analysis. Chloride concentrations in ppm were normally acquired in direct measurement mode and three consecutive measurements were taken after the meter indicated a stable reading. The mean of the three readings was calculated and taken as the result.

In cases where a stable reading was difficult to achieve such as in analysis of solutions produced by acid digestion of iron nails, the standard addition method of analysis was used. The specific ion meter was set to standard addition mode and the test sample analysed once. A 0.5ml volume of 0.1 M (3544ppm) chloride standard was then added and the chloride concentration measured again. Chloride concentration in the sample was then calculated by the meter software.

Pre measurement preparation was also required for some types of solutions as detailed in Appendices 8.1.3 and 8.1.4.

8.1.3 Preparation of chloride samples from alkaline sulphite wash solutions

Chloride concentration in alkaline sulphite solutions could not be measured directly as the sulphite (SO_3^{2-}) ion may interfere with chloride measurement. Samples from

treatment solutions were first prepared by adding hydrogen peroxide (H_2O_2) in the ratio of 2ml H_2O_2 to 100ml of solution. This procedure oxidizes sulphite ions to sulphate (SO_4^{2-}) which no longer interferes with chloride determination. Procedures for chloride analysis by the direct measurement method were then followed. In some cases where stable readings were difficult to obtain the standard addition method was used.

8.1.4 Preparation of chloride samples from nitric acid digestion

Solutions produced through 5M nitric acid digestion of iron samples contain high concentrations of ferrous and other interfering ions and required preparation prior to chloride measurement using the specific ion meter. Digestion solutions are highly acidic (pH 1-2) and were first raised to an alkaline pH with the addition of 3M NaOH. This caused precipitation of solid iron compounds which were then filtered out of the solutions through filter paper. Filters were rinsed through three times with deionised water and the rinse-water added to the filtrate. The volume of the filtrate was measured in a graduated cylinder and a 10ml sample taken for chloride analysis. The pH of the alkaline solutions were adjusted to neutral with 5M HNO_3 added during constant stirring. pH of the solutions were measured with a Kent Electronic Instruments Ltd. Model 7605 pH/millivolt meter with VWR 662-1759 gel filled pH electrode. Procedures for chloride analysis by the standard addition method were then followed.

8.2 Appendix 2: X-ray Diffraction

X-ray Diffraction was used to characterise iron corrosion products akaganeite transformation experiments. Analysis was performed using a PANalytical X'pert Pro X-ray Diffractometer with PANalytical HiScore software for interpretation of the diffractograms. The diffractometer was operated through an angle of 7-70 degrees 2θ , using $\text{CuK}\alpha$ radiation (1.54060 Å) at 40kV and 30mA. Powder diffraction samples were thoroughly ground in an agate mortar prior to analysis to minimise the effects of preferred crystal orientation. Powdered samples were suspended in acetone and deposited as thin films onto a pure silicon disc for analysis in a rotating 'spinner' stage to improve particle statistics (Cotterell 2015, Ermrich and Opper, 2013). Adjustment for background levels, peak fitting, and matching with diffractograms in the ICDD (International Centre for Diffraction Data) 2005 Database was done with PanAlytical HiScore software, which also allowed semi-quantitative determination of the percentage makeup of samples using the RIR (Relative Intensity Rating) method (Jenkins and Snyder 1996, 373, Ermrich and Opper, 2013, 67). Percentage of the total signal attributed to each crystallite is calculated by using the scale factor and reference intensity ratio (RIR) values for each constituent phase. XRD-RIR is not based on calibrated direct measurement of the mass or volume of crystallites present but gives a result proportional to both. It is therefore useful for comparing the relative amounts of iron corrosion products present semi-quantitatively.

A test to determine the error of XRD-RIR percentage phase measurements similar to that done by Rimmer (2010) was carried out with varying percentages of synthetic akaganeite, and natural geological samples of goethite hematite and magnetite. The

average error found was approximately 10%, in agreement with Rimmer's estimate (Rimmer 2010) (Appendix 2.1.2).

8.3 Appendix 3: FT-IR Spectroscopy

Analysis of samples by Fourier-Transform Infrared Spectroscopy (FT-IR) was carried out using an Attenuated Total Reflectance (ATR) cell on the Perkin-Elmer Spectrum One FT-IR Spectrometer with Perkin-Elmer Spectrum v. 10.03.09 software. The ATR cell and pressure plate were thoroughly cleaned by wiping with IMS before each use to prevent contamination from previous samples. The procedure for these measurements consisted of collecting a background spectrum without the sample in place, then placing the sample on the ATR cell and tightening the anvil to approximately 160 N as measured by a software force gauge. Spectra were collected from 380-4000 cm^{-1} wavenumbers for 20 scans and then compared with library spectra in the Infrared Users Group (IRUG) database for basic identification. Major peaks were also noted and the chemical bonds indicated by them were checked against the identification provided by a high (over 90%) match in the software to determine if the library spectra identification was a reasonable match. FTIR spectra were exported as PDF documents and included in Section 5.3 (Figures 5.72 and 5.74).

8.4 Appendix 4: Supplementary Analytical Data

8.4.1 SEM Images of Nails in Cross Section

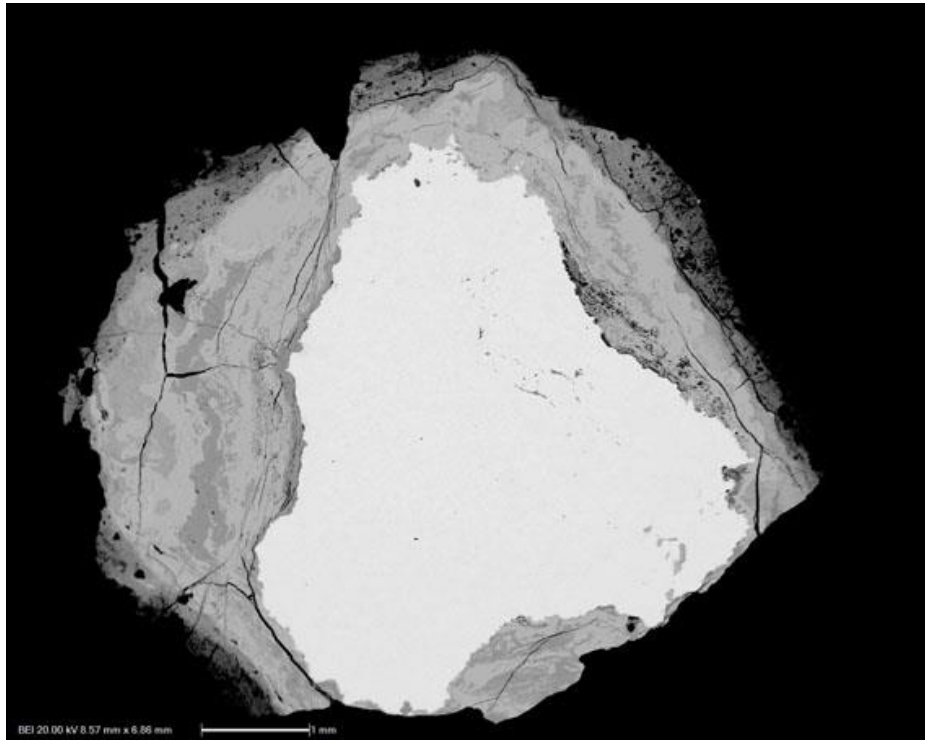


Figure 8.1 SEM-BSE image of Caerleon nail CAER_01 in polished cross-section at 13X magnification.

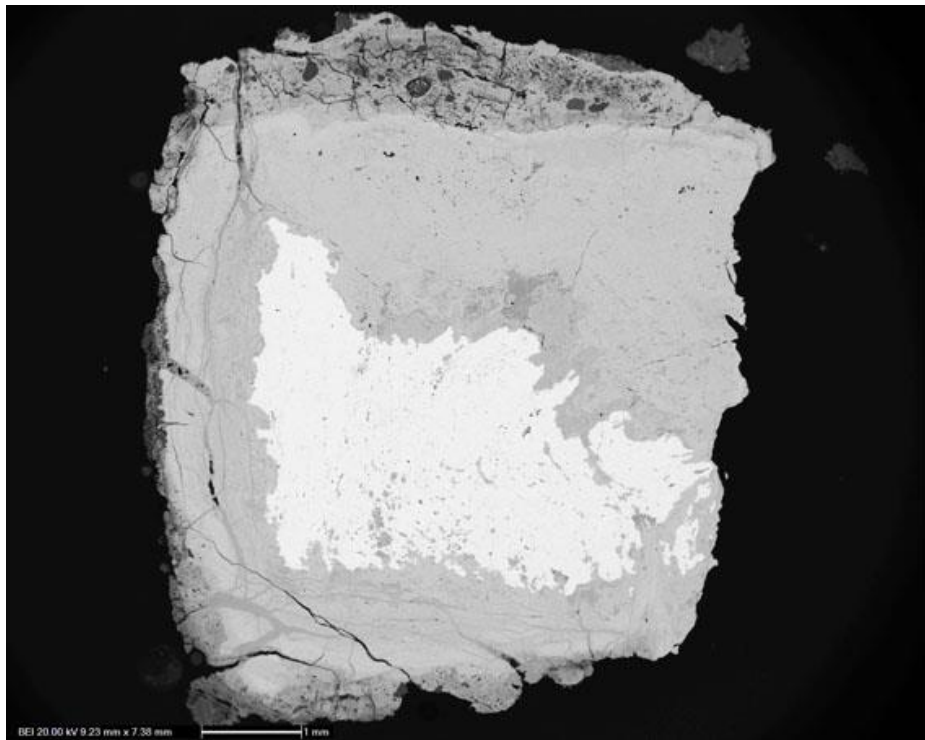


Figure 8.2 SEM-BSE image of Caerleon nail CAER_07 in polished cross-section at 13X magnification.

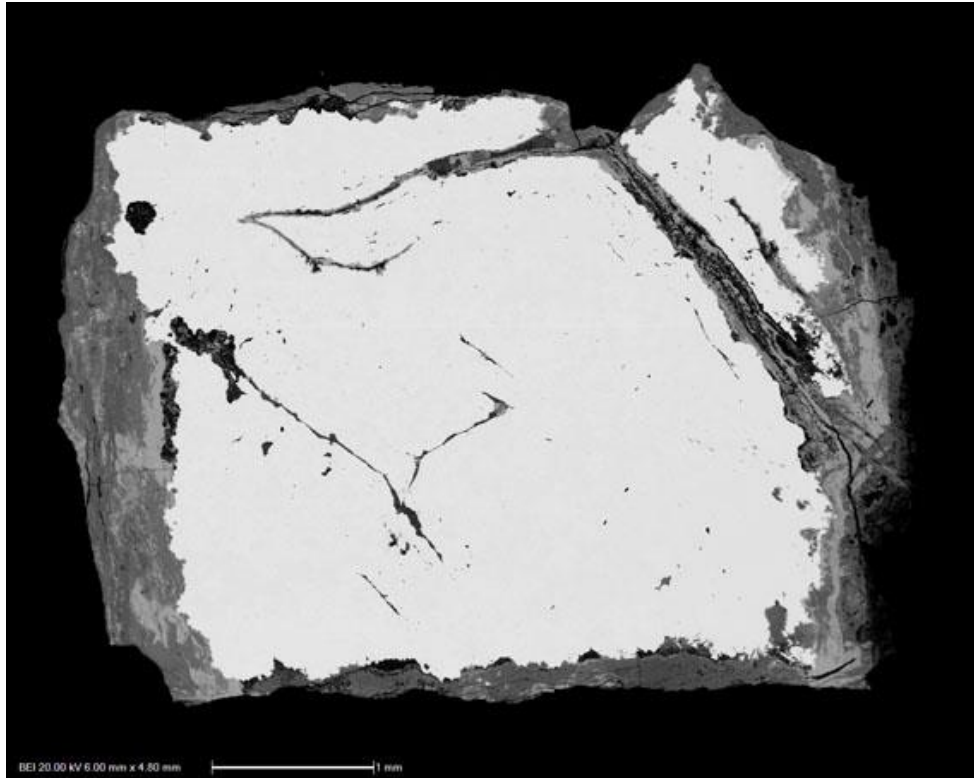


Figure 8.3 SEM-BSE image of Caerleon nail CAER_08 in polished cross-section at 20X magnification.

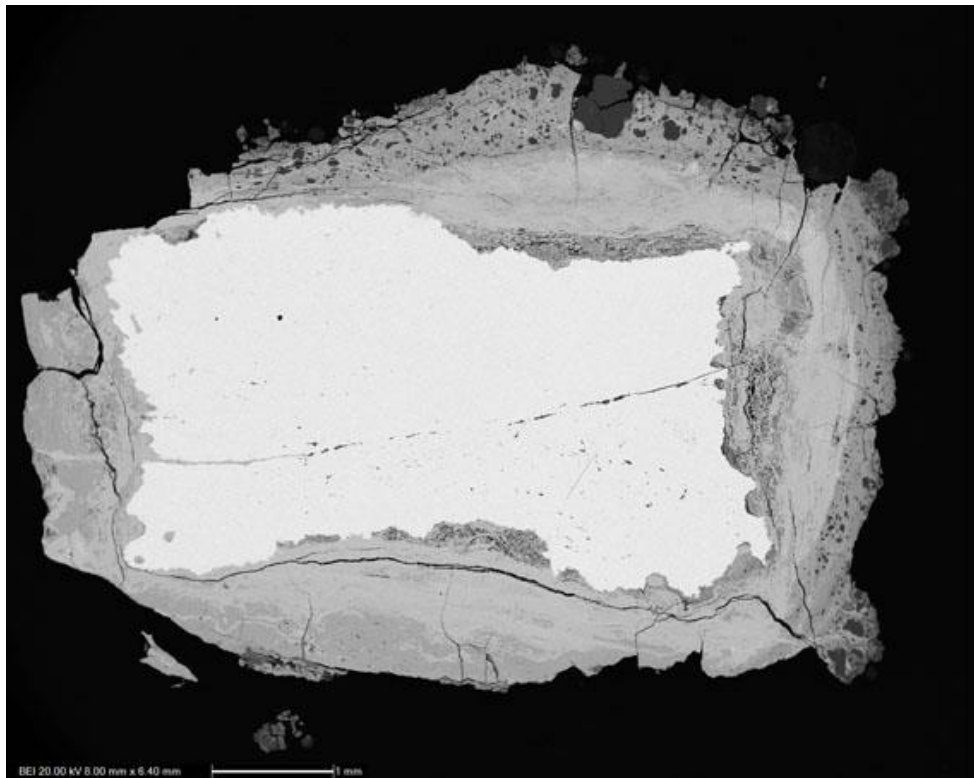


Figure 8.4 SEM-BSE image of Caerleon nail CAER_10 in polished cross-section at 15X magnification.



Figure 8.5 SEM-BSE image of Caerleon nail CAER_13 in polished cross-section at 13X magnification.

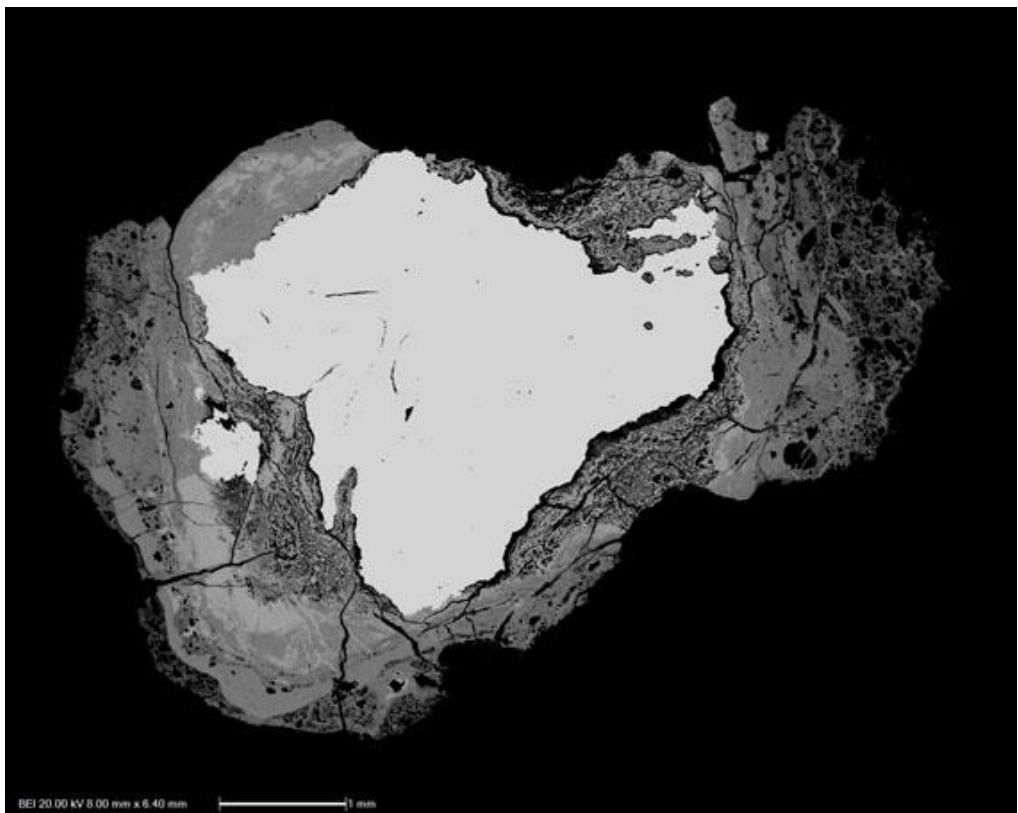


Figure 8.6 SEM-BSE image of Caerleon nail CAER_18 in polished cross-section at 15X magnification.

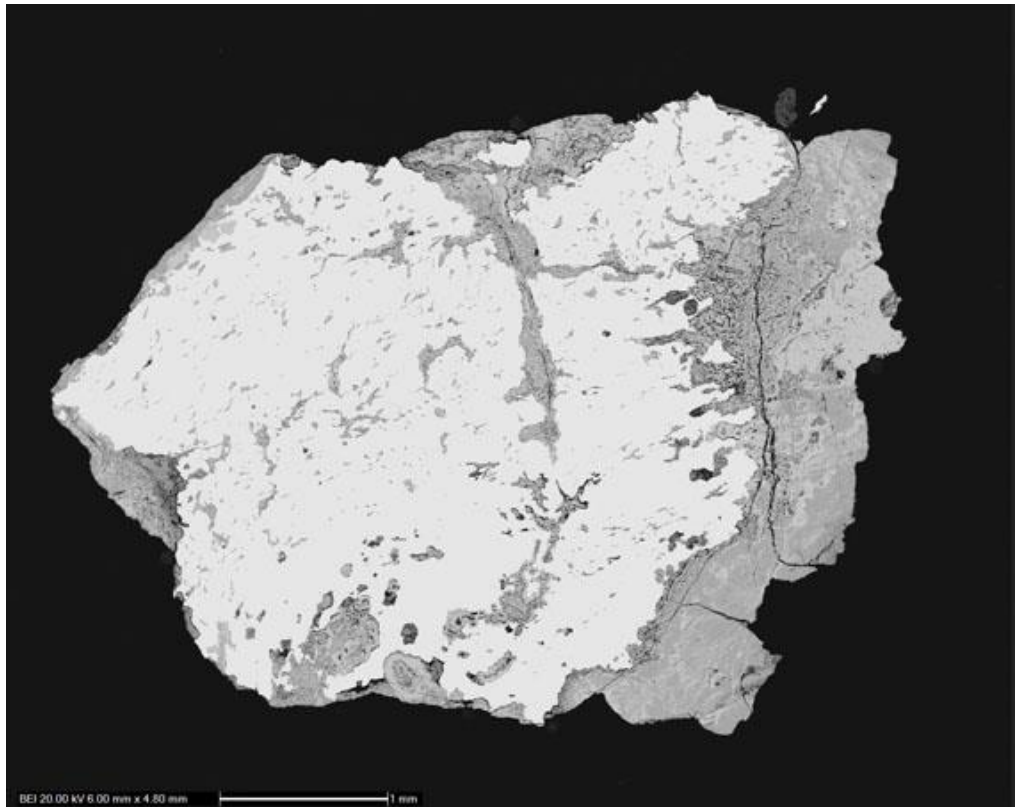


Figure 8.7 SEM-BSE image of Caerleon nail CAER_19 in polished cross-section at 20X magnification.

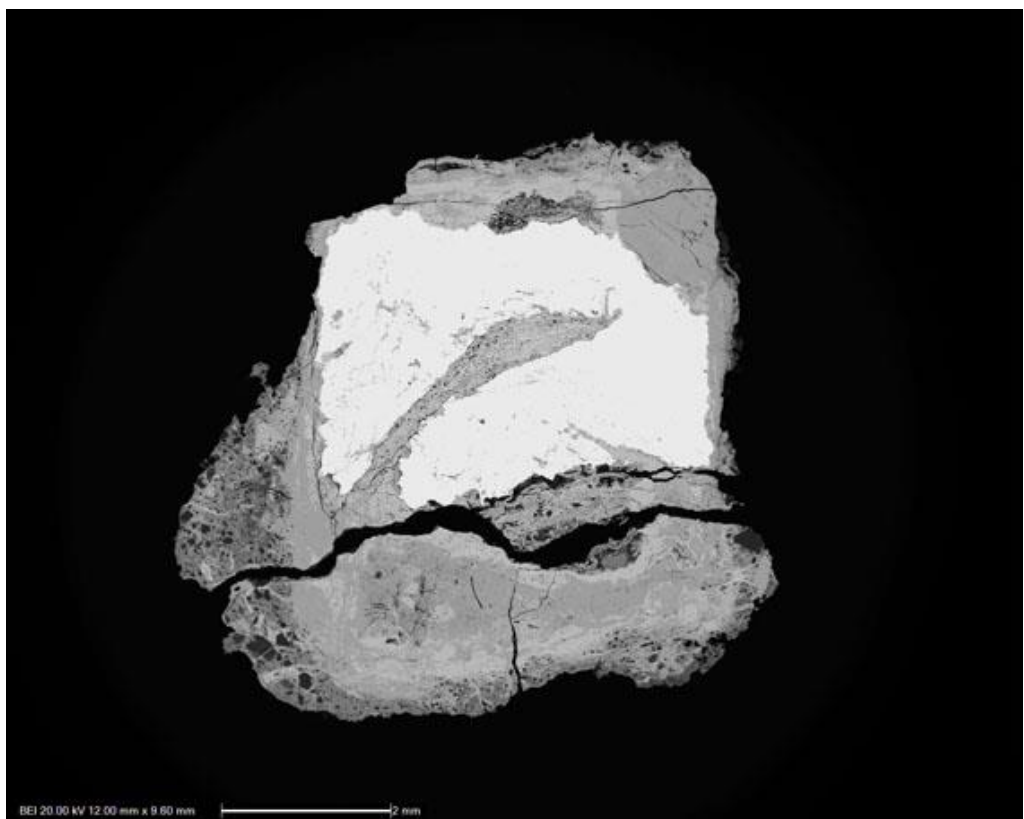


Figure 8.8 SEM-BSE image of Caerleon nail CAER_21 in polished cross-section at 13X magnification.

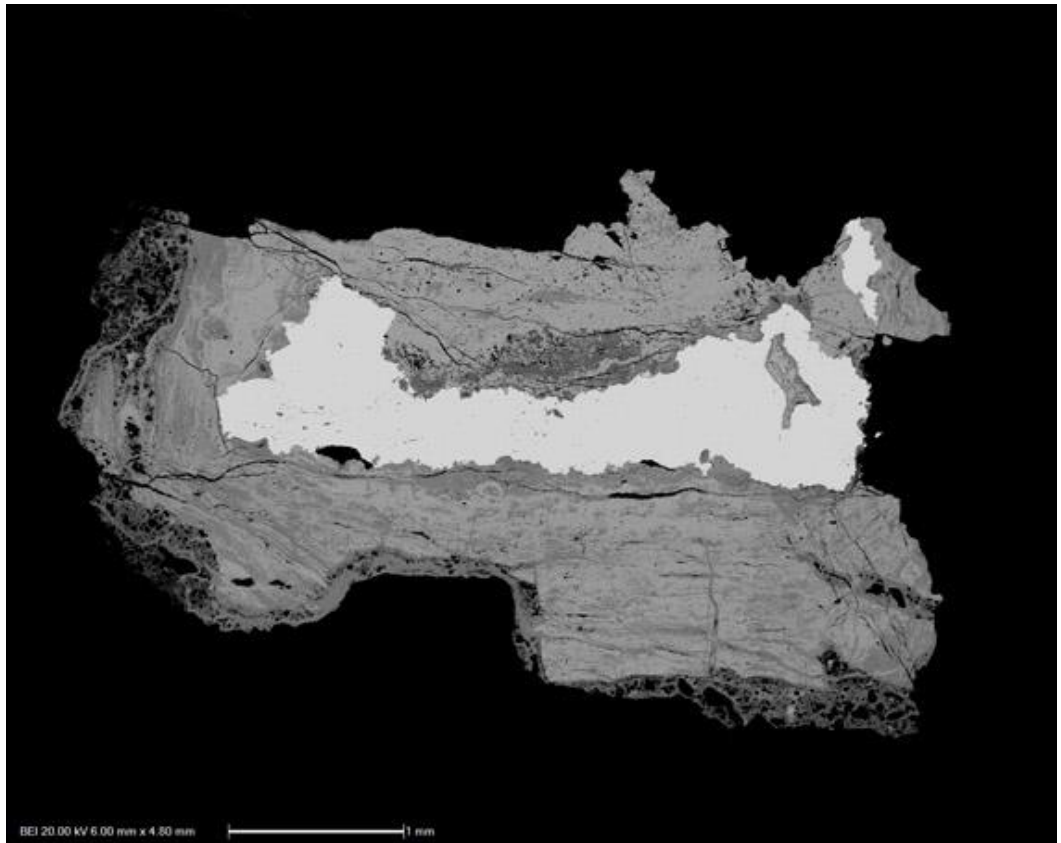


Figure 8.9 SEM-BSE image of Caerleon nail CAER_22 in polished cross-section at 20X magnification.

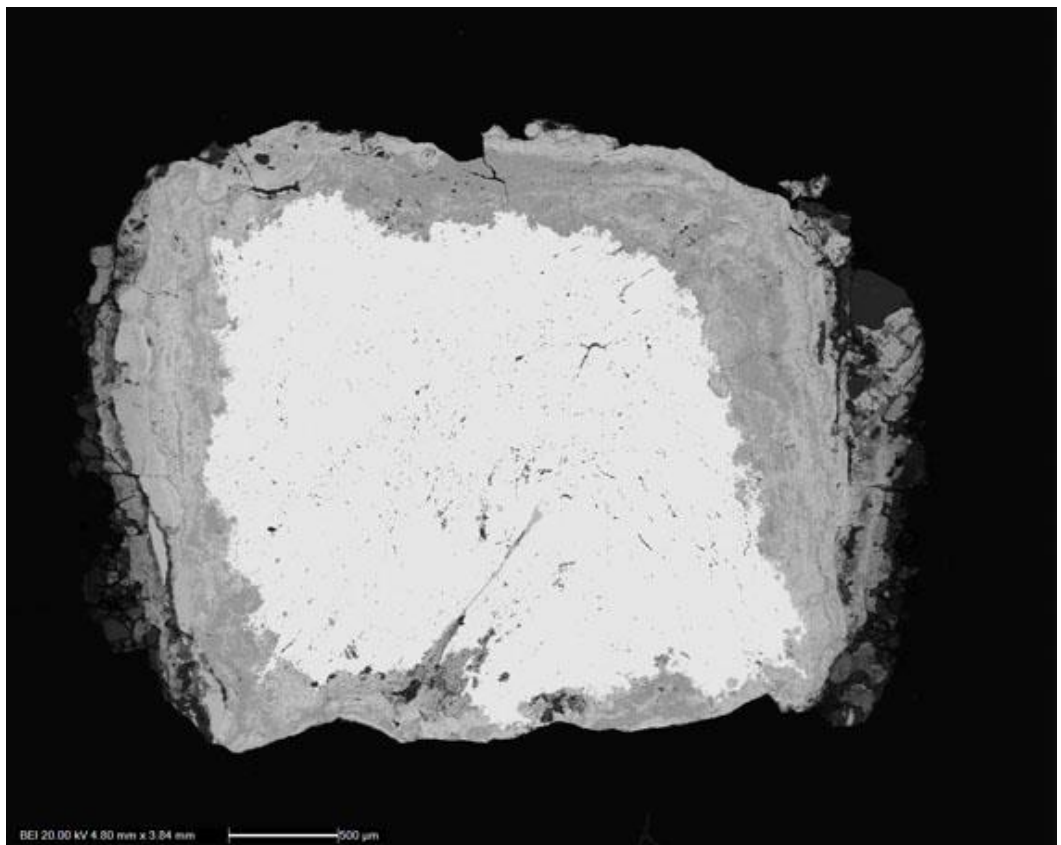


Figure 8.10 SEM-BSE image of Caerleon nail CAER_27 in polished cross-section at 25X magnification.

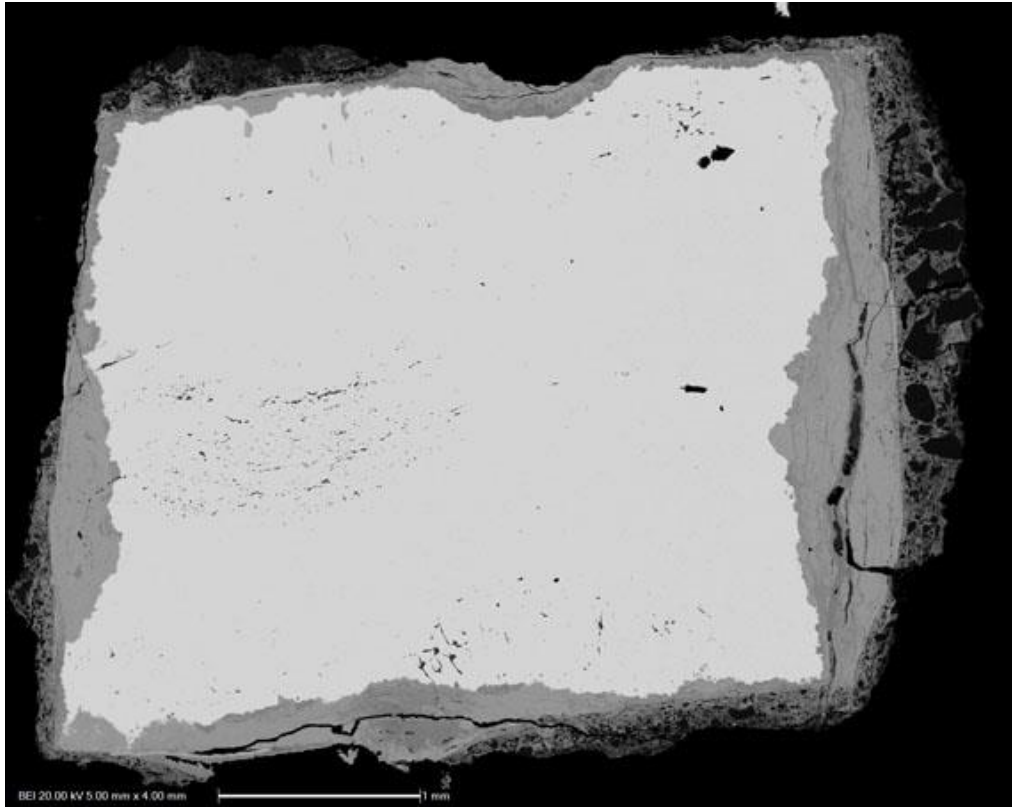


Figure 8.11 SEM-BSE image of Colonial Williamsburg nail CW_05 in polished cross-section at 24X magnification.

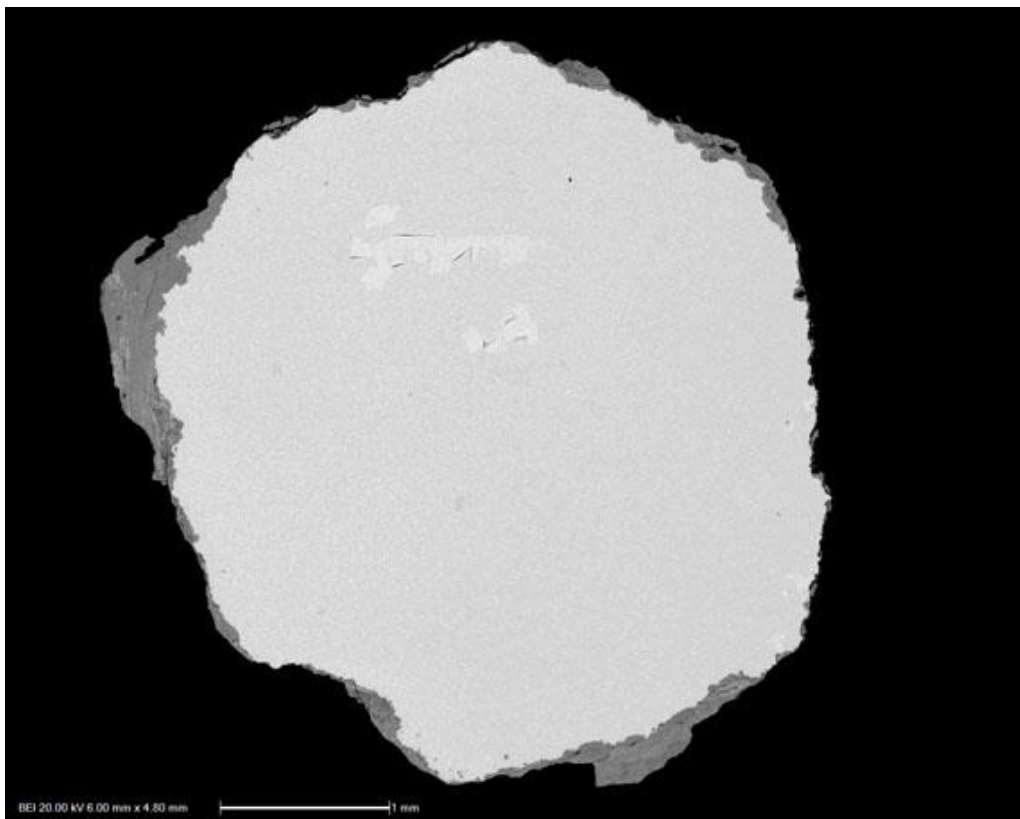


Figure 8.12 SEM-BSE image of Colonial Williamsburg nail CW_07 in polished cross-section at 20X magnification.

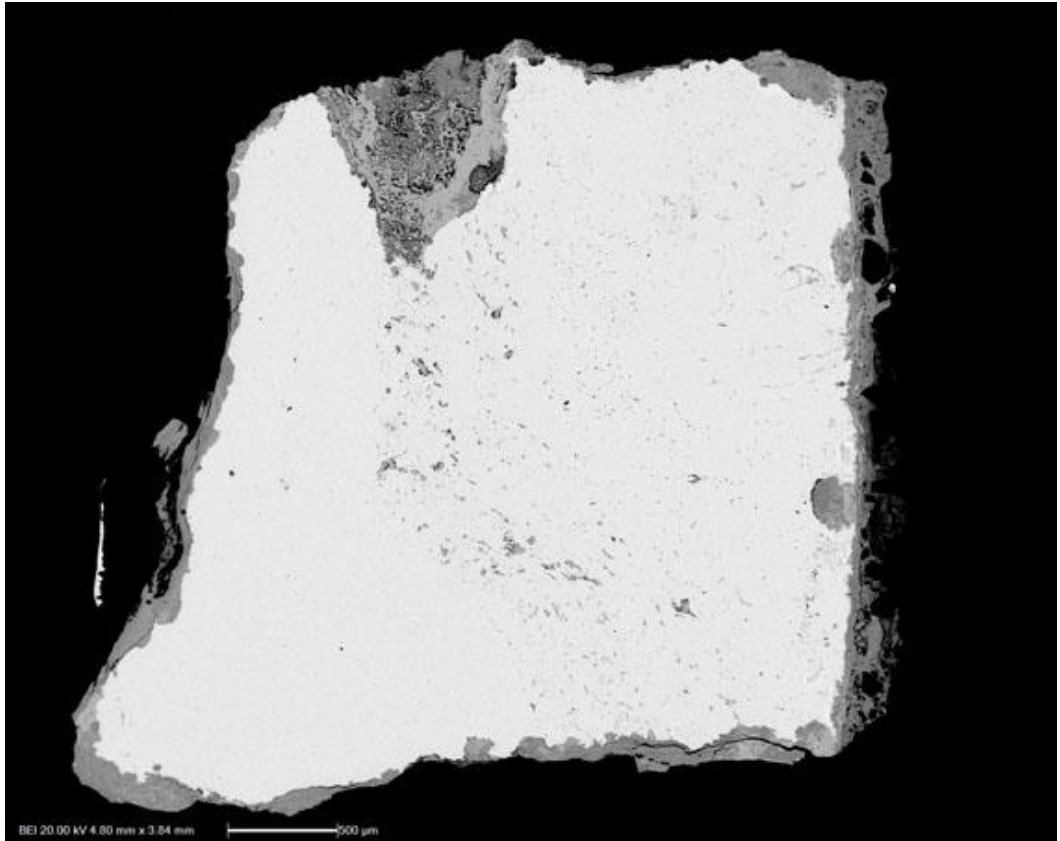


Figure 8.13 SEM-BSE image of Colonial Williamsburg nail CW_08 in polished cross-section at 25X magnification.

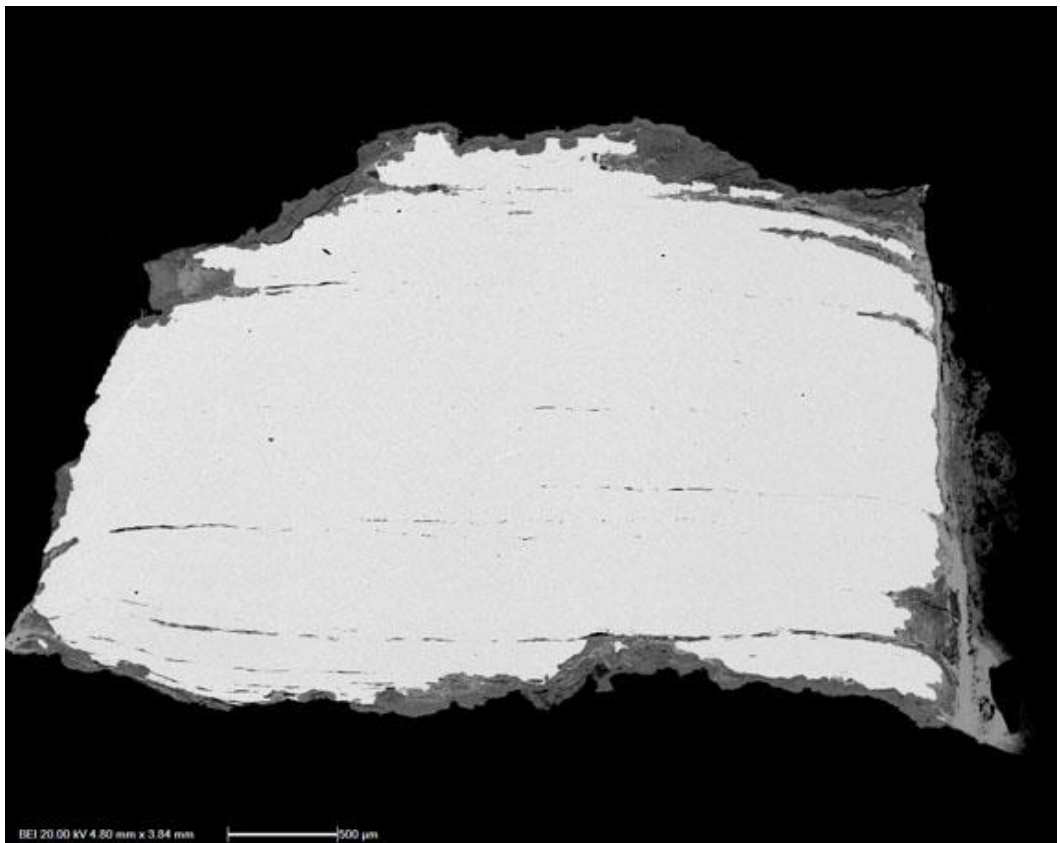


Figure 8.14 SEM-BSE image of Colonial Williamsburg nail CW_09 in polished cross-section at 20X magnification.



Figure 8.15 SEM-BSE image of Colonial Williamsburg nail CW_14 in polished cross-section at 20X magnification.

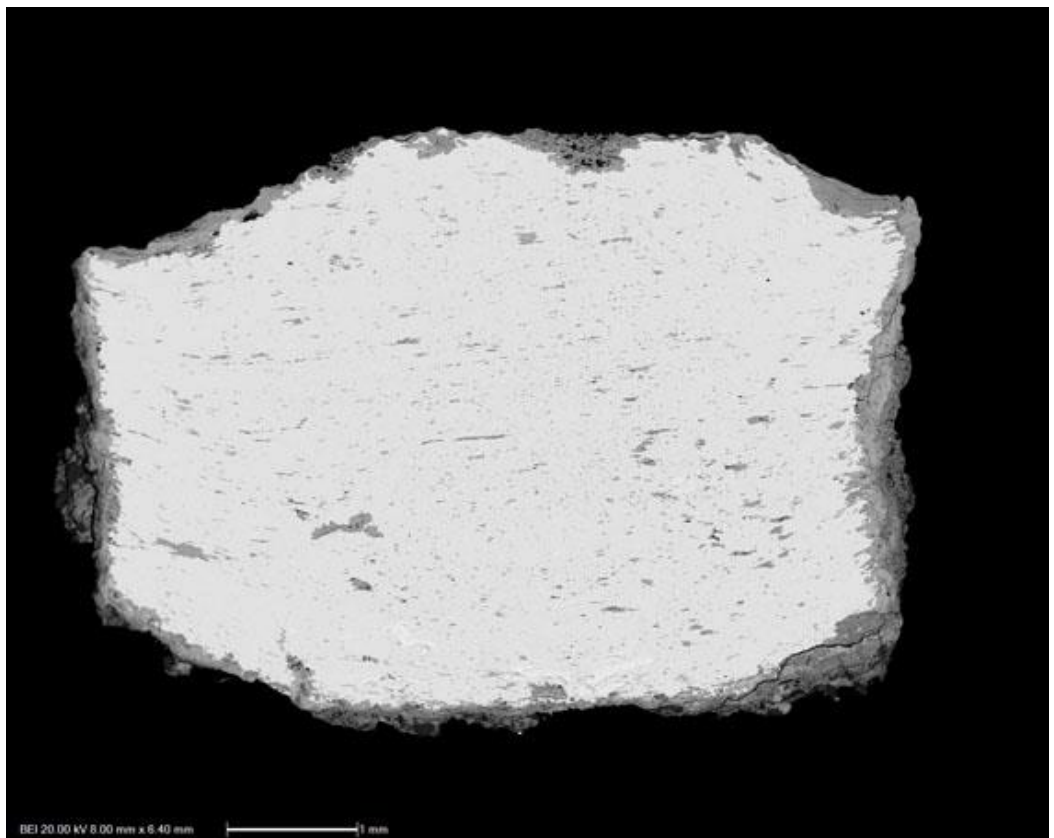


Figure 8.16 SEM-BSE image of Colonial Williamsburg nail CW_15 in polished cross-section at 15X magnification.

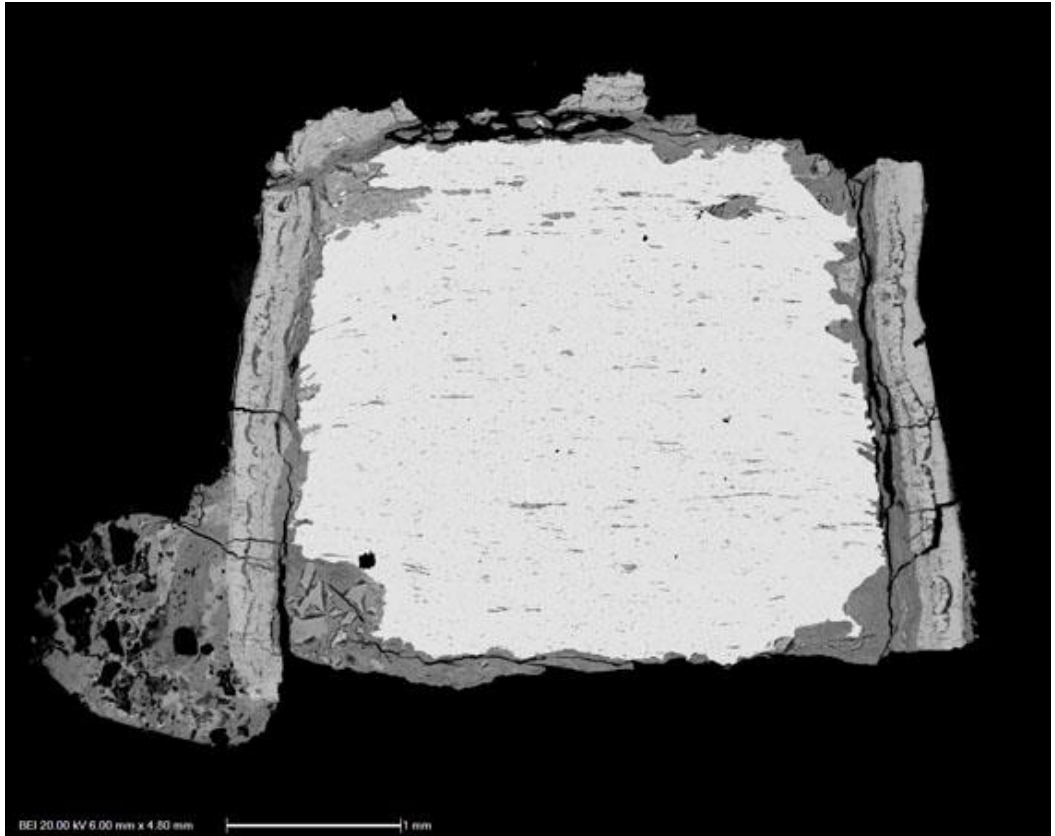


Figure 8.17 SEM-BSE image of Colonial Williamsburg nail CW_16 in polished cross-section at 20X magnification.

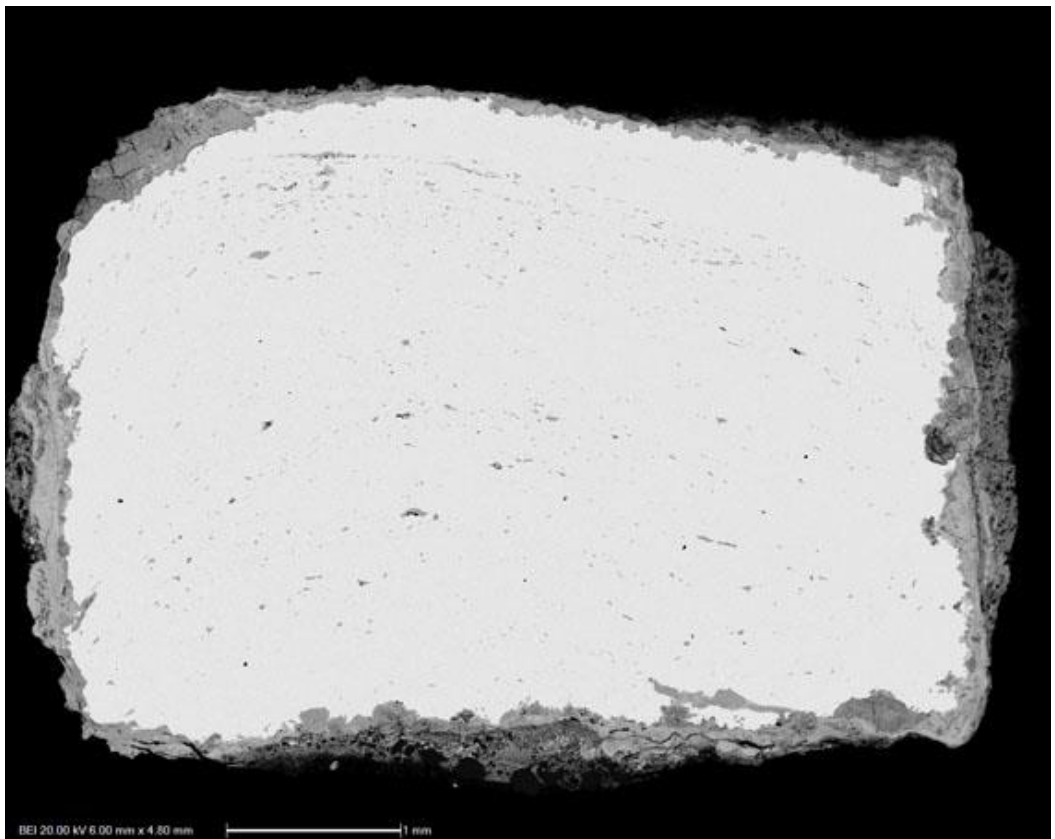


Figure 8.18 SEM-BSE image of Colonial Williamsburg nail CW_19 in polished cross-section at 20X magnification.

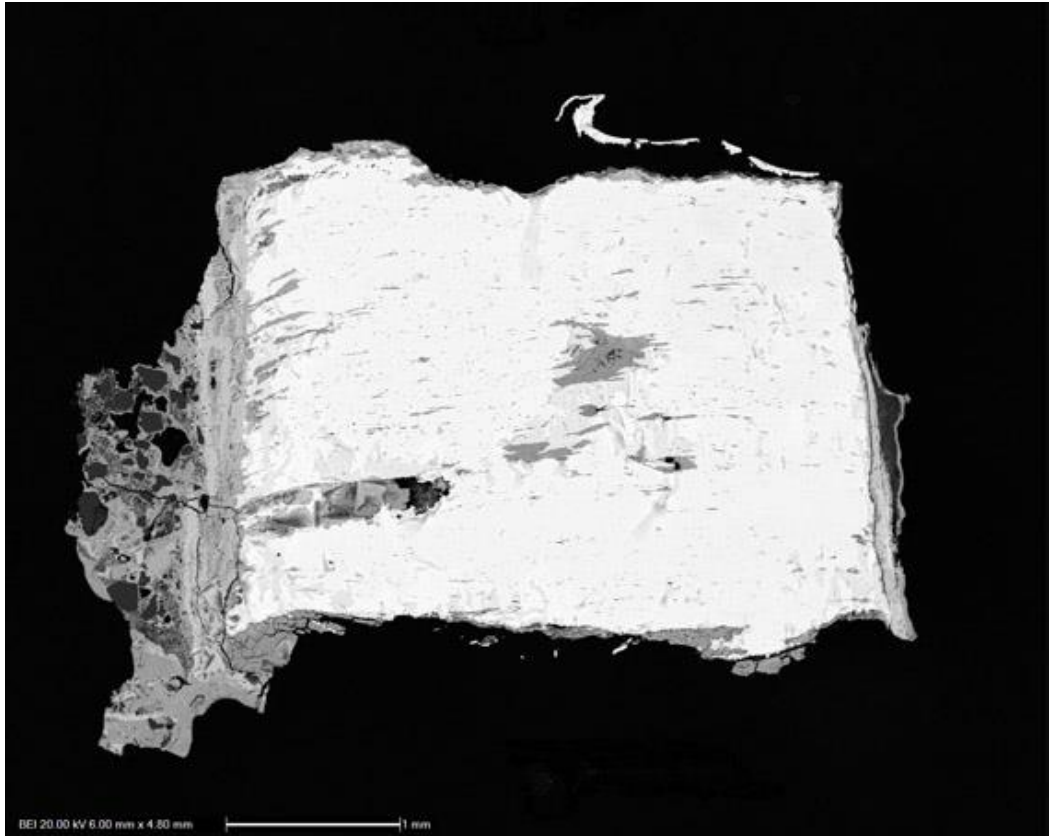


Figure 8.19 SEM-BSE image of Colonial Williamsburg nail CW_26 in polished cross-section at 20X magnification.

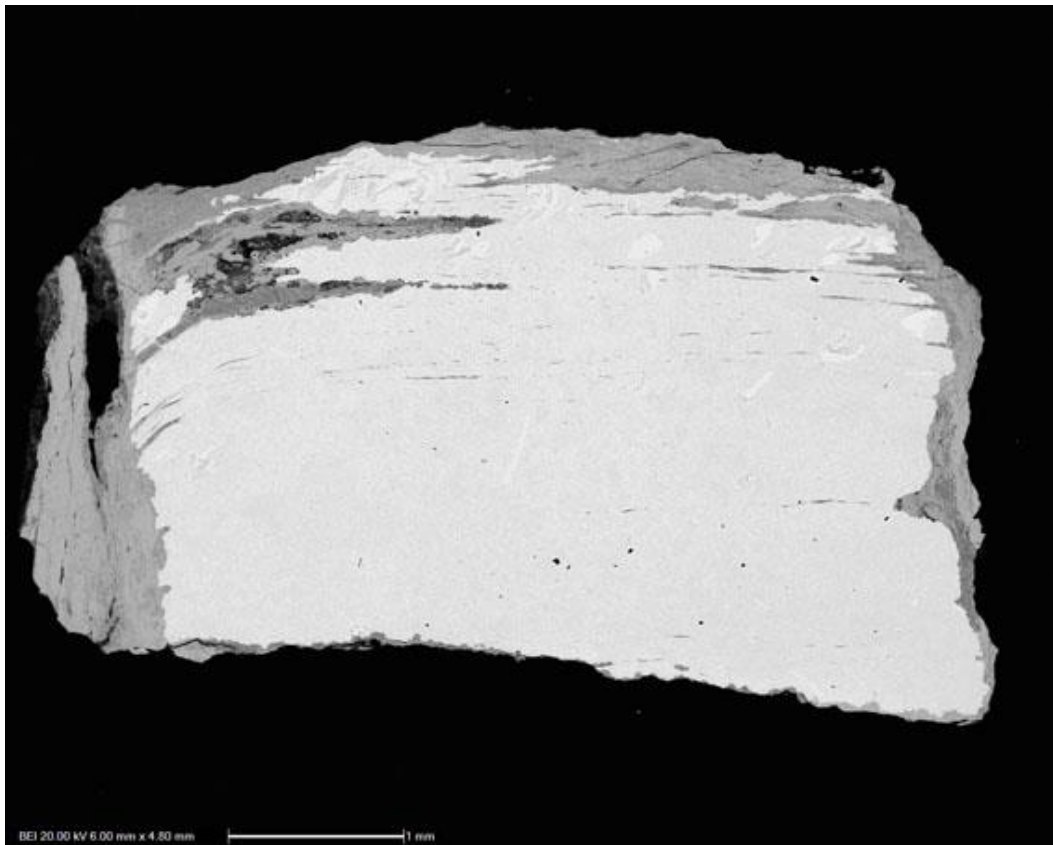


Figure 8.20 SEM-BSE image of Colonial Williamsburg nail CW_29 in polished cross-section at 20X magnification.

8.4.2 Elemental Maps of Nails in Cross Section

CAER_01

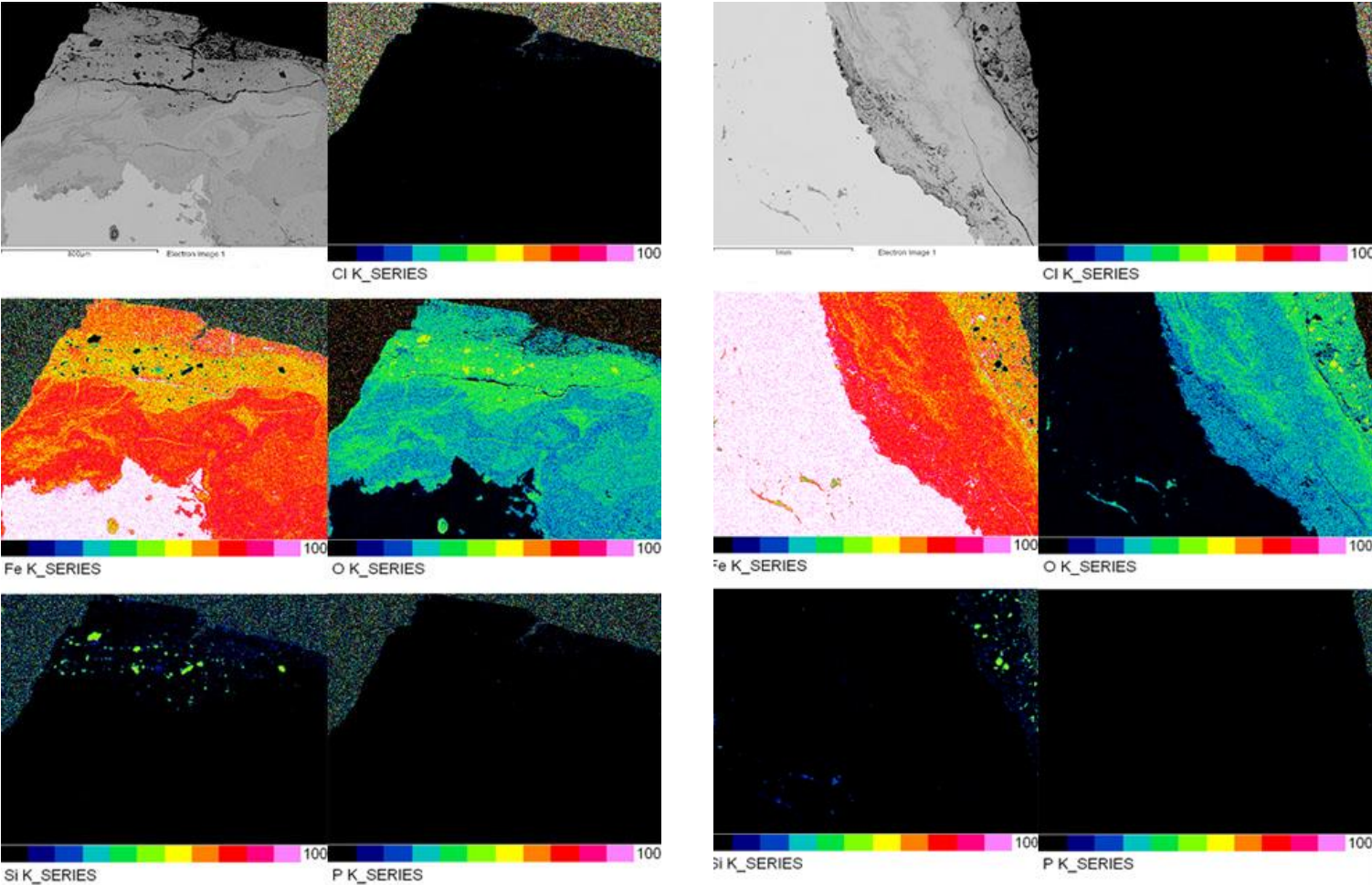


Figure 8.21 SEM-BSE image and corresponding EDS/WDS quantitative elemental maps for 5 elements detected in 2 sites of interest for sample CAER_01. Chlorine map acquired by SEM-WDS. Colours indicate wt% of element detected, in increments of 10%.

CAER_07

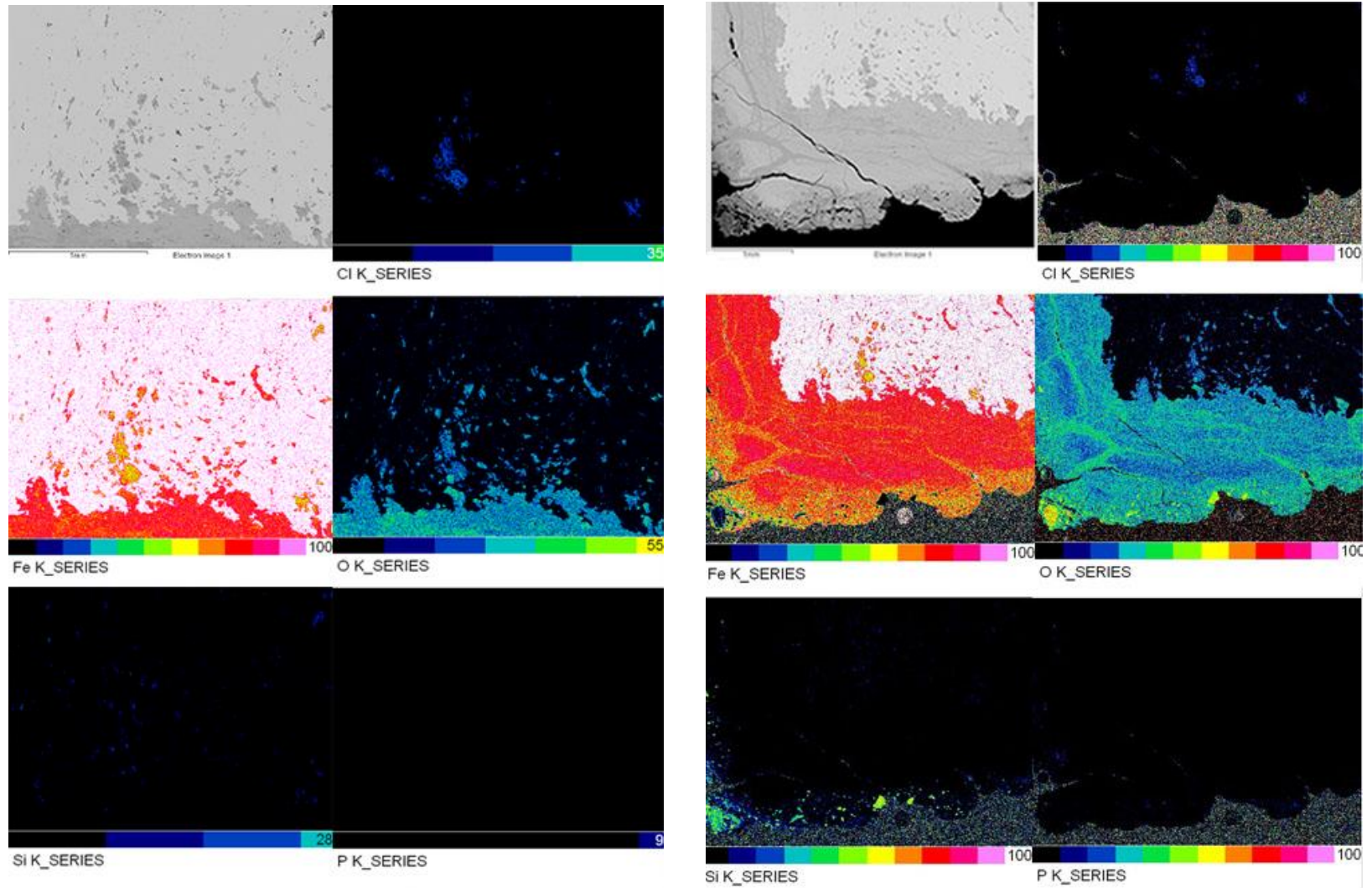


Figure 8.22 SEM-BSE image and corresponding EDS/WDS quantitative elemental maps for 5 elements detected in 2 sites of interest for sample CAER_07 Chlorine map acquired by SEM-WDS. Colours indicate wt% of element detected, in increments of 10%.

CAER_08

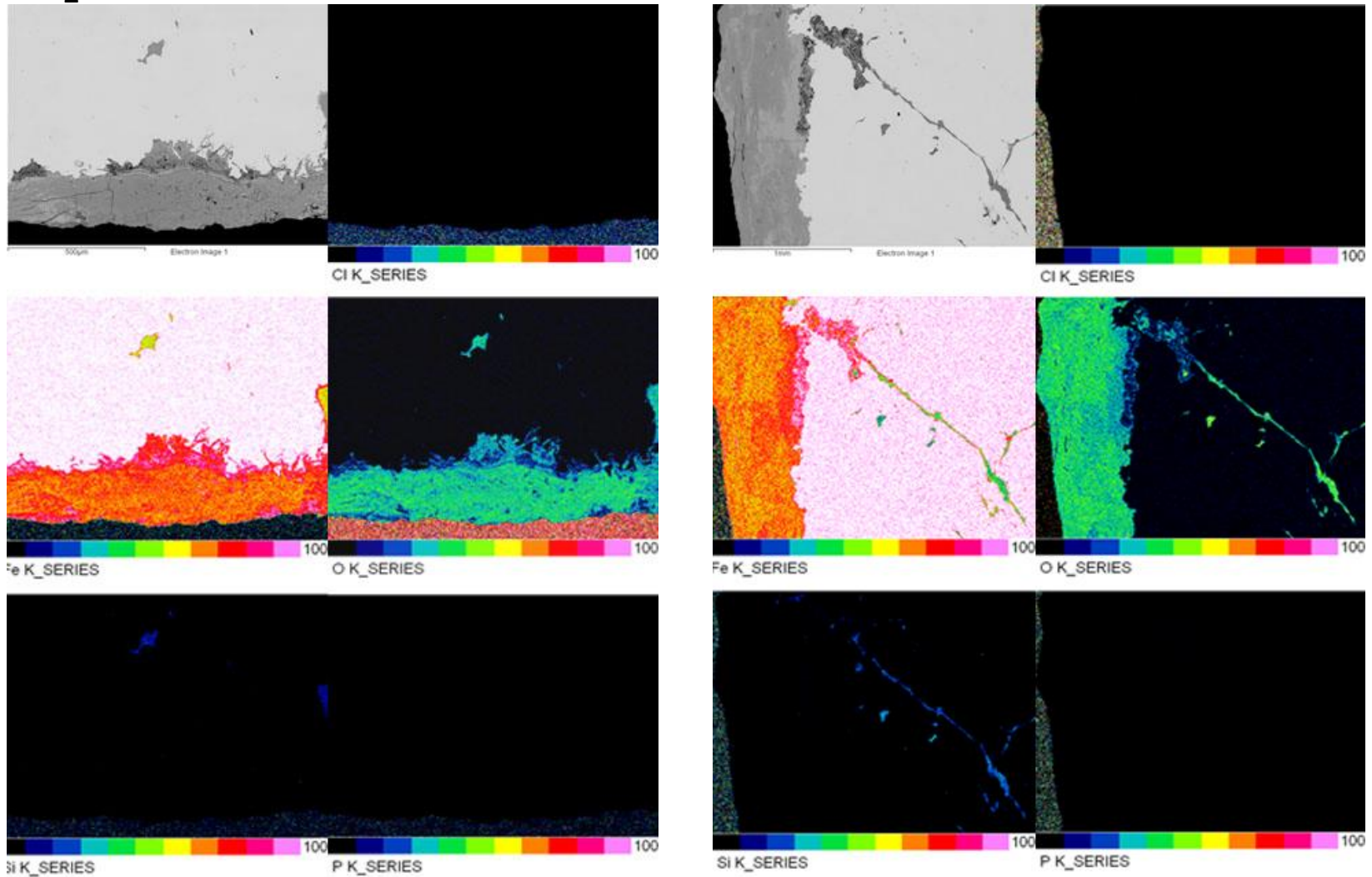


Figure 8.23 SEM-BSE image and corresponding EDS/WDS quantitative elemental maps for 5 elements detected in 2 sites of interest for sample CAER_08 Chlorine map acquired by SEM-WDS. Colours indicate wt% of element detected, in increments of 10%.

CAER_10

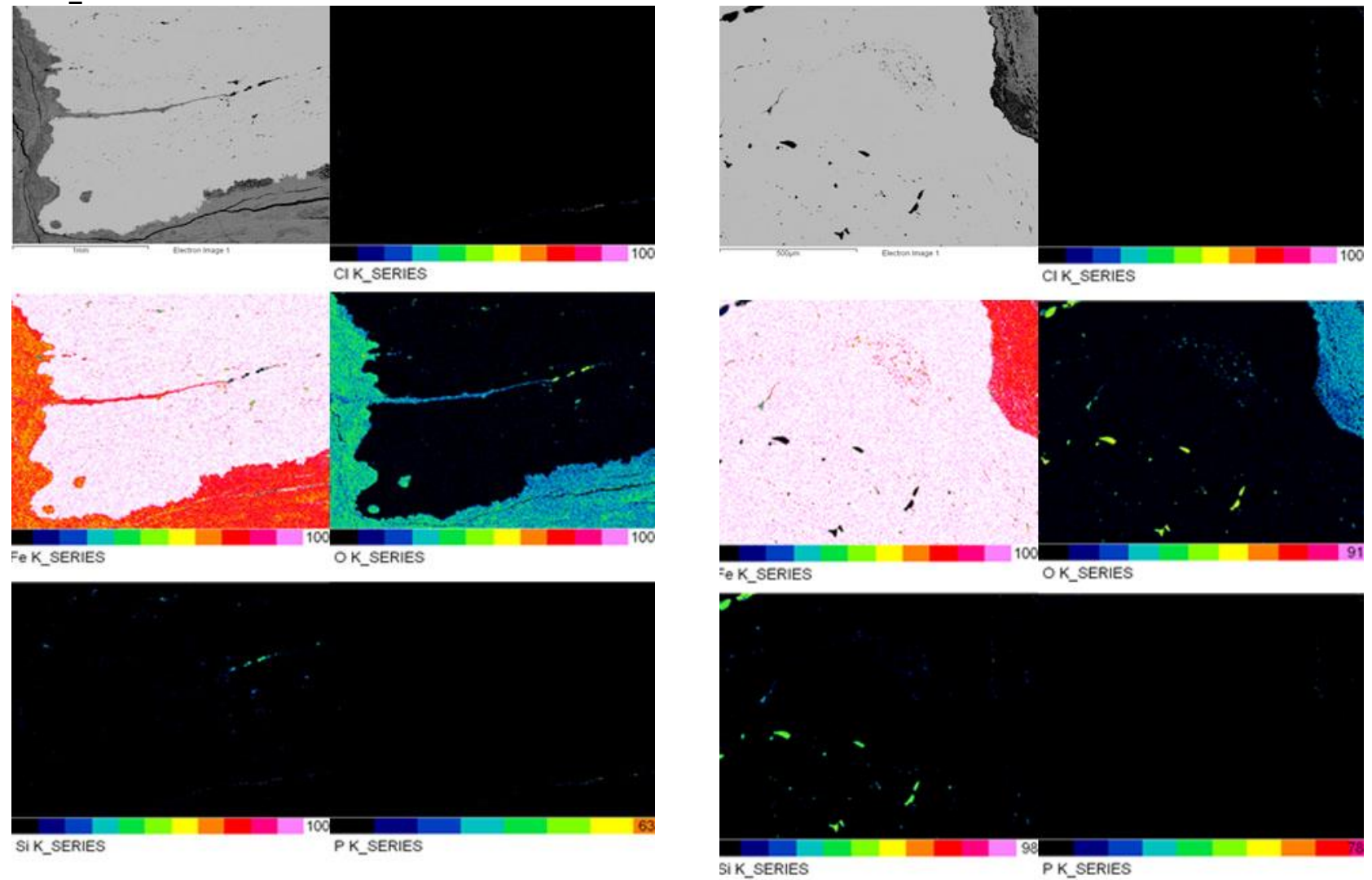


Figure 8.24 SEM-BSE image and corresponding EDS/WDS quantitative elemental maps for 5 elements detected in 2 sites of interest for sample CAER_10 Chlorine map acquired by SEM-WDS. Colours indicate wt% of element detected, in increments of 10%.

CAER_13

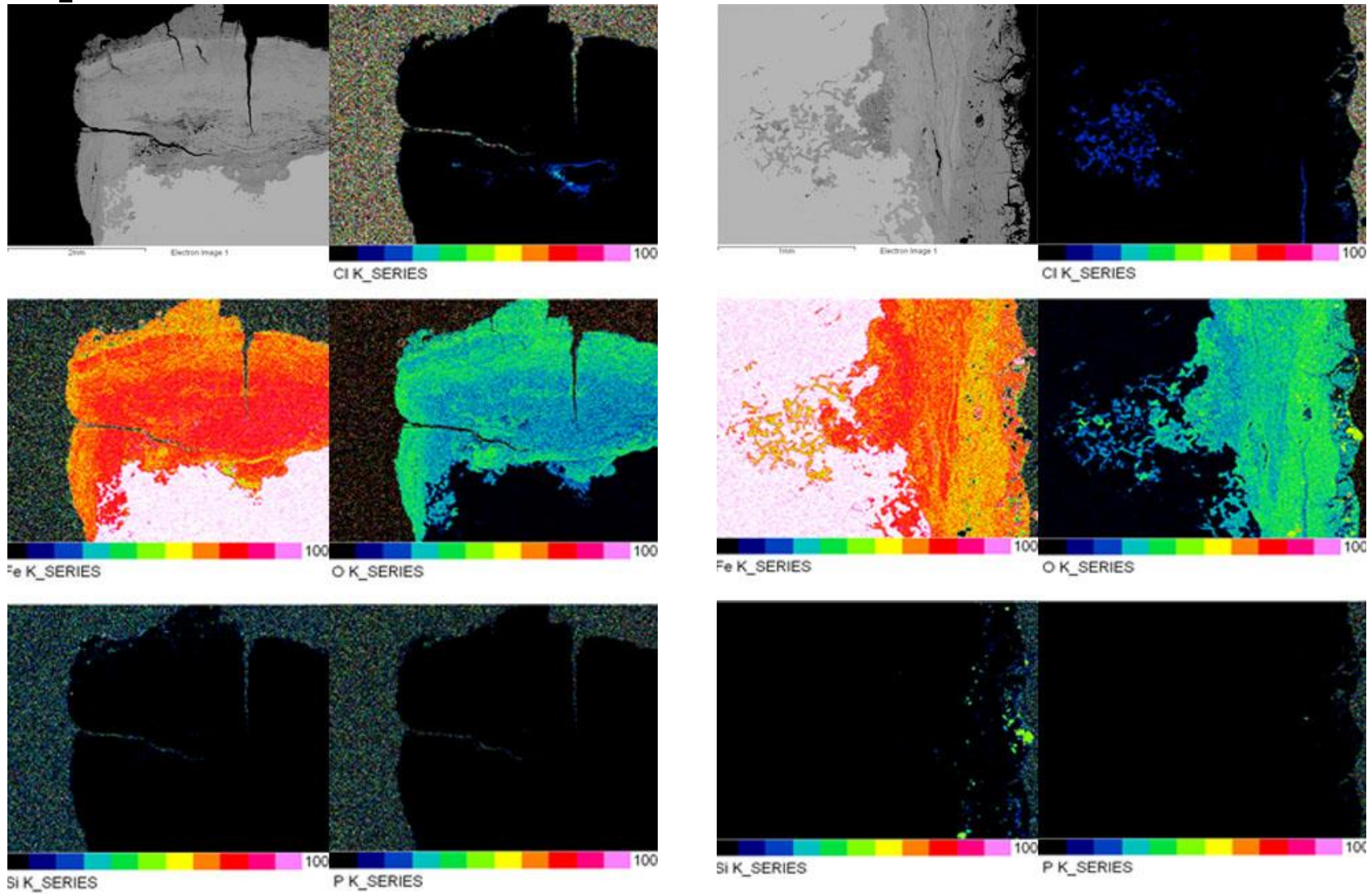


Figure 8.25 SEM-BSE image and corresponding EDS/WDS quantitative elemental maps for 5 elements detected in 2 sites of interest for sample CAER_13 Chlorine map acquired by SEM-WDS. Colours indicate wt% of element detected, in increments of 10%.

CAER_18

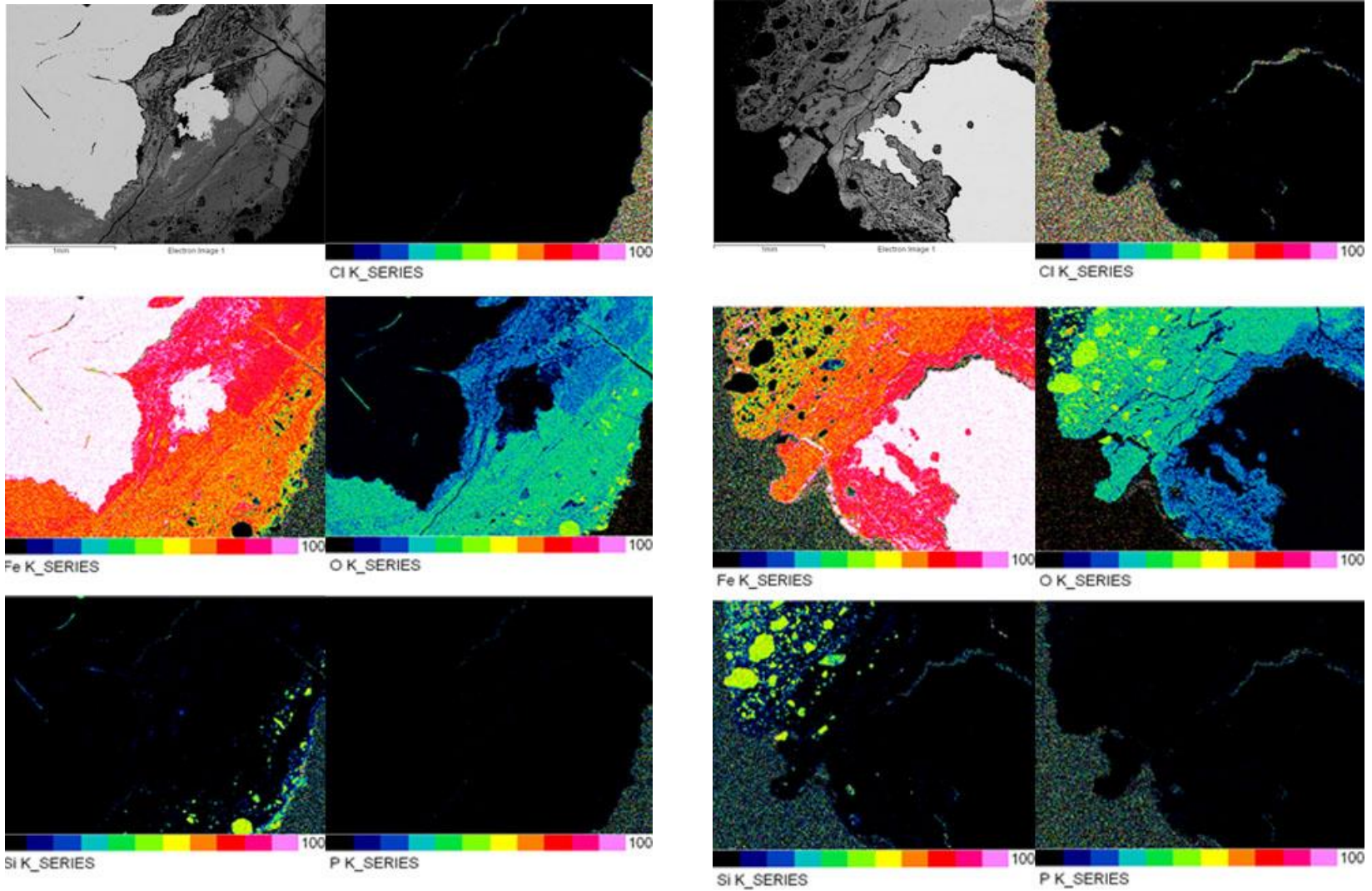


Figure 8.26 SEM-BSE image and corresponding EDS/WDS quantitative elemental maps for 5 elements detected in 2 sites of interest for sample CAER_18 Chlorine map acquired by SEM-WDS. Colours indicate wt% of element detected, in increments of 10%.

CAER_19

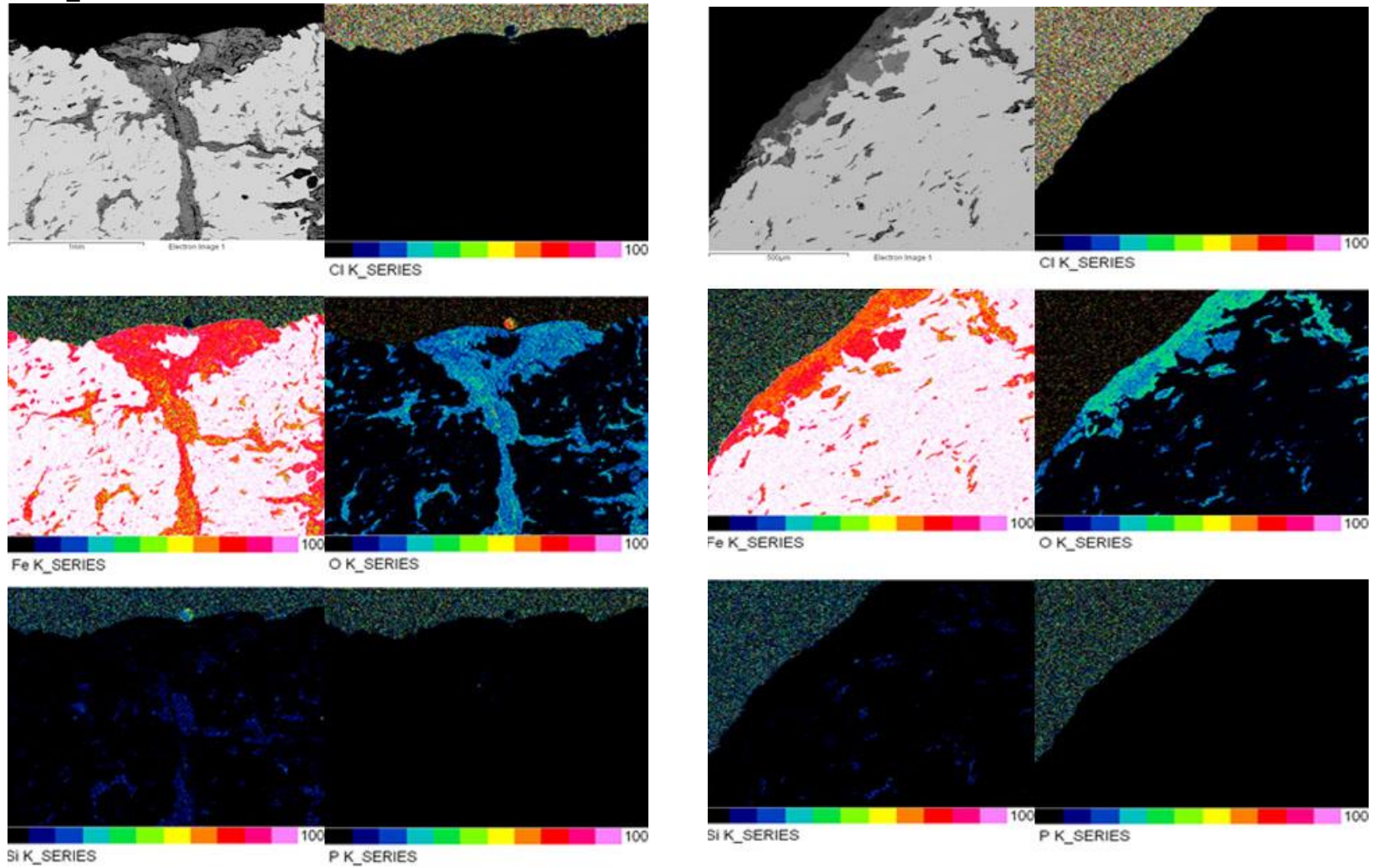


Figure 8.27 SEM-BSE image and corresponding EDS/WDS quantitative elemental maps for 5 elements detected in 2 sites of interest for sample CAER_19. Chlorine map acquired by SEM-WDS. Colours indicate wt% of element detected, in increments of 10%.

CAER_21

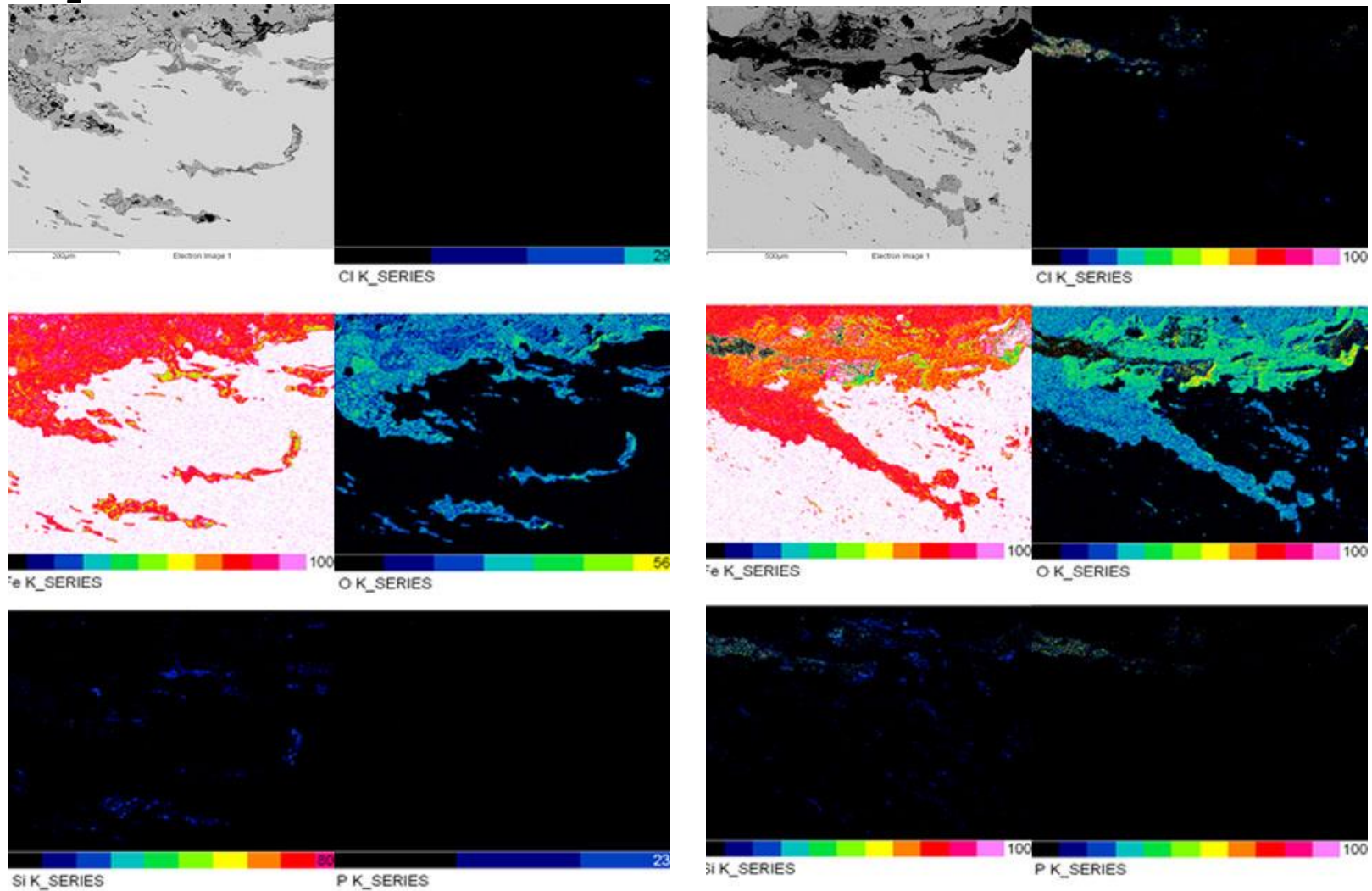


Figure 8.28 SEM-BSE image and corresponding EDS/WDS quantitative elemental maps for 5 elements detected in 2 sites of interest for sample CAER_21. Chlorine map acquired by SEM-WDS. Colours indicate wt% of element detected, in increments of 10%.

CAER_22

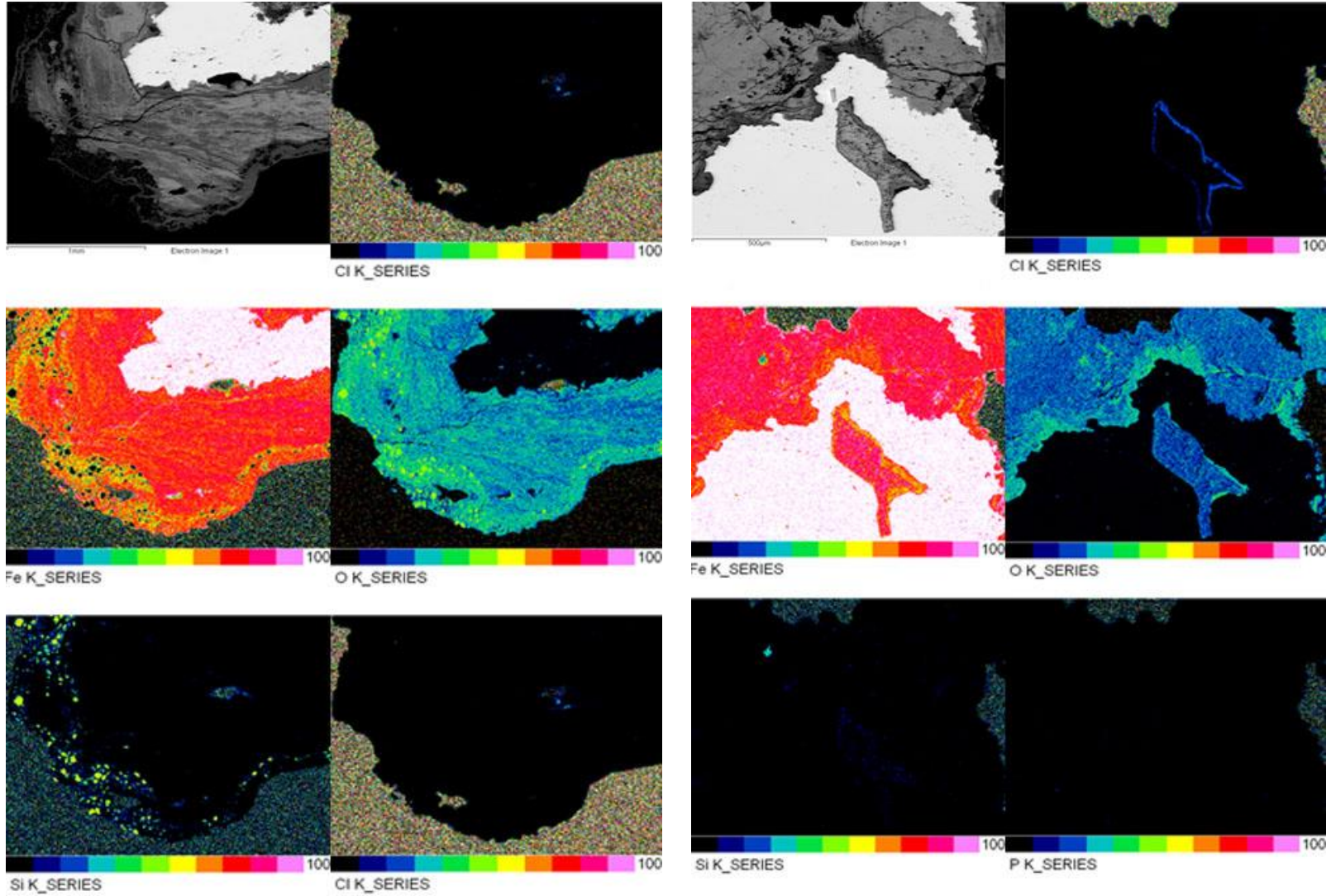


Figure 8.29 SEM-BSE image and corresponding EDS/WDS quantitative elemental maps for 5 elements detected in 2 sites of interest for sample CAER_22 Chlorine map acquired by SEM-WDS. Colours indicate wt% of element detected, in increments of 10%.

CAER_27

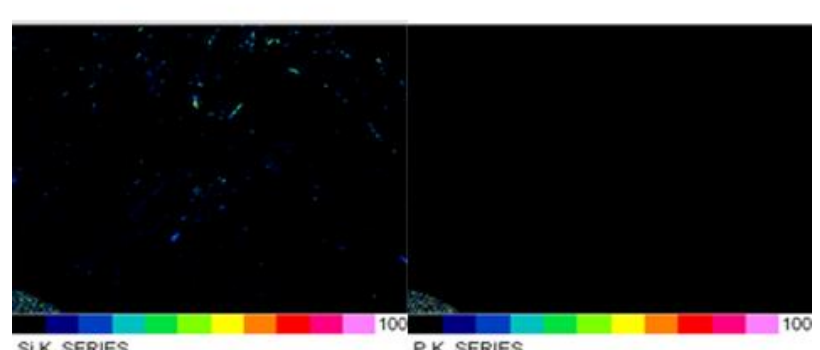
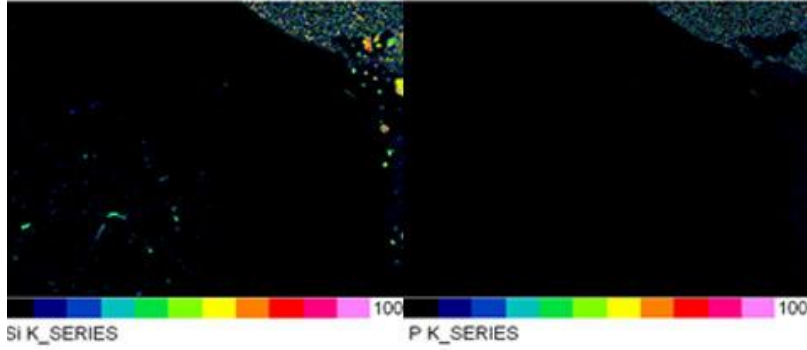
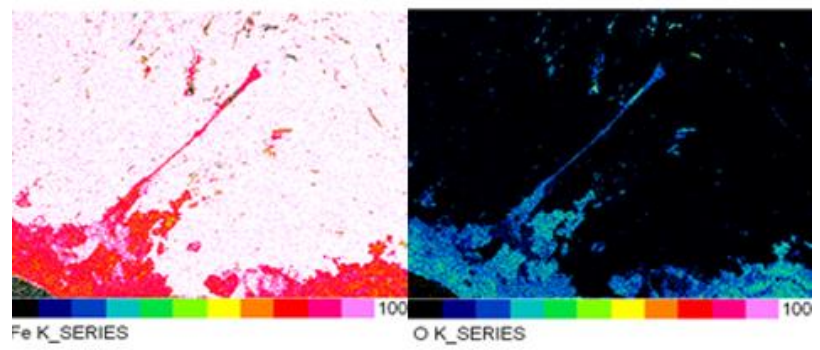
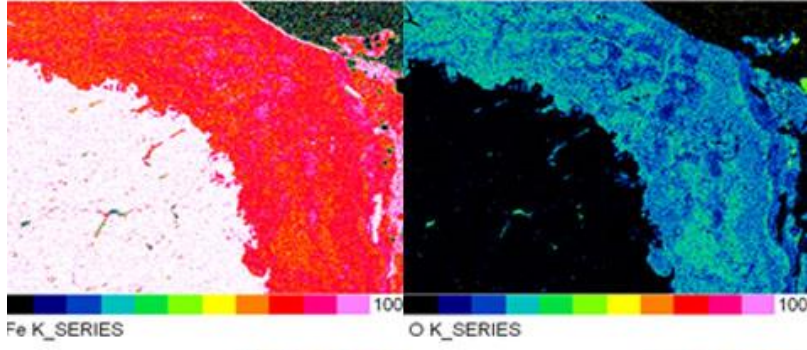
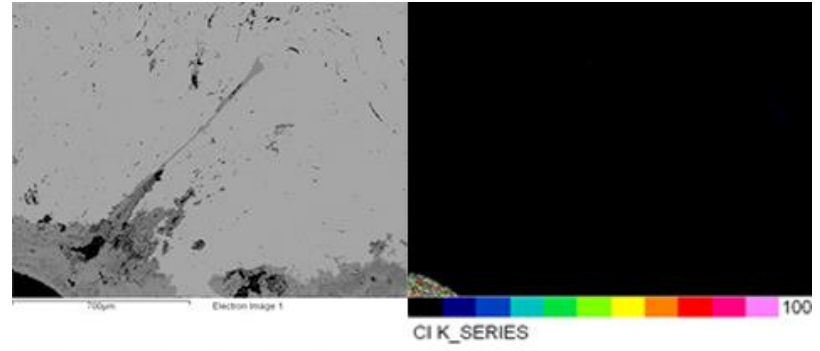
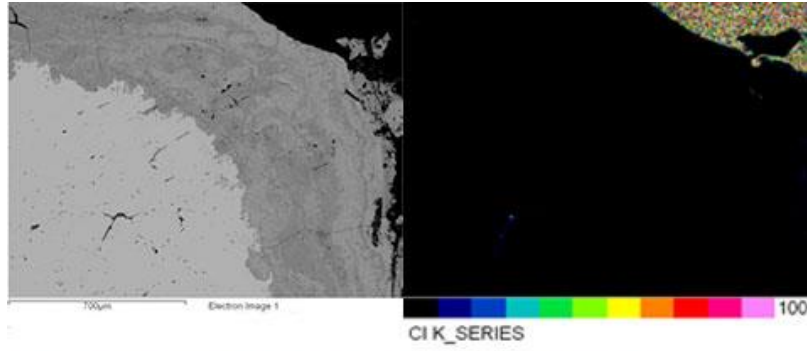


Figure 8.30 SEM-BSE image and corresponding EDS/WDS quantitative elemental maps for 5 elements detected in 2 sites of interest for sample CAER_28 Chlorine map acquired by SEM-WDS. Colours indicate wt% of element detected, in increments of 10%.

CW_05

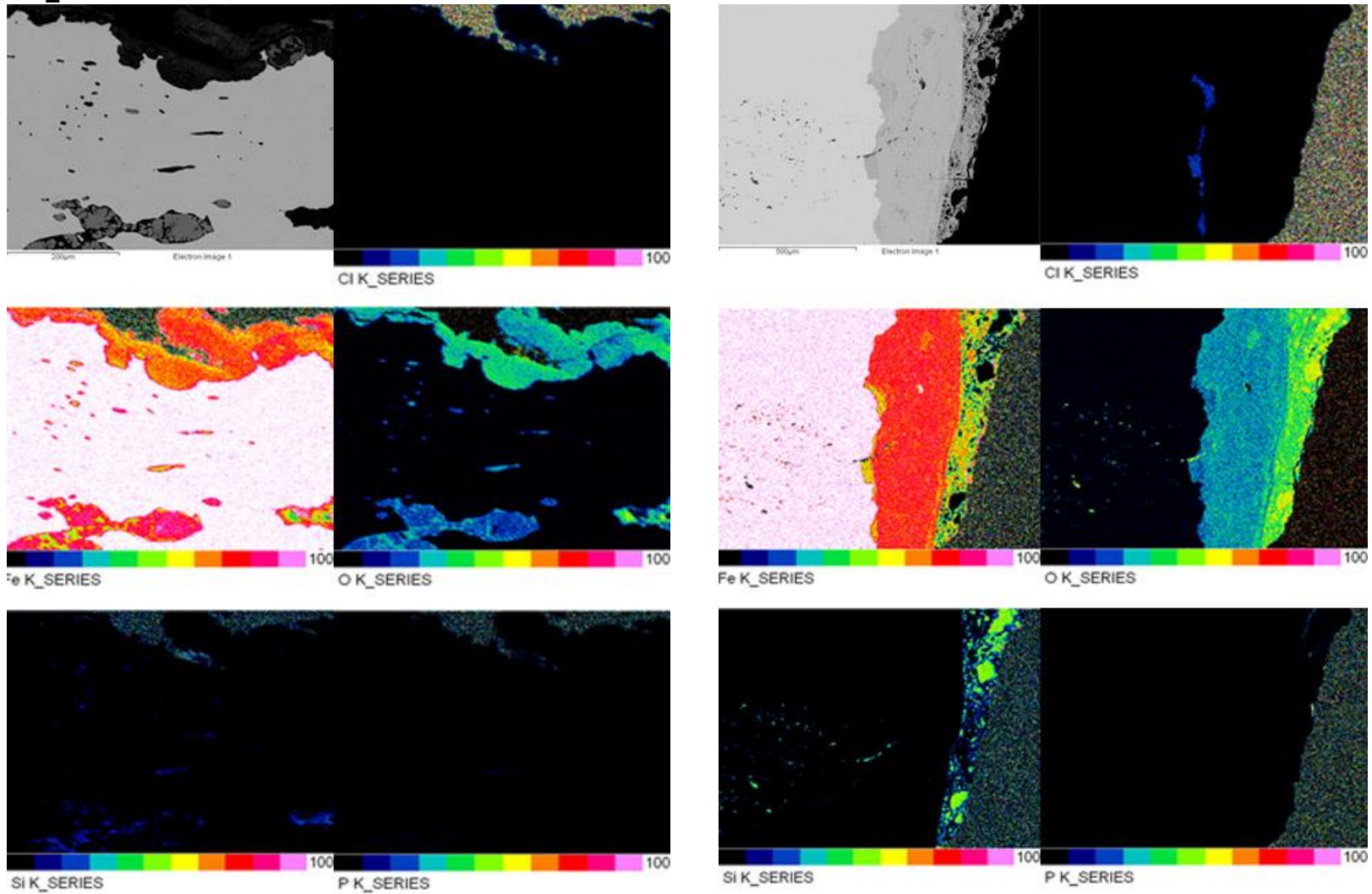


Figure 8.31 SEM-BSE image and corresponding EDS/WDS quantitative elemental maps for 5 elements detected in 2 sites of interest for sample CW_05. Chlorine map acquired by SEM-WDS. Colours indicate wt% of element detected, in increments of 10%.

CW_07

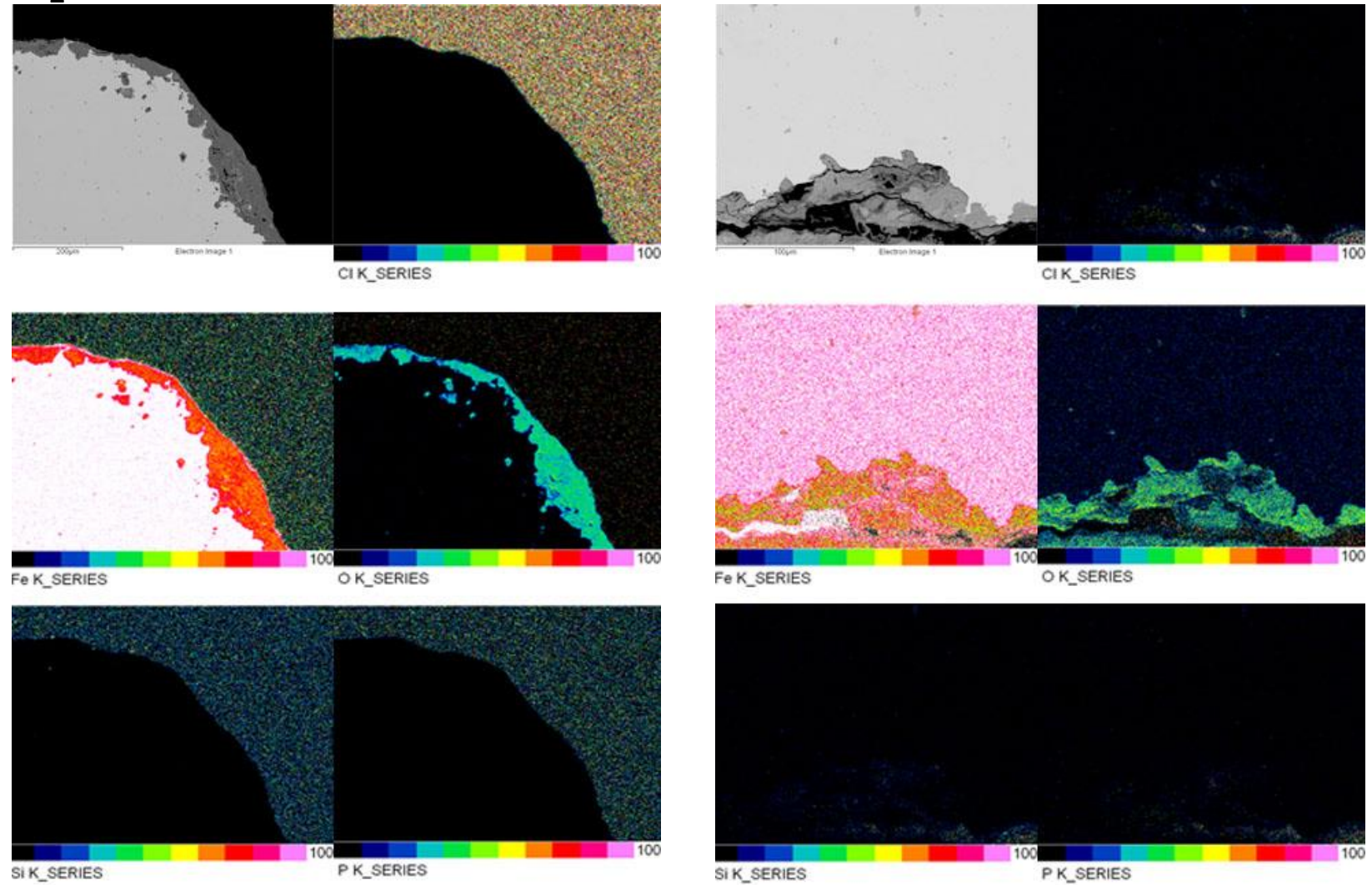


Figure 8.32 SEM-BSE image and corresponding EDS/WDS quantitative elemental maps for 5 elements detected in 2 sites of interest for sample CW_07. Chlorine map acquired by SEM-WDS. Colours indicate wt% of element detected, in increments of 10%.

CW_08

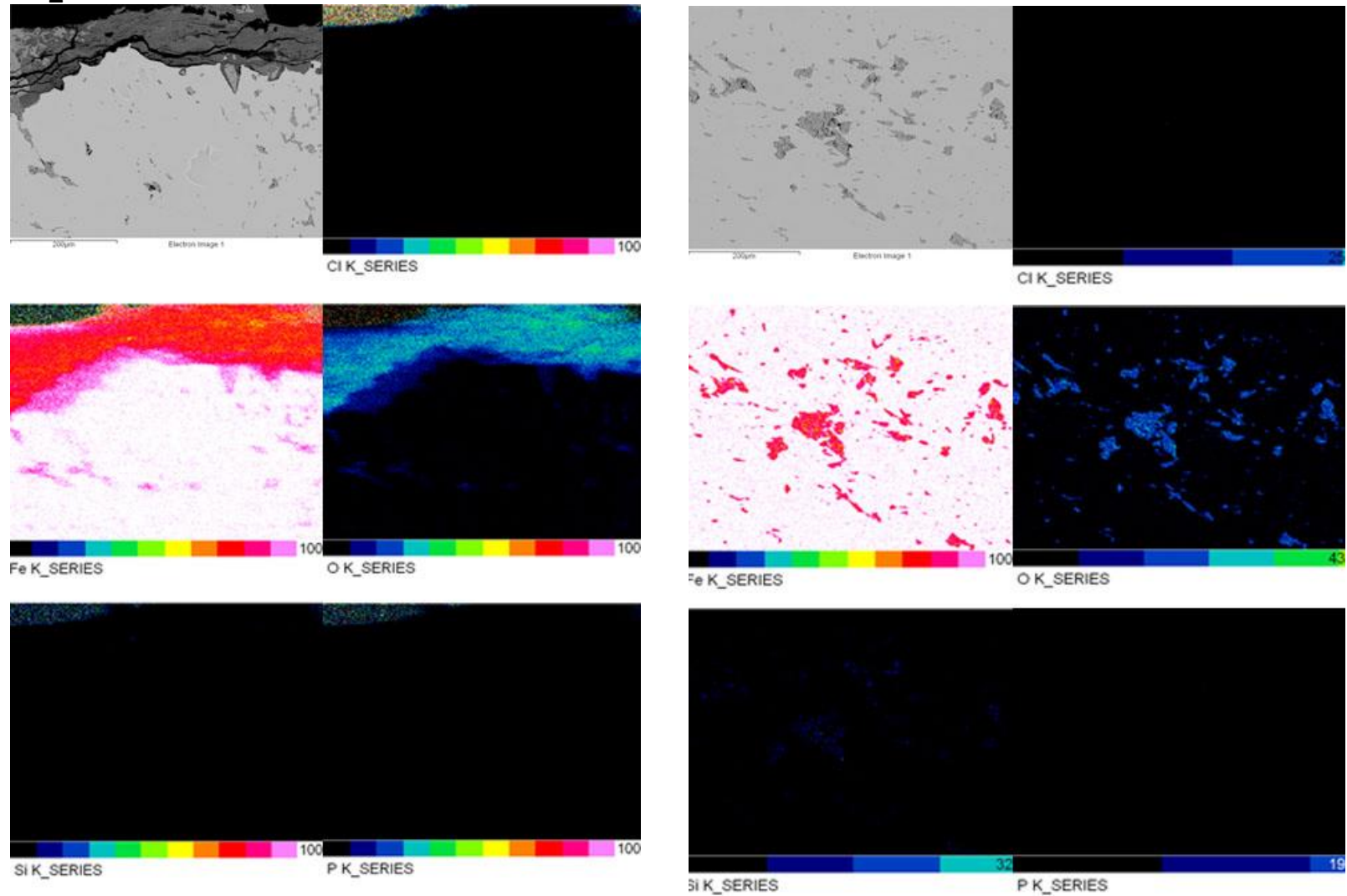


Figure 8.33 SEM-BSE image and corresponding EDS/WDS quantitative elemental maps for 5 elements detected in 2 sites of interest for sample CW_08. Chlorine map acquired by SEM-WDS. Colours indicate wt% of element detected, in increments of 10%.

CW_09

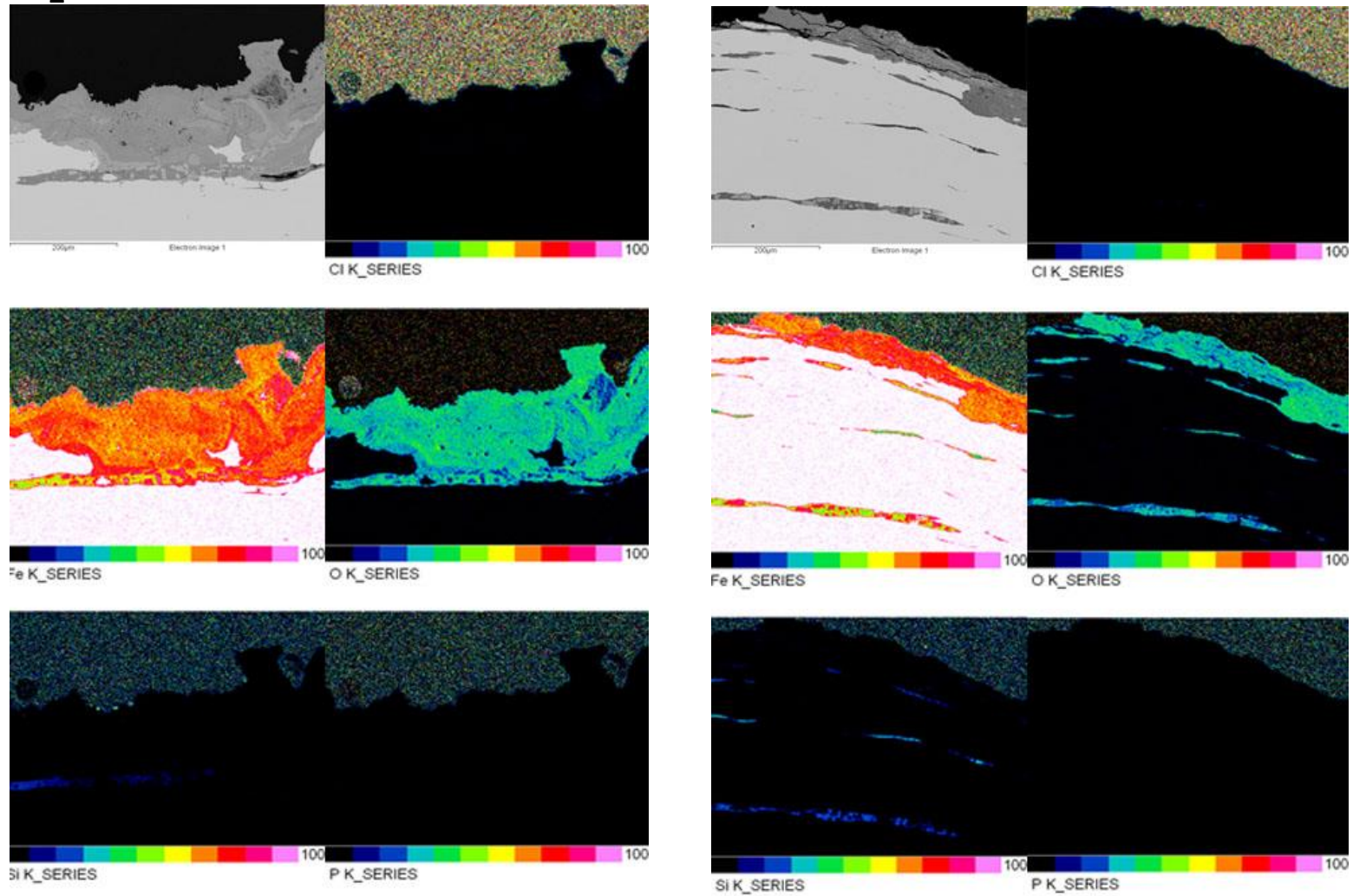


Figure 8.34 SEM-BSE image and corresponding EDS/WDS quantitative elemental maps for 5 elements detected in 2 sites of interest for sample CW_09. Chlorine map acquired by SEM-WDS. Colours indicate wt% of element detected, in increments of 10%.

CW_14

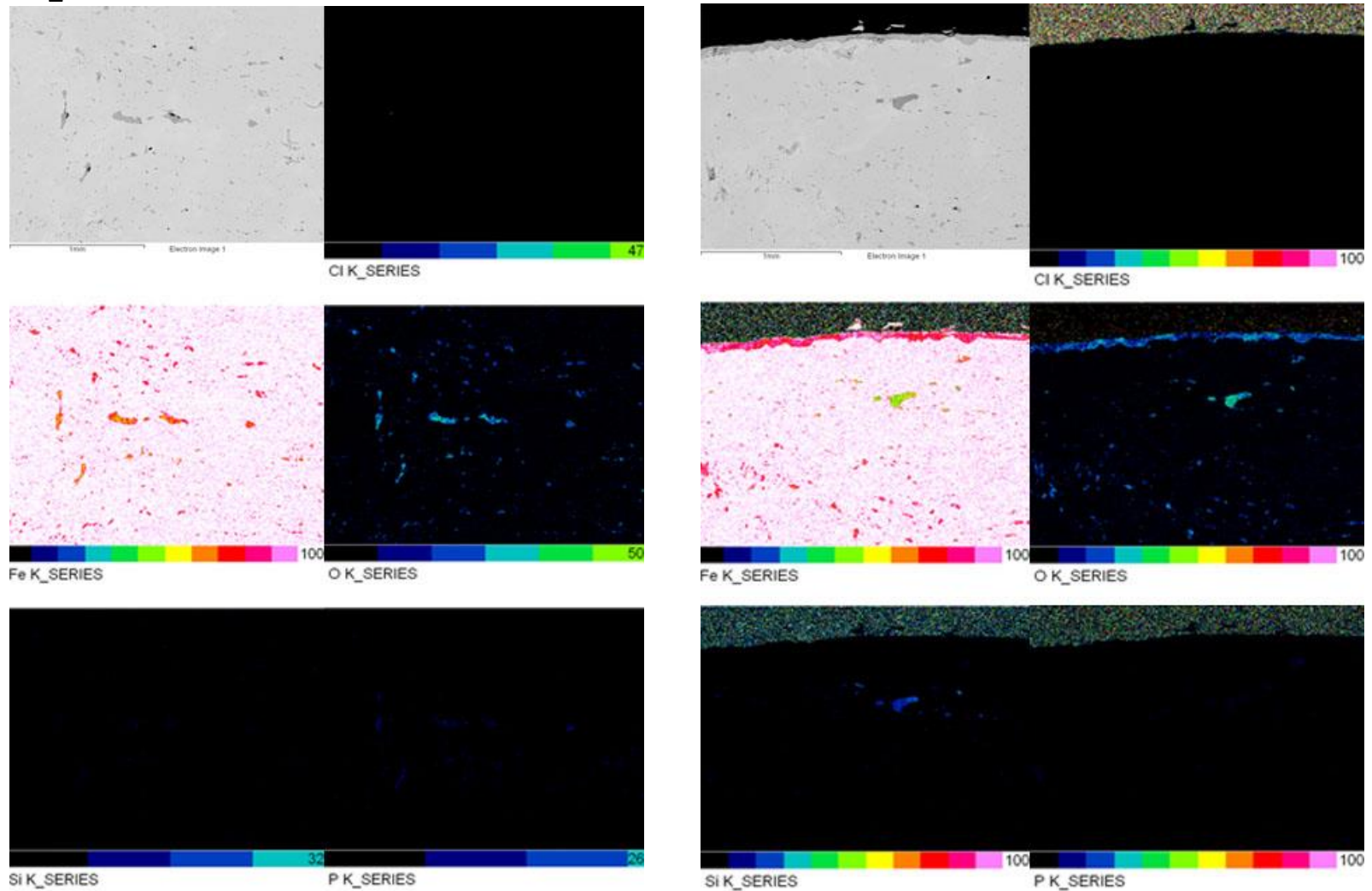


Figure 8.35 SEM-BSE image and corresponding EDS/WDS quantitative elemental maps for 5 elements detected in 2 sites of interest for sample CW_14. Chlorine map acquired by SEM-WDS. Colours indicate wt% of element detected, in increments of 10%.

CW_15

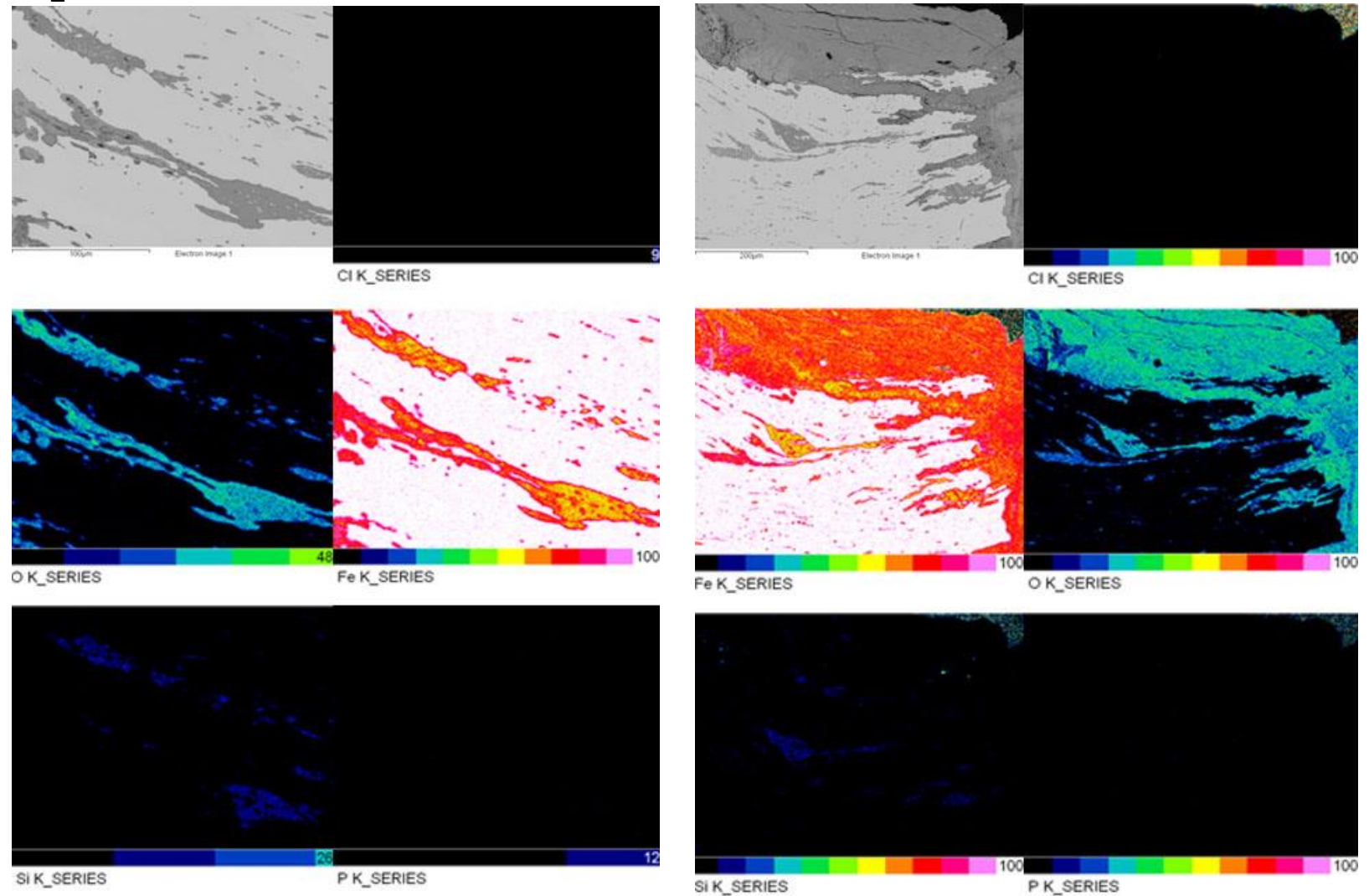


Figure 8.36 SEM-BSE image and corresponding EDS/WDS quantitative elemental maps for 5 elements detected in 2 sites of interest for sample CW_15. Chlorine map acquired by SEM-WDS. Colours indicate wt% of element detected, in increments of 10%.

CW_16

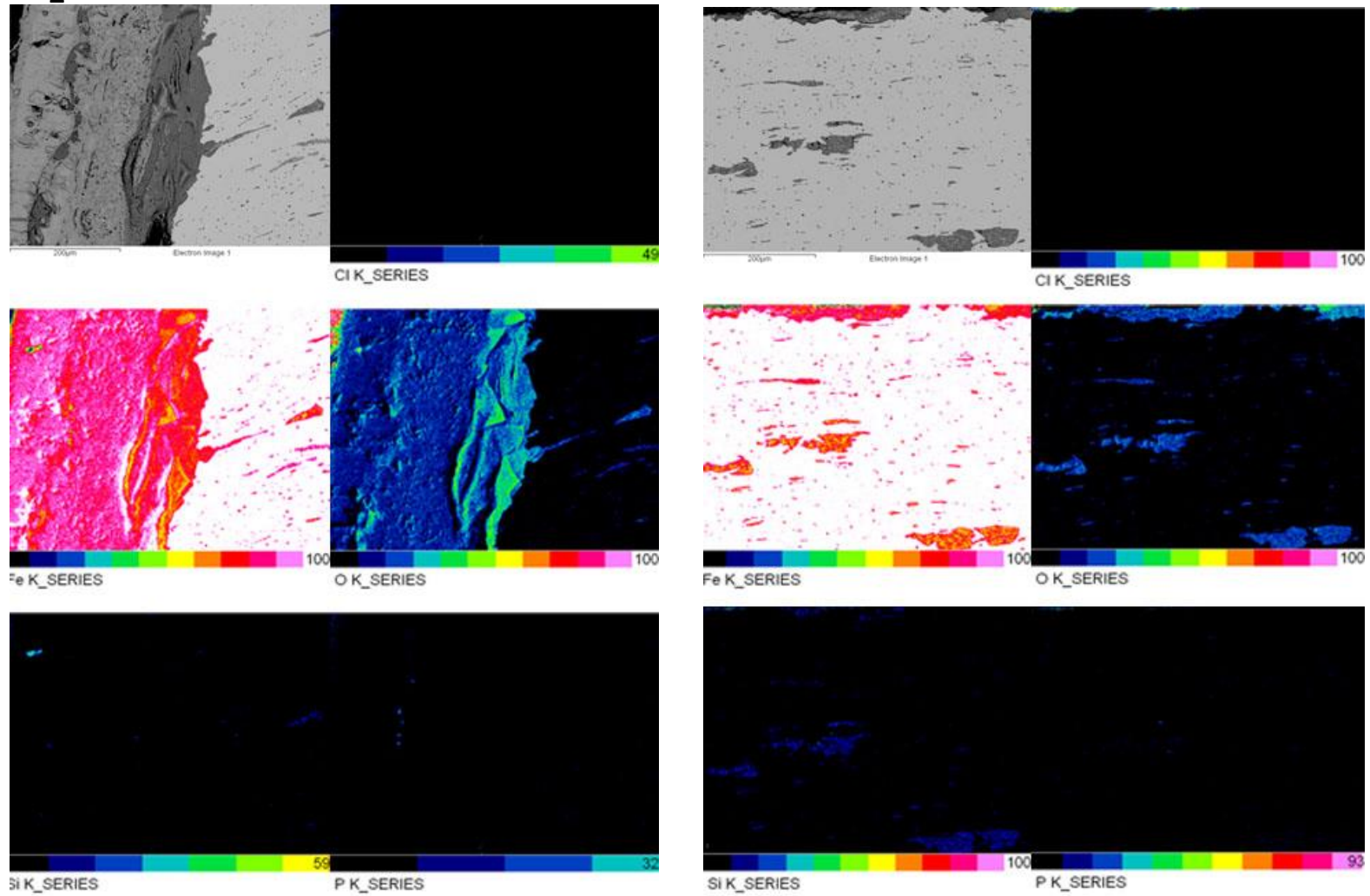


Figure 8.37 SEM-BSE image and corresponding EDS/WDS quantitative elemental maps for 5 elements detected in 2 sites of interest for sample CW_16. Chlorine map acquired by SEM-WDS. Colours indicate wt% of element detected, in increments of 10%.

CW_19

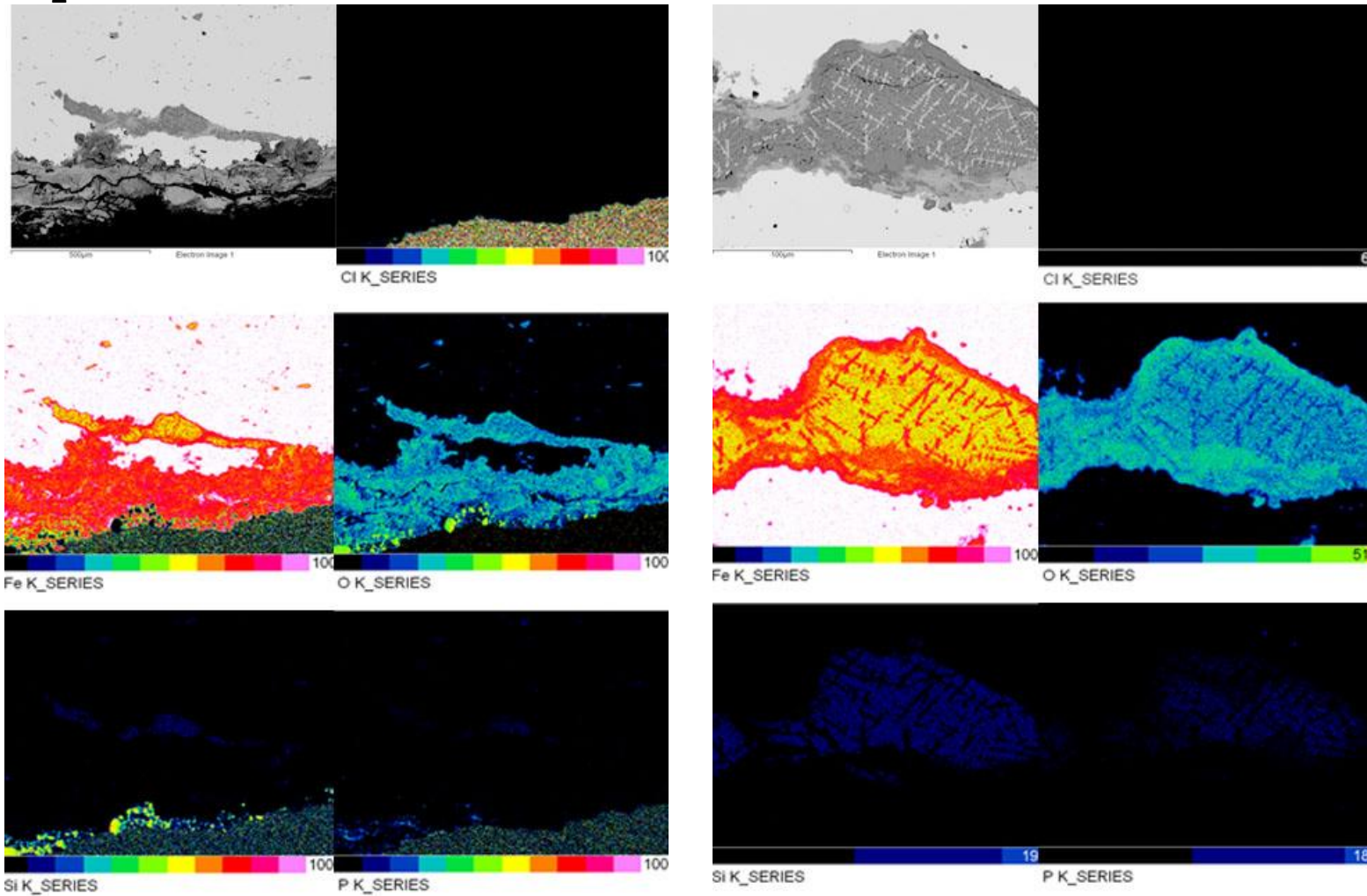


Figure 8.38 SEM-BSE image and corresponding EDS/WDS quantitative elemental maps for 5 elements detected in 2 sites of interest for sample CW_19. Chlorine map acquired by SEM-WDS. Colours indicate wt% of element detected, in increments of 10%.

CW_26

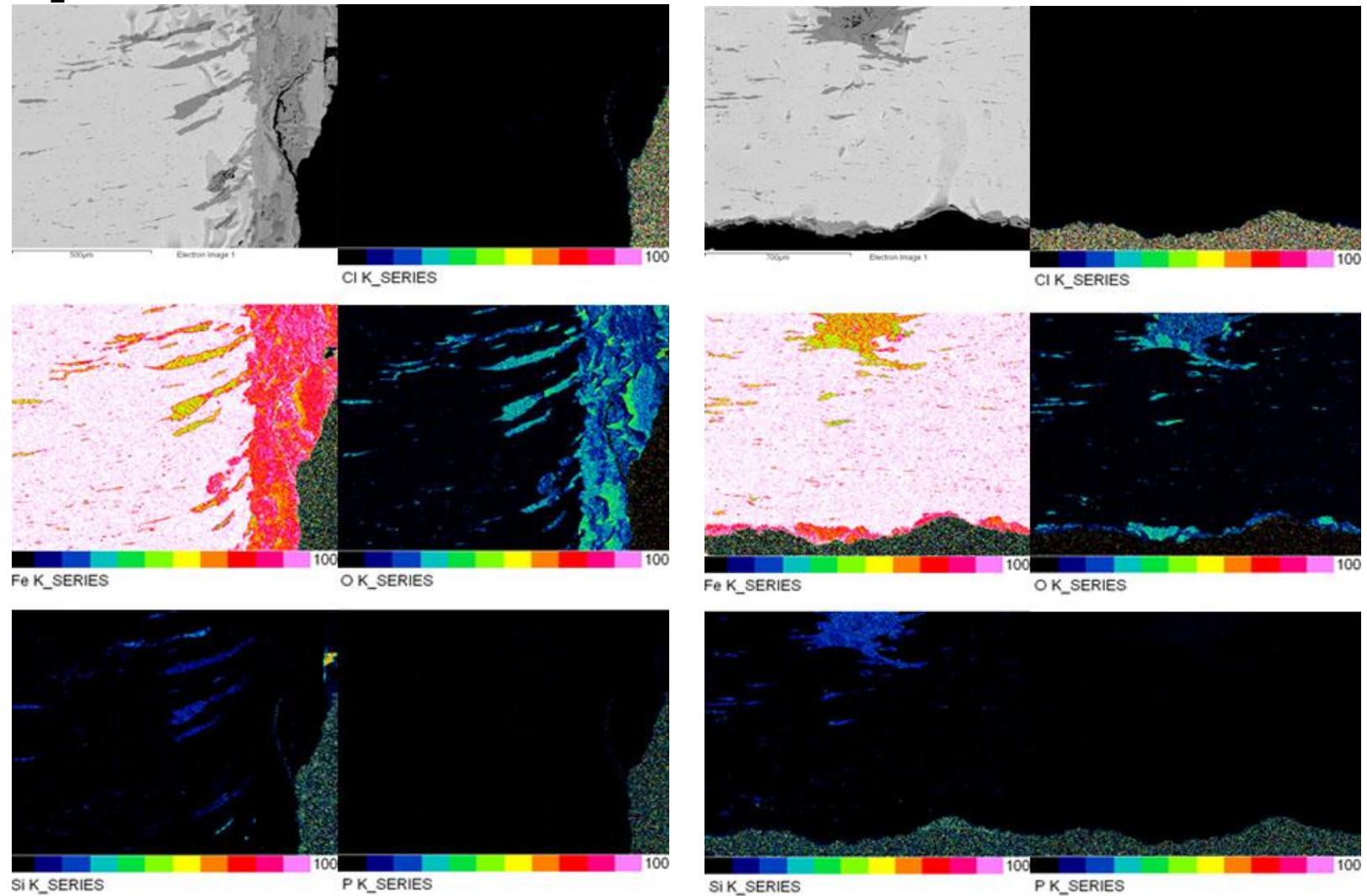


Figure 8.39 SEM-BSE image and corresponding EDS/WDS quantitative elemental maps for 5 elements detected in 2 sites of interest for sample CW_26. Chlorine map acquired by SEM-WDS. Colours indicate wt% of element detected, in increments of 10%.

CW_29

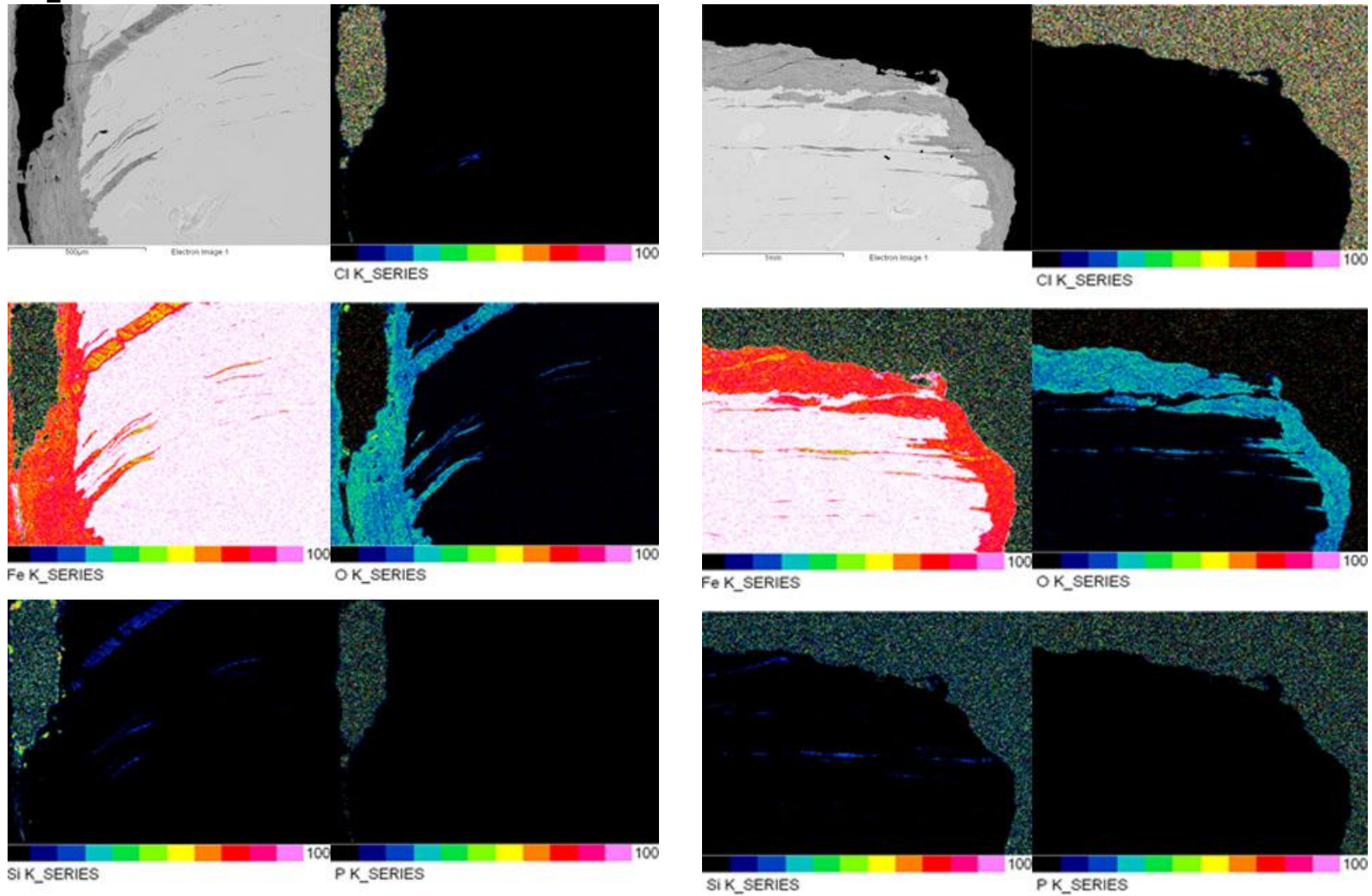


Figure 8.40 SEM-BSE image and corresponding EDS/WDS quantitative elemental maps for 5 elements detected in 2 sites of interest for sample CW_29. Chlorine map acquired by SEM-WDS. Colours indicate wt% of element detected, in increments of 10%.

8.4.3 SEM-EDS Elemental Analyses of Nails in Cross Section

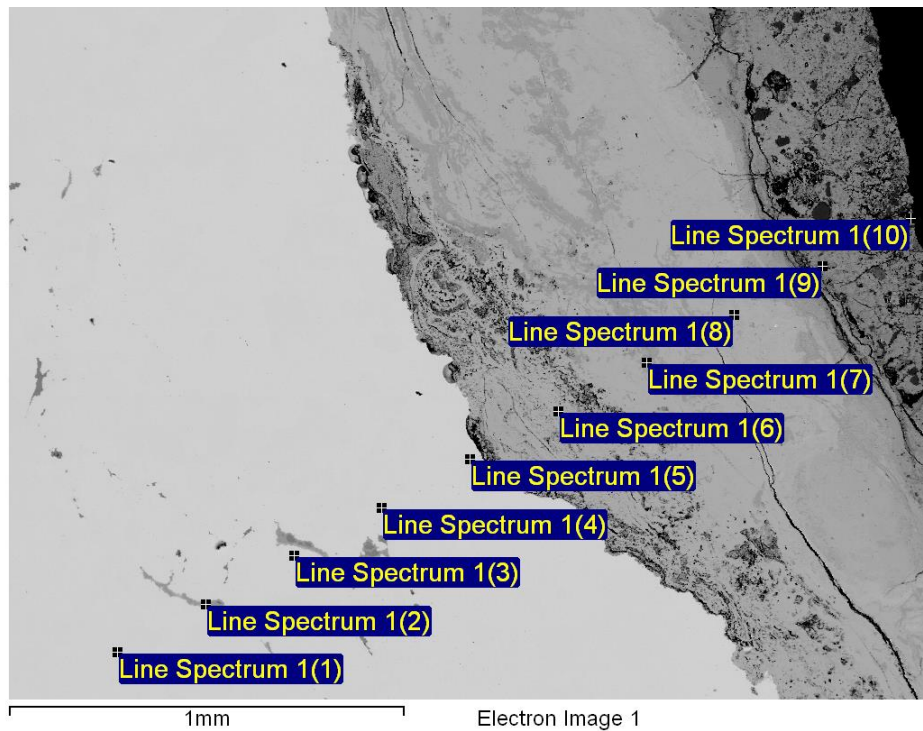


Figure 8.41 SEM (BEI) image of Caerleon sample CAER_01 with location of EDS line scan across a section of the sample from an interior slag inclusion to the outer CPL edge. Results of the analysis are given in Table 8.1.

CAER_01 EDS Line scan (Concentration in wt%-normalised)						
Spectrum	O	Si	P	Cl	Fe	Total
Line Spectrum 1(1)	0.96	0.07	0.06	0.00	98.91	100.00
Line Spectrum 1(2)	32.40	9.92	0.01	3.67	54.01	100.00
Line Spectrum 1(3)	1.15	0.11	0.05	-0.02	98.70	100.00
Line Spectrum 1(4)	1.00	0.05	0.06	0.01	98.87	100.00
Line Spectrum 1(5)	0.83	0.08	0.06	0.03	99.00	100.00
Line Spectrum 1(6)	26.80	0.14	0.10	0.16	72.80	100.00
Line Spectrum 1(7)	28.08	0.12	0.06	0.05	71.69	100.00
Line Spectrum 1(8)	26.43	0.12	0.07	0.06	73.32	100.00
Line Spectrum 1(9)	29.95	2.91	0.36	0.11	66.68	100.00
Line Spectrum 1(10)	30.37	2.64	0.61	0.35	66.03	100.00
Mean	17.40	1.53	0.14	0.41	80.52	100.00
Std. deviation	13.88	2.98	0.18	1.09	16.33	
Max.	32.40	9.92	0.61	3.67	99.00	
Min.	0.83	0.05	0.01	-0.02	54.01	

Table 8.1 SEM-EDS line scan results for Caerleon sample CAER_01 along the 10 data points indicated in Figure 8.41. EDS spectrometer standardised on cobalt before analysis, all points analysed for 30 seconds. Elemental concentrations given in wt% (data normalised to 100%).

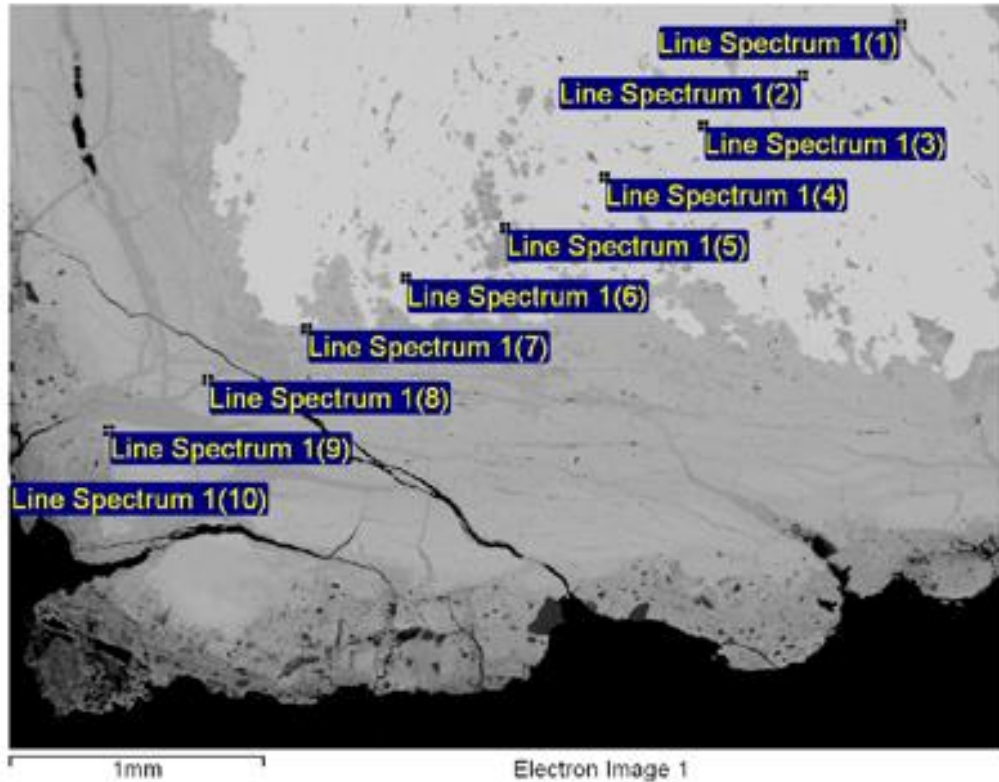


Figure 8.42 SEM (BEI) image of Caerleon sample CAER_07 with location of EDS line across a section of the sample from an interior slag inclusion to the outer CPL edge. Results of the analysis are given in Table 8.2.

CAER_07 EDS Line scan (Concentration in wt%-normalised)						
Spectrum	O	Si	P	Cl	Fe	Total
Line Spectrum 1(1)	25.53	2.91	0.03	0.21	71.32	100.00
Line Spectrum 1(2)	0.49	0.06	0.00	0.02	99.43	100.00
Line Spectrum 1(3)	0.06	0.07	-0.05	0.03	99.90	100.00
Line Spectrum 1(4)	0.14	0.05	-0.06	0.07	99.80	100.00
Line Spectrum 1(5)	-0.04	0.05	-0.06	0.07	99.97	100.00
Line Spectrum 1(6)	0.12	0.09	-0.05	0.04	99.80	100.00
Line Spectrum 1(7)	24.57	0.29	0.06	0.07	75.01	100.00
Line Spectrum 1(7)	24.57	0.29	0.06	0.07	75.01	100.00
Line Spectrum 1(9)	27.41	1.16	0.76	0.04	70.63	100.00
Line Spectrum 1(10)	25.56	10.15	0.33	0.45	63.51	100.00
Mean	13.82	1.55	0.14	0.13	84.36	100.00
Std. deviation	13.40	3.17	0.26	0.13	15.44	
Max.	31.53	10.15	0.76	0.45	99.97	
Min.	-0.04	0.05	-0.06	0.02	63.51	

Table 8.2 SEM-EDS line scan results for Caerleon sample CAER_07 along the 10 data points indicated in Figure 8.42. EDS spectrometer standardised on cobalt before analysis, all points analysed for 30 seconds. Elemental concentrations given in wt% (data normalised to 100%)..

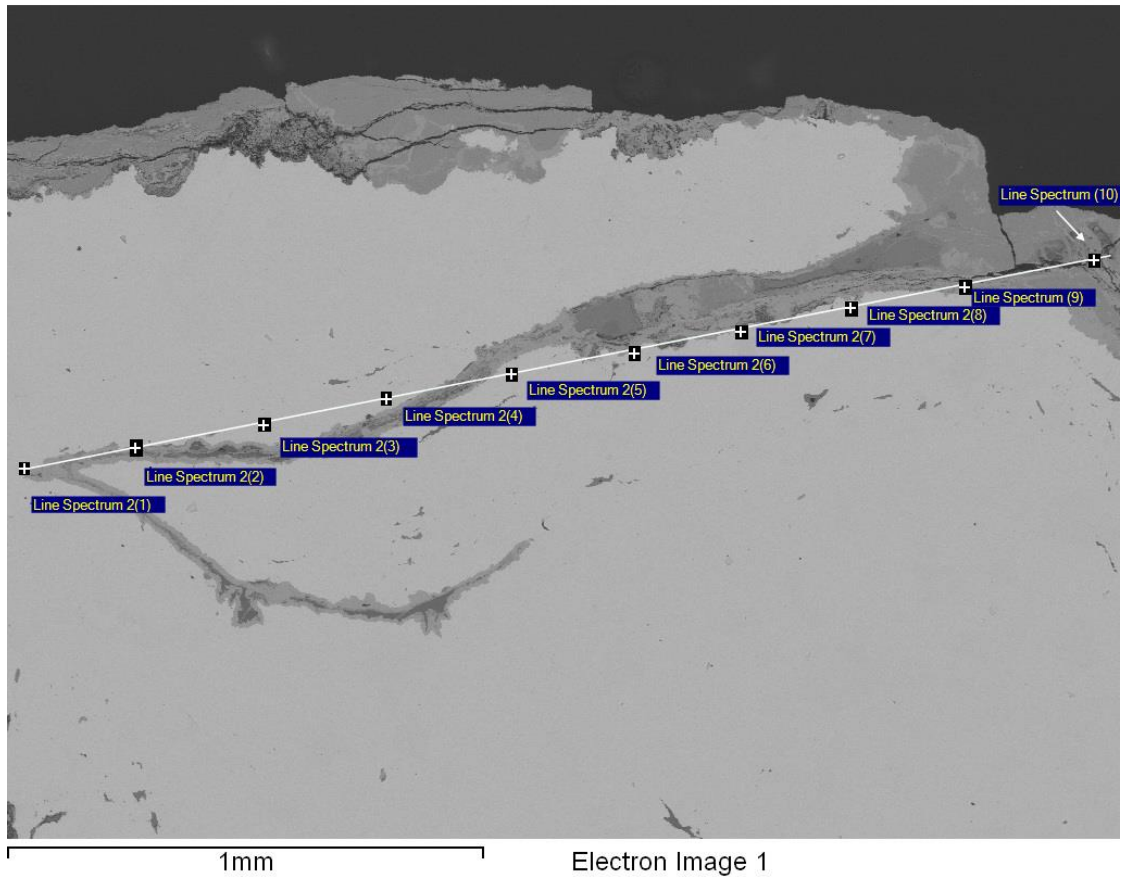


Figure 8.43 SEM (BEI) image of Caerleon sample CAER_08 with location of EDS line scan (10 data points from upper right to lower left) across a section of the sample from an interior slag inclusion to the outer CPL edge. Results of the analysis are given in Table 8.3.

CAER_08 EDS Line scan (Concentration in wt%-normalised)						
Spectrum	O	Si	P	Cl	Fe	Total
Line Spectrum 1(1)	28.71	0.13	0.10	1.02	70.04	100.00
Line Spectrum 1(2)	15.58	0.05	0.01	0.09	84.27	100.00
Line Spectrum 1(3)	1.11	0.08	0.11	0.01	98.69	100.00
Line Spectrum 1(4)	1.30	0.06	0.12	0.04	98.49	100.00
Line Spectrum 1(5)	1.03	0.08	0.12	-0.01	98.79	100.00
Line Spectrum 1(6)	30.64	0.68	0.51	0.09	68.09	100.00
Line Spectrum 1(7)	23.10	0.46	0.31	0.13	76.00	100.00
Line Spectrum 1(7)	1.14	0.07	0.15	0.05	98.59	100.00
Line Spectrum 1(9)	25.82	0.71	0.25	0.24	72.98	100.00
Line Spectrum 1(10)	38.58	1.18	0.09	0.01	60.14	100.00
Mean	16.70	0.35	0.18	0.17	82.61	100.00
Standard Deviation	14.57	0.39	0.14	0.31	15.06	
Max.	38.58	1.18	0.51	1.02	98.79	
Min	1.03	0.05	0.01	-0.01	60.14	

Table 8.3 SEM-EDS line scan results for Caerleon sample CAER_08 along the 10 data points indicated in Figure 8.43. EDS spectrometer standardised on cobalt before analysis, all points analysed for 30 seconds. Elemental concentrations given in wt% (data normalised to 100%).

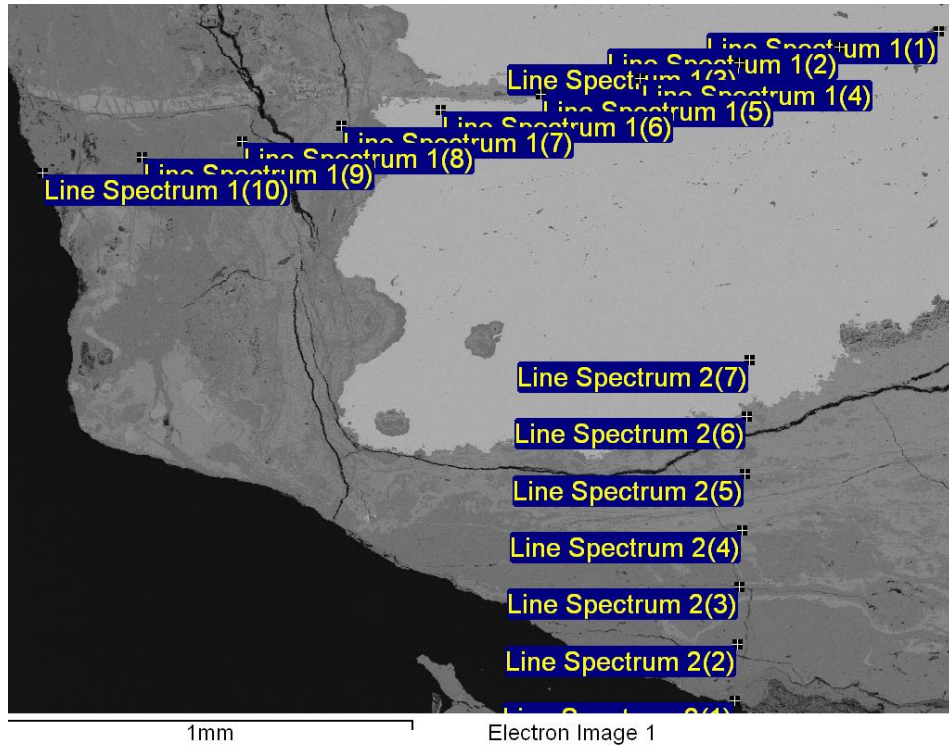


Figure 8.44 SEM (BEI) image of Caerleon sample CAER_10 with location of EDS line scan (10 data points from upper right to lower left) across a section of the sample from an interior slag inclusion to the outer CPL edge. Results of the analysis are given in Table 8.4 below

CAER_10 EDS Line scan (Concentration in wt% - normalized)						
Spectrum	O	Si	P	Cl	Fe	Total
Line Spectrum 1(1)	37.97	15.33	0.19	0.17	46.33	100.00
Line Spectrum 1(2)	26.20	3.65	0.15	0.11	69.89	100.00
Line Spectrum 1(3)	1.11	0.05	0.01	0.01	98.81	100.00
Line Spectrum 1(4)	1.48	0.06	-0.06	0.05	98.47	100.00
Line Spectrum 1(5)	23.88	0.23	-0.01	0.06	75.84	100.00
Line Spectrum 1(6)	1.20	0.06	0.04	0.06	98.63	100.00
Line Spectrum 1(7)	30.70	0.33	0.11	0.04	68.83	100.00
Line Spectrum 1(8)	36.15	0.35	0.26	0.04	63.20	100.00
Line Spectrum 1(9)	37.00	0.59	0.17	0.03	62.21	100.00
Line Spectrum 1(10)	37.25	0.75	0.41	0.06	61.52	100.00
Line Spectrum 2(1)	37.00	1.12	1.40	0.04	60.44	100.00
Line Spectrum 2(2)	35.88	0.28	0.37	0.01	63.46	100.00
Line Spectrum 2(3)	37.20	1.07	2.25	0.06	59.43	100.00
Line Spectrum 2(4)	28.36	0.29	0.12	0.06	71.16	100.00
Line Spectrum 2(5)	28.24	0.12	0.04	0.03	71.57	100.00
Line Spectrum 2(6)	27.77	0.06	0.09	0.06	72.02	100.00
Line Spectrum 2(7)	1.35	0.11	0.05	0.02	98.47	100.00
Mean	25.22	1.44	0.33	0.05	72.96	100.00
Std. deviation	14.39	3.68	0.59	0.04	16.11	
Max.	37.97	15.33	2.25	0.17	98.81	
Min.	1.11	0.05	-0.06	0.01	46.33	

Table 8.4 SEM-EDS line scan results for Caerleon sample CAER_10 along the 10 data points indicated in Figure 8.44. EDS spectrometer standardised on cobalt before analysis, all points analysed for 30 seconds. Elemental concentrations given in wt% (data normalised to 100%).

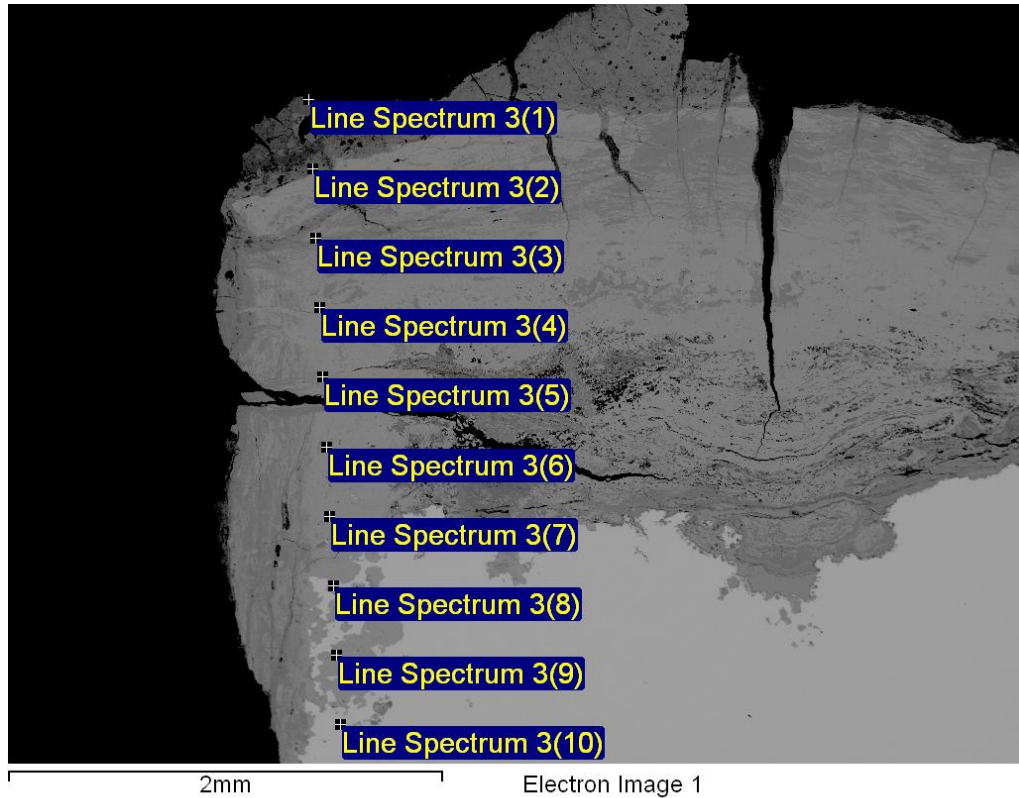


Figure 8.45 SEM (BEI) image of Caerleon sample CAER_13 with location of EDS line scan (10 data points from upper right to lower left) across a section of the sample from an interior slag inclusion to the outer CPL edge. Results of the analysis are given in Table 8.5.

CAER_13 EDS Line scan (Concentration in wt% - normalized)						
Spectrum	O	Si	P	Cl	Fe	Total
Line Spectrum 1(1)	23.01	3.74	0.48	0.92	71.85	100.00
Line Spectrum 1(2)	34.20	1.80	0.99	0.09	62.93	100.00
Line Spectrum 1(3)	34.95	0.65	0.24	0.04	64.11	100.00
Line Spectrum 1(4)	27.26	0.10	0.09	0.04	72.51	100.00
Line Spectrum 1(5)	31.63	0.35	0.00	0.04	67.98	100.00
Line Spectrum 1(6)	28.80	0.20	0.07	0.04	70.88	100.00
Line Spectrum 1(7)	27.07	0.10	0.03	0.01	72.79	100.00
Line Spectrum 1(7)	28.54	0.21	0.12	-0.01	71.13	100.00
Line Spectrum 1(9)	1.14	0.12	0.05	0.02	98.67	100.00
Line Spectrum 1(10)	0.98	0.08	0.07	0.04	98.83	100.00
Mean	23.31	0.71	0.20	0.17	75.59	100.00
Standard Deviation	11.92	1.12	0.29	0.32	12.31	
Max.	34.95	3.74	0.99	0.92	98.83	
Min.	0.98	0.08	0.00	-0.01	62.93	

Table 8.5 SEM-EDS line scan results for Caerleon sample CAER_13 along the 10 data points indicated in Figure 8.45. EDS spectrometer standardised on cobalt before analysis, all points analysed for 30 seconds. Elemental concentrations given in wt% (data normalised to 100%).

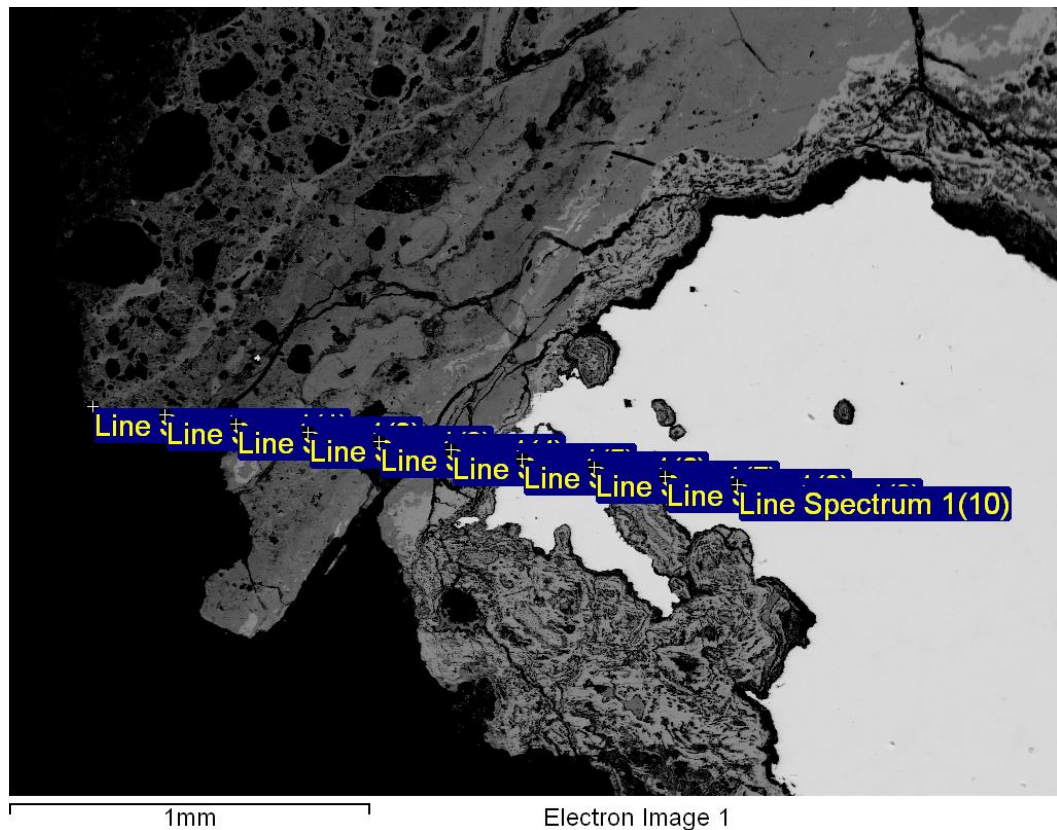


Figure 8.46 SEM (BEI) image of Caerleon sample CAER_18 with location of EDS line scan (10 data points from upper right to lower left) across a section of the sample from an interior slag inclusion to the outer CPL edge. Results of the analysis are given in Table 8.6.

CAER_18 EDS Line scan (Concentration in wt% - normalised)						
Spectrum	O	Si	P	Cl	Fe	Total
Line Spectrum 1(1)	40.54	13.09	0.34	0.1	45.93	100
Line Spectrum 1(2)	27.15	6.07	0.55	0.09	66.15	100
Line Spectrum 1(3)	500.12	-106.48	1.50	-108.47	-186.68	100
Line Spectrum 1(4)	0.34	0.06	0.01	0.02	99.55	100
Line Spectrum 1(5)	31.35	0.93	1.03	0.04	66.64	100
Line Spectrum 1(6)	32.14	0.43	0.26	0	67.17	100
Line Spectrum 1(7)	0.03	0.05	0.13	-0.03	99.82	100
Line Spectrum 1(7)	7.99	1.4	1.11	1.11	88.39	100
Line Spectrum 1(9)	0.06	0.08	0.1	0.01	99.74	100
Line Spectrum 1(10)	15.05	0.16	0.59	0.1	84.09	100
Mean	17.18	2.47	0.46	0.16	79.72	100
Standard Deviation	15.93	4.42	0.40	0.36	19.19	
Max.	40.54	13.09	1.11	1.11	99.82	
Min.	0.03	0.05	0.01	-0.03	45.93	

Table 8.6 SEM-EDS line scan results for Caerleon sample CAER_18 along the 10 data points indicated in Figure 8.46 above. EDS spectrometer standardised on cobalt before analysis, all points analysed for 30 seconds. Elemental concentrations given in wt% (data normalised to 100%). Line spectrum 1(3) produced anomalous data and was not factored into analytical statistics..

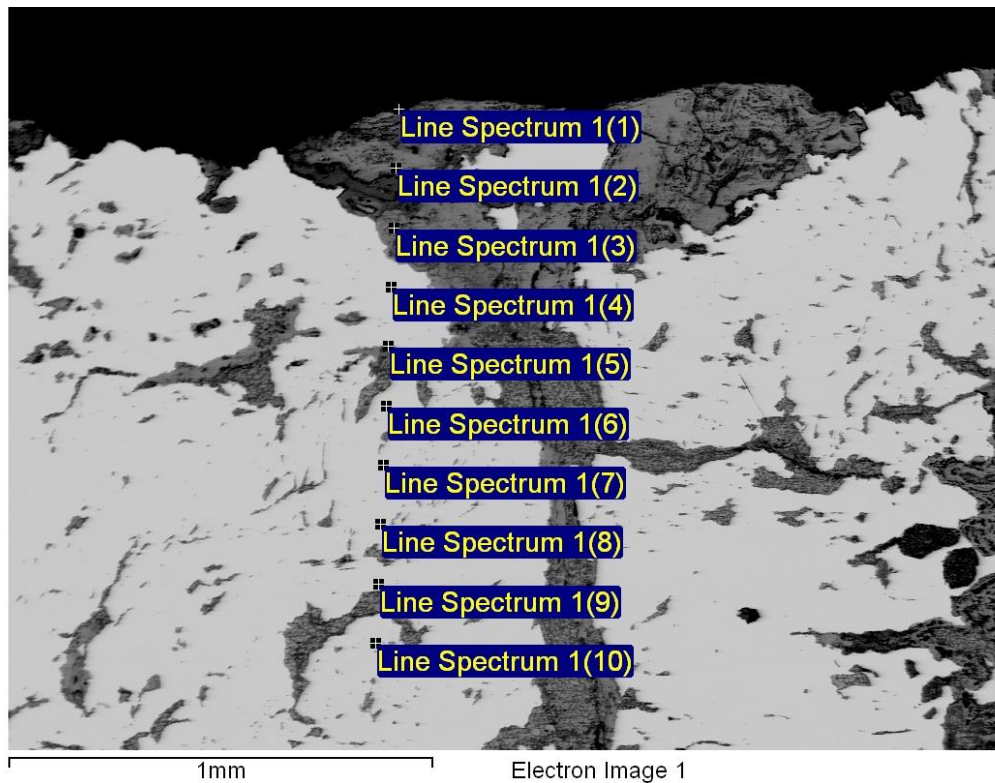


Figure 8.47 SEM (BEI) image of Caerleon sample CAER_19 with location of EDS line scan (10 data points from upper right to lower left) across a section of the sample from an interior slag inclusion to the outer CPL edge. Results of the analysis are given in Table 8.7 below

CAER_19 EDS Line scan (Concentration in wt%-normalised)						
Spectrum	O	Si	P	Cl	Fe	Total
Line Spectrum 1(1)	5.25	0.75	-0.06	5.24	88.83	100
Line Spectrum 1(2)	20.02	2.22	0.03	0.09	77.64	100
Line Spectrum 1(3)	26.29	3.20	0.08	0.11	70.32	100
Line Spectrum 1(4)	0.06	0.09	0.00	0.02	99.83	100
Line Spectrum 1(5)	12.30	0.88	-0.01	0.06	86.76	100
Line Spectrum 1(6)	-0.05	0.04	-0.07	0.04	100.04	100
Line Spectrum 1(7)	0.00	0.01	-0.06	0.01	100.04	100
Line Spectrum 1(7)	0.09	0.01	-0.04	-0.03	99.97	100
Line Spectrum 1(9)	0.00	0.09	0.02	0.01	99.89	100
Line Spectrum 1(10)	-0.07	0.05	-0.02	0.02	100.02	100
Mean	6.39	0.73	-0.01	0.56	92.33	100
Standard Deviation	9.79	1.11	0.05	1.65	11.02	
Max.	26.29	3.20	0.08	5.24	100.02	
Min.	-0.07	0.01	-0.07	-0.03	70.32	

Table 8.7 SEM-EDS line scan results for Caerleon sample CAER_19 along the 10 data points indicated in Figure 23 above. EDS spectrometer standardised on cobalt before analysis, all points analysed for 30 seconds. Elemental concentrations given in wt% (data normalised to 100%).

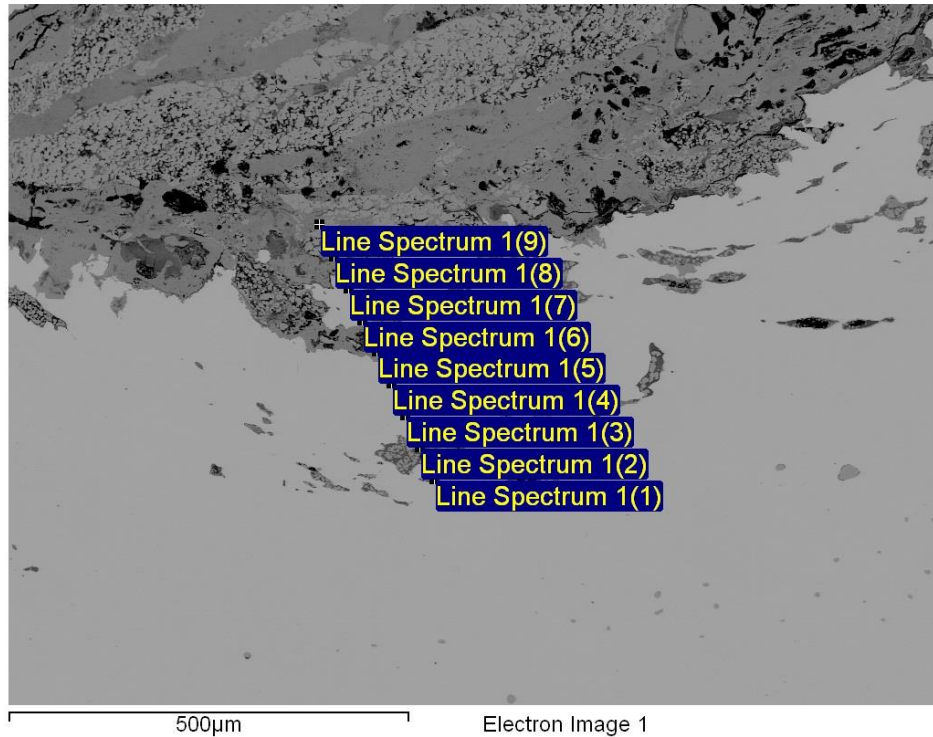


Figure 8.48 SEM (BEI) image of Caerleon sample CAER_21 with location of EDS line scan (9 data points) across a section of the sample from an interior slag inclusion to the outer CPL edge. Results of the analysis are given in Table 8.8.

CAER_21 EDS Line scan (Concentration in wt%-normalised)						
Spectrum	O	Si	P	Cl	Fe	Total
Line Spectrum 1(1)	0.34	0.06	-0.04	0.00	99.65	100
Line Spectrum 1(2)	20.04	4.28	0.09	0.22	75.36	100
Line Spectrum 1(3)	0.35	0.06	-0.03	-0.03	99.65	100
Line Spectrum 1(4)	0.25	0.06	0.00	0.00	99.70	100
Line Spectrum 1(5)	24.61	3.30	-0.02	0.19	71.91	100
Line Spectrum 1(6)	0.17	0.03	-0.06	0.00	99.86	100
Line Spectrum 1(7)	0.30	0.09	-0.05	0.02	99.64	100
Line Spectrum 1(7)	26.91	1.36	-0.03	0.11	71.65	100
Line Spectrum 1(9)	26.21	1.23	-0.06	0.08	72.53	100
Mean	11.02	1.16	-0.02	0.07	87.77	100
Standard Deviation	12.87	1.60	0.05	0.09	14.18	
Max.	26.91	4.28	0.09	0.22	99.86	
Min.	0.17	0.03	-0.06	-0.03	71.65	

Table 8.8 SEM-EDS line scan results for Caerleon sample CAER_21 along the 9 data points indicated in Figure 8.48 above. EDS spectrometer standardised on cobalt before analysis, all points analysed for 30 seconds. Elemental concentrations given in wt% (data normalised to 100%).

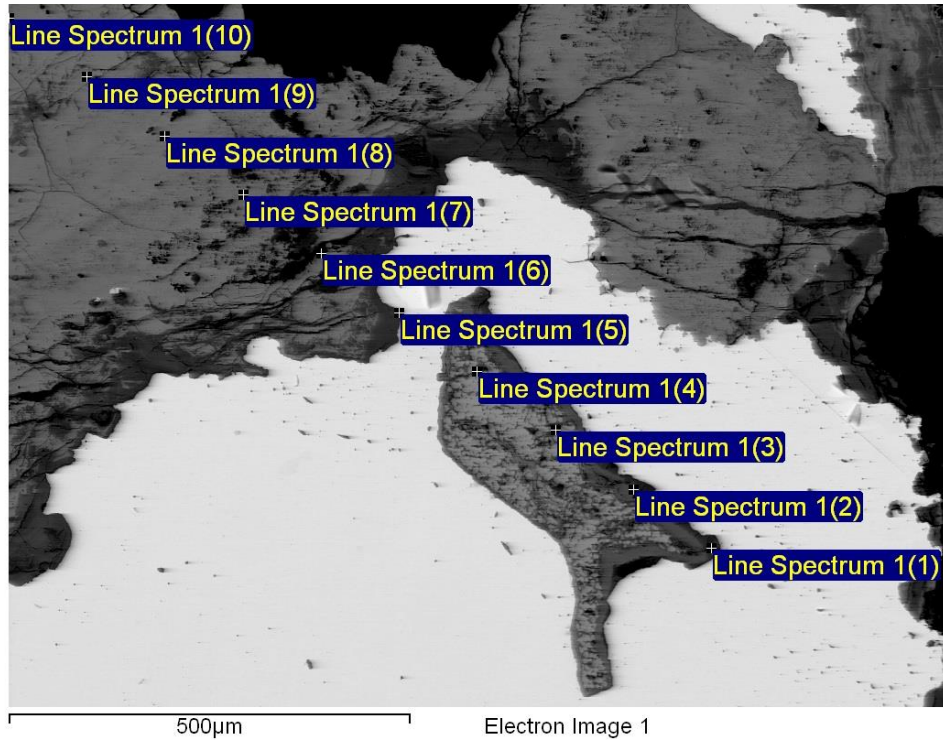


Figure 8.49 SEM (BEI) image of Caerleon sample CAER_22 with location of EDS line scan (10 data points from upper right to lower left) across a section of the sample from an interior slag inclusion to the outer CPL edge. Results of the analysis are given in Table 8.9.

CAER_22 EDS Line scan (Concentration in wt%-normalised)						
Spectrum	O	Si	P	Cl	Fe	Total
Line Spectrum 1(1)	28.89	0.09	-0.01	5.55	65.48	100.00
Line Spectrum 1(2)	23.18	0.05	0.00	9.13	67.63	100.00
Line Spectrum 1(3)	25.83	0.42	0.05	6.16	67.53	100.00
Line Spectrum 1(4)	27.22	7.85	1.29	0.03	63.61	100.00
Line Spectrum 1(5)	23.47	0.07	0.11	0.43	75.91	100.00
Line Spectrum 1(6)	24.73	0.12	0.20	0.05	74.90	100.00
Line Spectrum 1(7)	23.28	0.89	0.16	0.02	75.64	100.00
Line Spectrum 1(7)	21.14	0.16	0.15	0.04	78.50	100.00
Line Spectrum 1(9)	22.60	0.10	0.23	0.06	77.00	100.00
Line Spectrum 1(10)	22.84	0.12	0.02	0.06	76.95	100.00
Mean	23.06	0.93	0.22	1.99	73.80	100.00
Standard Deviation	4.73	2.31	0.37	3.30	7.22	
Max.	28.89	7.85	1.29	9.13	88.62	
Min.	10.50	0.05	-0.01	0.02	63.61	

Table 8.9 SEM-EDS line scan results for Caerleon sample CAER_22 along the 10 data points indicated in Figure 8.49 above. EDS spectrometer standardised on cobalt before analysis, all points analysed for 30 seconds. Elemental concentrations given in wt% (data normalised to 100%).

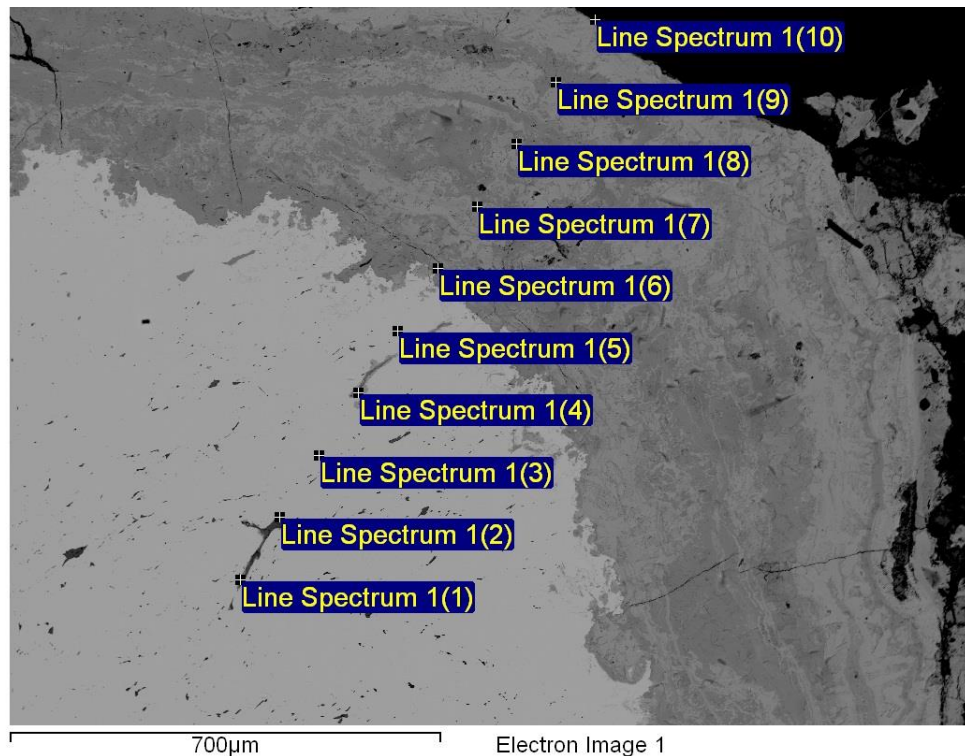


Figure 8.50 SEM (BEI) image of Caerleon sample CAER_27 with location of EDS line scan (10 data points from upper right to lower left) across a section of the sample from an interior slag inclusion to the outer CPL edge. Results of the analysis are given in Table 8.10.

CAER_27 EDS Line scan (Concentration in wt%-normalised)						
Spectrum	O	Si	P	Cl	Fe	Total
Line Spectrum 1(1)	9.47	2.52	-0.06	21.24	66.84	100.00
Line Spectrum 1(2)	-0.97	0.15	-0.01	0.06	100.76	100.00
Line Spectrum 1(3)	-0.25	0.06	0.00	0.01	100.17	100.00
Line Spectrum 1(4)	25.98	4.31	0.20	0.01	69.50	100.00
Line Spectrum 1(5)	-0.14	0.04	0.00	0.01	100.09	100.00
Line Spectrum 1(6)	25.89	0.18	0.09	0.06	73.78	100.00
Line Spectrum 1(7)	13.64	0.32	0.02	0.03	85.99	100.00
Line Spectrum 1(7)	19.81	0.34	0.20	0.02	79.63	100.00
Line Spectrum 1(9)	28.99	0.28	0.11	0.04	70.58	100.00
Line Spectrum 1(10)	-1.81	0.29	0.00	0.65	100.88	100.00
Mean	12.06	0.85	0.06	2.21	84.82	100.00
Standard Deviation	12.49	1.42	0.09	6.69	14.50	
Max.	-1.81	0.04	-0.06	0.01	66.84	
Min.	28.99	4.31	0.20	21.24	100.88	

Table 8.10 SEM-EDS line scan results for Caerleon sample CAER_27 along the 10 data points indicated in Figure 8.50. EDS spectrometer standardised on cobalt before analysis, all points analysed for 30 seconds. Elemental concentrations given in wt% (data normalised to

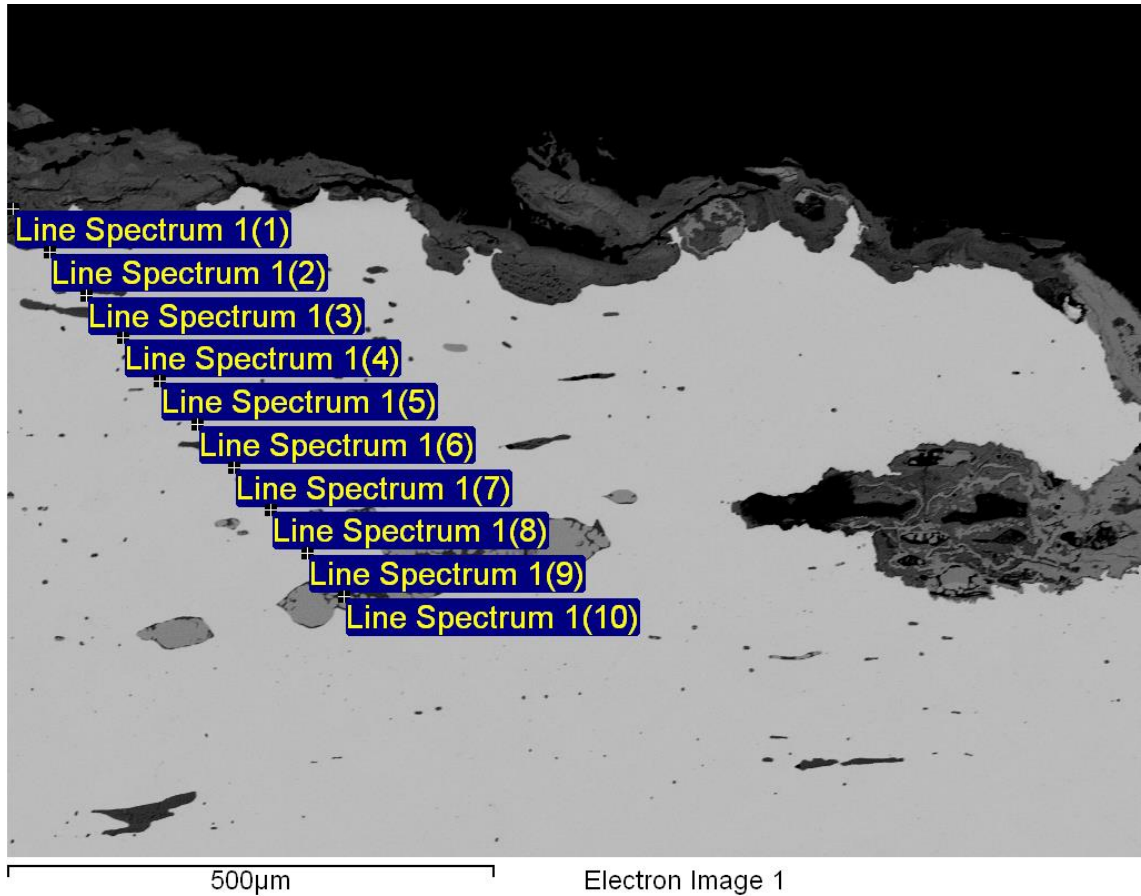


Figure 8.51 SEM (BEI) image of Colonial Williamsburg sample CW_05 with location of EDS line scan (10 data points from upper right to lower left) across a section of the sample from an interior slag inclusion to the outer CPL edge. Results of the analysis are given in Table 8.11 below.

CW 05 EDS Line scan (Concentration in wt%-normalised)						
Spectrum	O	Si	P	Cl	Fe	Total
Line Spectrum 1(1)	27.54	0.38	0.04	0.41	71.63	100.00
Line Spectrum 1(2)	0.19	0.10	0.07	0.01	99.63	100.00
Line Spectrum 1(3)	0.46	0.20	0.05	0.00	99.29	100.00
Line Spectrum 1(4)	0.11	0.05	0.02	0.00	99.82	100.00
Line Spectrum 1(5)	0.06	0.06	0.00	0.03	99.84	100.00
Line Spectrum 1(6)	0.03	0.04	-0.03	-0.01	99.96	100.00
Line Spectrum 1(7)	0.12	0.10	-0.02	-0.01	99.81	100.00
Line Spectrum 1(7)	0.09	0.07	-0.01	-0.02	99.87	100.00
Line Spectrum 1(9)	0.02	0.03	-0.05	0.02	99.97	100.00
Line Spectrum 1(10)	21.00	2.65	0.92	0.00	75.43	100.00
Mean	4.96	0.37	0.10	0.04	94.53	100.00
Standard Deviation	10.29	0.81	0.29	0.13	11.10	
Max.	27.54	2.65	0.92	0.41	99.97	
Min.	0.02	0.03	-0.05	-0.02	71.63	

Table 8.11 SEM-EDS line scan results for Colonial Williamsburg sample CW_05 along the 10 data points indicated in Figure 8.51 above. EDS spectrometer standardised on cobalt before analysis, all points analysed for 30 seconds. Elemental concentrations given in wt% (data normalised to 100%).

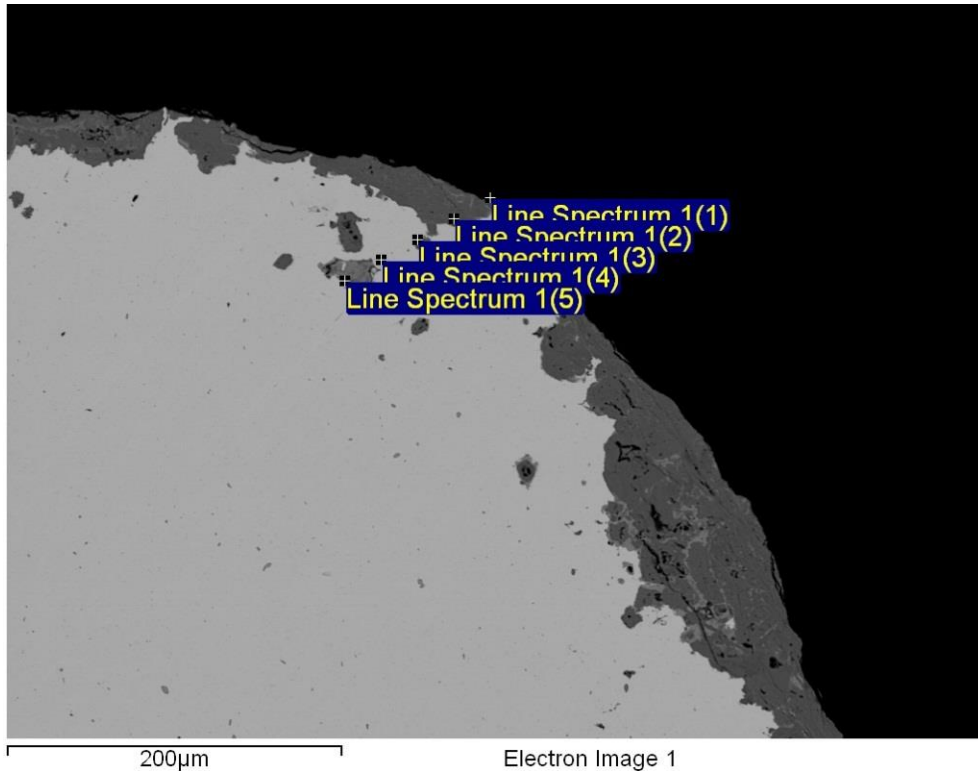


Figure 8.52 SEM (BEI) image of Colonial Williamsburg sample CW_07 with location of EDS line scan (10 data points from upper right to lower left) across a section of the sample from an interior slag inclusion to the outer CPL edge. Results of the analysis are given in Table 8.12.

CW_07 EDS Line scan (Concentration in wt%-normalized)						
Spectrum	O	Si	P	Cl	Fe	Total
Line Spectrum 1(1)	5.62	0.88	-0.02	6.05	87.48	100.00
Line Spectrum 1(2)	28.68	0.20	0.02	0.03	71.08	100.00
Line Spectrum 1(3)	17.01	0.15	0.09	0.00	82.74	100.00
Line Spectrum 1(4)	0.43	0.07	0.05	-0.01	99.46	100.00
Line Spectrum 1(5)	25.23	0.06	0.03	0.03	74.65	100.00
Mean	15.39	0.27	0.03	1.22	83.08	100.00
Standard Deviation	12.20	0.34	0.04	2.70	11.21	
Max.	0.43	0.06	-0.02	-0.01	71.08	
Min.	28.68	0.88	0.09	6.05	99.46	

Table 8.12 SEM-EDS line scan results for Colonial Williamsburg sample CW_07 along the 10 data points indicated in Figure 8.52. EDS spectrometer standardised on cobalt before analysis, all points analysed for 30 seconds. Elemental concentrations given in wt% (data normalised to 100%).

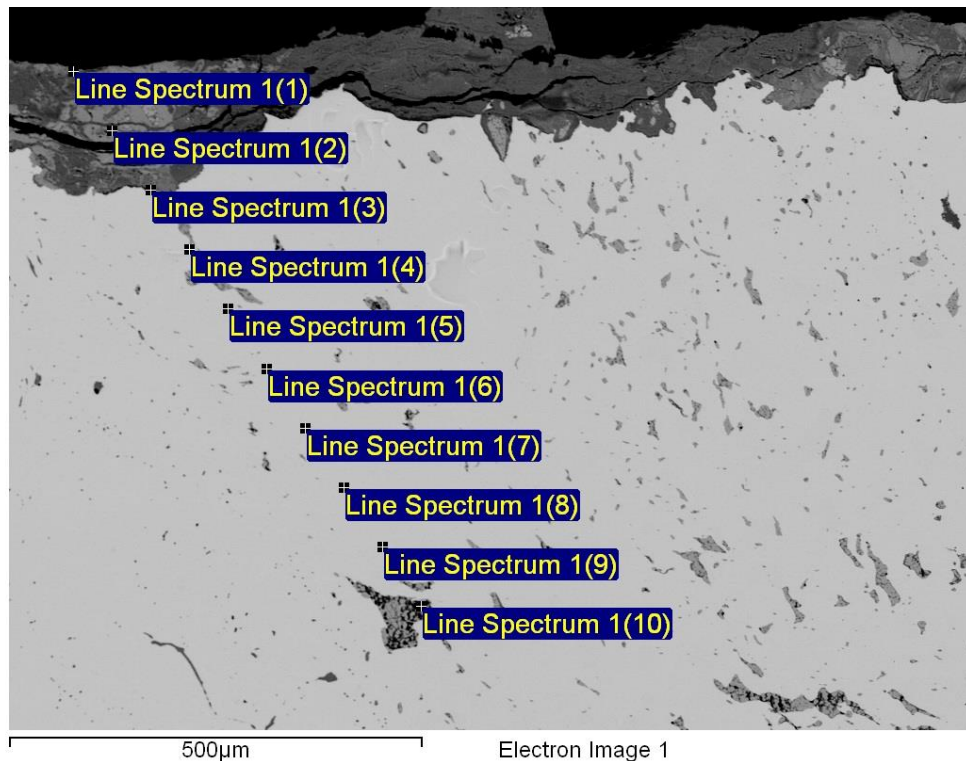


Figure 8.53 SEM (BEI) image of Colonial Williamsburg sample CW_08 with location of EDS line scan (10 data points from upper right to lower left) across a section of the sample from an interior slag inclusion to the outer CPL edge. Results of the analysis are given in Table 8.13.

CW_08 EDS Line scan (Concentration in wt%-normalised)						
Spectrum	O	Si	P	Cl	Fe	Total
Line Spectrum 1(1)	20.63	0.69	0.06	0.03	78.59	100.00
Line Spectrum 1(2)	27.44	0.28	0.01	0.09	72.17	100.00
Line Spectrum 1(3)	-0.16	0.04	0.02	0.00	100.10	100.00
Line Spectrum 1(4)	-0.40	0.04	0.00	0.03	100.33	100.00
Line Spectrum 1(5)	-0.13	0.07	0.02	0.00	100.04	100.00
Line Spectrum 1(6)	-0.13	0.07	-0.01	0.04	100.02	100.00
Line Spectrum 1(7)	-0.01	0.04	0.07	0.01	99.90	100.00
Line Spectrum 1(7)	-0.16	0.06	0.04	0.00	100.05	100.00
Line Spectrum 1(9)	-0.15	0.07	0.04	0.03	100.01	100.00
Line Spectrum 1(10)	19.93	3.60	1.08	0.19	75.20	100.00
Mean	6.69	0.50	0.13	0.04	92.64	100.00
Standard Deviation	11.20	1.11	0.33	0.06	12.05	
Max.	27.44	3.60	1.08	0.19	100.33	
Min.	-0.40	0.04	-0.01	0.00	72.17	

Table 8.13 SEM-EDS line scan results for Colonial Williamsburg sample CW_08 along the 10 data points indicated in Figure 8.53. EDS spectrometer standardised on cobalt before analysis, all points analysed for 30 seconds. Elemental concentrations given in wt% (data normalised to 100%).

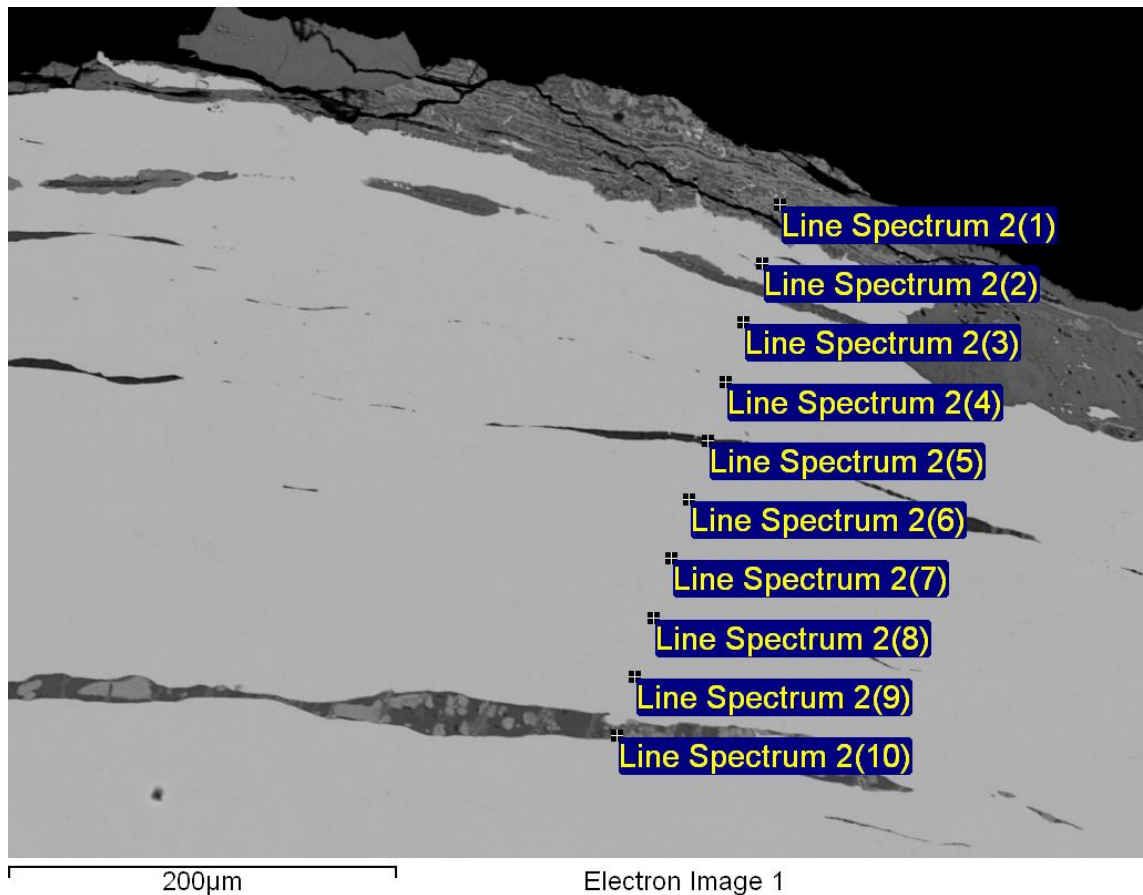


Figure 8.54 SEM (BEI) image of Colonial Williamsburg sample CW_09 with location of EDS line scan (10 data points from upper right to lower left) across a section of the sample from an interior slag inclusion to the outer CPL edge. Results of the analysis are given in Table 8.13.

CW_09 EDS Line scan (Concentration in wt%-normalised)						
Spectrum	O	Si	P	Cl	Fe	Total
Line Spectrum 1(1)	27.08	0.24	-0.04	0.06	72.67	100.00
Line Spectrum 1(2)	1.54	0.91	-0.01	0.02	97.54	100.00
Line Spectrum 1(3)	0.41	0.06	0.01	0.01	99.50	100.00
Line Spectrum 1(4)	0.45	0.05	0.00	-0.01	99.51	100.00
Line Spectrum 1(5)	35.17	29.03	-0.15	0.00	35.96	100.00
Line Spectrum 1(6)	0.46	0.02	-0.02	0.03	99.50	100.00
Line Spectrum 1(7)	0.34	0.05	-0.03	0.03	99.61	100.00
Line Spectrum 1(7)	0.42	0.05	0.00	0.02	99.51	100.00
Line Spectrum 1(9)	0.34	0.04	-0.05	0.03	99.64	100.00
Line Spectrum 1(10)	19.44	0.14	-0.05	0.67	79.80	100.00
Mean	8.57	3.06	-0.03	0.09	88.32	100.00
Standard Deviation	13.41	9.13	0.05	0.21	20.82	
Max.	35.17	29.03	0.01	0.67	99.64	
Min.	0.34	0.02	-0.15	-0.01	79.80	

Table 8.14 SEM-EDS line scan results for Colonial Williamsburg sample CW_09 along the 10 data points indicated in Figure 8.53. EDS spectrometer standardised on cobalt before analysis, all points analysed for 30 seconds. Elemental concentrations given in wt% (data normalised to 100%).

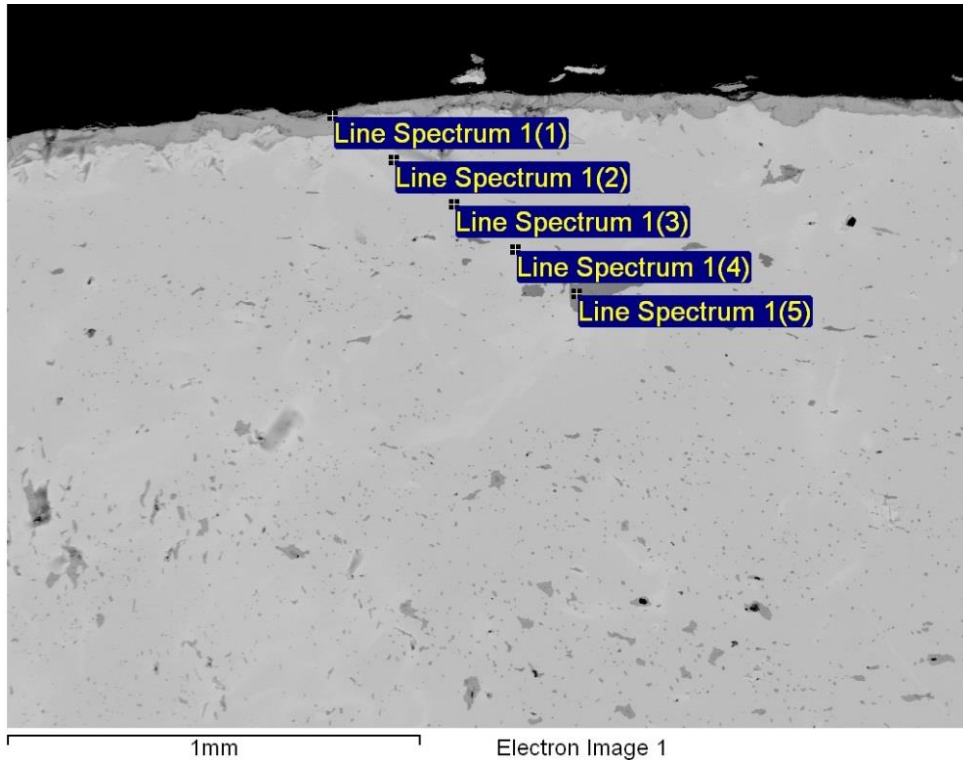


Figure 8.55 SEM (BEI) image of Colonial Williamsburg sample CW_14 with location of EDS line scan (5 data points from upper left to lower right) across a section of the sample from an interior slag inclusion to the outer CPL edge. Results of the analysis are given in Table 8.14.

CW_14 EDS Line scan (Concentration in wt%-normalised)						
Spectrum	O	Si	P	Cl	Fe	Total
Line Spectrum 1(1)	17.36	0.07	0.09	0.01	82.47	100.00
Line Spectrum 1(2)	-0.26	0.06	0.56	0.02	99.62	100.00
Line Spectrum 1(3)	-0.34	0.09	0.46	0.01	99.78	100.00
Line Spectrum 1(4)	0.10	0.06	0.26	0.05	99.53	100.00
Line Spectrum 1(5)	31.86	15.47	4.13	0.01	48.53	100.00
Mean	9.74	3.15	1.10	0.02	85.99	100.00
Std. deviation	14.51	6.89	1.70	0.02	22.22	
Min	-0.34	0.06	0.09	0.01	48.53	
Max	31.86	15.47	4.13	0.05	99.78	

Table 8.15 SEM-EDS line scan results for Colonial Williamsburg sample CW_14 along the 10 data points indicated in Figure 8.54. EDS spectrometer standardised on cobalt before analysis, all points analysed for 30 seconds. Elemental concentrations given in wt% (data normalised to 100%).

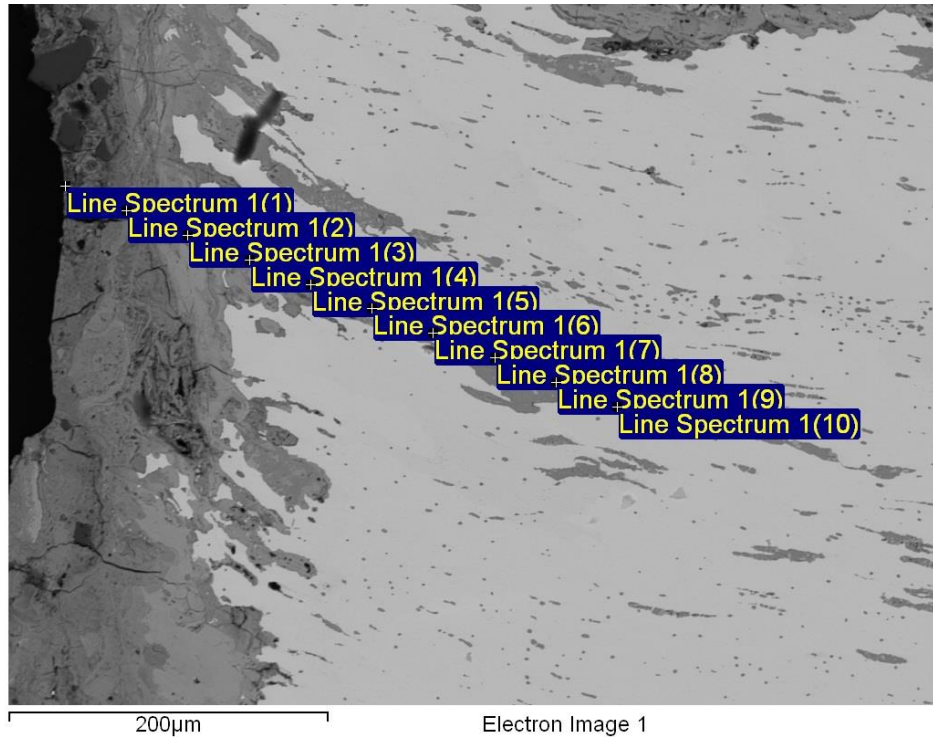


Figure 8.56 SEM (BEI) image of Colonial Williamsburg sample CW_15 with location of EDS line scan (10 data points from upper right to lower left) across a section of the sample from an interior slag inclusion to the outer CPL edge. Results of the analysis are given in Table 8.15 below.

CW_15 EDS Line scan (Concentration in wt%-normalised)						
Spectrum	O	Si	P	Cl	Fe	Total
Line Spectrum 1(1)	22.94	4.02	0.82	0.28	71.95	100.00
Line Spectrum 1(2)	19.77	1.03	0.30	0.24	78.66	100.00
Line Spectrum 1(3)	24.33	0.99	0.38	0.11	74.19	100.00
Line Spectrum 1(4)	23.95	1.01	0.04	0.05	74.95	100.00
Line Spectrum 1(5)	0.75	0.07	0.24	0.03	98.90	100.00
Line Spectrum 1(6)	26.84	1.77	0.42	0.05	70.92	100.00
Line Spectrum 1(7)	28.20	4.73	0.57	0.07	66.43	100.00
Line Spectrum 1(8)	27.93	0.26	0.09	0.18	71.53	100.00
Line Spectrum 1(9)	27.23	10.77	2.81	0.08	59.11	100.00
Line Spectrum 1(10)	26.45	7.44	1.95	0.10	64.07	100.00
Mean	22.84	3.21	0.76	0.12	73.07	100.00
Std. deviation	8.19	3.55	0.90	0.09	10.71	
Min	0.75	0.07	0.04	0.03	59.11	
Max	28.20	10.77	2.81	0.28	98.90	

Table 8.16 SEM-EDS line scan results for Colonial Williamsburg sample CW_15 along the 10 data points indicated in Figure 8.55. EDS spectrometer standardised on cobalt before analysis, all points analysed for 30 seconds. Elemental concentrations given in wt% (data normalised to 100%).

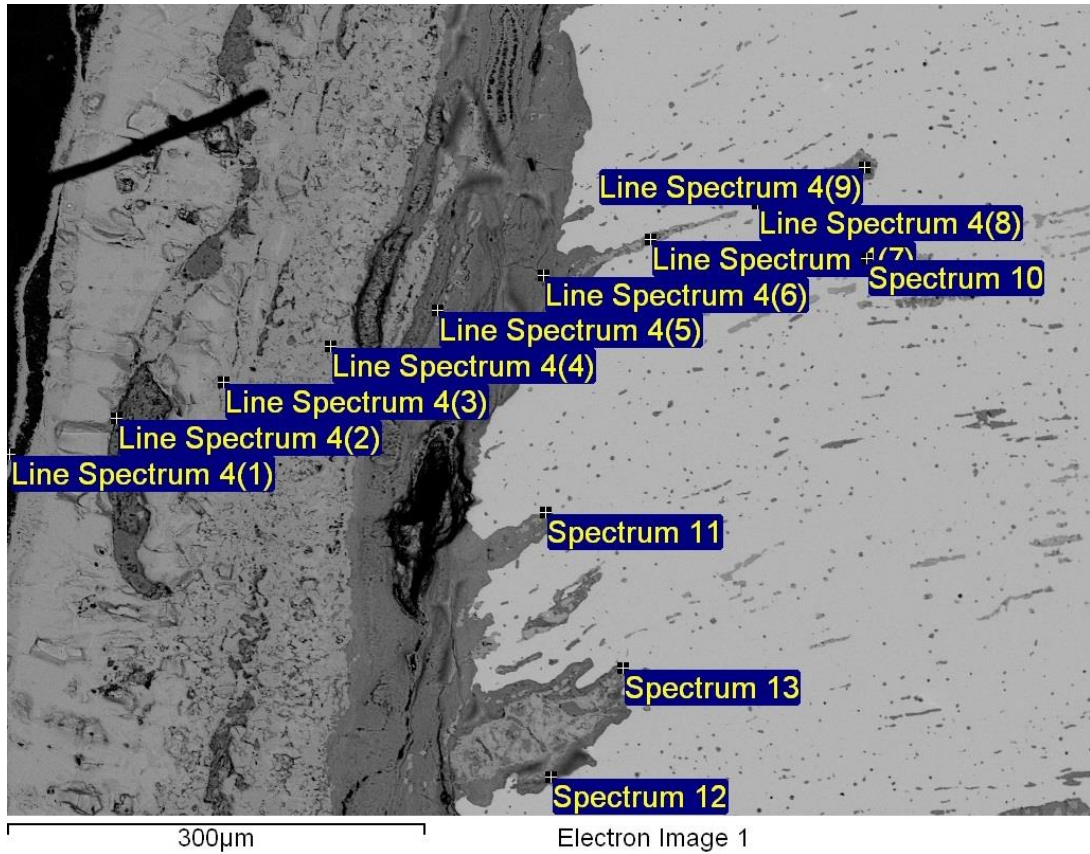


Figure 8.57 SEM (BEI) image of Colonial Williamsburg sample CW_16 with location of EDS line scan (13 data points) across a section of the sample from an interior slag inclusion to the outer CPL edge. Results of the analysis are given in Table 8.16.

CW_16 EDS Line scan (Concentration in wt%-normalised)						
Spectrum	O	Si	P	Cl	Fe	Total
Line Spectrum 1(1)	43.57	3.75	0.44	0.36	51.89	100.00
Line Spectrum 1(2)	37.48	1.05	0.24	0.35	60.87	100.00
Line Spectrum 1(3)	17.65	0.23	-0.02	0.01	82.13	100.00
Line Spectrum 1(4)	18.22	1.65	3.22	0.03	76.89	100.00
Line Spectrum 1(5)	25.48	1.10	0.08	0.25	73.09	100.00
Line Spectrum 1(6)	17.49	0.75	0.09	0.25	81.42	100.00
Line Spectrum 1(7)	24.74	1.45	0.93	0.10	72.78	100.00
Line Spectrum 1(8)	1.54	0.18	0.11	0.02	98.16	100.00
Line Spectrum 1(9)	15.14	4.11	1.79	0.09	78.88	100.00
Line Spectrum 1(10)	16.04	0.59	0.27	0.02	83.08	100.00
Spectrum (11)	27.90	0.84	0.25	0.35	70.66	100.00
Spectrum (12)	27.61	0.74	0.21	0.46	70.99	100.00
Spectrum (13)	20.97	1.30	0.09	0.04	77.60	100.00
Mean	22.60	1.36	0.59	0.18	75.26	100.00
Standard Deviation	10.57	1.22	0.93	0.16	11.16	
Max.	43.57	4.11	3.22	0.46	98.16	
Min.	1.54	0.18	-0.02	0.01	51.89	

Table 8.17 SEM-EDS line scan results for Colonial Williamsburg sample CW_16 along the 10 data points indicated in Figure 8.56. EDS spectrometer standardised on cobalt before analysis, all points analysed for 30 seconds. Elemental concentrations given in wt% (data normalised to 100%).

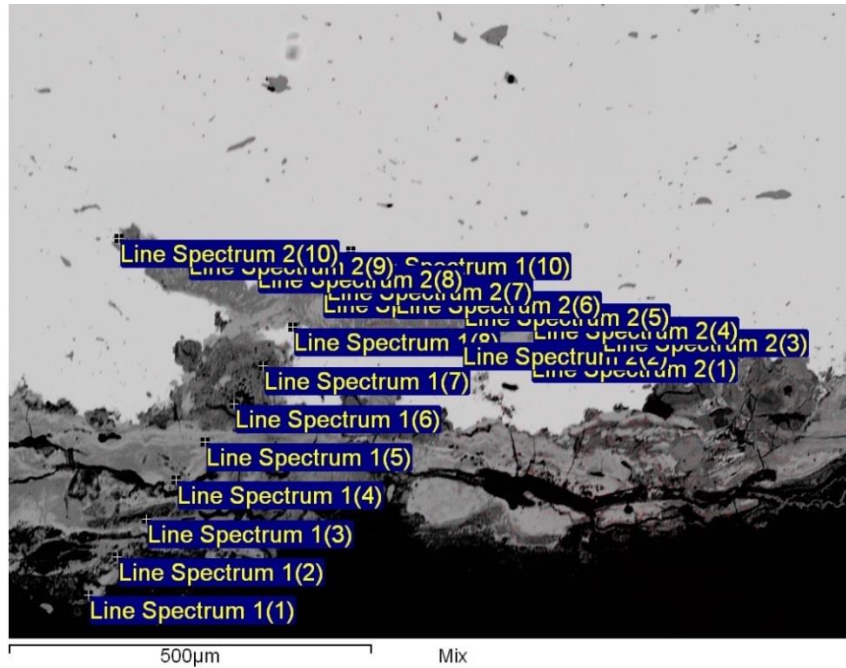


Figure 8.58 SEM (BEI) image of Colonial Williamsburg sample CW_19 with location of EDS line scan (20 data points) across a section of the sample from an interior slag inclusion to the outer CPL edge. Results of the analysis are given in Table 8.17.

CW_19 EDS Line scan (Concentration in wt%-normalised)						
Spectrum	O	Si	P	Cl	Fe	Total
Line Spectrum 1(1)	25.79	0.49	0.36	0.13	73.22	100.00
Line Spectrum 1(2)	32.62	1.21	17.58	0.17	48.42	100.00
Line Spectrum 1(3)	26.92	0.33	0.10	0.07	72.58	100.00
Line Spectrum 1(4)	25.85	0.87	0.56	0.03	72.68	100.00
Line Spectrum 1(5)	26.95	0.90	0.62	0.03	71.51	100.00
Line Spectrum 1(6)	32.50	0.60	3.19	0.04	63.67	100.00
Line Spectrum 1(7)	22.32	1.26	0.31	0.10	76.01	100.00
Line Spectrum 1(7)	13.74	0.11	0.62	0.02	85.51	100.00
Line Spectrum 1(9)	28.35	0.19	0.50	0.06	70.89	100.00
Line Spectrum 1(10)	-0.18	0.04	0.42	0.00	99.73	100.00
Line Spectrum 2(1)	27.60	9.55	5.21	-0.01	57.65	100.00
Line Spectrum 2(2)	27.81	6.85	4.31	0.02	61.01	100.00
Line Spectrum 2(3)	-0.04	0.07	0.44	0.02	99.52	100.00
Line Spectrum 2(4)	26.97	1.05	0.66	0.02	71.31	100.00
Line Spectrum 2(5)	26.15	8.92	8.93	0.01	56.00	100.00
Line Spectrum 2(6)	27.22	0.55	0.84	0.04	71.35	100.00
Line Spectrum 2(7)	26.77	0.53	0.24	0.04	72.41	100.00
Line Spectrum 2(8)	-0.20	0.08	0.27	0.00	99.85	100.00
Line Spectrum 2(9)	-0.16	0.05	0.46	0.00	99.65	100.00
Line Spectrum 2(10)	1.58	0.07	0.19	0.02	98.14	100.00
Mean	19.93	1.69	2.29	0.04	76.06	100.00
Standard Deviation	12.27	2.97	4.25	0.05	15.95	
Max.	-0.20	0.04	0.10	-0.01	48.42	
Min.	32.62	9.55	17.58	0.17	99.85	

Table 8.18 SEM-EDS line scan results for Colonial Williamsburg sample CW_19 along the 10 data points indicated in Figure 8.57. EDS spectrometer standardised on cobalt before analysis, all points analysed for 30 seconds. Elemental concentrations given in wt% (data normalised to 100%).

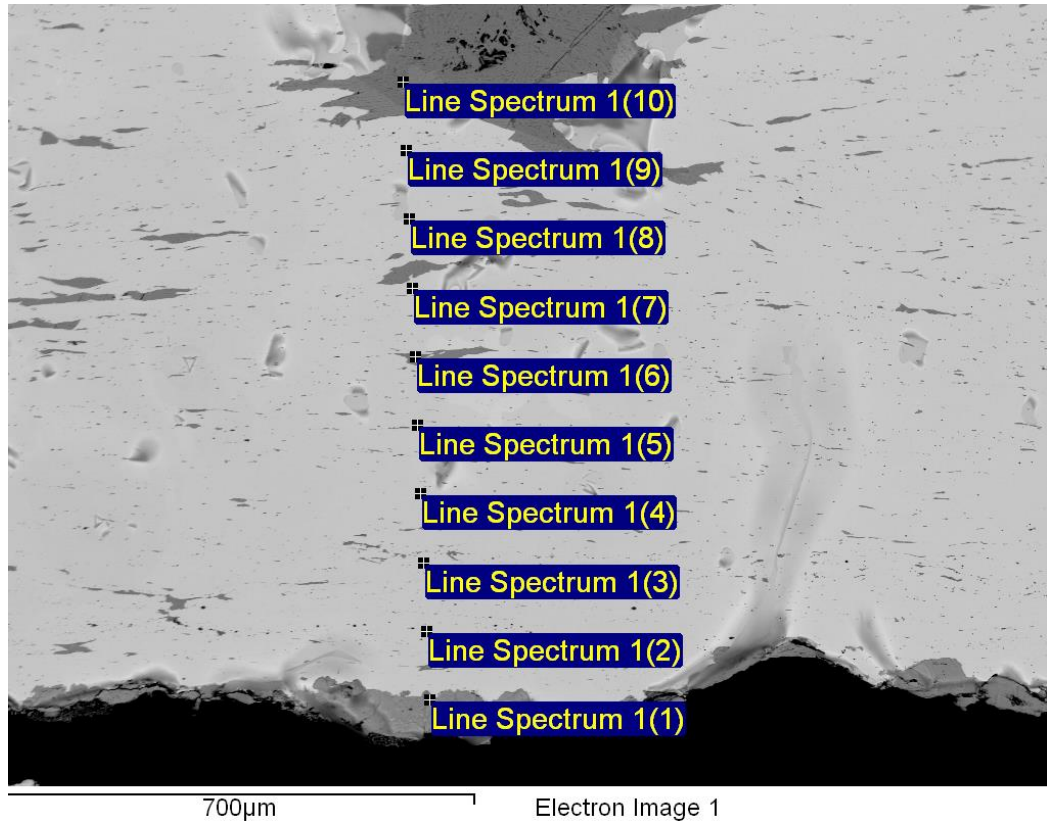


Figure 8.59 SEM (BEI) image of Colonial Williamsburg sample CW_26 with location of EDS line scan (10 data points from upper right to lower left) across a section of the sample from an interior slag inclusion to the outer CPL edge. Results of the analysis are given in Table 8.18.

CW_26 EDS Line scan (Concentration in wt%-normalised)						
Spectrum	O	Si	P	Cl	Fe	Total
Line Spectrum 1(1)	19.64	0.81	0.23	0.14	79.18	100.00
Line Spectrum 1(2)	-0.27	0.22	0.15	-0.01	99.91	100.00
Line Spectrum 1(3)	-0.19	0.07	0.20	0.01	99.91	100.00
Line Spectrum 1(4)	-0.28	0.09	0.32	0.00	99.87	100.00
Line Spectrum 1(5)	-0.30	0.08	0.45	0.02	99.74	100.00
Line Spectrum 1(6)	28.54	19.95	1.42	0.01	50.08	100.00
Line Spectrum 1(7)	-0.19	0.06	0.38	0.05	99.70	100.00
Line Spectrum 1(7)	-0.22	0.11	0.49	0.00	99.62	100.00
Line Spectrum 1(9)	-0.13	0.08	0.25	-0.01	99.81	100.00
Line Spectrum 1(10)	29.75	15.52	2.01	-0.01	52.74	100.00
Mean	7.64	3.70	0.59	0.02	88.06	100.00
Standard Deviation	12.92	7.47	0.62	0.05	20.37	
Max.	29.75	19.95	2.01	0.14	99.91	
Min.	-0.28	0.06	0.15	-0.01	50.08	

Table 8.19 SEM-EDS line scan results for Colonial Williamsburg sample CW_26 along the 10 data points indicated in Figure 8.58. EDS spectrometer standardised on cobalt before analysis, all points analysed for 30 seconds. Elemental concentrations given in wt% (data normalised to 100%)

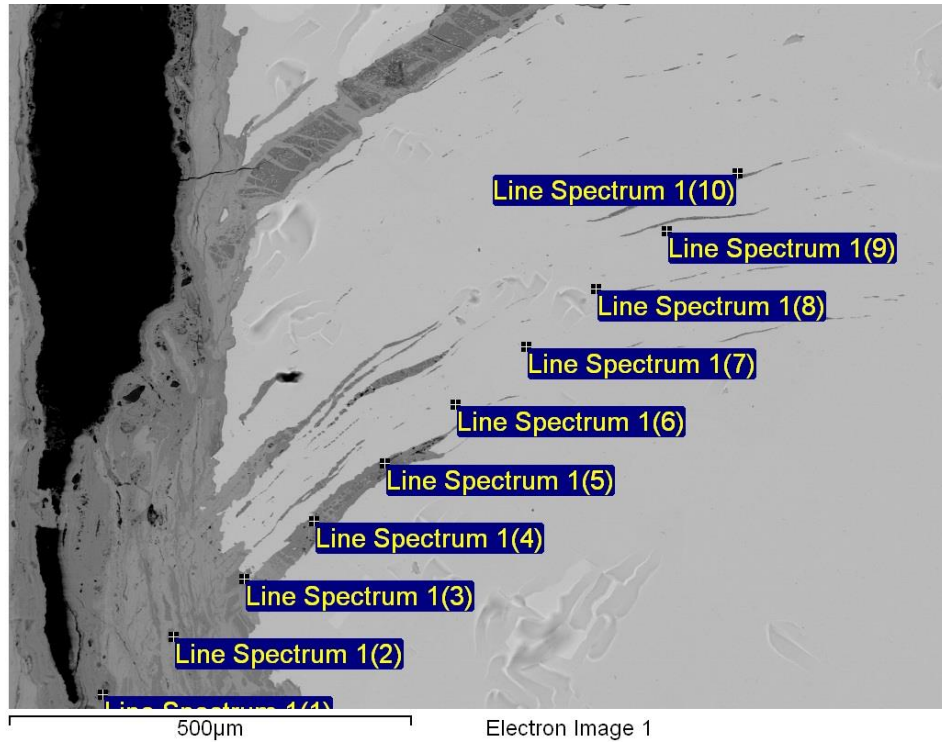


Figure 8.60 SEM (BEI) image of Colonial Williamsburg sample CW_29 with location of EDS line scan (10 data points from upper right to lower left) across a section of the sample from an interior slag inclusion to the outer CPL edge. Results of the analysis are given in Table 8.19.

CW_29 EDS Line scan (Concentration in wt%-normalised)						
Spectrum	O	Si	P	Cl	Fe	Total
Line Spectrum 1(1)	29.49	0.71	0.14	0.16	69.50	100.00
Line Spectrum 1(2)	23.14	0.10	-0.01	0.01	76.76	100.00
Line Spectrum 1(3)	30.24	0.17	0.01	0.07	69.51	100.00
Line Spectrum 1(4)	27.48	2.89	0.21	0.12	69.30	100.00
Line Spectrum 1(5)	31.64	11.41	0.33	3.23	53.38	100.00
Line Spectrum 1(6)	-0.39	0.07	0.03	0.04	100.25	100.00
Line Spectrum 1(7)	-0.21	0.09	0.05	0.02	100.06	100.00
Line Spectrum 1(7)	-0.17	0.06	0.01	-0.01	100.10	100.00
Line Spectrum 1(9)	-0.30	0.04	-0.01	0.04	100.24	100.00
Line Spectrum 1(10)	-0.26	0.06	-0.01	0.00	100.20	100.00
Mean	14.07	1.56	0.08	0.37	83.93	100
Standard Deviation	15.27	3.57	0.12	1.01	18.05	
Max.	-0.39	0.04	-0.01	-0.01	53.38	
Min.	31.64	11.41	0.33	3.23	100.25	

Table 8.20 SEM-EDS line scan results for Colonial Williamsburg sample CW_29 along the 10 data points indicated in Figure 8.59. EDS spectrometer standardised on cobalt before analysis, all points analysed for 30 seconds. Elemental concentrations given in wt% (data normalised to 100%).

8.4.4 X-ray Diffractograms of Synthetic Akaganeite Samples After Treatment (2-10)

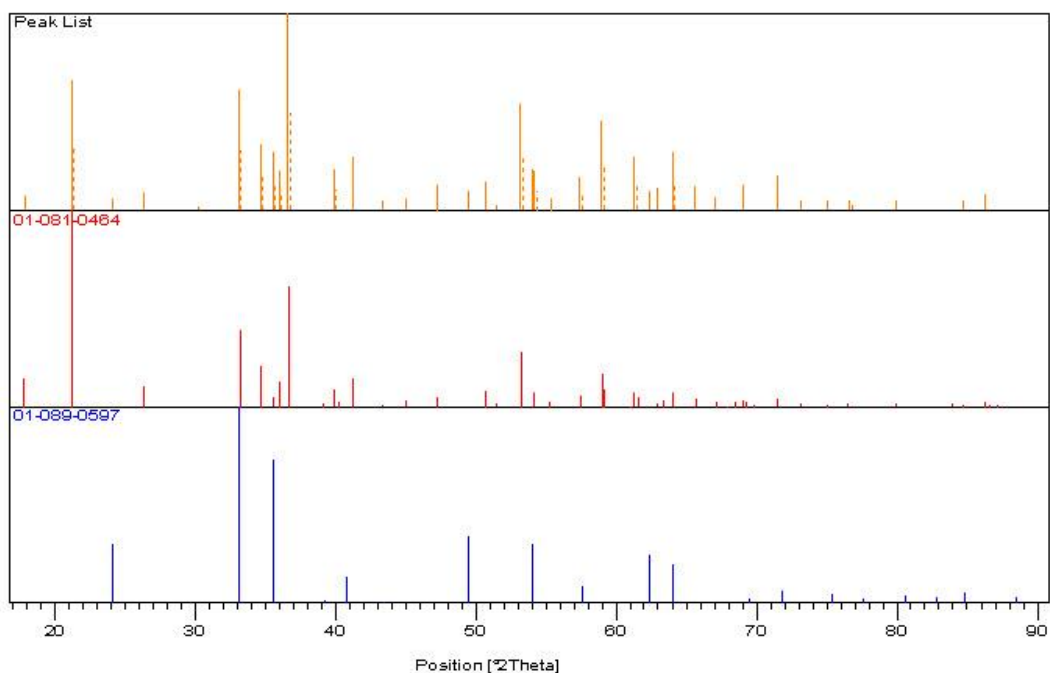


Figure 8.61 XRD stick plot of sample β -FeOOH-AS60-2 after AS60 treatment showing sample pattern (top band) and matching compounds goethite (01-081-0464) and hematite (01-089-0597).

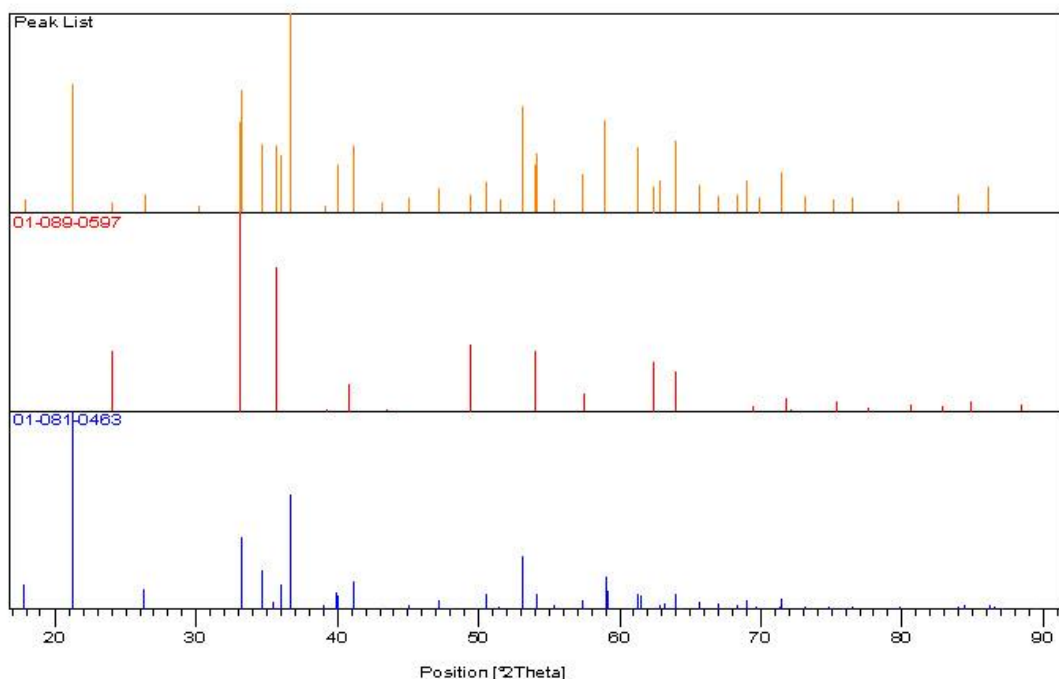


Figure 8.62 XRD stick plot of sample β -FeOOH-AS60-3 after AS60 treatment showing sample pattern (top band) and matching compounds goethite (01-081-0463) and hematite (01-089-0597).

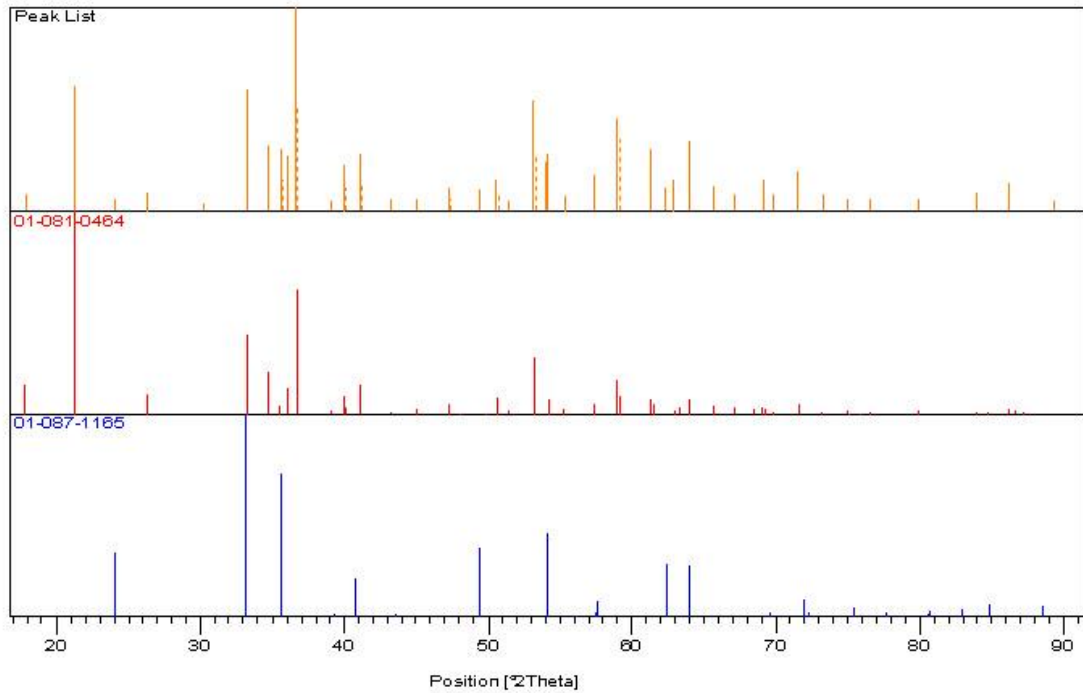


Figure 8.63 XRD stick plot of sample β -FeOOH-AS60-4 after AS60 treatment showing sample pattern (top band) and matching compounds goethite (01-081-0464) and hematite (01-087-1165).

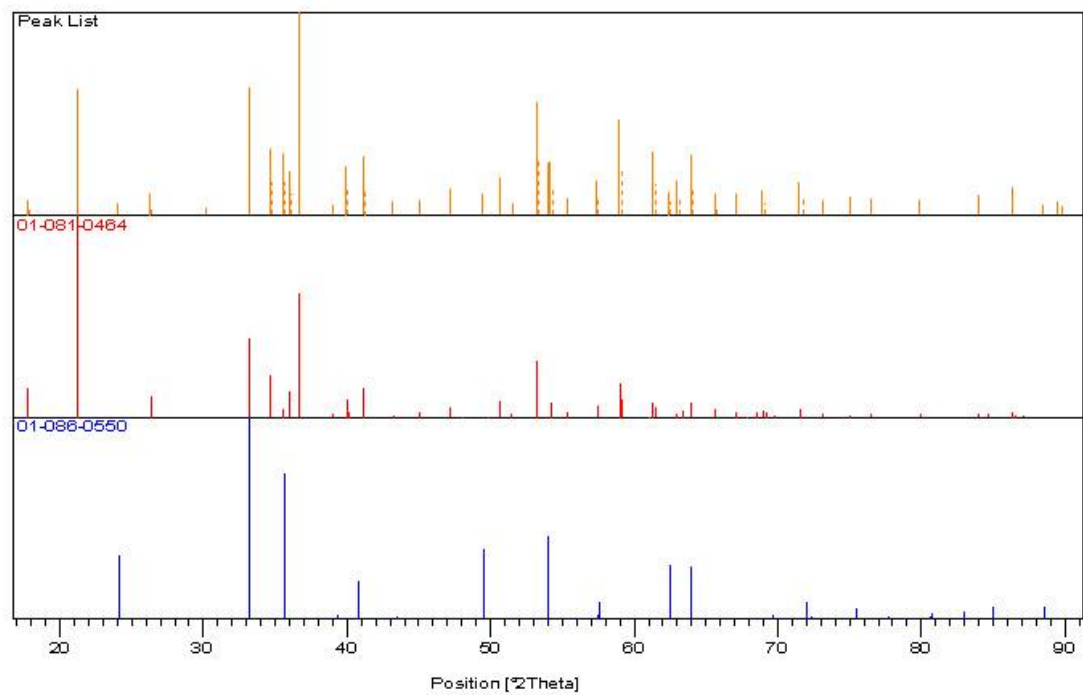


Figure 8.64 XRD stick plot of sample β -FeOOH-AS60-5 after AS60 treatment showing sample pattern (top band) and matching compounds goethite (01-081-0464) and hematite (01-086-0550).

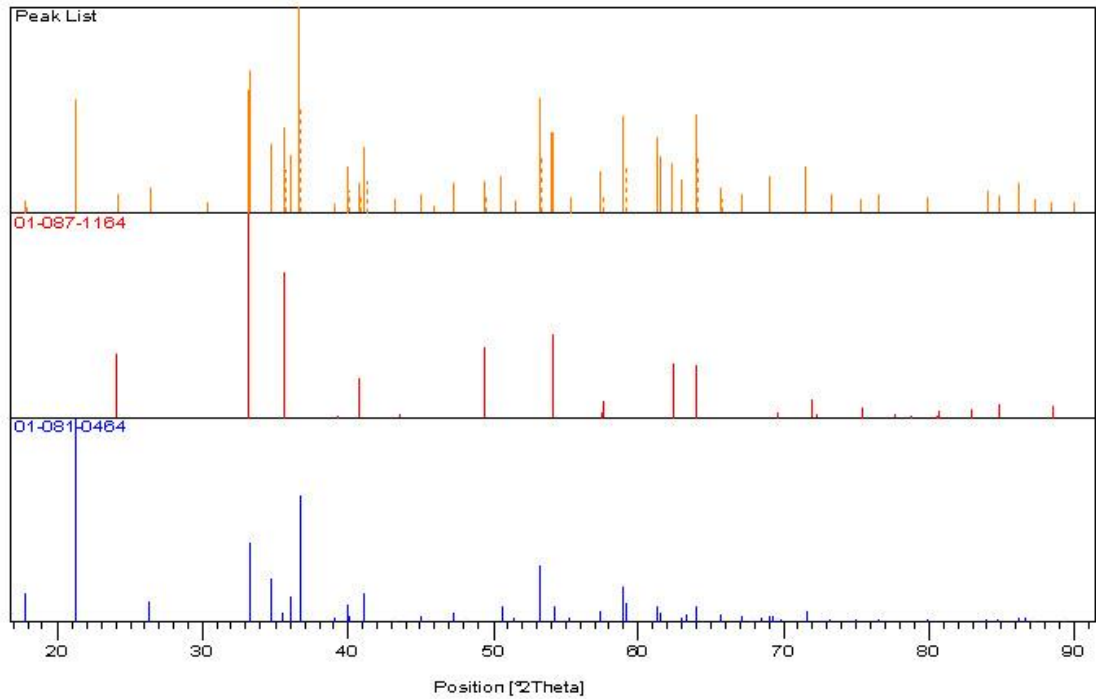


Figure 8.65 XRD stick plot of sample β -FeOOH-AS60-6 after AS60 treatment showing sample pattern (top band) and matching compounds and hematite (01-087-1164) and goethite (01-081-0464).

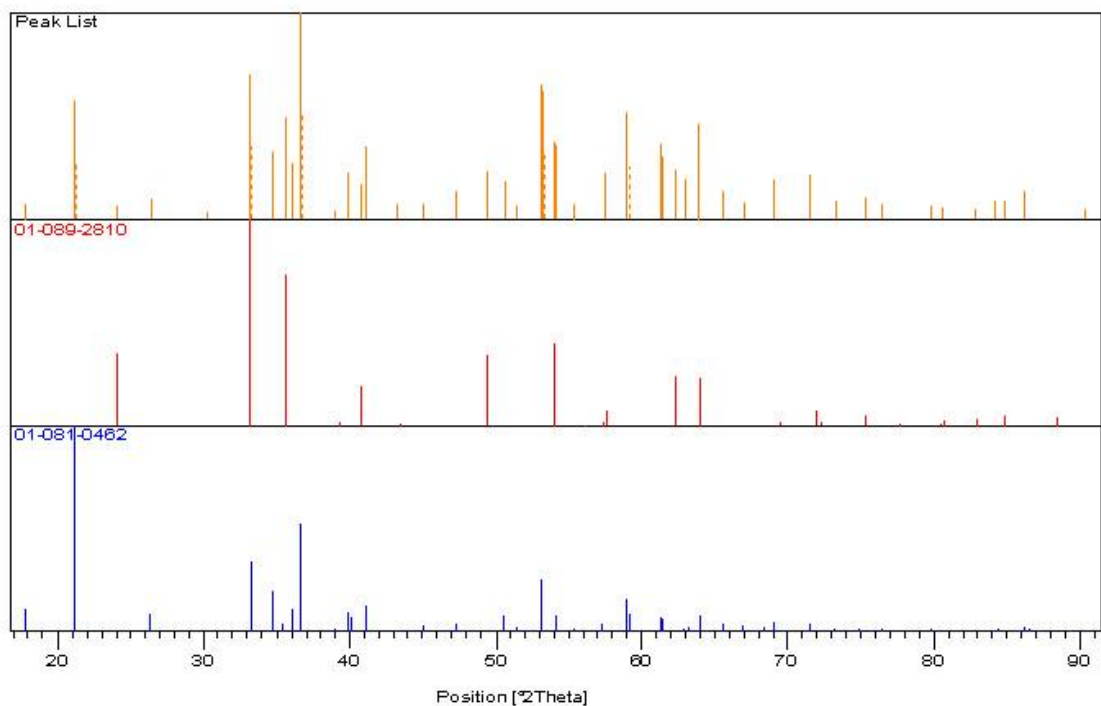


Figure 8.66 XRD stick plot of sample β -FeOOH-AS60-7 after AS60 treatment showing sample pattern (top band) and matching compounds and hematite (01-089-2810) and goethite (01-081-0462).

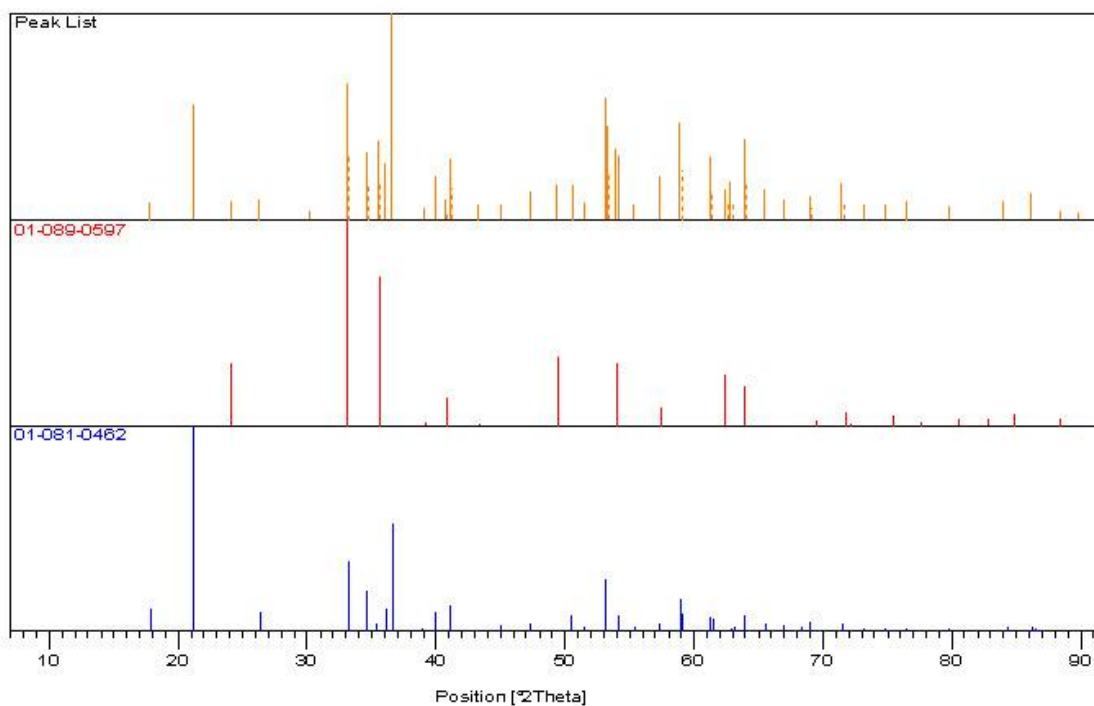


Figure 8.67 XRD stick plot of sample β -FeOOH-AS60-8 after AS60 treatment showing sample pattern (top band) and matching compounds hematite (01-089-0597) and goethite (01-081-0462).

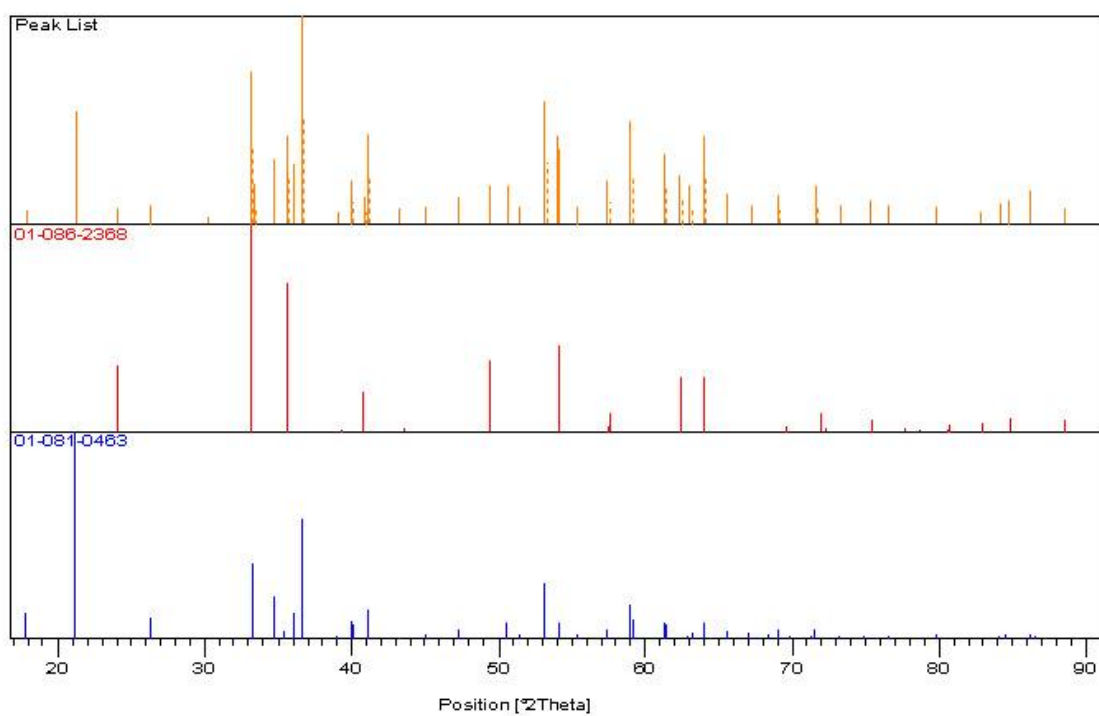


Figure 8.68 XRD stick plot of sample β -FeOOH-AS60-9 after AS60 treatment showing sample pattern (top band) and matching compounds hematite (01-086-2368) and goethite (01-081-0463).

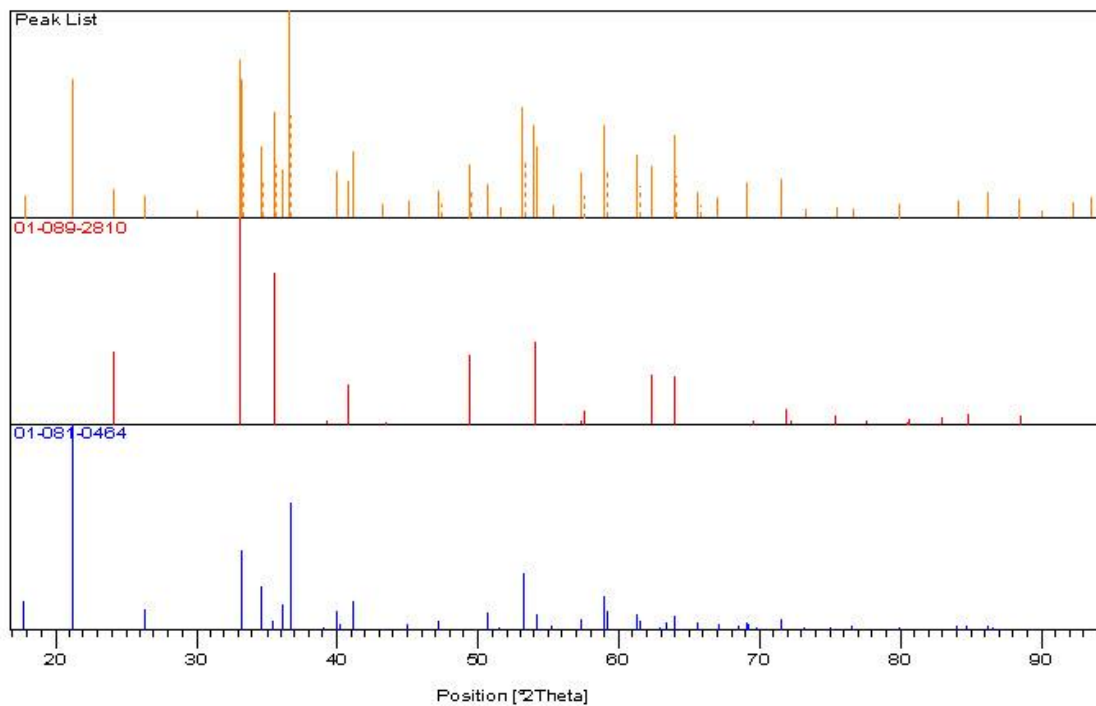


Figure 8.69 XRD stick plot of sample β -FeOOH-AS60-10 after AS60 treatment showing sample pattern (top band) and matching compounds hematite (01-089-2810) and goethite (01-081-0464).

8.5 Appendix 5: Archaeological Contexts of Sample Material

8.5.1 Roman Caerleon

Wrought iron nails from Roman Caerleon used in this study were excavated during 2008 at Caerleon Priory Field (CPF08) under the direction of Dr. Peter Guest (Department of Archaeology and Conservation at Cardiff University) and Andrew Gardiner (Institute of Archaeology, UCL) and the auspices of Cadw, historic environment supervisory body the Welsh Government (Guest and Gardner 2008). The site of Caerleon, the ancient Fortress Isca Augusta, was a major Roman Legionary centre active in the 1st-2nd C AD near Newport, South Wales. Samples for this study were selected from wrought iron nails from secure Roman period contexts kindly made available by Dr. Guest for study.

8.5.2 Colonial Williamsburg

Williamsburg was the 18th C AD capital of the Virginia Colony (now the State of Virginia, U.S.A.) during the British colonial period. The 17-19th C AD historic town and surrounding sites have been the subject of numerous archaeological excavations from the 1920s to the present day and made a large contribution to knowledge of colonial American material culture (Noel Hume 1991).

Wrought iron nails from Williamsburg examined in this study were part of a loan of 100 nails kindly made available for research by Emily Williams, Conservator of Archaeological Materials, and Kelly Ladd-Kostro Associate Curator of Archaeological Collections at The Colonial Williamsburg Foundation (CWF). These nails were selected by Williams from assemblages excavated by CWF archaeologists and come from sites

ranging from the late 17th to mid 19th century excavated between 1960 and 2001. They therefore represent iron production and nail-smithing involving a range of material sources and working techniques. The Colonial Williamsburg nails are from: Bassett Hall, Anderson Forge, Brush Everard, Carters Grove, the Public Hospital, Anthony Hay Shop, Wetherburn's Tavern, Peyton Randolph and Tazewell Hall. Archaeological reports from these sites are available online at:

<http://research.history.org/DigitalLibrary/research-reports/>.

8.6 Appendix 6: Sample Photographs

Caerleon			
Photograph	Sample Number	Find Number	Context
	CAER_01	CPF08 (001)01	CPF08 (001)
	CAER_02	CPF08 (001)02	CPF08 (001)
	CAER_03	CPF08 (001)03	CPF08 (001)
	CAER_04	CPF08 (001)04	CPF08 (001)
	CAER_05	CPF08 (001)05	CPF08 (001)
	CAER_06	CPF08 (001)06	CPF08 (001)
	CAER_07	CPF08 (001)07	CPF08 (001)
	CAER_08	CPF08 (001)08	CPF08 (001)
	CAER_09	CPF08 (001)09	CPF08 (001)

	CAER_10	CPF08 (001)10	CPF08 (001)
	CAER_11	CPF08 (001)11	CPF08 (001)
	CAER_12	CPF08 (001)12	CPF08 (001)
	CAER_13	CPF08 (001)13	CPF08 (001)
	CAER_14	CPF08 (001)14	CPF08 (001)
	CAER_15	CPF08 (001)15	CPF08 (001)
	CAER_16	CPF08 (300)16	CPF08 (001)
	CAER_17	CPF08 (001)17	CPF08 (001)
	CAER_18	CPF08 (001)18	CPF08 (001)
	CAER_19	CPF08 (001)19	CPF08 (001)

	CAER_20	CPF08 (001)20	CPF08 (001)
	CAER_21	CPF08 (001)21	CPF08 (001)
	CAER_22	CPF08 (001)22	CPF08 (001)
	CAER_23	CPF08 (001)23	CPF08 (001)
	CAER_24	CPF08 (300)24	CPF08 (001)
	CAER_25	CPF08 (001)25	CPF08 (001)
	CAER_26	CPF08 (001)26	CPF08 (001)
	CAER_27	CPF08 (001)27	CPF08 (001)
	CAER_28	CPF08 (001)28	CPF08 (300)
	CAER_29	CPF08 (001)29	CPF08 (001)

	CAER_30	CPF08 (001)30	CPF08 (001)
---	----------------	----------------------	--------------------

Colonial Williamsburg			
Photograph	Sample Number	Context Number	Site
	CW_01	01AD-00031AK	Basset Hall
	CW_02	10A-126	Anderson Forge
	CW_03	10F-38D	Anderson Forge
	CW_04	10F-35C	Anderson Forge
	CW_05	10F-42D	Anderson Forge
	CW_06	29F-614	Brush Everard
	CW_07	29F-617	Brush Everard
	CW_08	29F-894	Brush Everard

	CW_09	01AD-00033AS	Basset Hall
	CW_10	Vepco Trench Monitoring	Carter's Grove
	CW_11	CGER-164A-50AA	Carter's Grove
	CW_12	CGER-1740A	Carter's Grove
	CW_13	CGER-1755B	Carter's Grove
	CW_14	CGER-1773F	Carter's Grove
	CW_15	CGER-1902	Carter's Grove
	CW_16	ER-1712E-4C	Public Hospital
	CW_17	ER-243L-28D	Anthony Hay Shop

	CW_18	ER-364B-28D	Anthony Hay Shop
	CW_19	ER-364B-28D	Anthony Hay Shop
	CW_20	ER-1009Q-9NA	Wetherburn's Tavern
	CW_21	ER-1069-9NA	Wetherburn's Tavern
	CW_22	ER-1215R-31AA	Wray
	CW_23	ER-1712A-4CA	Public Hospital
	CW_24	ER-1712B-4C	Public Hospital
	CW_25	ER-1720-4CA	Public Hospital
	CW_26	ER-2334A-4C	Public Hospital

	<p>CW_27</p>	<p>ER-2531P-4C</p>	<p>Public Hospital</p>
	<p>CW_28</p>	<p>ER-2534A-4C</p>	<p>Public Hospital</p>
	<p>CW_29</p>	<p>28G-783R</p>	<p>Peyton Randolph</p>
	<p>CW_30</p>	<p>44B-473</p>	<p>Tazewell Hall</p>